



The  
University  
Of  
Sheffield.

**Aqueous Dissolution of Nuclear Waste  
and Analogue Glasses:  
Dissolution Behaviour, Surface Layers and Vermiform Features**

James T. Mansfield

*A thesis submitted in partial fulfilment for the degree of Doctor of Philosophy*

NucleUS Immobilisation Science Laboratory  
Department of Materials Science and Engineering  
The University of Sheffield

Sponsored by The Engineering and Physical Sciences Research Council (EPSRC) and The National Nuclear Laboratory (NNL) as part of the Next Generation Nuclear (NGN) program

May 2022

# Summary

In the United Kingdom (UK), High Level Waste (HLW) from nuclear energy generation will be incorporated into a glass before disposal in a deep geological facility. However, the ‘Safety Case’ for this depends on our understanding of the dissolution behaviour of such a glass over tens to hundreds of thousands of years. This work aims to contribute to this knowledge by conducting accelerated laboratory dissolution tests and studies of naturally dissolved samples.

Two HLW glasses, the International Simple Glass (ISG) and the UK’s Magnox Waste glass with a 25% waste loading (MW25) were dissolved in ultrahigh quality water via the Materials Centre Characterisation test 1 (MCC-1) and Product Consistency Test B (PCT-B) procedures. The presence of magnesium in MW25 allowed precipitation of clays and thus more rapid dissolution of this glass compared to ISG (which did not contain magnesium). This magnesium variability may also explain alteration layer differences in MCC-1 tests: sodium-depleted layers initially formed on both, but the outer region was enriched in magnesium for MW25 but zirconium-enriched for ISG. Similarly, the later-formed outer magnesium clays on MW25 are absent from ISG where a further ‘scalloped’ inner sodium-depleted region is instead observed.

Basaltic glasses with a variable magnesium-to-calcium ratio were synthesised and dissolved via the above procedures to further investigate this. Again, dissolution rates increased with magnesium content, potentially because the alteration layer on high-magnesium glasses is less passivating due to decreased aluminium content. Aluminium may instead incorporate into the secondary precipitates that form more readily during dissolution of high-magnesium glasses.

Surface layer thickness may be defined as the diameter of the largest sphere which can be entirely enclosed by the layer. Applying a method using this definition to the surface layers generated in the above MCC-1 tests provides thickness measurements comparable to those made using previous, though more subjective, methods. This improved definition also provides surface layer thicknesses for laboratory-dissolved basaltic glasses which are consistent with values from the equivalent naturally dissolved glasses, providing more confidence in laboratory dissolution methods. Finally, the method also implied the innermost HLW glass alteration layer component may account for some differences in basaltic and HLW glass dissolution behaviour.

Worm-like (‘vermiform’) features were observed to form in all of the aforementioned MCC-1 tests. These were more abundant and complex in basaltic glasses, potentially because their formation was more progressed in this case. Features also show highly variable interaction with alteration layer components: the alteration layer partially fills features on basaltic glasses but completely fills the vermiform structures in HLW glasses (where innermost alteration layer components also appear to deform around the structures). Feature formation methods remain unclear, but biological sources are near-impossible and a precursor scratch/crack seems likely. Regardless, features are significant in potentially increasing glass surface areas by up to 40%.

Samples from Dun Deardail vitrified hillfort were proposed as HLW glass analogues. These materials contain glass which is thought to form the highly-vesiculated aluminosilicate regions. By comparison with an undissolved synthesised replica glass, the microcavities and iridescence (initially thought to represent dissolution pits and alteration layers) in these ‘glassy’ areas were re-interpreted as micro-vesicles and surface fracture expressions. However, low density, low atomic number surface layers occur preferentially on potentially water-exposed surfaces and so may represent alteration layers comparable to the iron-rich layers observed within vesicles.

# Acknowledgements

Squillions of people have helped me over my PhD journey, but I cannot name them *all* here (and I'd inevitably forget someone even if I tried to!) So below are just the best of the best! 😊

First, my sincerest thanks goes to Dr Colleen Mann, without whom I would never have even known this PhD existed, let alone started and completed it! Next, I'd like to thank Prof Russell Hand and Prof Claire Corkhill for their outstanding academic supervision and unwavering patience (even after they'd explained the same thing to me for the thousandth time!) Dr Mike Harrison is thanked for his ongoing support and insight, with Dr Clare Thorpe, Dr Martin Stennett, Dr Hajime Kinoshita Dr Amy Gandy and Prof Neil Hyatt providing valuable thoughts and recommendations throughout. My thanks also extend to the technical staff who made this work possible: Dr Lisa Hollands assisted with glass melting and provided outstanding pastoral support; whilst Tes Monaghan provided insight into sample preparation and was great company during long polishing stints. Dr Ria Mitchell is thanked for conducting XCT scans and providing valuable advice on experimental design, with Dr Dan Sykes (Manchester University) also thanked for collecting XCT data and for introducing me to the '*Dragonfly*' software used in this work. Michelle Higgins (Open University) is thanked for thin section preparation.

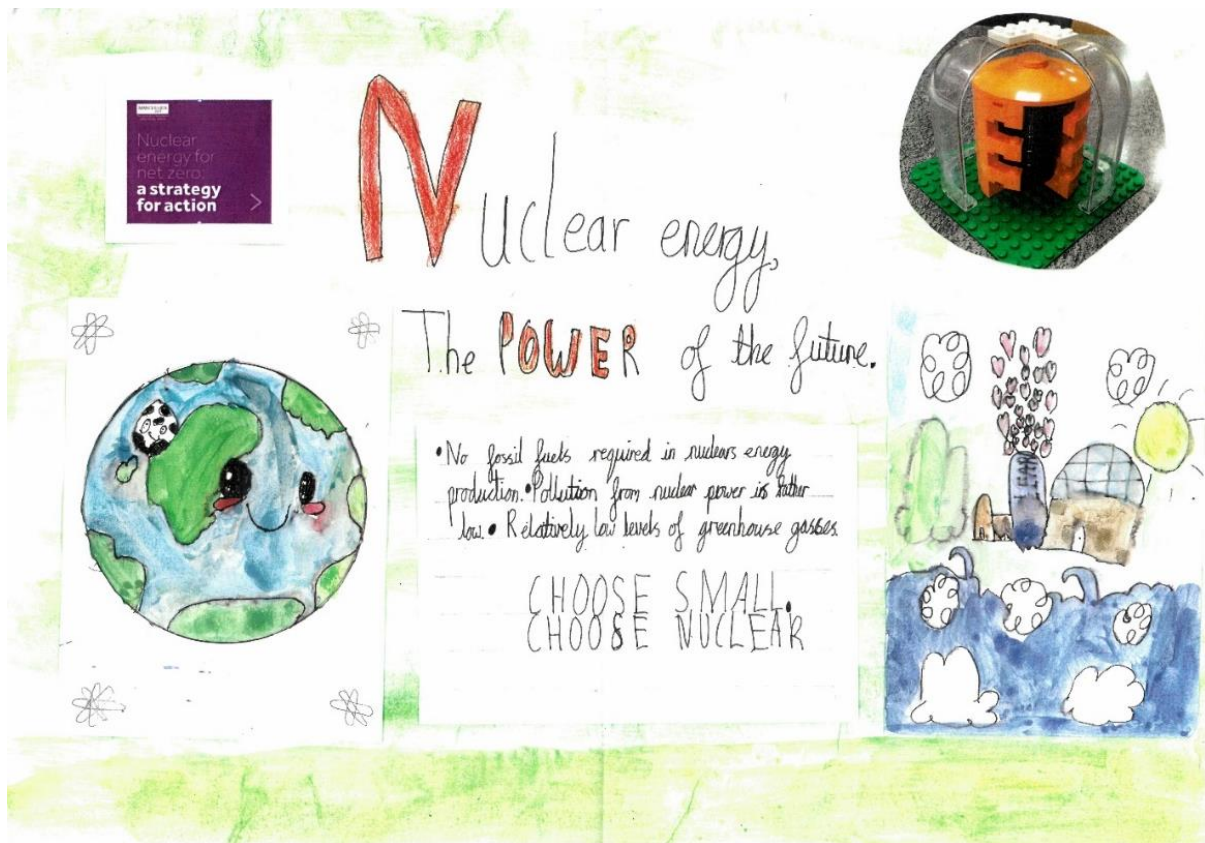
The entire Immobilisation Science Laboratory (ISL) team are thanked for their support. Dr Josh Radford provided guidance and good humoured discussions, whilst Dr Dan Geddes provided plentiful distraction and a warm welcome from day one. Dr Sam Walling, Dr Laura Gardner and Dr Amber Mason are thanked for keeping the laboratories operational and for their support and guidance, with Dr Adam Fisher thanked for his advice. Tom Wilkinson provided great office company, with Dan Parkes, Jenny Ayling and Rachel Crawford thanked for their friendship. Dr Ramya Ravikumar is thanked for her kindness, with Dr James Vigor thanked for his support and encouragement. My thanks also to Lucas-Jay, Clive, Rita, Antonia, Lucy, Lewis, Dan, Chris, Max, Gary, Ishy, Sarah, Merve, Jess, Joe, Liam and Shaun. Julie the cleaner is thanked for her company in the mornings and for always welcoming us so warmly.

Everyone at the Next Generation Nuclear CDT is thanked for their support and encouragement. This includes Prof Scott Heath and Mark Clegg; as well as Matt Jackson, Olivia Voyce, Dan Massey, Connor McBride, Alex Jackson and Sarah Butterworth. Hannah Smith, the most supportive person I know, deserves more 'Thank You's' than can ever be said. You are 'boss'.

Colleagues from elsewhere are also thanked. Dr Amanda-Jane Dolan (University of Stirling) is thanked for providing hillfort samples, with Dr John McCloy (Washington State University) proving insight into these and the opportunity to visit other hillforts. Dr Jamie Weaver and Dr Carolyn Pearce (Pacific Northwest National Laboratory) are thanked for their support and insight into hillfort materials and bio-alteration. Dr Cristina Persano (University of Glasgow) and Prof Adrian Chandler (University College London) are thanked for their previous academic supervision and for their patience and encouragement as I learned the scientific method.

Thank you, also, to my other friends and family. Thanks to my dad for his unrelenting support and interest in my studies, and to my mum for teaching me that thinking differently could be such a great quality. My brother is thanked for who knows what, with his daughter (Willow) thanked for her motivational artwork. My cousins provided entertaining respite from PhD life, with aunties and uncles delivering moral support. Friends from 'back home' (including Cat, Connall, Chris, Agnes, Ellen, Daisy and Charlotte) are thanked for their support through some interesting times; with Ben, Paul, Chrissie and Justyn thanked for their support from Sheffield.

Finally, I am also immeasurably grateful to the wider public and those who have supported my interactions with them. Rachel Law provided ample opportunities to interact with enthusiastic new audiences, with Tracy Badham and Mike Brophy similarly supportive in this. Without you I would never have enjoyed my PhD as much as I have. My thanks, also, to “the public” themselves: You supported me through nine years of university education, listening to my countless science ramblings and encouraging me to continue doing what I enjoy. Thank you. And my absolute final *FINAL* thanks go to the school pupils and young people who I have chatted to about science... You are my source of energy, the reason I love what I do, and the reason I have hope for the future of our planet.



**Above:** Poster, drawn by a Year 3 pupil (aged 7-8), presented to the author of this work during an outreach session at a local school. Note the illustrator’s belief that in the future the world will be happy love-filled place powered by nuclear energy.

(Image shared with permission).

# Contents

Summary.....	i
Acknowledgements .....	ii
Contents .....	iv
<b>1. Introduction .....</b>	<b>1</b>
1.1. Background .....	1
1.2. Aims and objectives .....	2
1.3. Thesis structure .....	2
<b>2. Literature Review .....</b>	<b>4</b>
2.1. Standard model of glass dissolution.....	4
2.2. Role of magnesium in glass dissolution.....	6
2.3. Glass alteration layers .....	8
2.3.1. Formation and destruction .....	8
2.3.2. Properties .....	9
2.3.3. Passivation mechanism .....	9
2.4. Localised attack in glass dissolution .....	10
2.4.1. Pits and pitting .....	10
2.4.2. Vermiform features.....	11
2.5. Nuclear waste glass analogues .....	15
2.5.1. Basaltic glass.....	16
2.5.2. Vitrified hillfort materials .....	17
2.5.3. Simplified and inactive nuclear waste glass analogues .....	18
<b>3. Experimental Methods .....</b>	<b>20</b>
3.1. Sample acquisition & synthesis .....	20
3.1.1. ISG acquisition.....	20
3.1.2. Hillfort sample acquisition.....	21
3.1.3. Basaltic glass batching .....	22
3.1.4. Replica hillfort glass batching .....	23
3.1.5. MW25 glass batching .....	23
3.1.6. Glass melting .....	24
3.2. Dissolution methodology .....	25
3.2.1. MCC-1 .....	25
3.2.2. PCT-B .....	27
3.2.3. Leachate normalised mass loss calculations .....	28
3.3. Post-dissolution sample preparation.....	29
3.3.1. SEM, Raman & XRD sample preparation .....	29
3.3.2. XCT sample preparation .....	30
3.4. Characterisation/Analytical methods .....	32
3.4.1. X-ray Diffraction .....	32
3.4.2. Scanning Electron Microscopy and Energy Dispersive X- ray Spectroscopy...33	
3.4.3. Raman Spectroscopy.....	35
3.4.4. X-ray Computed Tomography .....	36
3.4.1. Pycnometry .....	39
3.4.2. Inductively Coupled Plasma Optical Emission Spectroscopy .....	41
3.4.3. pH measurement .....	42

3.4.4.	Geochemical modelling .....	43
3.4.5.	Optical Microscopy .....	43
<b>4.</b>	<b>Dissolution of Simulant and Simplified HLW Glasses.....</b>	<b>44</b>
4.1.	Introduction .....	44
4.2.	Results .....	45
4.2.1.	Pristine glass characterisation .....	45
4.2.2.	pH.....	47
4.2.3.	Normalised mass losses .....	48
4.2.4.	SEM EDS analysis .....	52
4.2.5.	MCC-1 surface layer thickness analysis .....	66
4.2.6.	XRD .....	68
4.3.	Discussion of Results .....	69
4.3.1.	Pre-dissolution characterisation .....	69
4.3.2.	MCC-1 experiments.....	69
4.3.3.	PCT-B experiments.....	77
4.4.	Summary .....	81
<b>5.</b>	<b>The Role of Magnesium in Basaltic Glass Dissolution .....</b>	<b>83</b>
5.1.	Introduction .....	83
5.2.	Results .....	84
5.2.1.	Pristine glass characterisation .....	84
5.2.2.	pH.....	86
5.2.3.	Normalised mass losses .....	87
5.2.4.	SEM EDS analysis .....	90
5.2.5.	MCC-1 surface layer thickness analysis .....	99
5.2.6.	XRD .....	99
5.2.7.	XCT.....	100
5.3.	Discussion of Results .....	101
5.3.1.	Pre-dissolution characterisation .....	101
5.3.2.	MCC-1 experiments.....	102
5.3.3.	PCT-B experiments.....	105
5.4.	Summary .....	108
<b>6.</b>	<b>Surface Layer Thickness Quantification.....</b>	<b>109</b>
6.1.	Introduction .....	109
6.2.	Technique and literature review .....	109
6.2.1.	Alteration layer thickness estimation via leachate analysis .....	109
6.2.2.	Alteration layer thickness estimation via imaging techniques.....	110
6.2.3.	Alternative alteration layer thickness measurement techniques .....	113
6.3.	Methods.....	114
6.3.1.	Image segmentation .....	115
6.3.2.	Image analysis.....	116
6.3.3.	Data treatment/analysis .....	116
6.4.	Results .....	117
6.4.1.	Measurement location .....	117
6.4.2.	Method comparison .....	117
6.4.3.	Comparison with other works .....	120
6.5.	Discussion .....	122

6.5.1.	Measurement location .....	122
6.5.2.	Alteration layer thickness estimation via leachate and monolith analysis.....	122
6.5.3.	Application of the Sphere Method to XCT and SEM.....	123
6.5.4.	The Sphere and Ray Methods .....	123
6.5.5.	Localised attack/the effect or perturbations .....	124
6.5.6.	Comparison with other works .....	125
6.6.	Summary .....	127
<b>7.</b>	<b>Vermiform Features .....</b>	<b>129</b>
7.1.	Introduction .....	129
7.2.	Results .....	129
7.2.1.	SEM-BSE.....	130
7.2.2.	SEM-EDS .....	135
7.2.3.	XCT.....	135
7.3.	Discussion .....	137
7.3.1.	Feature comparison .....	137
7.3.2.	XCT and 3D feature morphology .....	139
7.3.3.	Significance of vermiform features .....	140
7.3.4.	Origin and formation of ‘typical’ (simple) vermiform features.....	142
7.3.5.	Origin and generation of atypical vermiform features.....	144
7.3.6.	Chemical garden experiments.....	145
7.4.	Summary .....	146
<b>8.</b>	<b>Potential Alteration Layers &amp; Dissolution Features in Vitrified Hillfort Materials</b>	<b>147</b>
8.1.	Introduction .....	147
8.2.	Results .....	148
8.2.1.	XRD .....	148
8.2.2.	Visual sample inspection .....	148
8.2.3.	SEM-EDS .....	149
8.2.4.	Optical microscopy .....	150
8.2.5.	XCT.....	151
8.3.	Discussion .....	154
8.3.1.	Bulk sample characterisation .....	154
8.3.2.	Identification and evaluation of potential dissolution features .....	155
8.3.3.	Absence of dissolution evidence is not evidence of dissolution absence .....	158
8.4.	Summary .....	159
<b>9.</b>	<b>Concluding Remarks and Future Work.....</b>	<b>160</b>
9.1.	Conclusions of work to date.....	160
9.2.	Suggestions for further work.....	162
<b>10.</b>	<b>References .....</b>	<b>164</b>
<b>11.</b>	<b>Appendix I: XCT Analysis Method.....</b>	<b>190</b>
11.1.	Data segmentation .....	190
11.2.	Statistical treatment .....	192
11.3.	Method verification .....	192
11.4.	Sensitivity/error analysis .....	193

# 1. Introduction

## 1.1. Background

Nuclear power provides a reliable source of low-carbon electricity [1] and generated ~15% of the United Kingdom's electricity in 2021 [2]. However, similar to all other energy generation mechanisms, nuclear energy production generates waste [3].

This waste, known as nuclear waste, accounts for the majority of the five million tonnes (4,560,000 m<sup>3</sup>) of radioactive waste in the UK, with the remainder arising from defence, research and medical activities [4]. A small proportion (< 0.1%) of this total waste is heat-generating High Level Waste (HLW) which emits considerable quantities of ionising radiation and thus poses a potential threat to health/life [5]. This threat is significant and will remain higher than that posed by naturally occurring radioactive materials for several hundred thousand years [3]. Combined, the magnitude and longevity of this hazard necessitates isolation of HLW from humans and nature for tens to hundreds of thousands of years [6].

The internationally favoured approach to achieve this is via disposal in an engineered underground facility termed a Geological Disposal Facility (GDF) [6]. This solution, termed the 'Geological Disposal' concept, is augmented with the 'Multi-barrier' concept (Figure 1.1), to ensure HLW remains contained for the required durations. This is achieved using an entire suite of engineered and natural systems and materials (Figure 1.1) to reduce or prevent the release of potentially harmful chemical elements into the anthropo/biosphere [3].

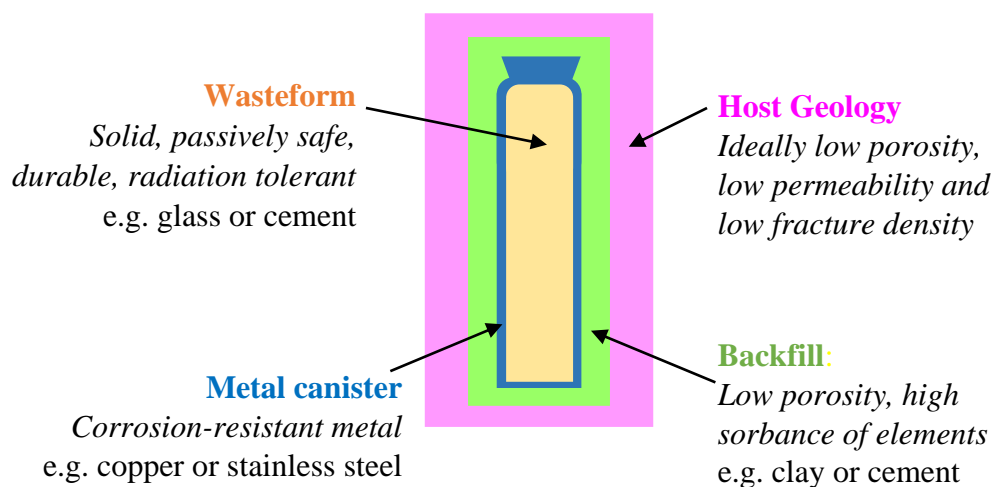


**Figure 1.1:** The multibarrier concept of nuclear waste disposal [3] showing the four main components ('barriers'), the required properties of these, and some example materials

Of these systems, arguably the innermost 'wasteform' barrier is the most crucial because the degradation of this ultimately controls release of potentially harmful radioactive elements [3]. Borosilicate glass is currently used for this purpose in the UK [7] and is the internationally favoured option owing to its high chemical-, mechanical-, and radiation-stability, its well-established manufacturing route and its ability to space-efficiently incorporate many of the elements within HLW [8]. However, assessing the potential for degradation, via dissolution, of this glass wasteform over tens to hundreds of thousands of years is crucial if we are to demonstrate that nuclear waste can be safely stored over the required durations [9].

## 1.2. Aims and objectives

This work aims to increase the scientific community's understanding of glass dissolution from a nuclear waste disposal perspective. To achieve this, various objectives have been established:

- Investigate the dissolution of HLW glasses in a simple aqueous system via laboratory testing; providing comparisons for other works and developing dissolution models
- Explore the role of magnesium (an element uniquely high in the UK's HLW) in glass dissolution via laboratory dissolution of a synthesised basaltic glass series with variable magnesium content
- Use basaltic glasses to gain further insight into glass dissolution processes
- Elucidate the properties and role of the layers developed on the aforementioned glasses via characterisation and development of an improved measurement method
- Identify, characterise and compare the 'worm-like' (vermiform) features which form on the surface of dissolved glasses; compiling previous and current examples of these, assessing their potential influence on glass dissolution and discussing their potential formation mechanisms
- Determine if and how materials collected from Dun Deardail vitrified hillfort can provide insight into glass dissolution by verifying and locating glassy material and seeking evidence of its dissolution

## 1.3. Thesis structure

This thesis comprises the following chapters:

Following this introduction, chapter two reviews the academic community's current understanding of glass dissolution. This includes a description of the most widely agreed upon kinetic model of glass dissolution and the potential role of magnesium in this. Glass alteration layers, a crucial component of this model, are also reviewed in terms of their formation, properties and potential effects on dissolution. Localised attack features generated during glass dissolution are then examined, with a particular focus on vermiform features. Finally, the value of using materials to analogue HLW glass dissolution is justified, with the role of these in the nuclear waste disposal safety case outlined.

Chapter three thoroughly outlines the experimental methods used in the current investigations, providing sufficient detail to allow result replication. Sample production and acquisition is described along with the methods used to dissolve some of these. The treatment and analysis of the resulting data, leachates, and samples following their dissolution is then summarised, with a detailed description of the instrumental methods and parameters used to achieve this.

Results from the aqueous dissolution of HLW glasses are outlined in chapter four. These glasses include the International Simple Glass (ISG) and a simulant of the UK's Magnox Waste (or Mixed Windscale) HLW glass with a 25% waste loading (MW25). Both of these were dissolved via the Materials Characterisation Centre test one (MCC-1) and Product Consistency Test B (PCT-B) accelerated laboratory dissolution methodologies, with a pure water leachate. Leachants and post-dissolution glasses from these experiments are analysed and compared in order to develop a dissolution model for both glasses.

In chapter five, results from identical accelerated dissolution experiments performed on a basaltic glass series with variable magnesium and calcium contents are presented. PCT-B experiments were conducted on all five glasses from the suite (comprising basaltic glasses with a magnesium-to-calcium ratio of 0:100, 30:70, 50:50, 70:30 and 100:0), with MCC-1 conducted on only the end- and mid-member compositions. Results including the dissolution rates and any surface layers generated during these experiments are discussed and compared, with the reliability of results from the two dissolution methodologies also compared.

Chapter six considers methods used to measure glass alteration layer thicknesses, evaluating previous techniques before proposing a new method. Results generated via this new method are compared to those generated by other measurement methods to gauge method reliability. These results are also re-presented alongside data from longer-term natural experiments to gauge whether laboratory dissolution techniques can adequately simulate natural processes.

Vermiform features are investigated in chapter seven. These features (observed on basaltic and HLW glasses dissolved via the aforementioned MCC-1 procedure) are fully characterised and compared, both in two- and three-dimensions. The potential impact of these features on glass dissolution is then discussed and estimated, before their formation mechanism is considered.

The final results chapter investigates what, if anything, materials from Dun Deardail vitrified hillfort may reveal about long-term glass dissolution processes. Samples are characterised via microscopy, tomography and X-ray Diffraction (XRD); with evidence of glassy material and its alteration sought. To elucidate if observed features (pits and iridescence) may have formed via dissolution, results are compared to those from an undissolved glass which was synthesised to replicate the glassy material within the hillfort materials. Similarly, the potential for observed surface layers to have been formed via dissolution was assessed by analysing layer occurrence locations relative to the water-accessibility of surfaces.

The concluding chapter provides a final discussion of the aforementioned topics, summarising the new glass dissolution understanding that has been achieved. Any implications this new knowledge may have on the nuclear waste disposal safety case are stated, with suggestions for future avenues of investigation also presented.

In addition, Appendix I provides an overview of the method used to assess whether layers observed in X-ray Computed Tomography (XCT) of hillfort materials (as in Chapter 11) may have formed via dissolution. This appendix outlines how images were segmented, quantified and statistically treated. Techniques used both to verify method reliability and estimate errors are also presented.

## 2. Literature Review

### 2.1. Standard model of glass dissolution

Aqueous glass dissolution can be subdivided into the three phenomenological regimes, as shown in Figure 2.1. Stage I is known as the ‘Initial’ or ‘Forward Rate’; Stage II is termed the ‘Residual Rate’; and Stage III is otherwise known as ‘Rate Resumption Regime’[10].

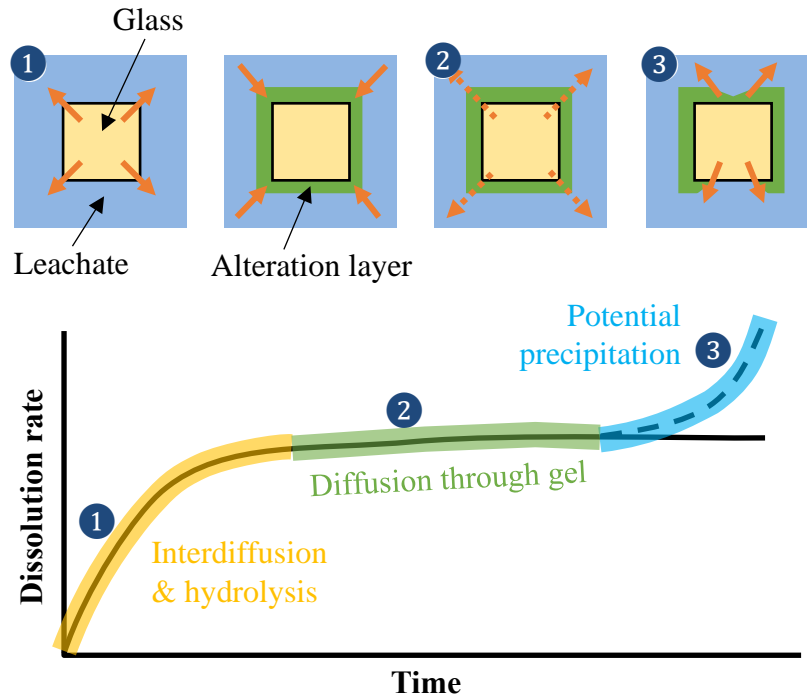
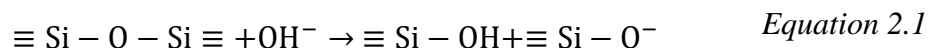


**Figure 2.1:** The three kinetic regimes of glass corrosion, demonstrated schematically (above) and as a simplified graph (below).

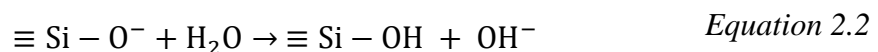
Two processes occur during Stage I: interdiffusion and hydrolysis.

Interdiffusion, or ion exchange, occurs as the inward diffusion of positively charged water species ( $\text{H}_2\text{O}$  and  $\text{H}_3\text{O}^+$ ) causes the concurrent outward diffusion of glass modifier cations (such as alkali metals) in order to maintain electric neutrality [11]–[15]. This selective release of alkalis is aided by the low stability (low energy of hydration) of silicon-oxygen-alkali bonds [15], and leaves a hydrated (water-enriched) glass layer.

The hydroxyl ions ( $\text{OH}^-$ ) formed during interdiffusion increase the solution pH [15], [16] and cause rapid hydrolysis of the covalent bonds linking oxygen with network forming elements such as silica:



This effect is then amplified via positive feedback, as the  $\text{Si-O}^-$  from Equation 2.1 can combine with water molecules to produce another hydroxyl ion:



which can then hydrolyse another siloxane bond as in Equation 2.1 [17]. Eventually, once all four bonds on the silica tetrahedron have been hydrolysed, an orthosilicic acid molecule ( $\text{Si}(\text{OH})_4$ ) is released into the solution.

In a static/closed system, dissolution will continue in this way until the concentration of orthosilicic acid in the solution reaches saturation. At this point an amorphous silica alteration layer precipitates on the glass surface [11], [12], [18] and the dissolution rate then falls during a ‘rate drop’ phase. Dissolution rates are likely limited during this phase by affinity and/or protective layer effects. In the former, as the solution concentration of silicic acid reaches saturation there is a reduced thermodynamic driving force for dissolution [19]. In the latter, the alteration layer formed on the glass surface may act as a transport barrier – minimising ion exchange between the glass and solution [20]–[23]. This may be encouraged by re-organisation of the gel-layer to minimise porosity [16]. Most authors consider both affinity and protective effects as contributing factors to the rate drop (e.g. [20], [24]), [25]); however, some instead favour the chemical affinity mechanism (e.g. [26], [27]) or protective gel theory (e.g. [28]).

Following the rate drop, dissolution is slowed by three to four orders of magnitude (compared to initial rates) during the ‘Residual Rate’ [16], [29], [30]. Here, two mechanisms are operative: secondary phase precipitation can promote dissolution, whilst limited interdiffusion through the alteration layer can impede it [12], particularly if the alteration layer densifies.

Silicate mineral precipitation consumes elements from both the solution and the alteration layer. This leads to a dual-effect: consumption of leachate elements promotes glass network hydrolysis [31], [32]; whilst consumption of network formers in the alteration layer reduces the layer’s ability to passivate [12], and/or leads to its continuous destruction and reformation [33], [34]. However, during Stage II, slowed interdiffusion (relative to initial rates) can act to counterbalance these effects. Decreased interdiffusion may be associated with alteration layer pore-closure [34], [35], other passivating layer property changes [36], [37], or silica-saturation of the pore solution in the interdiffusion zone [36]; however insufficient evidence exists to determine which of these dominates [10], [24].

A third “Rate Resumption” stage can - in some cases - follow, with dissolution resuming at rates approximately comparable to those in Stage I [38], [39]. This appears more probable in glasses with elevated Ca, Al, Fe or Mg (Section 2.2); and in high pH (>10.5), high temperature (>90 °C), and/or high sample surface area to leachant volume ratio (SA:V) systems [11], [16], [40], [16]. Stage III is typically hypothesised to result from precipitation of silicate minerals at the gel-solution interface [16], [39], [41]; however other explanations are speculated (see [16]).

Precipitates, like those formed during Stage III, are unlikely to offer any protection to the dissolving glass [42]. Instead, their precipitation is commonly hypothesised to promote accelerated dissolution by consuming elements from the alteration layer and thereby decreasing its passivating ability [10], [11], [39], [42], [43]. Some argue a different mechanism for this, however, whereby secondary phase precipitation increases the thermodynamic driving force for further glass dissolution by consuming  $\text{H}_4\text{SiO}_4$  from the leachant [40], [44]. This theory is less widely accepted, however, because  $\text{H}_4\text{SiO}_4$  consumption has not yet been shown to cause dissolution rates to climb to rates *comparable in magnitude* to forward rates [45], [46].

Typically, secondary phases are aluminosilicate compositions [42], however experimental parameters (including glass and leachant composition, temperature and time) strongly control this. Zeolites (particularly analcime and phillipsite) and clays (especially smectites) are most

common [15], [16], [47]. Experimentally determining minerals precipitation rates for these remains challenging, but accelerated dissolution testing can allow identification of probable phases [40]. Predicting which secondary phases will precipitate is paramount, because these strongly control dissolution rates and/or the occurrence of rate resumption [46].

## 2.2. Role of magnesium in glass dissolution

A comparison of international nuclear waste compositions (Table 2.1) illustrates that the UK's HLW is uniquely elevated in magnesium [48]. This element, entrained during spent fuel re-processing, is derived from the Magnox alloy used to clad nuclear fuel in the UK [49], [50].

Oxide (wt%)	USA (Hanford)	UK (Magnox)	France (UOX1)	Belgium (SM58)	Russia (Myack)	Japan (Tokaih)
Al <sub>2</sub> O <sub>3</sub>	-	19.6	-	-	-	-
Cr <sub>2</sub> O <sub>3</sub>	1.21	1.6	3.15	-	0.58	1.69
Fe <sub>2</sub> O <sub>3</sub>	29.09	10	18.06	10.81	6.07	9.02
K <sub>2</sub> O	-	-	-	-	22	-
MgO	-	21.6	-	-	2.07	-
Na <sub>2</sub> O	15.15	-	-	33.33	27.98	16.46
NiO	0.6	1.2	2.54	0.91	3.39	1.48
P <sub>2</sub> O <sub>5</sub>	1.52	-	1.76	-	-	0.93
FPOs	38.48	44.4	72.24	54.95	37.91	65.01
Actinides	13.95	1.6	2.25	-	-	5.41

**Table 2.1:** Comparison of International HLW compositions, on a weight percent (wt.%) calcine oxide basis. Note that the UK's Magnox waste is uniquely high in magnesium (highlighted in yellow). Table edited from [51] and references therein. FPO refers to Fission Product Oxides.

This elevated magnesium is widely considered to limit the durability of UK HLW glass [52], [53] and can explain differences observed between the French nuclear waste glass and its inactive analogue [54]. However, the mechanistic reason for this is unclear and requires further research. Furthermore, studies investigating whether similar effects can be noted in other glasses (including analogues such as basaltic glasses) remain lacking.

Magnesium content may have little effect on Stage I behaviour, with variable Mg:Ca ratios having minimal effect on the initial dissolution rate of MW25 glass [48], [50]. However, tentative evidence suggests Stage I may be prolonged in high-magnesium leachates at modest temperatures (60 °C) – though this effect appears inoperative at higher temperatures (90 °C) where stage divisions are clearer [55]. This potential temperature dependence requires further research given the temperature variability between other studies and the likely evolving temperatures in a GDF environment. The potential for compositional effects must also be considered given that other alkaline earth elements can increase Stage I dissolution rates by promoting Fe-Si mineral precipitation [16], [56], and that elevated iron or diminished alkali contents can reduce Stage I duration [57]–[59] by delaying alteration layer formation [42]. Whether magnesium can cause similar effects remains unclear.

Magnesium content likely has a greater influence on residual dissolution rates. Backhouse [60] found that residual dissolution rates increased with increasing Mg:Ca ratio, and hypothesised this to result from either (1) more rapid formation of Mg-containing precipitates and/or (2) decreased alteration layer passivation [60]. High magnesium has been correlated with increased secondary phase formation and thus increased residual dissolution rates in other studies [31], [42], [48], [54]. This effect occurs as the silica required for secondary phase precipitation is

gained from either the leachate (increasing the chemical driving force for dissolution [42]), the alteration layer (degrading its passivation ability [61]), and/or the glass itself (catalysing its degradation directly [31]). High magnesium may also cause formation of a *secondary* alteration layer which can disrupt the passivation of the primary alteration layer [48]. However, elevated magnesium can also improve the passivation ability of the alteration layer, thereby causing the reverse effect: a decrease in residual rates with increasing Mg [54]. Magnesium can replace sodium in the alteration layer [62] and this replacement may hinder diffusion through the gel [54]. The relative dominance of these counter processes is still debated, but appears dependant on leachate pH, with high pH ( $\text{pH} > 9$ ) favouring secondary phase precipitation, whilst more acidic conditions favour Mg incorporation into the gel [54]. This pH dependence leads to a self-buffering cycle, as shown in Figure 2.2: secondary phase precipitation (favoured at high pH) causes a pH drop as divalent cations ( $\text{Mg}^{2+}$ ) and hydroxide ions ( $\text{OH}^-$ ) are removed from the leachate simultaneously [63]. The wider effect of glass composition on these reactions, however, requires further research as it is currently unclear how these synergetic and further non-linear effects may interact [54]. Experiments aiming to elucidate the balance of this dual-effect are also complicated by a potential surface-area-to-leachant-volume (SA:V) dependency [64]. At higher SA:V ratios, oversaturation with respect to Mg clays is more probable, favouring the precipitation of Mg-silicates. However, at lower SA:V ratios the opposite holds true: oversaturation is less probable and so Mg incorporation into the alteration layer is dominant [64]. This SA:V dependency is, however, not widely reported and more evidence of it is required before its effect can be agreed upon and confidently stated.

Finally, occurrence of rate resumption is highly dependent on glass composition [16], with magnesium likely remaining influential. As with Stage II, high Mg (in the glass or solution) can promote magnesium silicate precipitation, and the silica required for this can be provided by partial or complete loss of the protective gel layer [54], [65] which may trigger Stage III.

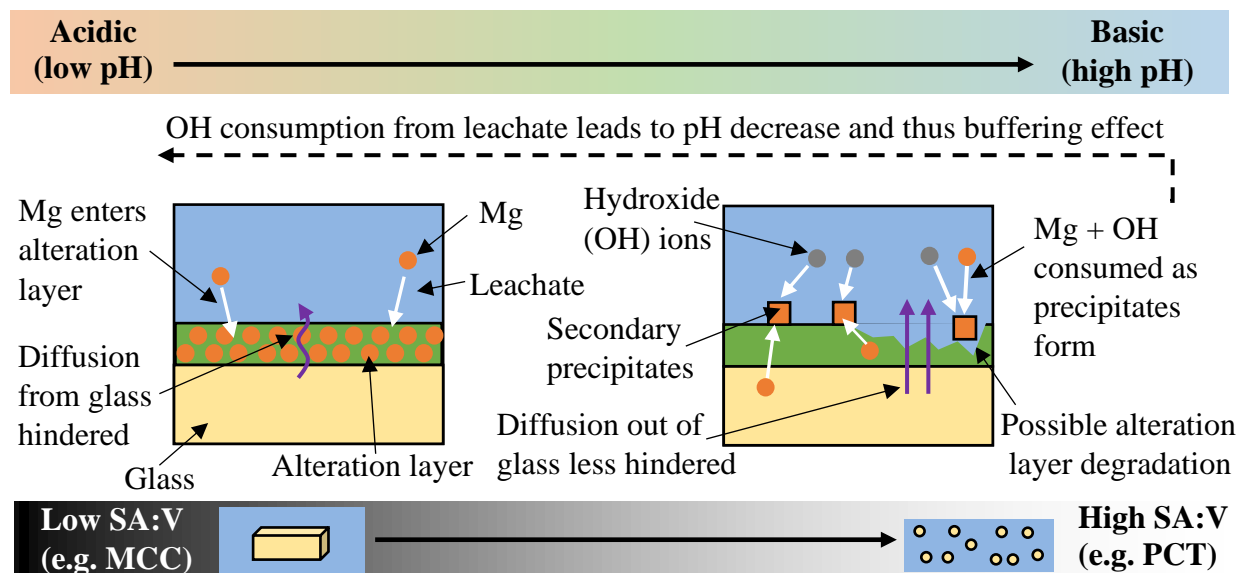


**Figure 2.2.** The effect of magnesium on residual glass dissolution rates. At low Surface Area to Volume ratios (SA/V) and/or at low pH (left hand side) magnesium has a greater propensity to enter the alteration layer and hinder further dissolution of the glass. At high SA/V or high pH, magnesium readily forms secondary precipitates which can degrade the alteration layer and cause dissolution rate increase. Precipitation also consumes hydroxide from the solution, driving conditions to a more acidic pH where secondary precipitate formation is less likely.

### 2.3. Glass alteration layers

The term ‘alteration layer’ encompasses all of the surface layers (alteration layer components) formed at the water/glass interface during glass alteration (Figure 2.3). This includes any hydrated glass layer; any amorphous, porous, silica gel layer; and any secondary precipitates.

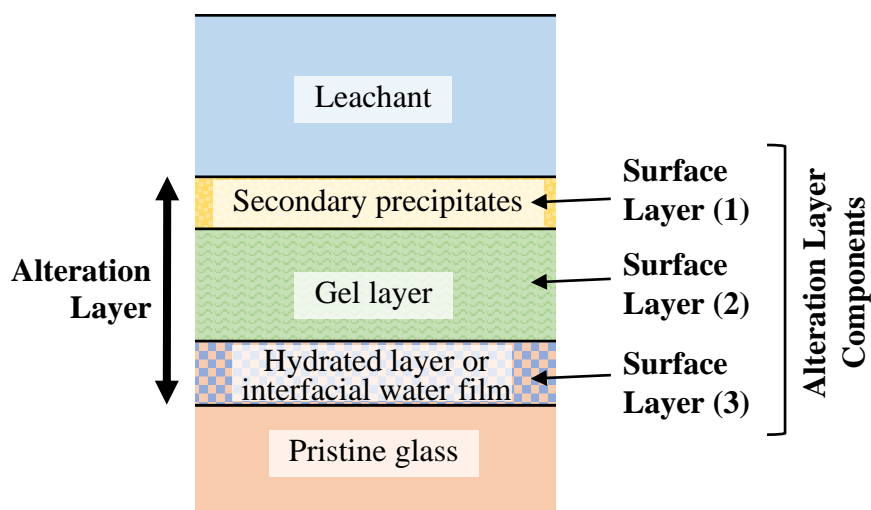


**Figure 2.3:** Schematic showing the surface layers encompassed by the term “Alteration layer”.

The presence or absence of the individual constituents may vary with dissolution duration and mechanism. For example, secondary phases may only precipitate after extended dissolution durations and some authors do not observe the element profiles characteristic of a hydrated glass layer [66].

Previously, it was hypothesised that *hydrated* layers (produced by selective cation removal) formed on synthetic ‘simpler’ glasses; whereas *gel* layers (generated by reprecipitation) formed during dissolution of more complex or naturally-altered glasses [67]. However, these layer components and formation models are no longer thought to be mutually exclusive [66]. Instead, the dominant constituent and formation mechanism may depend on alteration conditions.

#### 2.3.1. Formation and destruction

The hydrated layer is theorised to form as soluble cations rapidly diffuse out of the glass to leave a porous skeletal silicate network [47] which undergoes in-situ reorganisation [11], [42], [68], [69]. This theory is supported by isotopic evidence [68], diffusion-consistent sigmoidal cation depletion profiles through alteration layers [34], [70], [71], and the presence of alteration layers which are more polymerised than the parent glass they formed from [13].

Contrastingly, the silica gel layer is hypothesised to form via condensation and reprecipitation of species from the aqueous solution [66], [72], [73]. As elements dissolve from the glass, the leachant becomes increasingly saturated in (typically siliceous) phases which can precipitate out of the solution to form amorphous, porous, gel layer. This saturation may occur in an ultrathin interfacial fluid film surrounding the glass, allowing the bulk solution to remain unsaturated with respect to amorphous silica [66]. Formation in this way, via condensation and reprecipitation, is evident as atomically sharp chemical and structural-interface between the alteration layer and pristine glass [66] and the presence of compositionally banded alteration layers on archaeological and nuclear glasses [74]–[76].

Secondary phases form via direct precipitation from solution, or through transformation of the thermodynamically unstable gel layer into crystalline phases [11]. The exact timing and process behind the latter is unclear [8], however some authors theorise that crystalline phases form via sequential transformation of metastable phases until the most stable state is achieved [46].

### 2.3.2. Properties

The composition and properties of an alteration layer are spatiotemporally variable and depend on multiple intrinsic/environmental parameters [77], [78], however microstructural and compositional commonalities do exist [47].

Typically, alteration layers are amorphous and have a honeycomb morphology with an open porosity that is indicative of their low density ( $0.8\text{-}2 \times 10^3 \text{ kg/m}^3$ ; [11], [47]). These layers are frequently pitted (see Section 2.4.1), with scattered pits occasionally combining to produce ‘chain-like’ patterns that may evolve into a ridge-and-furrow micro-topography [47]. The friable, delicate nature of these layers [75], [79]–[81] means they are readily damaged and/or destroyed (intentionally or otherwise) during both laboratory and natural experiments.

Layers are highly inhomogeneous through their depth and across their surface [11]. The former is exemplified by the frequent presence of compositional sub-layers [60], [82] with typical thicknesses of  $0.5\text{-}2 \mu\text{m}$  [47]. Contrastingly, lateral inhomogeneity is evident as compositionally variable gel ‘patches’ [15] and changes in the relative thickness of each compositional layer across the surface [37].

The composition of these layers typically resembles that of the glass they formed on, though with an enrichment (relative to undissolved glass) in silica, aluminium, zirconium or iron [66]; and a depletion in easily-leached cations including sodium and calcium. Alteration layers also often contain molecular water [13], [83] and/or hydrogen [66].

### 2.3.3. Passivation mechanism

The degree to which an alteration layer can suppress dissolution (its ‘passivation ability’) likely depends on its thickness, diffusivity and porosity [11]. However, even with knowledge of these factors, alteration layer passivation ability remains impossible to predict because of our limited mechanistic understanding of *how*, exactly, an alteration layer can limit dissolution [37].

Though alteration layers may prevent outward diffusion of some species [37], kinetic models employing only this mechanism are unable to reproduce residual dissolution rates [11], [25], [84]. The diffusion barrier theory cannot totally explain an alteration layer’s passivation ability.

Instead (or additionally), water accessing the pristine glass may be slowed due to its confinement in constricted micropores [13], [85]. The submicroporous alteration layer may readily allow passage of small atoms (e.g. deuterium), but not molecules larger than a given diameter [13], [86]. In this theory, porosity remains open but diffusion of mobile species is slowed [85]. This theory has been inferred to occur during alteration of some simplified glasses, however its wider applicability remains unproven [11].

Complete gel porosity closure may prevent water ever reaching the pristine glass [34], [87]. This could occur as the gel layer undergoes restructuring and densification [34], [35], or as crystalline phases precipitate into the pores [88], [89], [37]. Though this porosity closure has been inferred to occur in some glasses [37], equally alteration layer passivation has been noted despite lack of any porosity closure [12].

## 2.4. Localised attack in glass dissolution

Localised attack (or localised corrosion) in the context of glass dissolution studies refers to the accelerated dissolution or degradation of a confined area on the glass surface, whilst the remaining glass surface appears to corrode at a much slower rate. The characteristic micron-scale features generated via this process are of interest because they may influence overall dissolution rates [90] (e.g. by affecting exposed surface areas [14], [47]) and could offer insight into mechanisms of glass corrosion. Formation of these features may also be a key mechanism in the glass dissolution process [91], with localised attack and gel layer formation potentially coupled [92] as the former provides the elements to form the latter.

### 2.4.1. Pits and pitting

Pitting is frequently observed on altered archaeological glasses [76], [93]–[96], naturally dissolved glasses [97]–[99] and laboratory-dissolved glasses [14], [47], [82], [91]. Boring microorganisms can generate these features (and are occasionally assumed to have done so without adequate evidence [100]), as colonising microbes carve out hemispherical cavities mirroring their own shape and size [101], [102]. However so too can abiotic dissolution mechanisms [103] controlled by simple diffusive processes [102].

Pits associated with glass dissolution typically occur on the glass below any alteration layers [14], [47]. Pits are approximately hemispherical, with diameters  $<10\ \mu\text{m}$  [14], [92]; though they may be elongated with lengths up to  $100\ \mu\text{m}$  [14]. The features may be solitary [14] or may combine to produce ‘chain-like’ patterns [47] or pitted troughs [91]. Pits may also show orientation effects as they align into rows [14], [47].

Pitting abundance appears to increase with dissolution duration and aggressiveness (e.g. high temperature/pH [47], [91], [92]). Pitting prevalence may also be positively correlated with surface precipitate abundance [47], with pits potentially forming preferentially around these precipitates [91]. The presence of a calcium-rich alteration layer may also favour pitting [104].

Many mechanisms of pit formation have been proposed. Initially it was thought that pits form due to either mechanical removal or dissolution of individual spheres (‘globules’) in the glass structure [99]. However, this theory was short-lived and is rarely, if ever, considered now. More commonly, analogies to the metallurgical theory of ‘Pitting Corrosion’ are drawn. In this, selective attack begins at a scratch, lattice defect, or compositional heterogeneity [105], [106]. This generates a cavity with a geometry which slows diffusion to and from the site, accelerating its further dissolution and deepening as a highly aggressive local chemistry develops at its tip [107]. Though this theory may not be directly applicable to glass corrosion, because glasses are amorphous, it may offer some insight into how comparable structures form on glasses.

Pit formation in glass corrosion may result from preferential dissolution at micro-heterogeneities such as alkali-rich areas [46], [92], [94], [108] or phase-separated components [91], [109]. Preferential dissolution around high energy sites is also possible, with these sites formed during sample production (e.g. residual un-annealed stresses [47], [91]) or sample preparation (e.g. cracks, or grinding/polishing defects [90], [91], [110]). Even without these flaws, all glasses inherently contain high energy sites due to their amorphous nature and variable bond angles. Finally, pits may also form due to localised pH increases (which enhance Si dissolution) in leachate trapped between the gel layer and hydrated/pristine glass [14], [47], [90], [111].

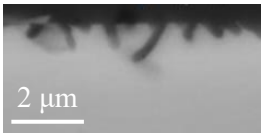
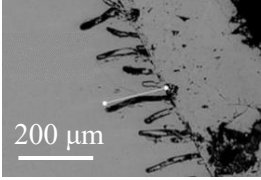
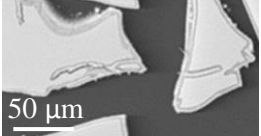
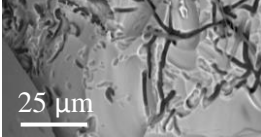
### 2.4.2. Vermiform features

Features resembling tunnels, borings, tubes and ‘wormholes’ have also been postulated as evidence of localised attack during glass dissolution. These have been observed by authors from a range of disciplines (see below), however never have they been comprehensively reviewed from a multidisciplinary perspective. Such a review is necessary if only to highlight the nomenclatural inconsistency and range of interpreted formation mechanisms.

When viewed in cross section, the features in question are curvilinear in nature: originating on the dissolved glass surface and penetrating down into the bulk glass a given distance before terminating arcuately. Features typically have a diameter on the order of microns and lengths of singular to tens of microns. These “tubes” may be hollow or filled and can be distinguished from fractures given their short (finite) length, smoothly curved non-angularity and rounded (high radius) termination.

Material scientists at The Immobilisation Science Laboratory in Sheffield have struggled to reach a consensus on the nomenclature surrounding these features (Table 2.2). Heath [112] was one of the first to observe the features during MCC-1 dissolution testing of a Hot Isostatically Pressed (HIPed) clinoptilolite. In reference to their resemblance of biopores (‘burrows’) formed by earthworms in the drilosphere [113], Heath playfully termed these features “*wormholes*”. Mann & Thorpe [114] noted similar (though longer; ~170  $\mu\text{m}$ ), features on discarded glass bottles from Peakdale (Derbyshire, England). They termed these “*chemiturbation channels*” in reference to their resemblance of bioturbation channels (in ichnotaxonomy) but without implications of a biological origin (hence substitution of the prefix “bio-“ by “chemi-”). Backhouse [60] used both of the aforementioned terms to characterise the ~30  $\mu\text{m}$  penetrating tunnel features formed during PCT-type dissolution testing of a simplified borosilicate glass. Fisher [91] observed morphologically similar features, though only ever in surface views, and termed these “channels” or “troughs” where they formed on the surface of nuclear-type glasses including Magnox Waste (MW) glass and the International Simple Glass (ISG). This array of cited occurrences demonstrates the ubiquity of these features throughout a range of experimental conditions (methodologies, glass compositions, leachate compositions etc.). Furthermore, the lack of nomenclatural consensus revealed above goes some way to explaining why such features remain unreviewed and unsystematically documented.

The occurrence of these features is also widely acknowledged by earth scientists studying volcanic (predominantly basaltic) glass alteration. However, these occurrences have already been comprehensively reviewed by those in this discipline (see [102], [115]). Again, however, a consensus has yet to be reached on naming, with morphologically-similar features referred to as “*putative endolithic microborings*” [116], “*Longish structures*” [117], “*Etch planes*” [100], “*Curved-branched irregular micropits*” [118], “*Asperities*” or “*Grooves*” [110], “*Tunnels*” [119], [120], or “*Tubular structures*” [121]. Though these features may have variable interpreted causal mechanisms (see below), all have similar morphologies and are named based on morphological appearance. This lack of consistent naming remains problematic if progress is to be made with a unifying scientific theory.

Author [reference]	Representative SEM Image	Name assigned to feature	Experiment conditions:
Heath [112]		Wormhole features	<ul style="list-style-type: none"> <li>• Vitreous phase(s) in clinoptilolite</li> <li>• MCC-1 (90°C, UHQ)</li> <li>• 28 days</li> </ul>
Mann & Thorpe [114]		Chemiturbation channels	<ul style="list-style-type: none"> <li>• Soda-lime-silica ‘Bottle Glass’</li> <li>• ‘Natural’ environment (hyper-alkaline water at 8-9 °C)</li> <li>• 2-70 years</li> </ul>
Backhouse [60]		Wormhole or Chemiturbation channels	<ul style="list-style-type: none"> <li>• Nuclear waste glass analogue</li> <li>• PCT-B experiment (50 °C, KOH)</li> <li>• 112 days</li> </ul>
Mann [82], [122]		Not discussed or named	<ul style="list-style-type: none"> <li>• ISG</li> <li>• PCT-B (30 °C, cement water)</li> <li>• 672 days</li> </ul>
Fisher [91], [92]		(Alkali-) Channel or trough	<ul style="list-style-type: none"> <li>• Nuclear waste glass analogues</li> <li>• SPFT experiment (40 °C; high-pH (&gt; 9) TRIS buffer solution)</li> <li>• 100 days</li> </ul>

**Table 2.2:** Vermiform features observed at The University of Sheffield’s Immobilisation Science Laboratory, including their author-assigned name(s) and formation conditions.

The origin of these features is similarly widely debated. Given the features resemblance to biologically formed structures, their biogenicity is often the first point of contention. Colonizing microbes are able to form borings that are morphologically similar to those discussed herein by continuously excreting substances like acids, chelating agents and enzymes which dissolve the glass [102]. Why microorganisms evolved to do this is debated, with the main theories [123] including reasons of nutrient acquisition or protection (from physical extremes, predatory grazing, substrate detachment, or the potential for mineralisation). An array of criteria have been suggested to evaluate whether a biological origin, such as that outlined above, is possible. Considerations here include the geological/experimental context, the feature’s morphology and any geochemical evidence, as outlined in Figure 2.4 [116].

Whilst some authors neglect to acknowledge potential abiotic generation mechanisms [100], others go as far to state that microtubes such as those shown above have never been recreated in laboratory experiments (even via biological mechanisms) [124]–[126] and “*Textures of biocorrosion features are too complex and too reminiscent of biological processes to be explicable by an abiotic process*” [127, p. 2]. However, abiotic explanations are possible [100].

Abiotic formation mechanisms, developed principally by material scientists, typically postulate that these features result from preferential dissolution of a precursor feature. This feature may be structural, morphological, chemical or a combination of these.

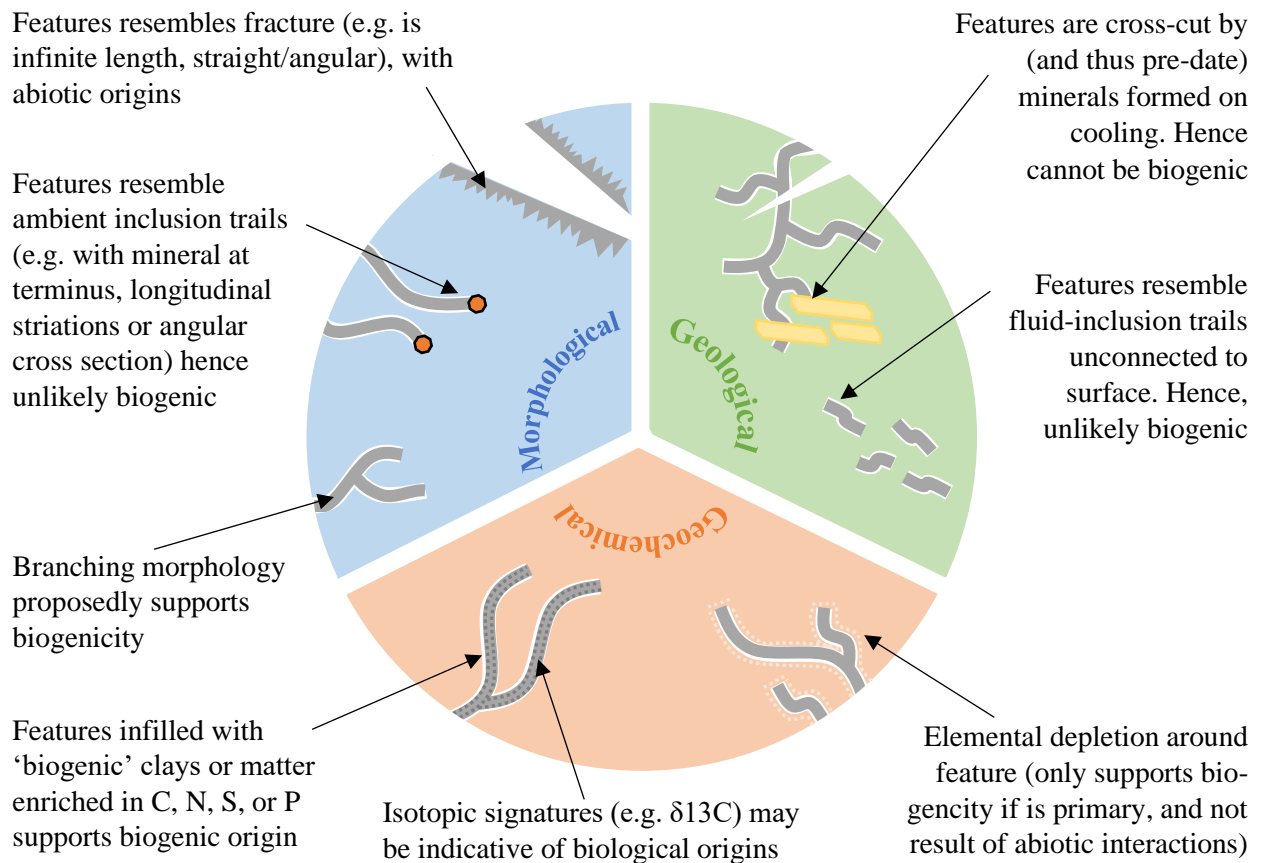


**Figure 2.4:** Schematic of microboring biogenicity-distinguishing criteria from [116].

Structural precursors may include lower-angle, and thus more highly strained, bonds in the glasses ringed micro-structure (Figure 2.5a). Contrastingly, postulated chemo-structural precursors include percolation channels (also known as alkali channels; Figure 2.5b). These may dissolve preferentially during Stage I dissolution and thereby cause a localised pH increase and accelerated attack due to the decreased silica solubility at high pHs [46], [91], [92]. The presence of these alkali channels has been inferred in some HLW glass previously [128], [129]. Preferential attack around more macro-scale compositional regions has also been considered, with purely chemical precursors including phase-separated alkali areas [109].

Morphological features, such as surface damage, cracks, scratches and polishing remnants may act as high-energy sites capable of promoting accelerated dissolution [60], [82], [110], [114], [130]. These features may break through a compressively-stressed surface layer, exposing regions of tensile stress below that dissolves more readily [112], [114]. Alternatively, these scratches/cracks may promote retention of the highly-aggressive high-pH leachate that forms during initial dissolution and this may promote localised attack [110], [130].

Many of the formation mechanisms relevant in pit formation (Section 2.4.1) may also be relevant to these features; with pit-coalescence itself another postulated cause [91], [131]. Preferential dissolution along lines of stress is also a possibility [100]. Finally, pre-existing contamination (e.g. dirt, finger grease etc.) may also provide preferential sites for corrosion [132], [133], however adequate sample washing should prevent this in laboratory experiments.

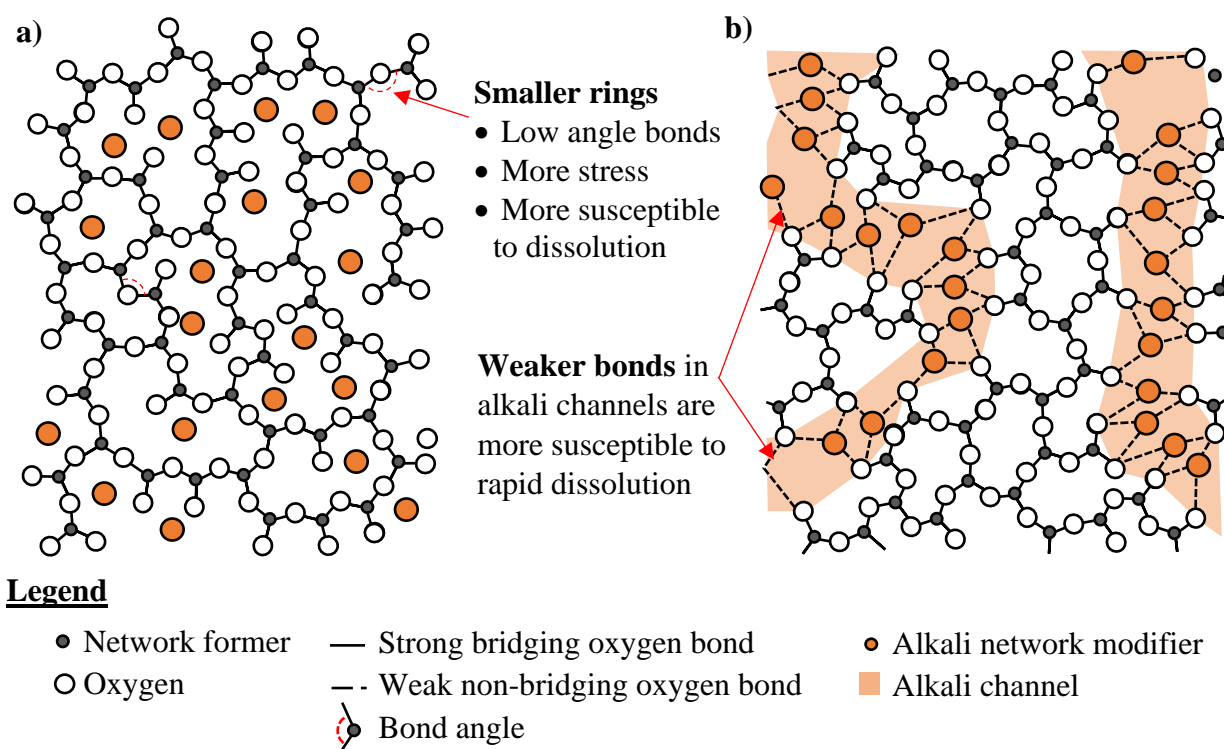


**Figure 2.5:** Potential structural precursors of vermiform features, including low-angle bonds (a) as shown in the continuous random network model [134], [135]; and alkali-channels (b) as shown in the modified random network model [136].

Aside from formation via dissolution [100], the focus of this work, other potential abiotic causes include burial metamorphism of organic matter or un/misidentified ambient inclusion trails [124]. Ambient inclusion trails form as mineral inclusions forcibly migrate through a material with enough force and energy to erode a hollow tubular structure [124], [137]. These can often be excluded where the diagnostic features (a terminal crystal and longitudinal striae) are missing [117], [138] and none of these mechanisms are relevant to laboratory-dissolved crystal-free glasses. Similarly, though some authors [139] have interpreted morphologically similar features to be microcracks [126]; cracks are distinguished herein on the basis of their sharp pointed terminations or infinite length.

Despite there being more studies conducted on abiotic glass alteration than biotic [140], the reverse appears to be the case when analysing these features specifically. Further experiments are needed to explore the abiotic explanations of these features [115], [116]. Such investigation are of pertinence to multiple scientific disciplines: earth sciences, palaeontology, biological sciences, material science [141] and even interplanetary science (given that subaqueous basaltic glass alteration on Mars has been postulated to involve both abiotic and biotic processes [142]). These features evidently require further research in order to understand their method of development, and to quantify their effect on the long term durability of glass wastefoms [114]. The latter is of particular importance given that features similar to those discussed herein have been known to increase glass surface areas by 240% [143].

These possibilities, as well as the findings of other studies [103], [144], imply that features regarded as indisputably biogenic previously may, actually, be caused by abiotic processes. Similarly, the belief that abiotic glass alteration can only cause a surface area *decrease* with time [143], [145] may need to be reassessed.

## 2.5. Nuclear waste glass analogues

Long-term nuclear waste glass corrosion studies are complicated by at least two factors: (1) the chemical complexity of nuclear waste glasses and (2) the necessarily large experimental timescales involved in dissolving these. To overcome the first of these, many researchers study ‘simplified’ nuclear waste glass compositions or alternative compositions which are often based on natural/archaeological glasses. The second challenge can be overcome by studying glasses that have been dissolving in the natural environment. All of these glasses can be considered as ‘analogues’: samples or systems that are analogous to the conditions or materials of interest in a nuclear waste repository [146], [147].

All of these analogues can contribute to the knowledge necessary to allow prediction of long-term nuclear waste glass corrosion as in Figure 2.6. Comparing studies of the same (analogue) glass after its dissolution in the laboratory *and* in nature allows laboratory-based techniques to be proven representative of the ‘real world’ [148]. The ability of an analogue glass to model a nuclear glass can then be further tested by comparing the results of laboratory tests on both nuclear and natural glasses. Simplified glass analogues may provide a ‘stepping-stone’ to achieving the latter: Natural glasses, containing relatively few elements, may be more comparable to simplified nuclear glasses which may, in turn, be reliably compared to nuclear waste glasses. Simplified glasses provide a valuable starting point for piecing together understanding and allow inter-study comparison [8]. Finally, naturally dissolved geo/archaeological analogues contribute significantly towards developing models which can subsequently be applied to predict nuclear waste glass corrosion (Figure 2.7).

However, prior to their confident application to long-term nuclear waste glass durability studies, the phenomenological and mechanistic comparability of analogue systems must be proven [29] [149]. Reliability must be evaluated to ensure analogues are suitably similar to the nuclear waste system/materials and that any differences are acknowledged [149].

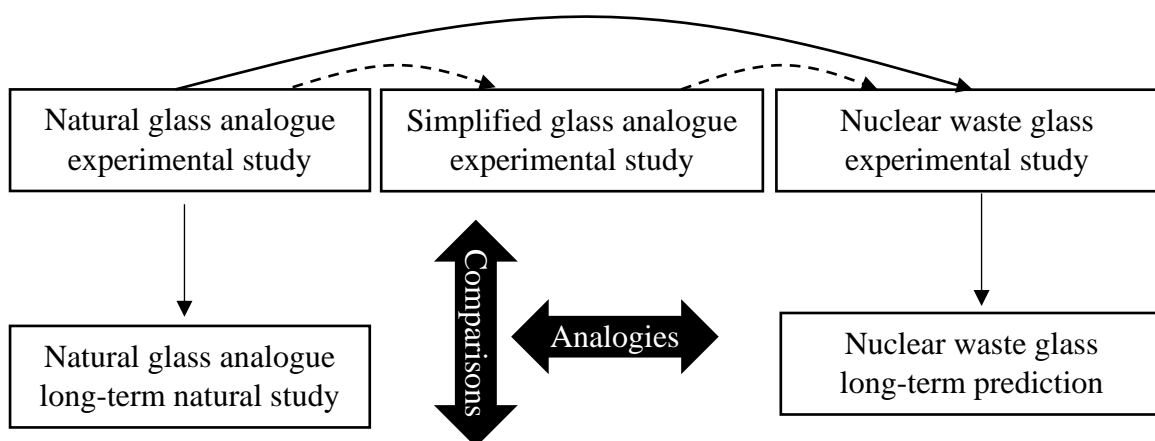


**Figure 2.6:** Principle of reasoning by analogy and comparison. If all comparisons (vertical arrows) and all analogies (horizontal arrows) are proven reliable, then short-term experimental data may be used to predict nuclear waste glass corrosion. Figure after [149].

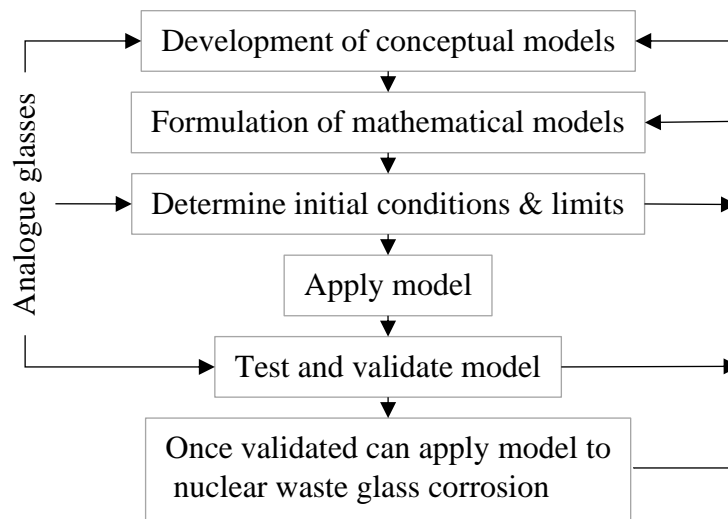


**Figure 2.7:** The role of analogues in the development and validation of glass corrosion models applicable to nuclear waste glass corrosion

### 2.5.1. Basaltic glass

Geological glasses have been used as nuclear waste glass analogues for decades [150]–[153]. Of these, basaltic glasses are considered the most reliable [151] based on their comparable silica content to nuclear waste glass (40-55 wt.% SiO<sub>2</sub> for basalt compared to ~35-50 wt.% SiO<sub>2</sub> for nuclear waste glasses [151], [154]). Both basaltic and nuclear waste glasses are known to have similar alteration mechanisms/kinetics [149], [155]–[157] and a similar free energy of hydration [151]. The alteration layers formed on basaltic and nuclear glasses have also been found to be analogous, with similar secondary precipitates reported (particularly analcime, with zeolites and clays, [15], [47], [60], [151]) and similarities in the composition, zonation and morphology of alteration layers [151], [152]. Comparable trends in alteration layer thickness development with time and temperature have also been observed [151]. Finally, similar debate concerning methods of alteration layer formation exists in both basaltic and nuclear waste glass discussions [155], [158]; with the potentially protective effect of alteration layers noted for both [159].

However, basaltic glass dissolution is not always entirely analogous to nuclear waste glass dissolution. In high-pH environments, for example, the secondary phases evolution for basaltic and simulant nuclear waste glasses can differ considerably [60]. Many authors attribute such differences to the lack of appreciable boron and lithium in basaltic glasses compared to their nuclear counterparts [154], [159]. Comparisons with *naturally* altered basalts are further limited by the absence of appreciable thermal or radiation-damage effects in basaltic glasses and the incompatibility between the submarine environments (where most natural glasses are collected) and the GDF or laboratory environments [154], [159].

Previous studies reveal that basaltic glasses exposed to groundwater develop an internally-layered brown/orange crust which has a sharp, often scalloped, boundary with the pristine glass [97], [155] [15]. Mineralogically, this layer is palagonite [15], [158] and is hypothesised to transform from an amorphous state (‘gel-palagonite’) to a poorly-crystalline form (‘fibro-

palagonite’) with time [155], [158]. Typically, this palagonite layer contains Si, Al, Fe and Mg in proportions that resemble ferromagnesian clay minerals [15]. An enrichment, relative to the ‘parent’ glass, in iron and titanium and a depletion in alkalis/alkaline earths is also often observed [15], [155]. However, some palagonites can be compositionally near-identical to their parent glasses, only differing in their far greater (20-30%) water content [160].

Evidently, the dissolution of basaltic glasses may offer considerable insight into the potential longevity of nuclear waste glasses. However, further research is required to better understand the similarities and differences between the dissolution of nuclear and basaltic glasses [60]. Furthermore, increasing our understanding of the role of magnesium, which may be crucial to nuclear waste glass longevity, in basaltic glass dissolution is desirable.

### **2.5.2. Vitrified hillfort materials**

Archaeological glasses may also be valuable nuclear waste glass analogues [149], with glasses from vitrified hillforts being a particularly novel example of these [161]. These vitrified hillforts were constructed in the late-Bronze to Iron-age by fusing together (vitrifying) the wall rocks of hilltop fortifications across Europe [162]–[165].

Glasses from vitrified hillforts have many unique advantages as nuclear waste glass analogues. Vitrified hillfort glasses do not show the same alkali/alkaline earth enrichment as other archaeological glasses; potentially making them more viable as nuclear waste glass analogues [161], [164]. Furthermore, the vast array of glass compositions found at a single site benefit compositional-dependency studies, whilst the large compositional diversity *between* sites ensures a compositional range broad enough to overlap with nuclear waste glass compositions [165]. Finally, the environmental history of vitrified hillfort sites can be well-characterised if they are of archaeological importance or are in the vicinity of ancient settlements [81].

However, providing high-certainty long-term geochemical constraints for archaeological sites – a necessity for any analogue study [29] – remains challenging. Furthermore, vitrified hillfort glasses are low in boron and lithium compared to nuclear glasses [161] and the surface alteration conditions may differ from those expected in a GDF. The low-temperature oxidising environment in which vitrified hillfort glasses alter may be a poor proxy for the warmer more reducing environment at depth. Alteration *mechanisms* may also differ as surface weathering and erosion of vitrified hillfort materials is expected to be replaced by exclusively chemical corrosion in the GDF. The biological actors that can be influential in vitrified hillfort glass degradation [81] will also likely be absent or at least different in a repository environment.

Regardless of these limitations, studies of vitrified hillfort glasses have provided a wealth of information valuable to those interested in nuclear waste glass dissolution and/or the use of vitrified hillfort materials analogues of this. Broborg vitrified hillfort, in Sweden, is the only site which is well-studied from a nuclear waste glass analogue perspective [165]. Here, initial studies devised a “top-down” analysis technique whereby non-destructive characterization of excavated samples (via XCT and photography) was to be followed by semi-destructive techniques (including dry-cutting to allow SEM analysis) and finally by destructive analyses [81]. The importance of water and oil-free preparation in this was emphasised, to avoid biasing results or irreversibly contaminating samples [165]. XCT was also recognised as a particularly valuable technique, as it provides internal characterisation whilst preserving artefact stability [165].

Initial sample characterisation identified two distinct glasses at Broborg: a clear glass containing Na, K, Al and Si; and a darker more basaltic glass enriched in Fe and Ca [81], [166]–[168]. Alteration of the clear glass was evident as micron-scale semi-circular depletions of Na and K, however this was only found in areas showing significant evidence of microbial colonization [81], [166]. Subsequent microbiome characterisation found that the species colonising the vitrified material indeed had bio-corrosive properties [169]. Contrastingly, dark glass surfaces without organic material showed pitting; however, no semi-circular alteration patterns were found irrespective of the presence or absence of organics on the dark glass [81], [166]. These glasses remain under active investigation, with potential glass alteration phases within micro-cracks [170], corrosion-related surface layers [171] and biological factors [172] the current foci.

Recent archeological investigations of Dun Deardail vitrified hillfort have provided new materials which may provide further information relevant to nuclear waste glass dissolution. Significant quantities of vitrified material were collected from within the excavated trenches of this site in 2015 [173], [174]. This material, unearthed from beneath a well-humified peat-rich topsoil, is known to comprise variably vitrified clasts of calcareous pelite and schist alongside porphyry and quartz-diorite [175]. The degree of sample vitrification was noted to vary with location (more vitrification on the outer edges and the top of the rampart) and protolith composition (metamorphic clasts melted more readily than granitic boulders) [175]. Previous mineralogical analysis has implied vitrification temperatures were 850-1100 °C, with Mössbauer spectroscopy indicating reducing conditions [176]. The corrosion, dissolution and weathering of this vitrified material has not previously been studied, despite the unique information that such investigations could provide.

Aside from this glassy material, charred organic matter (the hypothesised remnants of a supporting timber framework) was also found [173], [174]. Radiocarbon dating of this and other organic matter indicate a 5<sup>th</sup> Century BC construction for the Dun Deardail hillfort, with inhabitation between the 5<sup>th</sup> – 2<sup>nd</sup> Century BC and vitrification in ~310 BC [176]. Evidence of re-occupation post-vitrification was found [177], alongside a crucible fragment and metalworking waste which were both inferred to evidence ferrous and non-ferrous metalworking during occupation [173]. Two hearths, paved flooring [177] and an un-vitrified internal dividing wall was also found alongside a heavily corroded iron object, speculatively identified as a knife [178].

### **2.5.3. Simplified and inactive nuclear waste glass analogues**

Simplified glasses provide an elementary system which can be built upon as researchers gain understanding of nuclear waste glass alteration [8]. These glasses also provide a ‘benchmark’ which allows comparison of results from differing research groups, using differing analytical methods and experimental techniques [10]. Contrastingly, inactive glass analogues are essential to researchers because these are more manageable, in terms of synthesis and processing, than their radioactive counterparts. However, the reliability of both as analogues to ‘true’ nuclear waste glasses should be evaluated prior to their use.

### *Simplified glass*

The International Simple Glass (ISG) is one of the most widely studied simplified nuclear waste glass analogues. This simplified six-oxide glass was devised by the International Glass Corrosion Working Group [10] such that its main components were common to most borosilicate nuclear waste glasses used internationally. The specific abundances of these elements was based on the composition of SON68 (an inactive simulant of the R7T7 glass formed to incorporate spent-fuel reprocessing products in France [10], [179]). Though researchers generally agree that this glass adequately replicates the dissolution behaviour of French HLW glass [25], [179], it is not a perfect or 'replica' analogue. ISG remains less durable than SON68 and develops different phyllosilicate secondary phases after extended dissolution durations [25]. More complex glasses can better analogue this HLW glass [25] because more complex glasses are more able to reproduce the cumulative and/or synergistic effects of major *and* minor oxide constituents in nuclear waste glass [16], [60].

The comparability of the French HLW glass system and the UK HLW glass system may also be questioned. Simulants of the UK's nuclear waste glass (MW) have been found to dissolve faster than SON68 by a factor of ten in neutral pH conditions [31]; and by a factor of two compared to ISG in alkaline environments [60]. The secondary phases developed on MW in both of these experiments also differed from those developed on SON68 or ISG [31], [60].

### *Inactive glass*

The reliability of modelling nuclear waste glass dissolution using non-radioactive (inactive) glasses must also be considered [180]. Radiation may alter the composition, microstructure and bonding within a glass, thereby impacting dissolution rates and behaviour [181].

Generally, initial dissolution rates of radioactive glasses and their inactive analogues differ minimally [182]–[187]. This likely results from the inherently high radiation stability of glass [3] and the glass compositions already containing significant amounts of the elements produced (in a comparatively small quantity) by transmutation [188]. Radiation also appears to have minimal effect on alteration layer properties including thickness, composition and morphology [180]. This implies that inactive glasses are able to well-model the dissolution rates and mechanisms of their radioactive equivalents during early stages [187].

However, longer-term (e.g. Stage II) rates have been shown to vary more considerably with radiation effects. Long-term dissolution rates are typically ten to fifteen times greater in active relative to inactive glasses [189]; with the majority of this attributable to radiation-induced structural changes [190]. In some cases, radioactive waste glasses may be up to 40 times more durable than their inactive counterparts, as radiolysis-induced acid generation suppresses or delays rate resumption [180].

Evidently, careful considerations must be made when comparing the expected dissolution of the UK's nuclear waste glass with the dissolution of 'simplified' compositions (potentially based on other nation's HLW glass compositions), inactive simulants, or other glass types (e.g. basaltic or archaeological) dissolved in potentially incomparable environments. However, the study of all of these glasses may offer considerable insight into the mechanisms and dynamics of HLW glass dissolution; and so their study remains imperative.

## 3. Experimental Methods

### 3.1. Sample acquisition & synthesis

Samples used in this study were acquired or synthesised as outlined in Figure 3.1 and below.

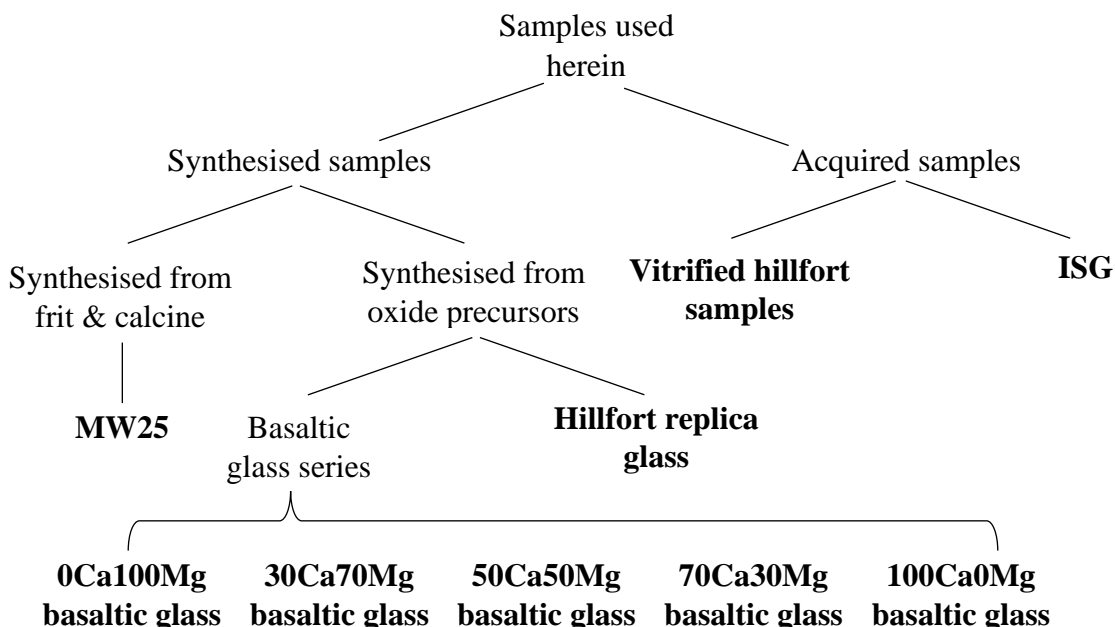


**Figure 3.1.** Overview of glasses utilised in this study and their method of synthesis/acquisition.

#### 3.1.1. ISG acquisition

The International Glass Corrosion Working Group provided two 500-gram annealed blocks of the International Simple Glass (ISG) for this study. These glasses were produced by Mo-Sci Corporation (Rolla, MO, USA) and were melted in a platinum-rhodium crucible within an electric furnace at 1300 °C for four hours. The melt was cast into a graphite mould, with the resulting ingots annealed at 569 °C for six hours before being cooled to room temperature at 1 K min<sup>-1</sup> [13]. Two batches, both with the composition shown in Table 3.1, were used in this work: Lot L12012601-M12042001 and Lot L12012601-M12042501. Batches were assumed to be identical, hence further traceability was not maintained.

Oxide	Mol. %
SiO <sub>2</sub>	60.32
B <sub>2</sub> O <sub>3</sub>	16.43
Na <sub>2</sub> O	12.65
Al <sub>2</sub> O <sub>3</sub>	3.68
CaO	5.27
ZrO <sub>2</sub>	1.64

**Table 3.1.** Analysed composition, in oxide molar percent (Mol. %), of the International Simple Glass (ISG) used in this study, as stated (originally in mass %) in reference [191].

### 3.1.2. Hillfort sample acquisition

Seven vitrified stone samples were provided for this project by Amanda-Jane Dolan (of The University of Stirling). Samples were originally collected by the AOC Archaeology group (on behalf of the Nevis Landscape Partnership and Forestry Commission Scotland) from Dun Deardail vitrified hillfort in August 2017 [178]. For traceability purposes, sample numbers used herein are preserved from the original archaeological record card provided with the samples. The prefix three digits (e.g. ‘601-’) relate to a sample context number, with the suffix three digits reflecting the find number. No further contextual information was provided or available on request, however ‘context’ numbers appear to be consistent with those used in accompanying archaeological reports [178]. The latter implies that all samples studied in this work (with context numbers beginning ‘6...’ or ‘4...’) are from the vitrified ramparts uncovered at Trench 6 and Trench 4 of the site (Figure 3.2).

Samples were *not* washed upon collection; however, they were left exposed to the elements after collection for an unspecified duration. Ordinarily, on-site wet-sieving is typically conducted during archaeological excavations, however this was not completed at the Dun Deardail excavations due to the absence of nearby running water [175] and the logistical challenges associated with carrying sufficient quantities of water to the hill-top location.

Hillfort samples were thoroughly catalogued and photographed before preparation. The potential archaeological significance of the samples necessitated minimisation of destructive testing and retention/re-use of by-products wherever possible.

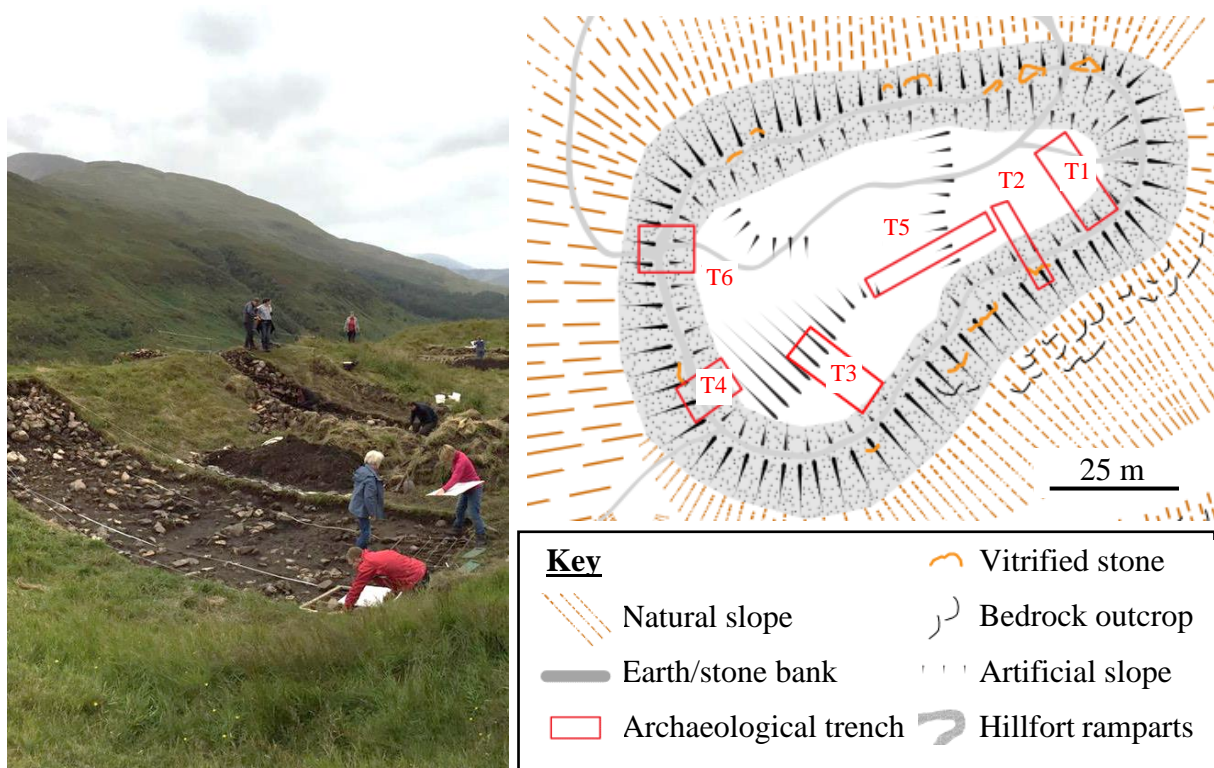


**Figure 3.2.** A photograph taken during archaeological excavations at Dun Deardail (left) and a site plan (right) showing the location of the archaeological trenches. Photograph shared with permission from Dr Amanda-Jane Dolan, with Trench Location Plan shared with permission from AOC Archaeology Group [178].

### 3.1.3. Basaltic glass batching

A standard tholeiitic basaltic glass composition [156] was modified such that the total molar percentage of magnesium- and calcium-oxide remained constant whilst the ratio between these constituents varied from 0:100 to 100:0 (at 30% intervals) as in Table 3.2. Aside from differences in magnesium and calcium, these glasses are expected to be chemically equivalent. Glasses were synthesised by batching and mixing the appropriate quantities of oxide precursors (Table 3.3), before melting as described in Section 3.1.6.

Oxide	Oxide mol. %					
	Techer et al. [156]	0Ca 100Mg	30Ca 70Mg	50Ca 50Mg	70Ca 30Mg	100Ca 0Mg
SiO <sub>2</sub>	53.654	53.295	53.295	53.295	53.295	53.295
Al <sub>2</sub> O <sub>3</sub>	9.478	9.414	9.414	9.414	9.414	9.414
Fe <sub>2</sub> O <sub>3</sub>	4.439	4.409	4.409	4.409	4.409	4.409
Na <sub>2</sub> O	2.815	2.796	2.796	2.796	2.796	2.796
Li <sub>2</sub> O	2.187	2.172	2.172	2.172	2.172	2.172
<i>CaO</i>	<i>12.642</i>	<i>0.000</i>	<i>7.779</i>	<i>10.844</i>	<i>18.151</i>	<i>25.932</i>
<i>MgO</i>	<i>12.791</i>	<i>25.932</i>	<i>18.151</i>	<i>15.088</i>	<i>7.779</i>	<i>0.000</i>
P <sub>2</sub> O <sub>5</sub>	0.046	0.046	0.046	0.046	0.046	0.046
SrO	0.227	0.225	0.225	0.225	0.225	0.225
MnO <sub>2</sub>	0.143	0.142	0.142	0.142	0.142	0.142
K <sub>2</sub> O	0.132	0.131	0.131	0.131	0.131	0.131
TiO <sub>2</sub>	1.448	1.438	1.438	1.438	1.438	1.438

**Table 3.2.** Compositions, in oxide molar percentage as batched, of basaltic glasses synthesised in this study (no shading) and the base glass which they were based on (grey shading). Note the variable CaO:MgO ratio (in italics).

Oxide precursor	Composition	Supplier	Purity
Silica sand	SiO <sub>2</sub>	Loch Aline sand	99.5%
Sodium carbonate	Na <sub>2</sub> CO <sub>3</sub>	Sigma-Aldrich	99.9%
Calcium carbonate	CaCO <sub>3</sub>	Sigma-Aldrich	99.9%
Potassium carbonate	K <sub>2</sub> CO <sub>3</sub>	Alfa Aesar	99%
Magnesium carbonate, hydrated	MgCO <sub>3</sub>	Fisher	99%
Aluminium hydroxide	Al(OH) <sub>3</sub>	Sigma-Aldrich	99%
Ammonium dihydrogen phosphate	NH <sub>4</sub> H <sub>2</sub> PO <sub>4</sub>	Alfa Aesar	98%
Titanium (IV) oxide	TiO <sub>2</sub>	Sigma-Aldrich	99.8%
Strontium nitrate	Sr(NO <sub>3</sub> ) <sub>2</sub>	Aldrich	>=98%
Lithium carbonate	Li <sub>2</sub> CO <sub>3</sub>	Alfa Aesar	99%
Iron (III) oxide	Fe <sub>2</sub> O <sub>3</sub>	Alfa Aesar	98%
Manganese (II) carbonate	MnCO <sub>3</sub>	Alfa Aesar	99.9%

**Table 3.3.** Oxide precursors used to synthesise the basaltic glass series.

### 3.1.4. Replica hillfort glass batching

Scanning Electron Microscopy and Energy Dispersive X- ray Spectroscopy (SEM-EDS; Section 3.4.2) was used to estimate the composition of the assumed-glassy material within the vitrified stone samples. Seven SEM-EDS spectra were taken from featureless (crystal-free) locations within the interior of *Sample #410-401*; with the average composition of these used to give a ‘target glass composition’ (Table 3.4). This glass was synthesised by batching and mixing oxide precursors (Table 3.3), before it was melted as in Section 3.1.6.

Oxide	Mol. %	
	Actual Hillfort “glass”	Replica hillfort glass
SiO <sub>2</sub>	61.55	62.74
Al <sub>2</sub> O <sub>3</sub>	11.36	11.05
K <sub>2</sub> O	6.91	5.44
Na <sub>2</sub> O	11.08	11.03
Fe <sub>2</sub> O <sub>3</sub>	2.36	2.50
CaO	4.58	5.20
MgO	2.16	2.03

**Table 3.4:** Composition of areas hypothesised to be glassy in an actual hillfort sample (“Actual Hillfort ‘glass’”) and the replica glass synthesised based on these values (“replica hillfort glass”). Compositions, in oxide mole percentage, as measured by SEM-EDS.

### 3.1.5. MW25 glass batching

Alkali borosilicate base glass ‘frit’ (MW0.5Li) and simulated Magnox waste ‘calcine’ (WRW17), both provided by Mike Harrison at NNL, were combined in proportions calculated to ensure the final glass comprised 25 weight percent Magnox waste (MW25 glass; Table 3.5). The effect of de-nitration upon heating was mitigated by calculating the expected nitrate loss (RN%) using Equation 3.3

$$RN\% = 100 \times \frac{w_2 - w_3}{w_2 - w_1} \quad \text{Equation 3.3}$$

where  $w_1$  is the mass of empty crucible (g),  $w_2$  is the mass of crucible and calcine sample before heating to 1000 °C (g) and  $w_3$  is the mass of crucible and calcine (g) after heating to 1000 °C. The required calcine quantity can then be calculated using Equation 3.4

$$W_c = 100 \times \frac{25}{100 - RN\%} \quad \text{Equation 3.4}$$

where  $W_c$  is the amount of calcine to add for a 25% waste loading.

Lithium carbonate (Table 3.3) was added to simulate processes at the Sellafield vitrification plant (where lithium is added during calcination to suppress spinel formation). The additional lithium quantity required was equal to the lithium already present in the frit. These components were added to a platinum-rhodium crucible and melted as outlined in Section 3.1.6.

Oxide	Mol. %	Oxide	Mol. %
Al <sub>2</sub> O <sub>3</sub>	2.80	Na <sub>2</sub> O	8.84
B <sub>2</sub> O <sub>3</sub>	15.86	Nd <sub>2</sub> O <sub>3</sub>	0.36
BaO	0.20	NiO	0.32
CaO	0.00	Pr <sub>2</sub> O <sub>3</sub>	0.11
CeO <sub>2</sub>	0.43	RuO <sub>2</sub>	0.37
Cr <sub>2</sub> O <sub>3</sub>	0.26	SiO <sub>2</sub>	50.50
Cs <sub>2</sub> O	0.25	Sm <sub>2</sub> O <sub>3</sub>	0.07
Fe <sub>2</sub> O <sub>3</sub>	1.19	SnO	0.00
La <sub>2</sub> O <sub>3</sub>	0.12	SrO	0.18
Li <sub>2</sub> O	8.93	TeO <sub>2</sub>	0.07
MgO	7.52	Y <sub>2</sub> O <sub>3</sub>	0.05
MnO <sub>2</sub>	0.00	ZnO	0.00
MoO <sub>3</sub>	0.65	ZrO <sub>2</sub>	0.74

**Table 3.5.** Nominal composition of MW25 glass in oxide molar percentage [192], [193].

### 3.1.6. Glass melting

All batched reagents/components were then added to separate platinum-rhodium crucibles and were melted under the conditions outlined in Table 3.6.

	Basaltic glass	MW25	Hillfort glass
Melt temp, °C	1450	1050	1650
Melt duration (static + stir), hours	5 (1+4)	5 (1+4)	2.5 (2.5+0)
Annealing temperature, °C	670	500	N/A
Annealing duration, hours	1	1	N/A
Cooling rate, °C min <sup>-1</sup>	1	1	Uncontrolled
Furnace type	Electric	Electric	Muffle
Stirred	Yes	Yes	No
Crucible material	Platinum	Platinum	Platinum

**Table 3.6.** Melting and processing conditions used in glass synthesis for this study.

Basaltic and MW25 melts were then poured into a pre-heated iron ingot mould and were transferred into the annealing furnace within minutes of pouring. Replica hillfort glasses could not be poured owing to their high viscosity. Instead, the crucible was partly submerged in water for ~1 minute, before being allowed to cool (unaided) to room temperature. The glass was then removed from the crucible using a hammer and chisel.

### 3.2. Dissolution methodology

A comparison of the dissolution methodologies utilised in this work is provided in Table 3.7, with further details below. Monolith testing was completed to allow detailed examination of alteration layers; whilst the larger surface area provided by a powder test allowing greater reaction progress to be probed (though the latter is arguably limited by the more modest temperatures necessitated by the greater evaporative loss in these tests).

	MCC	PCT
Sample type	Glass monoliths	Glass powders
Temperature	90 °C ( $\pm 2$ °C)	50 °C ( $\pm 2$ °C)
Glass SA	0.0004 m <sup>2</sup> (400 mm <sup>2</sup> ; $\pm 10\%$ )	0.02 m <sup>2</sup> (20000 mm <sup>2</sup> $\pm 5\%$ )
Leachant V	0.00004 m <sup>3</sup> (40 ml; $\pm 10\%$ )	0.00001 m <sup>3</sup> (10ml; $\pm 5\%$ )
SA:V	10 m <sup>-1</sup>	2000 m <sup>-1</sup>
Glasses tested:		
Basaltic glass		
0Ca100Mg	✓	✓
30Ca70Mg	✗	✓
50Ca50Mg	✓	✓
70Ca30Mg	✗	✓
100Ca0Mg	✓	✓
ISG	✓	✓
MW25	✓	✓
Leachant	UHQ (Ultra High Quality) water	UHQ (Ultra High Quality) water
Atmosphere	Oxic (atmospheric air)	Oxic (atmospheric air)
Timesteps (days)	28, 56, 112, 224, 461(/468), 672	7, 14, 28, 56, 112, 224 days

**Table 3.7.** Summary comparison of dissolution experiment parameter used in this study.

#### 3.2.1. MCC-1

Chosen glasses from the synthesised basaltic glass series (0Ca100Mg, 50Ca50Mg & 100Ca0Mg) alongside both ISG and MW25 were prepared following the Materials Characterisation Centre Test-1 (MCC-1) procedure, as defined by ASTM standard C1220-17 [194]. This static leaching test utilises monolithic samples which are stored (at 40, 70, or 90 °C) in a leachant volume such to ensure a glass surface area to leachant volume (SA:V) ratio of  $10 \pm 0.5$  m<sup>-1</sup>. A temperature of 90 °C was utilised to allow comparisons with other works and to maximise probable dissolution rates whilst limiting potential evaporative losses (likely to be problematic at temperatures > 100 °C). Samples were tested in triplicate, with two additional blank vessels containing only leachant, prepared per timepoint.

For this, glass ingots were cut into ‘coupons’ (measuring ~10 x 10 x 5 mm) using a Struers Secatom-50 and/or Buehler Isomet slow saw, both with a diamond blade and Isomet cutting fluid. Coupons were then ground (using P600-, P800- and P1200-grit SiC abrasive papers successively) and polished using a Buehler EcoMet 250 Pro and/or a Kemet 300 Lapping and Polishing wheel (the three-stage polishing procedure utilised a 6 µm and 3 µm oil-based diamond suspension liquid with separate MetPrep planocloths and then 1 µm oil-based diamond suspension with a MetPrep cashmere cloth). Coupons were subsequently placed in an ultrasonic bath containing Ultra High Quality (UHQ) water and isopropanol sequentially, for three minutes per cycle, before samples were allowed to dry at 90 °C overnight.

Coupons were then placed into clean (washed via an in-house modified version of the method outlined in ASTM C1285 [195]) Savillex 60 ml perfluoralkoxy (PFA) Teflon standard vessels containing a support screen (‘basket’) of the same material. Leachant, in the form of Milli-Q® Ultra-High Quality (UHQ) water (with a resistivity of 18.2 MΩ), was added in appropriate quantities to these vessels using a FinnPipette F1 variable-volume pipettor, with 10 ml FinnPipette tips. The required leachant volume for each timestep was calculated based on the average geometric surface area measured for all monoliths of a given timestep. Though it is possible to vary this depending on specific monolith dimensions, this was not undertaken here to minimise the likelihood of human error and time-spent making arbitrarily fine adjustments. Subsequent calculations (Section 3.2.3) utilised monolith-specific surface areas.

Vessels (containing leachant and a monolith) were then closed and placed into a 90 °C GenLab MINO/40 oven, as shown in Figure 3.3. After the durations (‘timesteps’) outlined in Table 3.7 the vessels were removed from the oven, weighed and allowed to cool to room temperature before the monolith was removed and allowed to air-dry for 24-48 hours before further processing. Two aliquots of solution were then taken using a FinnPipette F1 variable-volume pipettor (as previously): The first 10-15 ml aliquot was transferred into a polypropylene centrifuge tube where the pH was measured as in Section 3.4.3. The second, similarly sized, aliquot was forced (using a polyethylene/polypropylene syringe) through a Puradisc 0.2 µm cellulose acetate filter and then acidified with 1 vol. % ultrapure concentrated nitric acid (to avoid precipitation of secondary phases prior to elemental analysis). Any remaining solution was disposed of; however, the first (unfiltered/un-acidified) aliquot taken was speculatively retained for possible further investigation. Acidified solutions were subsequently analysed via ICP-OES (Section 3.4.2), with monoliths prepared for SEM analysis (Section 3.4.2).

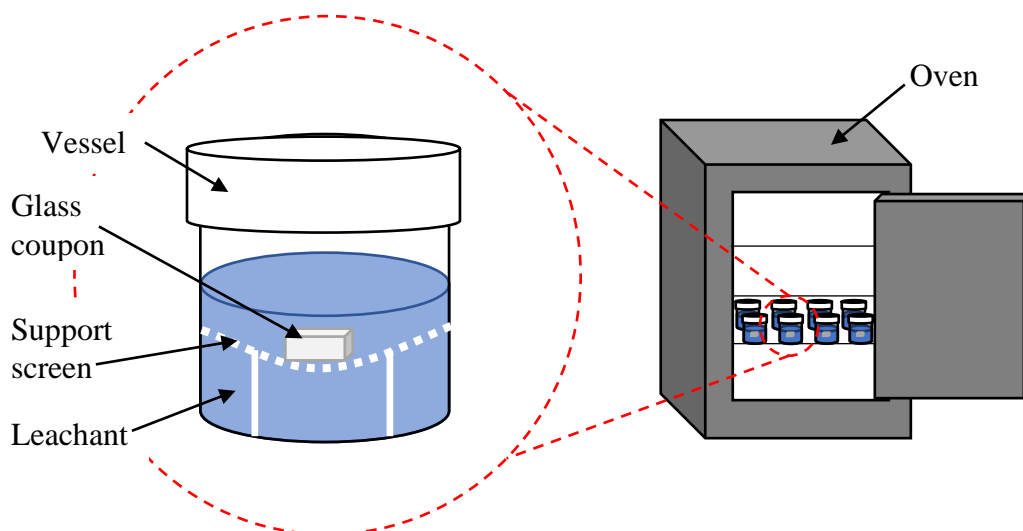


**Figure 3.3:** Schematic representation of MCC-1 procedure followed in this study.

### 3.2.2. PCT-B

The entire basaltic glass series, alongside ISG and MW25, were tested following the Product Consistency Tests (PCT-B) as defined by ASTM standard C1285-14 [195]. This temperature-controlled static test utilises powdered samples submerged in a leachate in quantities to ensure an SA:V ratio of  $2000 \text{ m}^{-1}$ . An experiment temperature of  $50 \text{ }^\circ\text{C}$  was selected after trials at  $90^\circ\text{C}$  resulted in unacceptably high evaporative loss, to allow comparison with other authors [60], [82] and based on the current GDF specifications (max air temperature =  $50^\circ\text{C}$ ) in the UK [196]. Temperatures of  $40\text{-}50 \text{ }^\circ\text{C}$  are also more consistent with geothermal gradients which state that temperature typically increase by  $25\text{-}30 \text{ }^\circ\text{C}$  with every kilometre of depth [197]. Experiments were undertaken in triplicate, with duplicate blank vessels per timepoint.

Glass ingots were size-reduced using a percussion pestle and mortar and were sieved to obtain the  $75\text{-}150 \text{ }\mu\text{m}$  size fraction. Powder samples were then cleaned (to remove adhered fines) in an ultrasonic bath containing UHQ water and isopropanol sequentially until each waste solution was visibly particulate-free (circa  $30\text{-}60$  minutes per washing stage). After oven-drying (at  $90^\circ\text{C}$  for  $\sim 8$  hours), powder density (measured via pycnometry in Section 3.4.1) was used to calculate the sample volume required to achieve the desired target surface area (Table 3.7). These geometric surface area calculations assumed spherical particles of a fixed diameter equal to the mean of the size fraction [195].

Powders were then weighed and added to  $15 \text{ ml}$  PFA test vessels, which had previously been cleaned via an modified version of the method outlined in ASTM C1285 [195]. UHQ water, of the same type added in Section 3.2.1, was added to these vessels (using the same pipettor/tips outlined in Section 3.2.1), before vessels were closed, tightened and placed into a  $50 \text{ }^\circ\text{C}$  GenLab MINO/40 oven, as shown in Figure 3.4.

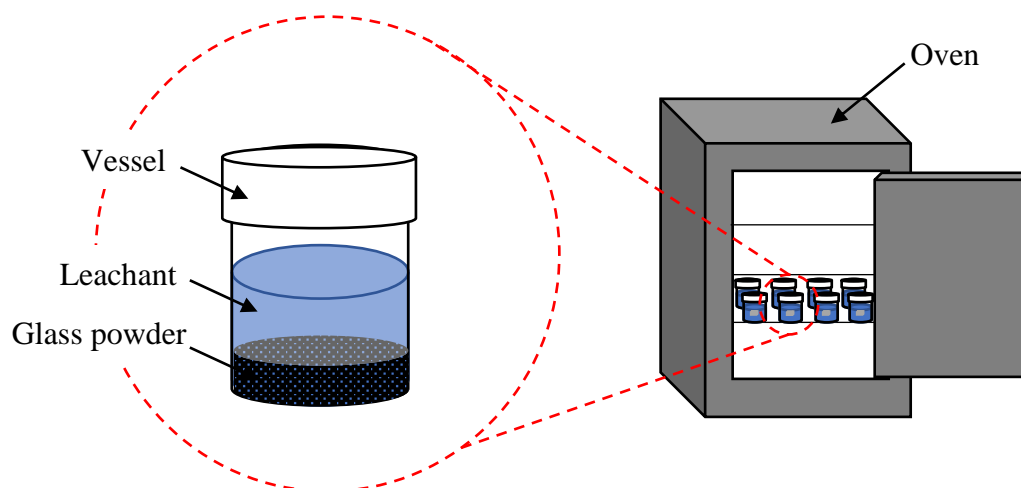


**Figure 3.4.** Schematic representation of PCT-B procedure followed in this study.

After a given time interval (Table 3.7) vessels were removed from the oven, allowed to cool to ambient temperatures and then weighed. Two aliquots of solution were then taken: One seven millilitre aliquot was filtered and acidified (as in Section 3.2.1), whilst the remaining  $2\text{-}3 \text{ ml}$  was removed and used for pH measurement (Section 3.4.3). No un-acidified solutions were retained, however acidified solutions were subsequently analysed via ICP-OES (section 3.4.2). Vessels (containing glass powder and minimal leachate) were then placed into a modestly-heated ( $30 \text{ }^\circ\text{C}$ ) drying oven for  $8\text{--}48$  hours before powder was removed and prepared for SEM analysis (Section 3.3.1).

### 3.2.3. Leachate normalised mass loss calculations

Leachate concentrations (from ICP-OES analysis, Section 3.4.2) were numerically processed to correct for four factors: (1) evaporative loss of solution during testing (post-dissolution vessel mass was used to estimate this); (2) background elemental concentrations (potentially derived from inadequate vessel cleaning or leaching of the vessel itself and measured from a “blank” vessel containing only leachant); (3) glass surface area (based on the measurements made on *individual* samples, including the monolith dimensions in MCC and the exact powder mass for PCT), and; (4) the initial glass composition.

These corrections were made via the calculation of a normalised mass loss ( $NL_i$ ; in  $\text{gm}^{-2}$ ) for each element (i) in each glass, as outlined by ASTM [194], [195] and given by

$$N_L(i) = \frac{C_i - C_{i,b}}{x_i \times (SA/V)} \quad \text{Equation 3.5}$$

where  $C_i$  and  $C_{i,b}$  are the average concentration (in  $\text{g m}^{-3}$ ) of element i in the triplicate analysed leachates and duplicate “blank” vessels (containing only UHQ water) respectively;  $SA/V$  is the sample Surface Area ( $\text{m}^2$ ) to leachant Volume ( $\text{m}^3$ ) ratio ( $\text{m}^{-1}$ ); and  $x_i$  (unitless) is the elemental fraction of i in the initial glass composition.

The uncertainty in the normalised mass loss was calculated, following Backhouse [60] using

$$\sigma_{NL_i} = NL_i \times \sqrt{\frac{(\hat{\sigma}_{C_i} \times C_i)^2 + (\hat{\sigma}_{\bar{C}_{i,b}} \times \bar{C}_{i,b})^2}{(C_i - \bar{C}_{i,b})^2} + \hat{\sigma}_{x_i}^2 + \hat{\sigma}_{SA}^2 + \hat{\sigma}_V^2} \quad \text{Equation 3.6}$$

where  $\hat{\sigma}$  denotes the relative uncertainty in the subscripted parameter and the macron diacritical mark denotes the average of the accented parameter (e.g.,  $\bar{C}_{i,b}$  denotes the average concentration of element i in the blank vessels: the average  $C_{i,b}$ ). *Relative* uncertainties are equal to *absolute* uncertainties on a given measurement divided by the value of that measurement. Absolute uncertainties for  $x_i$ ,  $SA$  and  $V$  were taken to be 5%, 15% and 5% respectively; the term ‘uncertainty’ can be equated to ‘standard deviation’ for average measurements.

### **3.3. Post-dissolution sample preparation**

#### **3.3.1. SEM, Raman & XRD sample preparation**

MCC monoliths were lifted from their support screens, using soft plastic tweezers. Despite the considerable care, minimal handling and careful choice of manipulating equipment, some damage to alteration layers during this process was noted. In some cases even the static energy (from the user/tweezers) was sufficient to cause the visible loss of thin (near optical transparency) alteration layer fragments. Nevertheless, most damage was localised (restricted to the area in contact with tweezers) and crucially samples were not washed post-dissolution. Two of the triplicate monoliths per composition/timestep were placed into plastic sample clips (which themselves also likely caused localised alteration layer damage), before being mounted in epoxy resin (80% Buehler EpoxiCure™ 2 Epoxy Resin thoroughly mixed with 20% Buehler EpoxiCure™ 2 Epoxy Hardener) which was then allowed to set for at least 12 hours. The remaining monolith of the triplicate samples was stored (unmounted) under ambient conditions within a standard plastic container.

For PCT tests, a small quantity (~0.2 g) of dried powder from each composition/timestep was mixed in a ~50:50 ratio with epoxy resin/hardener (see above for details), before the resulting ‘paste’/‘slurry’ was transferred into a cylindrical plastic sample clip (~0.5 mm in diameter) and additional epoxy/hardener was poured around this. The remaining (~0.8 g of) powder was stored in a sealed plastic vial prior to, in some cases, XRD analysis.

To reveal a cross section, epoxy-mounted samples were then ground and polished to a 1 µm finish as outlined for MCC monoliths in Section 3.2.1. Considerable effort was made to limit alteration layer damage by minimising platen speed (~121 rpm) and applied force (8 N) during this process. Water, previously used as a grinding lubricant was also replaced with isopropanol at this stage of sample preparation. Raman analysis (Section 3.4.3) was also conducted at this stage (prior to carbon coating).

After preparation, copper-tape was applied to electrically connect the bottom and top of the resin-mounted samples which were then carbon-coated using a Quorum Q150T ES Plus. This was conducted to allow incident electron dissipation and prevent ‘charging’ during SEM analysis, as this can cause beam repulsion and image stability and contrast issues [198], [199].

Based on initial observations, three vitrified hillfort samples (Samples #410-401, #601-607 and #601-602) were selected for further analysis. These were observed to contain optically vitreous material and had evidence of exposure to an aqueous alteration environment in the form of probable plant roots. These were prepared as an unmounted fragment and as geological thin sections for SEM analysis. To prevent disturbance or removal of water-soluble alteration products, preparation involved no water usage and oil-based lubricant was used only when strictly necessary (partly because of the difficulties envisaged in subsequently removing this from the highly porous samples). Samples #410-401 and #601-607 were prepared, in a water-sensitive manner, as double-polished geological thin sections (30 µm thick) by The Open University, with sampling location carefully considered (Figure 3.5). A fragment was also cut from Sample #601-602 using a hand-operated Vitrex tungsten carbide-tipped tile saw without lubricant. To minimise additional sample modification/preparation, and to allow unhindered Raman analysis subsequently, hillfort samples were not carbon coated prior to SEM analysis. Instead, the ‘Charge Reduction’ SEM mode was used to introduce a small amount of atmospheric air into the sample chamber, thereby allowing some electron discharging.

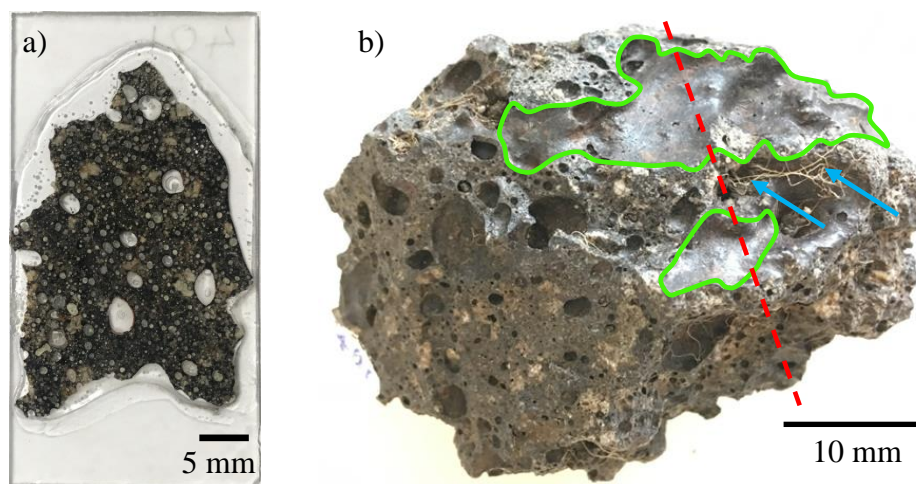


**Figure 3.5:** Thin section (a) cut from hillfort sample monolith (b) for this study. The section was cut (red dashed line) to maximise intersection with vitreous material (outlined in green) and evidence of surface-exposure (roots, arrowed in blue).

XRD was conducted on dissolved and undissolved PCT powders without further preparation. For XRD of hillfort materials, a fragment of Sample #601-602 was removed (using a geological hammer) and crushed into a powder (of  $\sim 100 \mu\text{m}$ ) using a percussion pestle and mortar.

### 3.3.2. XCT sample preparation

Hillfort samples were placed into the XCT as received, without any further sample preparation. However, MCC monoliths and PCT powders (after dissolution) were prepared as below.

Attempts were made to scan entire epoxy-mounted MCC monoliths without further size reduction, however trial scans of this type (and at the desired resolution) contained significant noise. This likely resulted from excess sample thickness which greatly attenuated x-rays reaching the detector despite the high beam power. The necessitated high beam power also potentially over-saturated the detector after the sample had rotated and the significantly thinner dimension was scanned. XCT samples should be of a minimal thickness and aspect ratio [200]; parameters not fulfilled by MCC monoliths prior to further size reduction.

Instead, epoxy-mounted post-dissolution monoliths were size reduced into slender ‘pillars’ using an Isomet slow saw (as above). The resulting samples, shown and prepared as in Figure 3.6, comprised: a glass pillar with an intact alteration layer embedded in epoxy; a standalone glass pillar without the attached alteration layer or epoxy coating; and an alteration layer embedded into the surface of an epoxy ‘pillar’. Such sample diversity was necessitated by the novel nature of this methodology.

Samples selected for XCT monolith analysis were of a single glass composition (50Ca50Mg basaltic glass) and had been dissolved for the maximum durations considered herein (672 days and 468 days). The former choice, of consistent sample composition, allows self-comparison of XCT data; whilst the latter choice maximised the probability of observing (thick) alteration layers and other features.

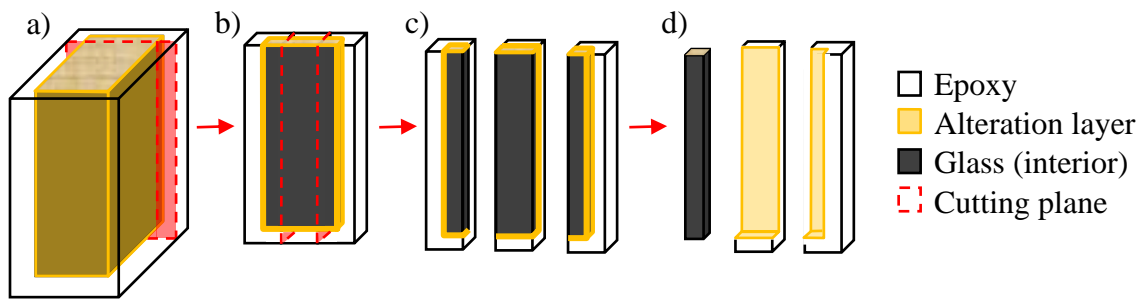


**Figure 3.6.** Schematic showing how MCC samples were prepared for XCT scanning. Whole MCC monoliths were first mounted in epoxy (a), before a plane was cut from this (b) and this plane was cut into pillars (c). Some of these pillars disintegrated upon cutting (d), however these samples were retained and scanned. Sectioning was performed using a Buehler Isomet slow saw, with a diamond blade and Isomet cutting fluid.

Post-dissolution PCT powders were also characterised via XCT. These were scanned as ‘dry’ powders (funnelled into a plastic drinking straw capped with sponge at both ends and supported by adhesive tack) and as powders submerged in their original leachate (‘wet’ samples; transferred into a micro-pipette tip which was sealed using quick-bonding superglue and loosely placed adhesive tack, as shown in Figure 3.7). Such novel sample mounting methods were developed to minimise excess x-ray attenuation through containment vessels.

Samples selected for XCT powder analysis were all dissolved 50Ca50Mg basaltic glasses. One sample, scanned only as a dry powder, had been subjected to 112 days of dissolution (at temperatures of 50 °C, as outlined in Section 3.2.2); whilst the other, scanned both ‘wet and ‘dry’, had been dissolving for 353 days at an increased temperature (of 90 °C). The latter sample was part of a (failed) trial to test the viability of conducting long-term PCT testing at high temperatures. All other powder dissolution testing completed herein was conducted at 50 °C, however samples subjected to this increased dissolution temperature were selected for XCT analysis after SEM analysis revealed minimal visible dissolution at 50 °C and in the knowledge that increased dissolution temperatures allow analysis of later-stage dissolution. For clarity, the potentially incomparable dissolution temperature of this sample will be highlighted in future discussions and sample nomenclature.

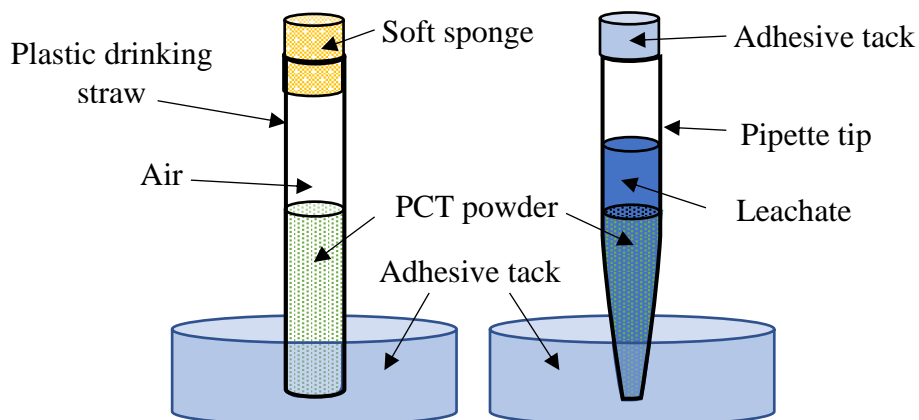


**Figure 3.7.** Schematic showing dissolved glass powder samples as prepared for XCT scanning both ‘dry’ (left) and ‘wet’ (right).

### 3.4. Characterisation/Analytical methods

#### 3.4.1. X-ray Diffraction

X-ray diffraction (XRD) is used to investigate a material's crystal structure. It was used to determine if un-dissolved synthesised 'glasses' and hillfort samples were amorphous; and to identify any crystalline components in hillfort and post-dissolution PCT samples.

In powder XRD, an approximately parallel beam of x-rays with a known wavelength ( $\lambda$ ) is directed at a powder specimen. These X-rays interact with the sample to generate secondary diffracted x-ray beams at specific diffraction angles ( $\theta$ ) that can be related to spacing between crystallographic planes ( $d$ ) via the Wulff-Bragg equation [201]

$$n\lambda = 2d \sin \theta \quad \text{Equation 3.7}$$

where  $n$  is the diffraction order. Bragg's law will be satisfied (to give constructive interference and diffraction peak) only at certain diffraction angles and the angles at which this occurs can be used to calculate the interplanar spacing that generated the diffraction (Figure 3.8). A diffraction pattern is generated by varying the diffraction angle (the angle of the incoming x-ray beam) and measuring the amount/strength of refracted x-rays observed at each angle [202].

Crystalline materials generate characteristic diffraction patterns (peaks with specific positions and intensities) that can be compared to reference spectra to allow phase identification. Instead of sharp 'Bragg' peaks, the diffraction patterns of amorphous materials, which lack long-range crystallographic order, are dominated by a single broad peak corresponding to the average short-range atomic distances between pairs/clusters of atoms [201].

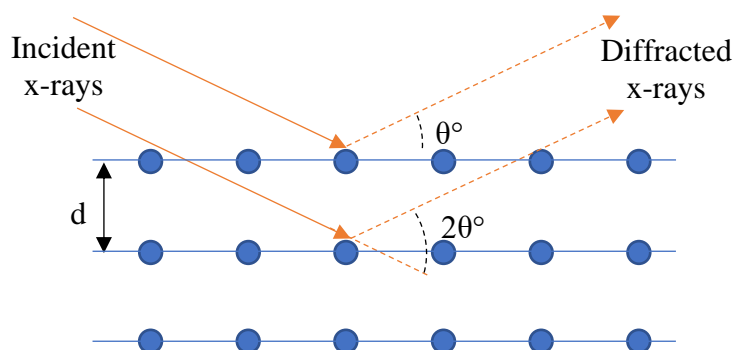


**Figure 3.8.** Illustration of the Wulff-Bragg Law (Equation 3.7).

#### *Experimental parameters*

Powder samples (with a grain size of approximately 75-150  $\mu\text{m}$ ) were front-loaded into a zero background (polymethyl methacrylate/PMMA) sample holder before the sample surface was made flush with the container using a glass microscope slide. The sample and holder were then placed into a Bruker D2 Phaser XRD with a Cu  $K\alpha$  X-ray source ( $\lambda = 1.54056 \text{ \AA}$ ), Lynx-Eye detector (with a lower and upper discriminator set to 0.19 and 0.27 in order to reject Fe fluorescence), 1 mm divergence slit, nickel filter, and a working voltage and current of 30 kV and 10mA respectively. Data was collected, in  $0.02^\circ$  intervals with a count time of  $0.6 \text{ s step}^{-1}$ , between  $10\text{-}90^\circ 2\theta$ , in scans lasting  $\sim 40$  minutes per sample. Diffraction patterns containing sharp peaks were compared to those in the PDF4+ database from the International Centre for Diffraction Data (ICDD) for phase analysis [203].

### 3.4.2. Scanning Electron Microscopy and Energy Dispersive X-ray Spectroscopy

Scanning Electron Microscopy (SEM) is used to characterise sample morphology at a (sub-)micron scale, with the accompanying Energy Dispersive X-ray Spectroscopy (EDS) able to elucidate compositional heterogeneity.

Typically in an SEM, electrons (produced via thermionic emission from a tungsten filament) are accelerated through a potential difference down a column towards an anode. The accelerated electrons, now in a beam, are then shaped by a series of apertures and electromagnetic lenses: condenser lenses reduce the beam size, whilst apertures exclude extraneous electrons. This beam is then focussed by applying variable current to an objective lens and rastered (using deflector coils) across the sample as shown in Figure 3.9.

The electron beam then interacts with a small volume of the sample (known as the interaction volume) to generate backscattered electrons, secondary electrons, Auger electrons and X-Ray photons. Secondary electrons result from inelastic collision of incident electrons with specimen electrons. Because of their low energy (<50 eV), only secondary electrons emitted close to materials surface (<20 nm) are detected [198]; hence these can be used to provide topographical information [204]. In contrast, backscattered electrons (BSE) result from *elastic* collision between incident electrons and *nuclei* in the specimen surface (depth < 1  $\mu\text{m}$ ). These result from the coulombic force of the nuclei (which repels the incident electron away), hence their abundance depends on the size (atomic number) of the element: More backscattered electrons are generated from regions with a higher atomic number, hence their appearance as ‘brighter’ areas in BSE images [205]. BSEs are collected close to the beam aperture because they are scattered  $\sim 180^\circ$ . X-ray photons are generated when electrons in the beam cause ejection of a so-called Auger electron from a low-energy orbital in the target atom to leave a vacancy. An electron from a higher energy level in this atom subsequently drops down an energy level to fill this vacancy, and in doing so releases its excess energy (equivalent to the energy difference between the two electron shells) in the form of X-ray radiation [206]. The amount of energy released is unique for each element, hence elemental composition can be determined via Energy Dispersive X-ray Spectroscopy (EDX/S). Composition can then be approximately quantified by measuring the number of emitted X-rays per given energy per unit time (i.e. “peak heights” [207]).

Electrons of all types (distinguished on the basis of their energy and scatter angle) and x-rays are collected and amplified by detectors. The number of interactions (‘counts’) of each type per scan dwell point is then used to define the greyscale intensity of an image pixel. This process is repeated for every pixel in the grid scan, until a full image is generated.

#### *Experimental parameters*

Samples were characterised with a Hitachi TM3030 Plus SEM coupled with Bruker Quantax 70 EDS. An accelerating voltage of 15kV and a beam current of  $2 \times 10^{-9}$  A was used at a working distance of seven to nine millimetres and various magnifications. EDS spectra were collected for at least ten minutes, with BSE images collected at the maximum available resolution. Micrograph post-processing (including segmentation and quantification) is described in subsequent sections.

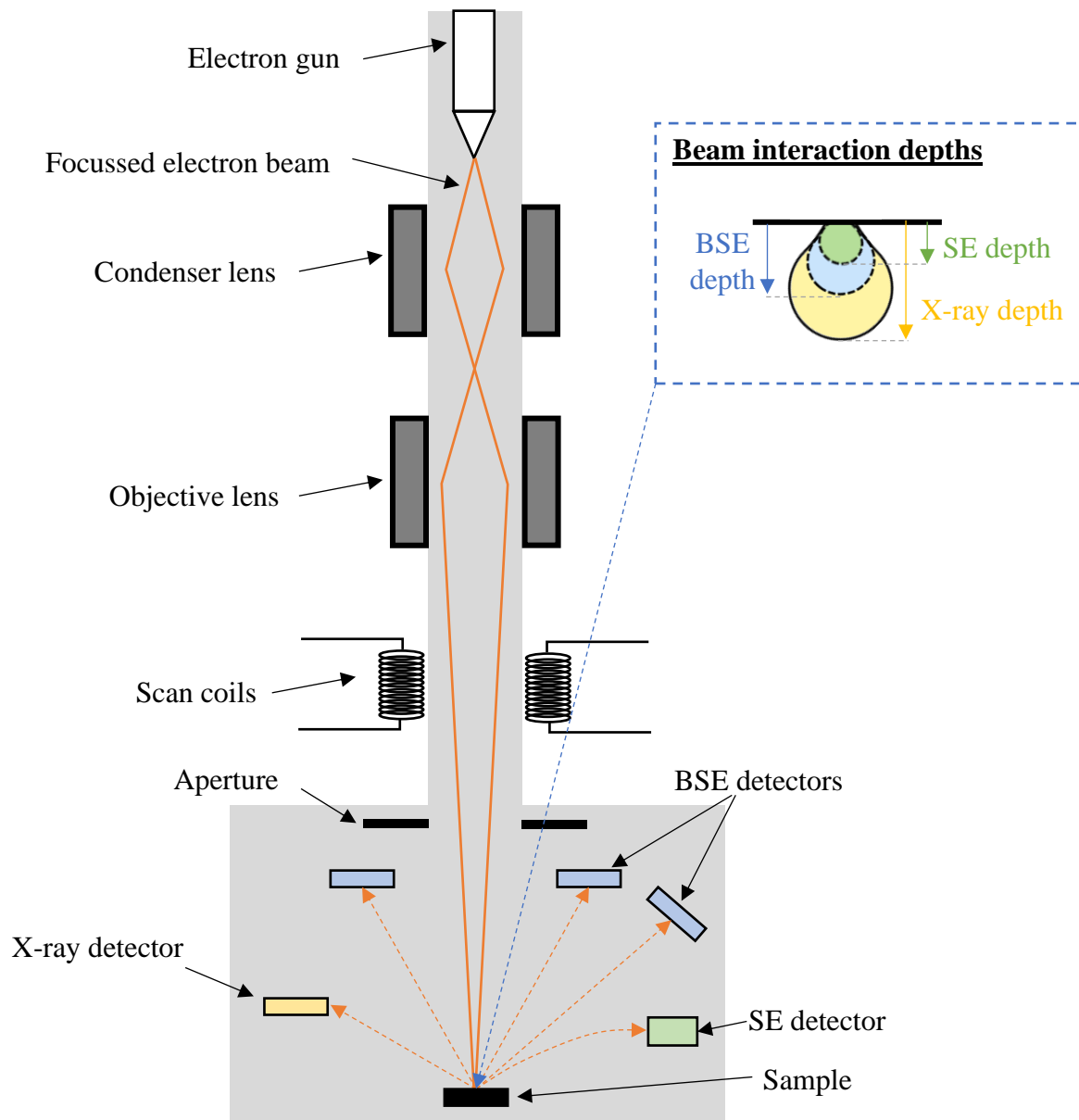


**Figure 3.9:** Schematic of Scanning Electron Microscope including inset showing beam-sample interaction volumes. Adapted from [207] and [198].

### 3.4.3. Raman Spectroscopy

Raman spectroscopy, which provides data on the vibrational modes of bonds in a material, was used in this study to elucidate the mineralogical composition of hillfort samples and to reveal structural differences (attributable to the variable Ca:Mg content) in the basaltic glass series. Raman spectra were also taken from unaltered regions of the nuclear-type glasses to allow comparison with other work.

In this technique, a laser (most commonly producing radiation in the visible range of the electromagnetic spectrum (400-660 nm), but also potentially the ultraviolet or near-infrared range) produces monochromatic radiation that is focussed onto a point on the sample using a confocal microscope (which utilises spatial filtering -a pinhole aperture- to eliminate out-of-focus light).

The photons comprising this radiation interact with the sample in two ways: Most photons are elastically scattered at the same wavelength as the incoming radiation (in a process known as Rayleigh scattering); however, in Raman-active molecules a small proportion of incoming photons (roughly 1 in  $10^6$ - $10^{15}$ ) are *inelastically* scattered at a wavelength *differing* from (typically lower than) the radiation source. The wavelength difference, or Raman shift (in  $\text{cm}^{-1}$ ), between the incident ( $\lambda_{\text{incident}}$ ) and scattered ( $\lambda_{\text{scattered}}$ ) photon wavelength is given by

$$\text{Raman shift} = \frac{1}{\lambda_{\text{incident}}} - \frac{1}{\lambda_{\text{scattered}}} \quad \text{Equation 3.8}$$

This Raman shift can provide information about the vibrational and rotational energies of molecular bonds.

In the Raman technique, this scattered radiation is collected and focussed (using a concave mirror) onto a diffraction grating containing a certain number of lines or grooves on its surface per unit length. This grating (part of a 'dispersive' or Czerny-Turner spectrometer as shown in Figure 3.10) spatially splits the beam into its constituent wavelengths which can then be projected on to a Charge Coupled Device (CCD) detector in the focal plane of another focussing mirror. The CCD, typically a photosensitive silicon device containing a two-dimensional array of light sensitive elements (pixels) that converts the electrical charge into a digital value, transmits these data to a computer where it is converted to a spectrum showing the intensity of scattering versus the Raman shift. The position and intensity of features in the spectrum reflect the molecular structure and are attributable to specific chemical bonds.

#### *Experimental parameters*

For this study, Raman spectra between  $100$ - $2000 \text{ cm}^{-1}$  were collected using a Renishaw InVia Raman microscope with a grating of  $2,400$  lines/mm. Spectra were excited for ten seconds using a  $514 \text{ nm}$  line of  $25 \text{ mW}$  Argon ion laser at  $80\%$  power, with ten acquisitions per sampled area and an image magnification of  $50\times$ .

Samples of dissolved glass powders were analysed using this technique, however only grain *interiors* were measured. These were assumed to be pristine/unaltered based on minimal visible evidence of dissolution on the grain surfaces and the minimal dissolution duration ( $< 112$  days at  $50 \text{ }^\circ\text{C}$ ).

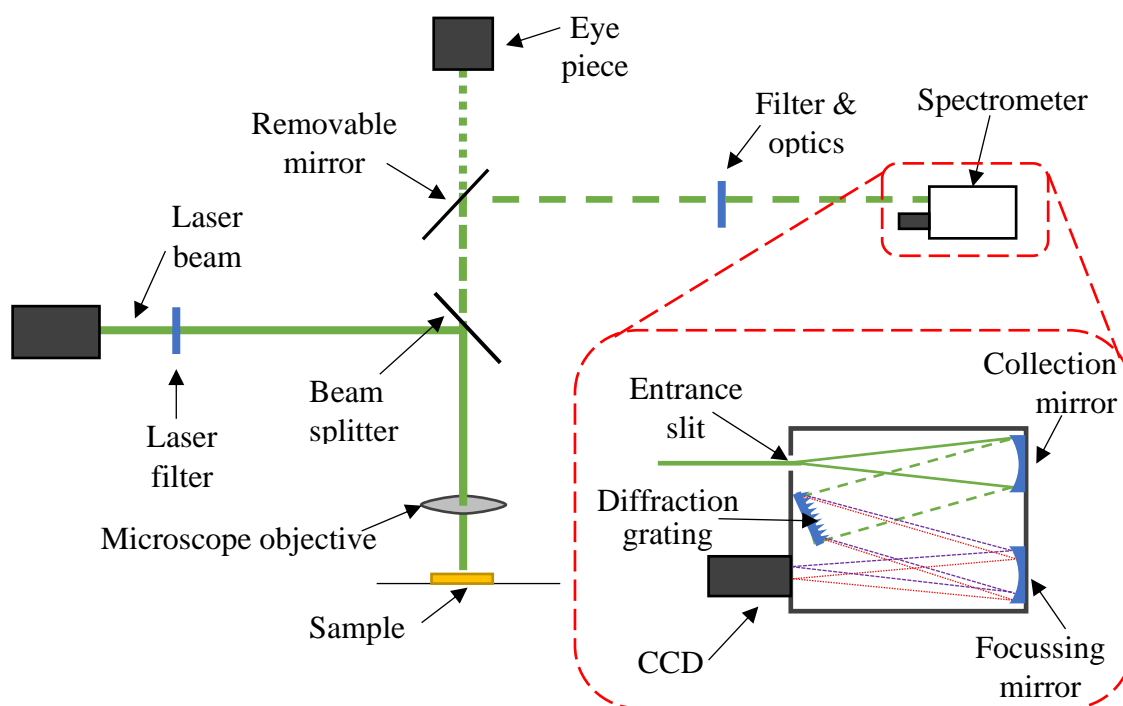


**Figure 3.10.** Schematic of Raman microscope, including inset showing details of the Czerny-Turner design for a spectrometer. Figure after [204].

### 3.4.4. X-ray Computed Tomography

X-ray Computed Tomography (XCT), which primarily provides data concerning sample morphology and local density, was used for two purposes in this study: first, to broadly characterise hillfort samples (including their probable glass content) before seeking potential evidence of dissolution in them; and second to characterise the alteration layers and features formed on laboratory-dissolved glasses. Both of these applications are considered novel, allowing a third purpose to be considered: the development of a methodology to allow XCT scanning of MCC- and PCT-type materials post-dissolution; and the development of quantitative techniques to analyse surface-features and their potential relation to aqueous surface processes in naturally weathered macro-porous (pumiceous) materials.

In XCT, electrons are generated (typically via thermionic emission from a heated element), before being accelerated by an applied current between the cathode and anode. These electrons are then focussed into to a spot (of a size specified by the “spot size”) on a target material of tungsten, molybdenum or copper, as shown in Figure 3.11. The interactions of these electrons with the target material generates Bremsstrahlung X-rays and characteristic radiation. The former occurs as electrons approaching the nucleus decelerate and lose energy via photon emission; whereas the latter occurs as a displaced electron in the target material is substituted by an electron from a higher energy level [208]. These X-rays are then released from the X-ray source (through the vacuum envelope) and propagate, in the direction of travel, as a cone-shaped beam.

The sample to be scanned, placed in the path of this beam, interacts with these incident X-rays via two processes: the photoelectric effect (whereby an incident x-ray photon collides with and ejects an *inner*-shell electron from the sample, causing characteristic x-ray photon emission as an outer electron ‘jumps’ down an energy-level to take its place) and Compton scattering (whereby incident photon is deflected as it collides with an *outer shell* electron in the target). The magnitude of these effects can then be quantified using Lambert-Beer’s law for monochromatic x-rays [208]

$$I = I_0 e^{-\mu x} \quad \text{Equation 3.9}$$

Here, the x-ray intensity transmitted through the sample ( $I$ ) can be related to the initial X-ray intensity ( $I_0$ ) via the beam travel distance ( $x$ ) and the local linear attenuation coefficient ( $\mu$ ). The latter (energy-dependant) coefficient depends primarily on the material density, however to a lesser extent it is also dependant on the mass attenuation coefficient (approximately proportional to the cubed atomic number for the X-ray energies typically used in XCT; [209], [210]). Notably, because of the co-dependency of the local linear attenuation coefficient, neither density or composition can be determined or quantified without *a priori* knowledge of one of these factors. Instead, quantitative XCT results are usually considered as relative rather than absolute numbers [211].

Any transmitted X-rays then travel through a scintillator (converting the x-ray photons to visible light) and potentially also a series of high-resolution detector optics (lenses), before being converted into an electrical signal by a detector (typically a CCD). This produces a two-dimensional radiograph (sometimes termed a ‘projection,’ ‘tomogram’ or ‘shadow’) showing local variations in  $\mu$  throughout a sample’s *entire* thickness. The sample is then rotated, step by step, through 360°, with radiographs taken at each step.

Two dimensional tomograms can then be ‘reconstructed’ into a three-dimensional volume using computational algorithms. Most commonly this involves using is a filtered back projection algorithm to back-project a one-dimensional dataset across two dimensions (Figure 3.11), however a full discussion of these algorithmic methods is outside the scope of this work (though [212] does provide this). During this processing various correction methods are applied to minimise noise, blurring and imaging artefacts; however these artefacts are frequently impossible to entirely eradicate and are often considerations in XCT studies [208], [211].

For this study, data (once collected and reconstructed) was subsequently analysed using Dragonfly software from the Object Research Systems. Details of the software methodologies developed for this analysis are provided in Appendix I.

#### *Experimental parameters*

XCT was completed in two ‘cycles’ for this study.

The first experimental ‘batch’ analysed only vitrified hillfort materials and was conducted at the Manchester X-Ray Imaging Facility (MXIF), with image acquisition by Daniel Sykes. In this, all six hillfort samples were scanned with a Nikon XT H 225 XCT scanner (Figure 3.12) equipped with a 190 kV, 50-58 uA X-Ray beam and a 0.25 mm copper filter. Table 3.8 illustrates how beam current and resolution were varied inter-sample to account for variable sample densities and dimensions, whilst maximising spatial resolution and contrast [213], [214].

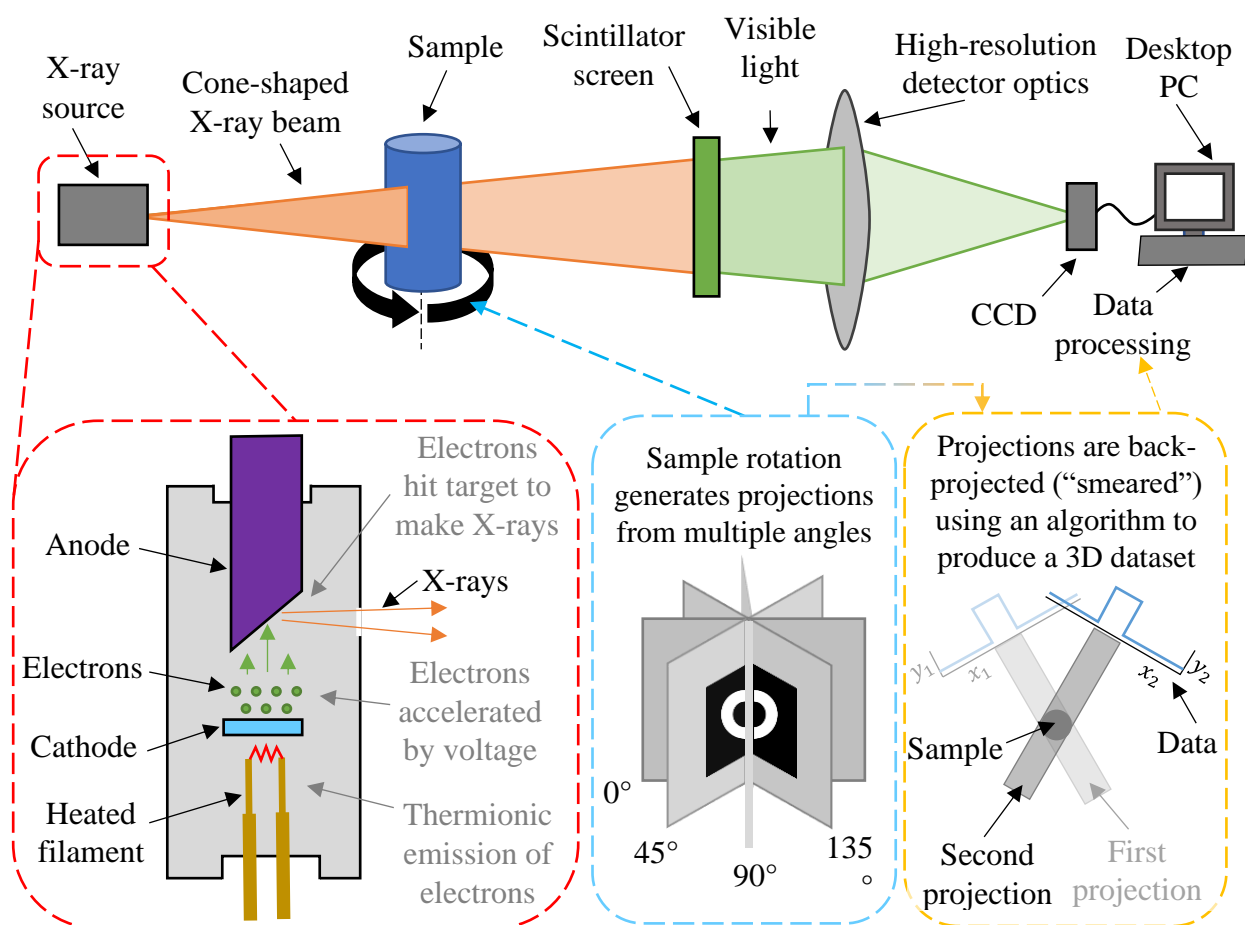


**Figure 3.11.** Schematic illustrating a typical XCT system, including insets showing an x-ray generation method (below; left), and how a three-dimensional dataset is constructed by taking projections at various angles (below; centre), and then back-projecting one dimensional dataset across two dimensions (below; right) and 2D datasets into 3D space.

Sample number	Beam current ( $\mu\text{A}$ )	No. of projections	Voxel size ( $\text{mm}^3$ )
601401	53	5013	0.020647
601602	53	4396	0.042757
601604	58	4377	0.060972
601612	58	4238	0.060111
601655	50	3306	0.026572
602639	50	3750	0.03271

**Table 3.8.** Scanning parameters used in XCT of hillfort samples.



**Figure 3.12.** The Nikon XT H 225 XCT scanner used in this study (a) and the sample positioning within the cabinet (b). Samples were not removed from their sample bag and were held in place using phenolic foam of a sufficiently low density to appear identical to the surrounding air in scanned images. Note that during scanning the sample appears darker than the surrounding air – a correlation which is inverted during image reconstruction (see below).

A second experimental plan was devised to study laboratory-dissolved (PCT and MCC-type) samples. These data were collected at the Sheffield Tomography Centre (STC), with scans and reconstructions performed by Ria Mitchel (who also aided considerably in experiment design). These laboratory-dissolved samples (described in Section 3.2.1) were scanned in a Zeiss Xradia 620 Versa equipped with a 30-160 kV, <25 W X-Ray beam and 0.25 mm copper filter. The 620 Versa is also equipped with a range of objective lenses (0.4x, 4x, 20x, 40x) and various Zeiss proprietary filters. The latter, used to filter low energy x-rays, were selected by the operator to optimise the quality of each scan.

Table 3.9 illustrates the range of samples (MCC and PCT, in different forms, with dissolution durations from 353 - 672 days) and scan conditions utilised. The range of resolutions (pixel sizes) utilised represent the initial low resolution “overview scans” which were used to identify regions of interest to be re-scanned at high resolutions.

### 3.4.1. Pycnometry

Pycnometry was used to determine the density of the hillfort replica glass and the glasses used in laboratory dissolution experiments. Knowledge of this variable was necessary to determine the mass of PCT powder required to achieve the desired surface area (see [195] for more details).

Densities were determined via gas pycnometry. In this, inert gas is introduced (at a known pressure) into an empty sealed sample chamber and a baseline pressure measurement is made. The sample is then placed into the same chamber and the same quantity of gas is introduced at the same pressure, before a second pressure measurement is made. The pressure differential can then be used to determine the sample volume (the volume of gas displaced by the sample), which can be combined with the known sample mass, to calculate the sample density.

#### *Experimental parameters*

Circa one gram of glass powder (<75  $\mu\text{m}$ ) was measured per composition using an AccuPyc II 1340 Gas Displacement Pycnometry System. The average density measurement across ten purge cycles was calculated using helium introduced at 2.23  $\text{kPa s}^{-1}$ .

Scan no.	Res.	Diss. dur. (days)	Diss. exp. type	Sample type	Filter	kV	$\mu$ A	Objective lense mag.	No. of proj.	Pixel size ( $\mu$ m)
309	Low	672	MCC	Glass + A.L.	Air	60	108	0.4x	801	8.6
310	High	672	MCC	Glass + A.L.	LE3	120	146	20x	1601	0.7
311	High	672	MCC	Glass + A.L.	LE3	120	146	20x	1601	0.6
312	Low	353	PCT (90 °C)	Dry powder	LE3	110	141	4x	801	1.37
313	Low	353	PCT (90 °C)	Dry powder	LE3	110	141	4x	1601	1.37
314	High	353	PCT (90 °C)	Dry powder	LE6	110	141	20x	1601	0.55
315	Low	353	PCT (90 °C)	Wet powder	LE3	110	141	4x	801	1.37
316	High	353	PCT (90 °C)	Wet powder	LE3	110	141	4x	1601	1.37
317	High	353	PCT (90 °C)	Wet powder	LE6	110	141	20x	1601	0.55
318	Low	468	MCC	A.L. only	Air	90	133	4x	1601	1.00
319	High	468	MCC	A.L. only	LE2	90	133	20x	1601	0.54
320	High	468	MCC	A.L. only	LE2	110	141	40x	1601	0.35
321	Low	468	MCC	Glass only	LE2	110	141	4x	1601	1
322	High	468	MCC	Glass only	LE4	120	146	20x	1601	0.54
333	High	468	MCC	Glass only	LE5	140	150	40x	1601	0.34

**Table 3.9:** Scanning parameters used in XCT of laboratory-dissolved samples (all 50Ca50Mg basaltic glasses), including the duration for which samples were dissolved (Diss. dur.), the experiment type (Diss. exp. type), the number of projections (No. of proj.) and the Zeiss proprietary Low Energy (LE) filters used for each scan. For more details of dissolution experiment meanings/parameters see Section 3.2.

### 3.4.2. Inductively Coupled Plasma Optical Emission Spectroscopy

Inductively Coupled Plasma Optical Emission Spectroscopy was used to determine unaltered glass compositions and to quantify the elemental contents of leachates post-dissolution.

In this, the filtered and acidified liquid sample is peristaltically pumped into a nebuliser where it combines with argon gas to produce an aerosol spray as shown in Figure 3.13. This is introduced into a spray chamber which separates the larger droplets (subsequently drained) from the finer droplets which are directed into the fused silica torch. In the torch, the aerosol mix is forced through the centre of an induction coil which generates an electromagnetic field sufficient to ionize the argon into a plasma. This causes excitation (atomisation and ionization) of electrons in the sample via two mechanisms: inelastic scattering of an electron ( $e$ ) from an atom ( $M$ ) to leave this atom in an excited state ( $M^*$ );



and by recombination of an ion ( $M^+$ ) with an electron ( $e$ ) which leads to photon ( $h\nu$ ) emission:



These photons have an energy (wavelength) which is characteristic of each element, and they are emitted in quantities proportional to the amount of that element in the sample.

Emitted photons pass through a ‘window’ positioned axially and radially to the plasma (a ‘duo’-type setup which combines the improved sensitivity provided by axial views with the increased precision when analysing multi-elements given by radial viewing [215]). These optical photons then travel through a high-resolution optical system including a spectrometer (used to separate photons based on their energies) and CCDs (used to convert the optical signal to an electronic one).

Using an accompanying computer, the intensity of the characteristic emission is quantified before being compared to a calibration curve generated apriori by measuring a set of standard solutions that contain all measured elements in a range of concentrations.

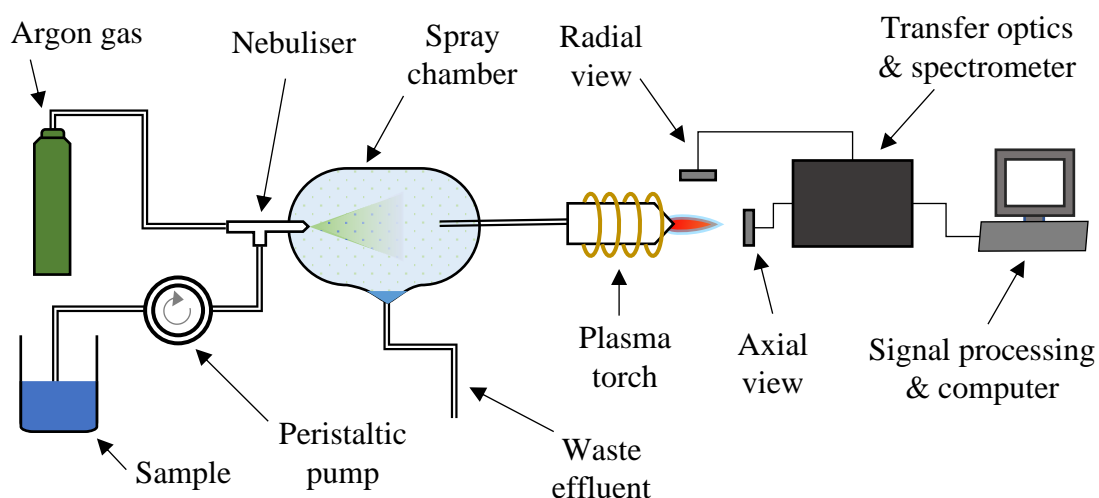


Figure 3.13. Schematic of a standard ICP-OES system after [215].

### Experimental parameters

ICP-OES of glasses prior to their dissolution was conducted externally (by Heather Grievson of The University of Sheffield's Faculty of Science Mass Spectrometry Centre - ICP Facility). For this, all seven glass types studied herein (five basaltic glasses, MW25 and ISG) were provided as fine ( $< 75 \mu\text{m}$ ) powders. Prior to ICP-OES analysis these were fully digested/dissolved in Teflon beaker containing ultra-pure hydrofluoric acid.

Leachate analysis was carried out by the author using a ThermoFisher iCAPDuo 63000 ICP-OES equipped with a fused silica torch. A suite of ten multi element standards were used in the calibration of this instrument. Each was prepared using high-quality Fluka elemental standards of a known concentration ( $10,000 \text{ mg L}^{-1}$ ) which were diluted in 1% ultra-pure nitric acid to achieve the concentrations outlined in Table 3.10.

Standard number (name)	Elemental contents	el. conc. (ppm)
0 (blank)	Nitric acid only	0
1	Minor + Major elements	0.01
2	Minor + Major elements	0.1
3	Minor + Major elements	1
4	Minor + Major elements	10
5	Minor + Major elements	25
6	Minor + Major elements	50
7	Only Major elements	100
8	Only Major elements	150
9	Only Major elements	250

**Table 3.10:** Contents and elemental concentration (el. conc.) of chemical standard solutions prepared for ICP-OES analysis. "Major Elements" are those expected at concentrations  $> \sim 10 \text{ ppm}$  (K, Cr, Fe, Na, Al, Zr, Mn, Li, Mg, B, Ca, Si) and "Minor Elements" are those expected to be present at  $< \sim 10 \text{ ppm}$  (Pr, Cs, Nd, Mo, Ti, Sr, La, P, Ce).

### 3.4.3. pH measurement

Leachate pH was measured post-dissolution to inform geochemical modelling and to aid in elucidation of dissolution mechanisms. Digital potentiometric pH meters typically comprise two electrodes: a measuring electrode and a reference electrode. These are housed within a single 'probe' in the case of combination electrode system. Both electrodes typically comprise an Ag/AgCl wire submerged within a potassium chloride solution

The *measuring electrode* consists of a glass membrane (or 'bulb') which separates the solution to be tested and the internal buffer solution (KCl). Hydrogen ions in the test solution can diffuse into or out of the outermost layer of the glass membrane: in alkali test solutions  $\text{H}^+$  ions diffuse *out* and set up a negative potential on the outer surface, whereas the reverse is true for acidic solutions (Figure 3.14). Contrastingly, the electrical charge on the *inside* of this probe remains constant and thus the *total* membrane potential is dependent on the  $\text{H}^+$  content of the test solution.

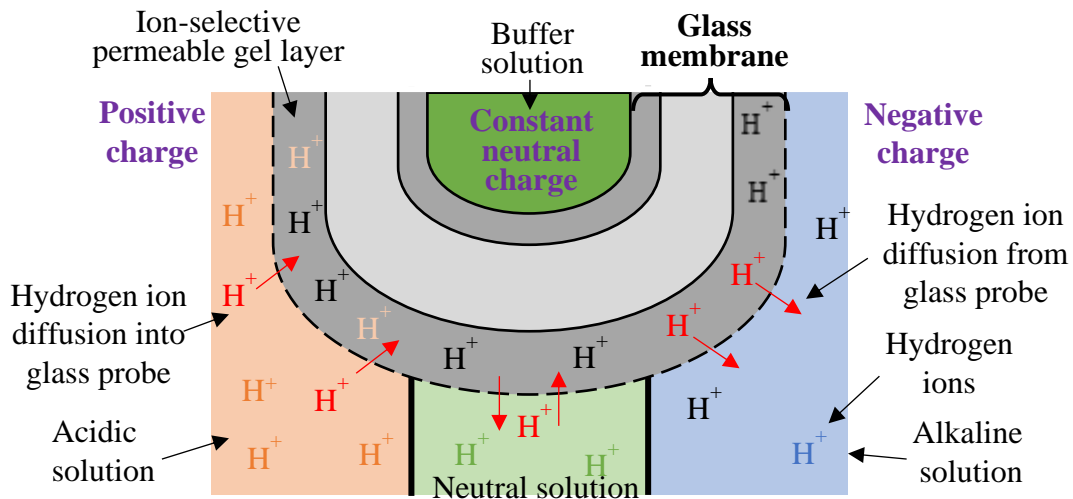


**Figure 3.14.** A glass membrane and its function in a pH probe. Redrawn after [216].

The reference electrode is also submerged (and in electrical contact with) the test solution, however it does not contain a glass membrane through which H<sup>+</sup> ions can diffuse. The voltage of this electrode thus remains constant, allowing comparisons to be drawn between the voltage of the measuring and reference electrode. The electrical potential voltage difference between the two electrodes can then be correlated to the test solution pH.

#### *Experimental parameters*

pH measurements were conducted at room temperature (~ 20 °C) using a Mettler Toledo Five Easy Plus reader and Mettler Toledo LE422 probe. This was calibrated using Lovibond Water Testing (Tintometer Group) buffers at pH 4, 7 and 11.

#### **3.4.4. Geochemical modelling**

Geochemical modelling was used to gain an indication of which mineral phases may be at saturation at each measurement timepoint. Note that this modelling gives no indication of mineral saturations *between* the timepoints.

For each timestep, leachate elemental concentrations (measured via ICP-OES) and leachate pH were inputted. Boundary conditions were set identically for all timesteps, with pressure set to 1 atmosphere and temperature set to either 50°C for PCT-B or 90°C for MCC-1. Equilibrium with atmospheric air (gaseous carbon dioxide and oxygen) was also set.

These data were inputted into the PHREEQC (version 3.0) software package [217]. This used the aforementioned input parameters to calculate Ion Activity Products (*IAP*) and combined these with equilibrium constants ( $K_s^0$ ) from the Lawrence Livermore National Laboratory (LLNL) thermodynamic database [218] to calculate a saturation index (*SI*) for each phase using

$$SI = \log \left( \frac{IAP}{K_s^0} \right) \quad \text{Equation 3.12}$$

In the resulting output data, phases with a saturation index greater than zero were assumed to be potentially saturated in the leachate.

#### **3.4.5. Optical Microscopy**

Optical microscopy was used to characterise hillfort samples and seek evidence of dissolution. Samples were magnified (by a 50 to 200 times) using a Nikon Eclipse LV150 microscope.

# 4. Dissolution of Simulant and Simplified HLW Glasses

## 4.1. Introduction

Studying dissolution of simulant and simplified glasses analogous to those which will be used in the geological disposal of HLW can significantly aid the global effort to demonstrate the long-term safety of this disposal method. Such glasses are particularly valuable because of their ease of synthesis/handling. Furthermore, comparison between different glasses and methodologies used to dissolve these can also provide insight into the glass dissolution processes that may, in the future, impact the safety of communities within the hydrological vicinity of any GDF.

The International Simple Glass (ISG) and the UK's Magnox Waste (MW) glasses represent some of the most well-studied examples of these analogues. Significant differences have previously been observed during the long-term dissolution of these glasses in  $\text{Ca}(\text{OH})_2$  leachants [60]; however comparative studies using simpler aqueous leachates have until now been absent. This is in spite of the value of 'simplified' leachates in elucidating key dissolution mechanisms and the significant uncertainty in the composition of any solutions reaching HLW glass in future disposal scenarios. Further investigations of these glasses is also necessary to elucidate any differences in their dissolution behaviour [60].

In light of that, this chapter presents results from the dissolution of an ISG glass and an MW25-type glass in a pure water leachant via the MCC-1 and PCT-B procedures outlined in Section 3.2. Dissolution rates are calculated and compared for both glasses, with glass alteration layers thoroughly characterised and (where available) used to develop models outlining the alteration mechanisms of these glasses.

## 4.2. Results

### 4.2.1. Pristine glass characterisation

#### SEM-EDS

SEM (Figure 4.1) of undissolved samples shows ISG to be uniform and single-phase, as in other studies [219]. In contrast, unaltered MW25 samples contain clusters of angular precipitates, each of 1-2  $\mu\text{m}$  in size. EDS indicates these predominantly comprise chromium and iron as quantified in Figure 4.1. Powder samples, prior to dissolution, show surface fracturing within a  $\sim 1 \mu\text{m}$  perimeter of their edges.

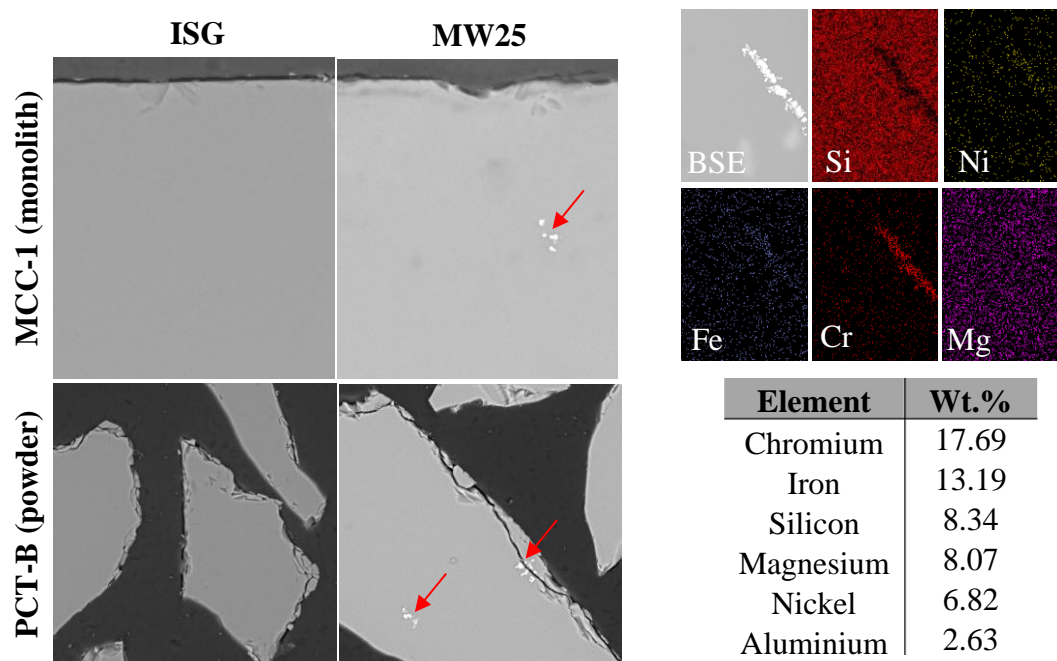


**Figure 4.1.** BSE images of MW25 and ISG after preparations as monoliths and powders (left), with precipitates (arrowed in red) shown and quantified using EDS (right).

#### Acid-digest & ICP-OES

Glass compositions, measured via acid digest and ICP-OES are given in Table 4.1 (for constituents present in at least one glass in quantities greater than one weight percentage).

	ISG	MW25
<b>SiO<sub>2</sub></b>	56.35	50.10
<b>B<sub>2</sub>O<sub>3</sub></b>	18.60	17.56
<b>Na<sub>2</sub>O</b>	14.10	9.01
<b>Al<sub>2</sub>O<sub>3</sub></b>	3.57	2.55
<b>CaO</b>	5.77	0.24
<b>ZrO<sub>2</sub></b>	1.29	0.67
<b>Li<sub>2</sub>O</b>	0.00	6.93
<b>MgO</b>	0.08	7.83
<b>Fe<sub>2</sub>O<sub>3</sub></b>	0.08	1.56

**Table 4.1.** Compositions, in oxide molar percentage, of ISG and MW25. MW25 also contains a range of minor elements (<1 wt. % each), which are not shown here for brevity. Errors assumed to be  $\pm 1\%$  for major elements and  $\pm 5\%$  for minor elements.

### XRD

Figure 4.2 presents XRD patterns taken from pristine, undissolved, MW25. Diffuse scattering is evident as the dominant broad peak from  $\sim 15$  to  $40^\circ 2\theta$ , and as a lower amplitude peak from  $\sim 40$  to  $50^\circ 2\theta$ . No other notable peaks are discernible. ISG has already been verified as X-ray amorphous in previous studies [219].

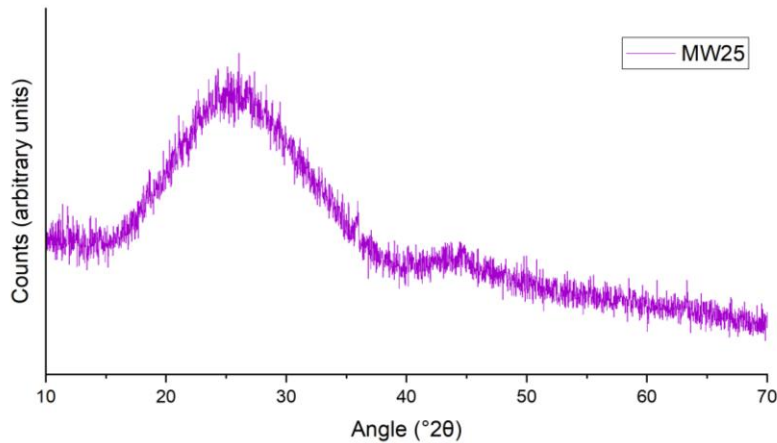


**Figure 4.2:** XRD pattern of pristine (undissolved) MW25.

### Raman Spectroscopy

Raman spectra collected from both a precipitate and the ‘matrix’ of MW25 sample are shown in Figure 4.3. In the glass ‘matrix’ a broad ( $\sim 350\text{ cm}^{-1}$  wide) double-peak was observed to be centred around  $\sim 340$  and  $480\text{ cm}^{-1}$ , with another similar width peak at  $\sim 920\text{ cm}^{-1}$  containing a shoulder at  $\sim 875\text{ cm}^{-1}$ . Lower amplitude ( $\sim 200\text{ cm}^{-1}$  wide) peaks were also observed at  $\sim 1400\text{ cm}^{-1}$  and  $1680\text{ cm}^{-1}$ . All of these peaks are similarly evident, though with a reduced amplitude, in Raman of the precipitate component, however this spectrum is dominated by the presence of a narrower ( $100\text{ cm}^{-1}$  width) peak at  $\sim 700\text{ cm}^{-1}$ .

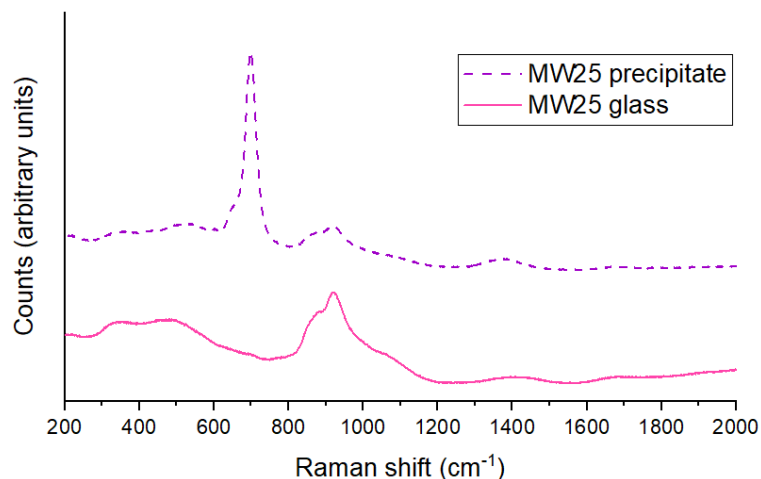


**Figure 4.3:** Raman spectra of pristine MW25 sample from an area observed to be crystal-free (‘glass’) and a precipitate.

#### 4.2.2. pH

Leachate pH evolution during the dissolution of ISG and MW25 is shown in Figure 4.4, with error bars indicating the standard deviation between triplicate samples.

In all experiments blank vessels, containing only UHQ water, typically have a large repeatability error (frequently > 1 pH units), with measured pH values of 6 - 7.5. Two blanks are shown for the penultimate MCC-1 timestep because samples from this timestep were initiated asynchronously with separate blanks for each initiated ‘batch’.

MW25 and ISG show a similar trend in MCC-1 experiments, though MW25 shows somewhat higher absolute pH values (typically exceeding ISG by ~0.5 pH units). Assuming a neutral pH initially, pH rises to a value of 9.5 by 56 days of dissolution for MW25 and to a pH value of 9.3 by 112 days for ISG. Measured pH for both glasses then decrease to pH ~9.1 (by 224 days of dissolution), before plateauing at this value for MW25 or continuing to fall slightly (to values of 8.9) and then plateauing beyond 468 days for ISG.

In PCT-B tests, MW25 shows a similar trend to that shown for MCC-1 tests, increasing to pH values of 9.9 within 14 days of dissolution before decreasing and plateauing at a value of 9.4 by day 112. For ISG, pH rises to 9.4 within 7 days of dissolution, before plateauing at this level until somewhere from 28 to 56 days of dissolution where pH values decrease to 9.2. This pH value is then approximately sustained until at least day 224 of dissolution.

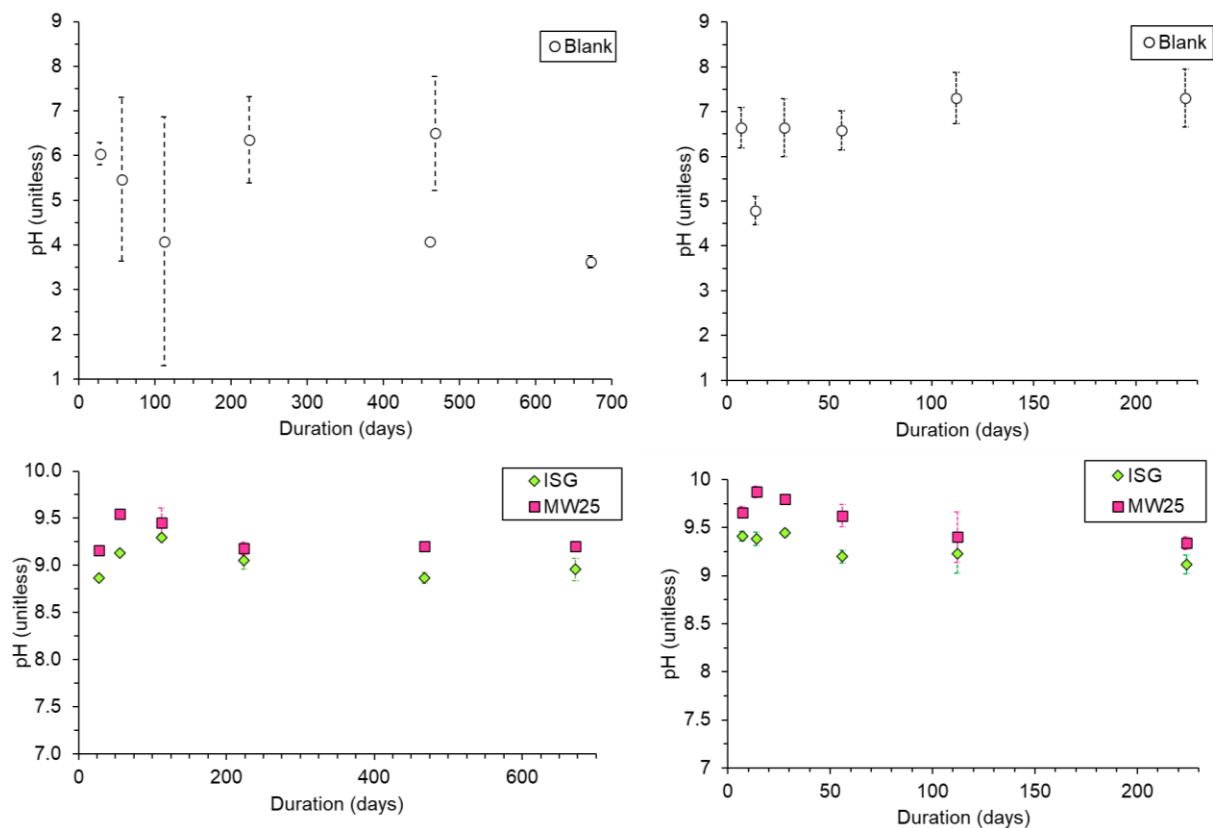


**Figure 4.4.** Measured leachate pH after MCC-1 (left) and PCT-B (right) dissolution of ISG, and MW25. Note that in MCC-1 experiments the pH of 50Ca50Mg and MW25 were near-identical at 28 days, as also occurs for ISG and 50Ca50Mg at 56 days. Error is within the extent of the plotted datapoint in MCC-1 blank vessels after 461 and 672 days of dissolution.

### 4.2.3. Normalised mass losses

Normalised mass loss (NL) values calculated for selected elements (*i*) are shown in Figure 4.5 and Figure 4.6 for MCC-1 and PCT-B experiments respectively. Elements include all those measured in ISG (see Table 4.1) and all elements present in MW25 in quantities greater than five weight percent. Zirconium, although present in ISG, is omitted for brevity and because it shows no meaningful or consistent trend for either glass composition.

Boron and sodium mass loss values in MCC-1 experiments show similar *trends* to each other, however sodium normalised mass losses are typically three to four times larger in terms of absolute values. In both sodium and boron, all glasses show an approximately logarithmic increase initially, reaching an approximate plateau within 112 days of dissolution for ISG. For MW25 this plateau is never achieved, with a circa linear increase instead observed from 112 days of glass dissolution onwards. With regard to *absolute* values,  $NL_{Na}$  and  $NL_B$  values for ISG and MW25 are approximately within error for the first 224 days of dissolution, before values for MW25 begin exceeding those for ISG by an ever-increasing factor.

Silicon normalised mass loss values show similar trends to those for Na and B with a few exceptions. For MW25, for example,  $NL_{Si}$  values appear to plateau after 112 days, whilst for  $NL_{Na}$  and  $NL_B$  this was not observed. Absolute  $NL_{Si}$  values beyond 112 days of ISG dissolution also exceed those for MW25 (by a factor of 1.5-2.5) in a manner not observed for  $NL_{Na}$  and  $NL_B$  data.

For MW25,  $NL_{Mg}$  shows a decrease from  $\sim 0.25 \text{ g m}^{-2}$  (at 28 days of dissolution) to near-zero values (where they remain for the remainder of the test duration) by dissolution day 56. For  $NL_{Al}$ , both glasses show an exponentially decreasing trend with dissolution duration, with absolute values typically two to three times lower for MW25 compared to ISG.

For ISG, calcium normalised mass losses appear approximately constant, though with some evidence of a modest linear increase from values of  $\sim 4 \text{ g m}^{-2}$  by dissolution day 28 to  $\sim 5 \text{ g m}^{-2}$  by 672 days. Values for MW25 are consistently zero until dissolution day 672 when values reach  $\sim 2 \text{ g m}^{-2}$ , however the error on this measurement is substantial.

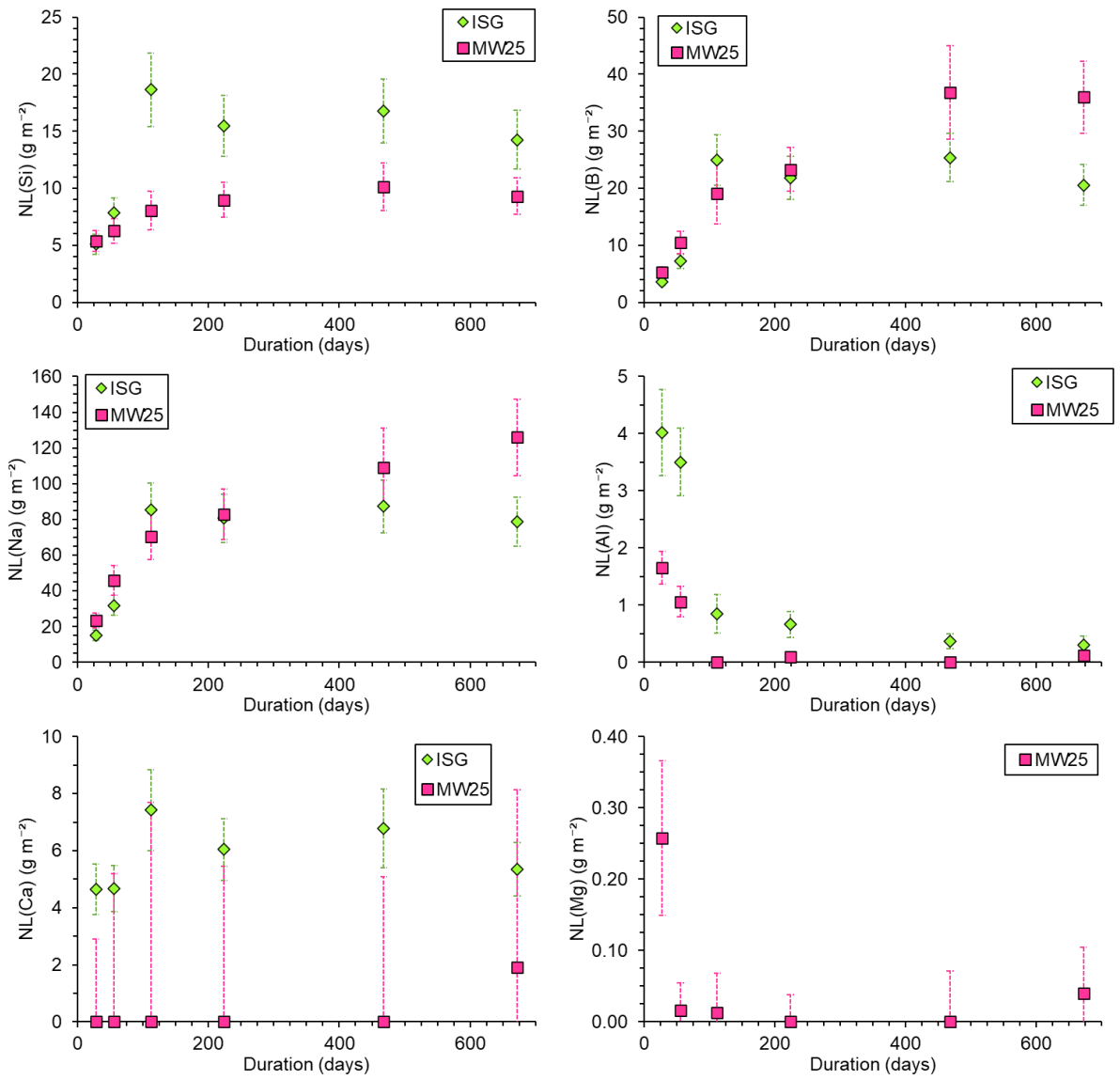


**Figure 4.5.** Normalised mass loss (NL) values calculated after the dissolution, via the MCC-1 procedure, of ISG and MW25.

In PCT-B experiments,  $NL_B$  shows a similar trend to  $NL_{Na}$ . Values rise linearly throughout the experiment, but at different rates. This increase is relatively rapid between 7-28 days, with the greatest rate of increase observed for MW25. Rates of increase then slow from 28 to 112 days of dissolution, with this again appearing slightly more rapid for MW25. By 28 days of dissolution, the absolute  $NL_{Na}$  and  $NL_B$  values for MW25 exceed those for ISG, with this deviation then increasing from a difference of  $1 \text{ g m}^{-2}$  (at 28 days) to  $3 \text{ g m}^{-2}$  (by day 112). Absolute values for MW25 exceed those for ISG for all timesteps excluding seven days of dissolution. A final more rapid increase may be speculated between 112-224 days of dissolution (although this is dependent on the two bounding datapoints for this period), with this rate of increase again appearing larger for MW25.

For silicon normalised mass loss, values for ISG are constant for the first 112 days of dissolution ( $\sim 0.06 \text{ g m}^{-2}$ ), before increasing to  $\sim 0.08 \text{ g m}^{-2}$  by day 224. For MW25,  $NL_{Si}$  values increase linearly from  $\sim 0.04 \text{ g m}^{-2}$  to  $\sim 0.06 \text{ g m}^{-2}$  between seven and 28 days of dissolution. The latter value is then approximately maintained for the remaining test duration, although there may be a subtle (within error) decrease of  $0.005 \text{ g m}^{-2}$  at day 112 of dissolution, which is recovered by alteration day 224. Absolute  $NL_{Si}$  values for ISG and MW25 are within error for all dissolution durations except day seven, where MW25 has a value of  $\sim 0.02 \text{ g m}^{-2}$  below that for ISG.

For  $NL_{Ca}$ , ISG shows similar trends to those for  $NL_B$ : an approximate linear increase in values for the first 56 days of dissolution, before this rate of linear increase slows between dissolution day 56 and 224. For MW25, the  $NL_{Ca}$  trend is more complex: with an increase from near-zero values to  $0.025 \text{ g m}^{-2}$  between day seven and 28 of dissolution followed by a decrease back to zero, where normalised mass losses remain, by alteration day 112.

ISG consistently maintains a near-zero ( $\sim 0.0001 \text{ g m}^{-2}$ ) aluminium normalised mass loss for the entire experiment duration. MW25  $NL_{Al}$  is similarly negligible until dissolution day 28, before values increase to  $\sim 0.005$  and then to  $\sim 0.01 \text{ g m}^{-2}$  at 56 to 112 days of dissolution respectively.  $NL_{Al}$  has fallen to zero by day 224 for MW25.

MW25  $NL_{Mg}$  values show a little consistent trend: decreasing from  $0.025 \text{ g m}^{-2}$  to  $0.01 \text{ g m}^{-2}$  between seven and 14 days of dissolution, before remaining at this value until dissolution day 28.  $NL_{Mg}$  then rapidly increases to  $0.03 \text{ g m}^{-2}$  by day 56, before linearly decreasing to near-zero by day 224 of alteration.

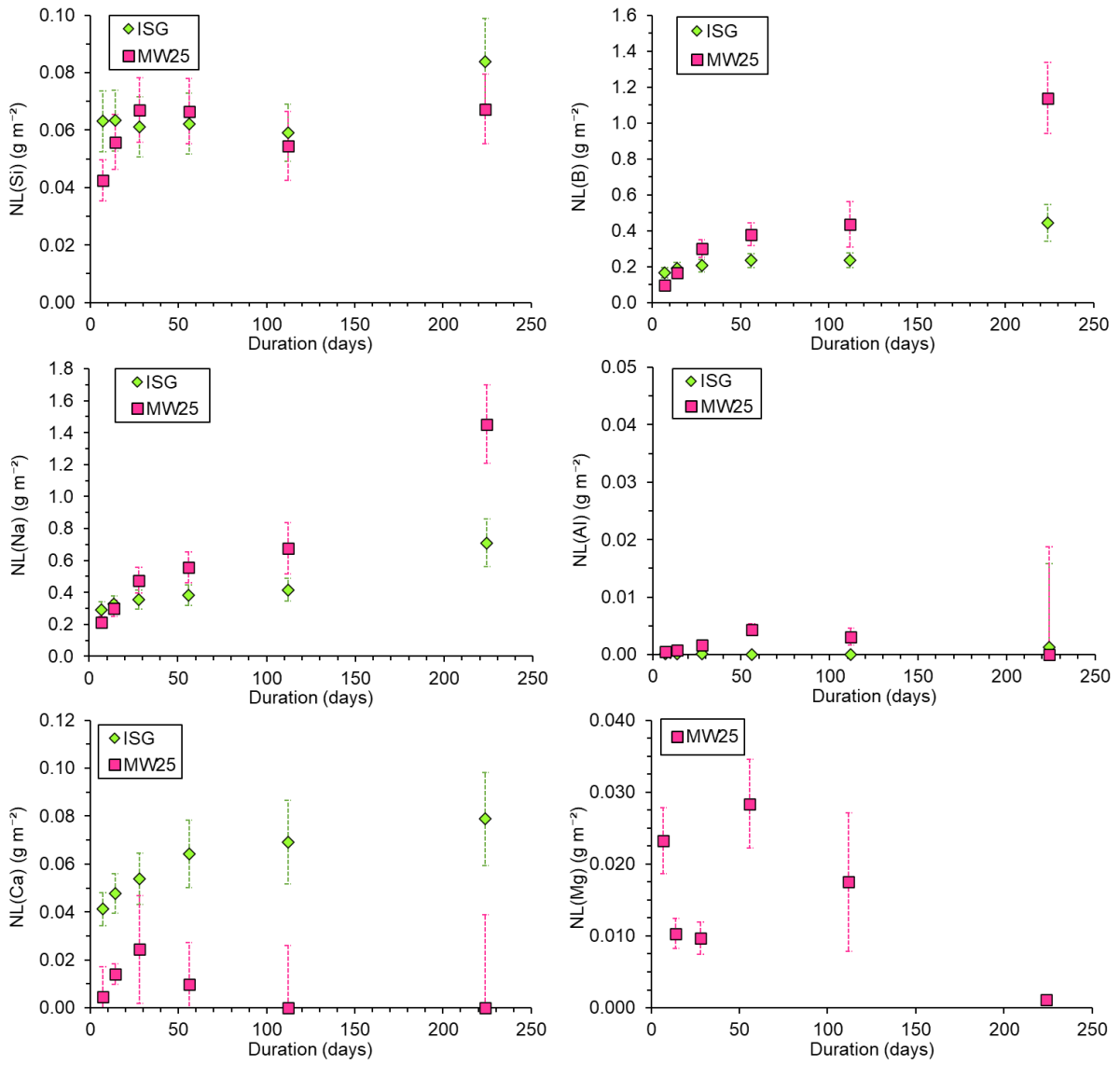


**Figure 4.6.** Normalised mass loss (NL) values calculated after the dissolution, via the PCT-B procedure, of ISG and MW25.

#### 4.2.4. SEM EDS analysis

##### *MCC-1/BSE*

Figure 4.7 shows representative SEM-BSE images from ISG and MW25 at each MCC-1 timestep. To facilitate comparison, images are of an identical magnification and wherever possible are from areas free from vermiform features (see Chapter 6). Note that layer thicknesses are further described and quantified in Section 4.2.5.

For ISG, two distinct surface layers are evident by day dissolution 28. The outermost ‘blocky’ layer (**Layer 1**) has a roughly constant thickness across the monolith (see Section 4.2.5 for quantification), though it is laterally discontinuous due to regular breakages across its length. This layer is of comparable greyscale intensity to the pristine sample internally. Moving inwards from this, the second layer (**Layer 2**) is notably darker in greyscale intensity than either the pristine glass or Layer 1. The layer also varies considerably in depth/thickness across the monolith, with occasional scallop-shape protrusions penetrating microns into the pristine glass.

By day 56 of dissolution, Layer 1 has increased in thickness (see Section 4.2.5) and the edges of its constituent fragmented ‘blocks’ increasingly curl upwards at their ends to form more arcuate or curvilinear features than were evident previously. Layer 2 shows minimal growth in thickness, however the scallop-protrusions have increased in their depth of penetration (now reaching up to 10-15  $\mu\text{m}$  from the apparent glass surface). Though these features appear similar in greyscale intensity to Layer 2 to the unaided eye, detailed analysis of greyscale histograms (Figure 4.8) reveal these to be slightly ‘darker’ than Layer 2. This justifies classification of these protrusions as a separate layer: **Layer 3**. This is separated from Layer 2 by a thin ( $<1 \mu\text{m}$ ) ‘bright’ layer which is unquantifiable using EDS, but is evident in BSE images.

Layer 1 remains relatively unchanged after 112 days of dissolution, with Layer 2 also showing little difference except a potential increase in thickness (Section 4.2.5). Layer 3 now penetrates up to  $\sim 60 \mu\text{m}$  from the apparent glass surface. In accordance with their semi-circular shape (in cross section), these protrusions have increased in width at the same rate they have grown in penetration depth. This increase in radii allows individual protrusions to have, by this stage, combined to form a more continuous layer, though the scalloped edge to this layer remains.

Little change in Layer 1 and 2 is observed between 112 to 224 days of dissolution, although both may have modestly increased in depth. Layer 3, by this stage, is nearly entirely un-broken across the surface of the monolith. The scalloped edge to this layer observed at 112 days of dissolution is by now increasingly replaced by an irregular boundary. This is characterised by angular (approximately rectangular) protrusions which can be accompanied by isolated globular or well-rounded ‘islands’ of altered glass within the altered monolith cross sections.

By 468 days of dissolution, Layer 3 appears compositionally-banded in BSE images. Though uniform for its outermost 20-30  $\mu\text{m}$ , moving inwards from this (towards the pristine glass) the layer shows micron-thickness ‘stripes’ of material similar in greyscale intensity to the outer zone. These are separated by ‘brighter’ zones of similar thickness (microns). At semi-regular intervals ( $\sim 30 \mu\text{m}$ ) these bright zones extend outwards (towards the leachate) in micrometre-thin bright bands orientated perpendicular to the surface. This provides a ‘bread-loaf’ like morphology (as if bread rolls or bread-based patisseries have coalesced as they extended laterally during their batch-baking).

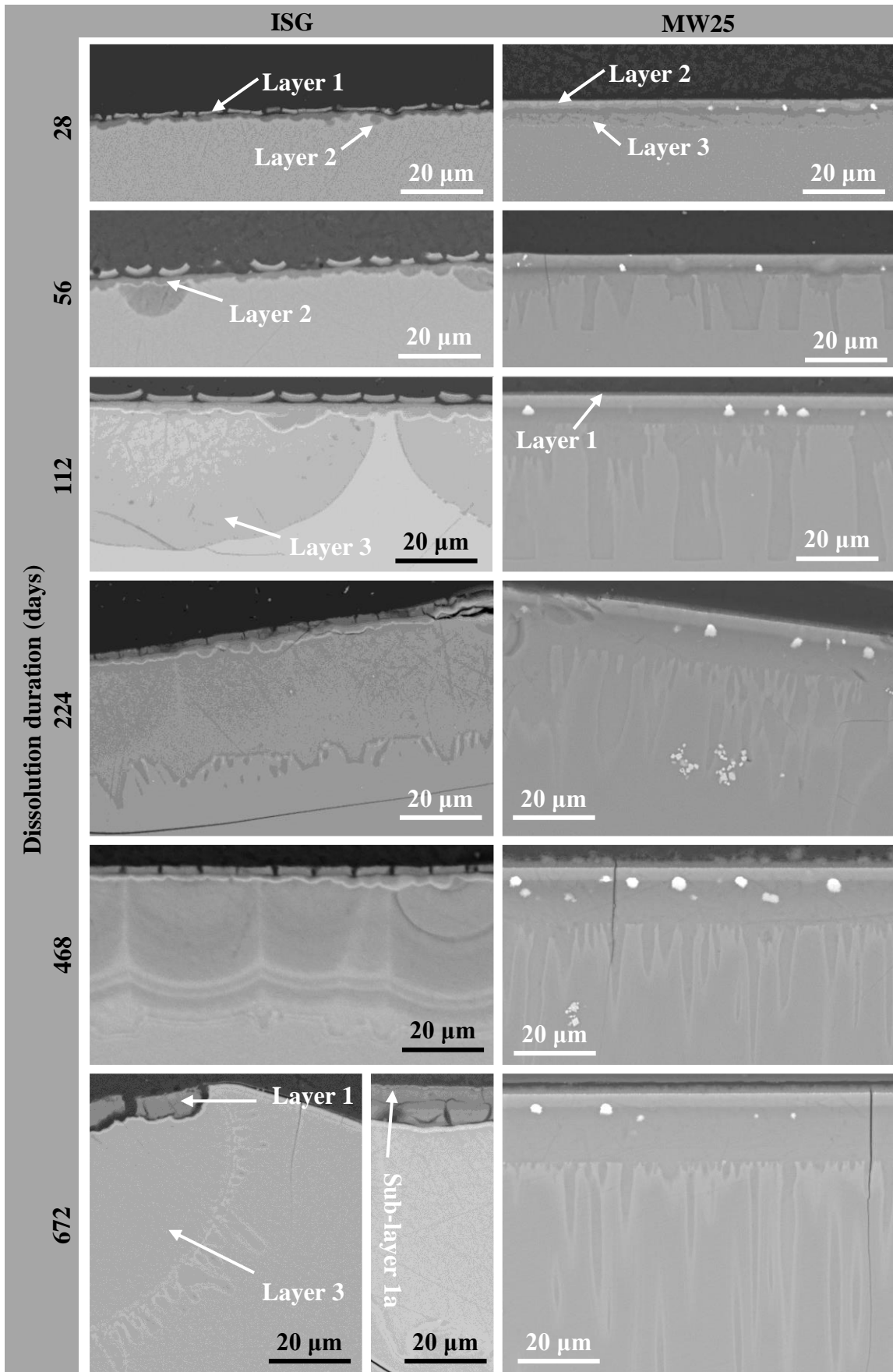


**Figure 4.7.** SEM-BSE images of MW25 and ISG after MCC-1 dissolution for various times. Images all of same scale, with a 20  $\mu\text{m}$  scale bar and epoxy orientated towards image top.

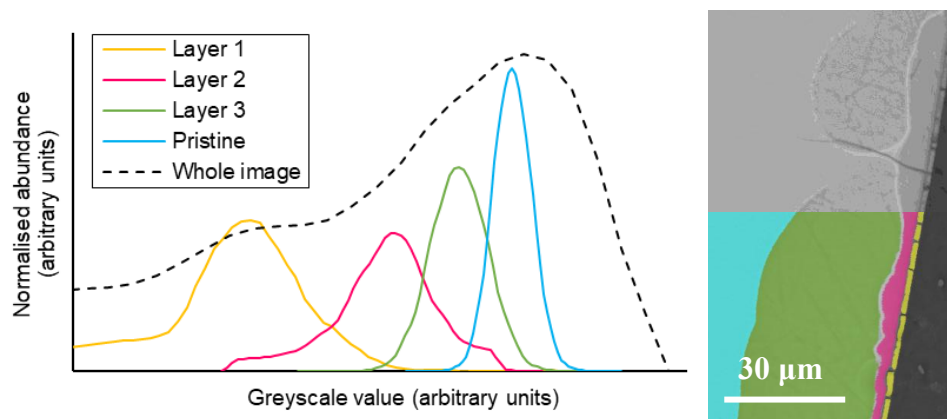


**Figure 4.8.** Left: Histogram of pixel greyscale intensities for ISG MCC-1 monolith (dissolved for 112 days) with deconvolution to show the distinct contributions from three separate layers. Right: The three identified surface layers illustrated and segmented in an SEM-BSE image.

The surface layers developed on ISG show significant changes by 672 days of dissolution. Layer 1 appears to be absent across much of the monolith surface, however where it *is* present it appears thicker than after 468 days of dissolution. A second more laterally continuous sub-layer (of similar greyscale intensity to Layer 1, hence its classification as **sub-layer 1a**) has formed atop the initial more broken/blocky layer in some places. Layer 1, where present, appears to have grown in depth at the expense of Layer 2 which is also frequently absent. Instead, Layer 1 (where present) is regularly in near-direct contact with the bright layer that previously demarcated the boundary between Layer 2 and Layer 3. Layer 3 may have increased in thickness, with the compositional sub-zoning no-longer evident. The boundary between Layer 3 and the pristine glass remains characterised by finger- or globular-like protrusions of up to 10 μm in length.

For MW25, two distinct zones or layers are visible by 28 days of dissolution. The outermost layer at this stage (**Layer 2**) is of similar greyscale intensity to the pristine sample. The otherwise relatively diffuse boundary between this layer and the below Layer 3 is often demarcated by the presence of well-rounded globular bright occurrences approximately one to two microns in diameter. **Layer 3**, initially of a similar thickness to Layer 2, appears darker than the pristine glass; exhibiting a slightly scalloped boundary with it. Layer 2, much like Layer 3, is laterally continuous across the surface of the monolith – with no significant breaks.

Within 56 days of dissolution Layer 2 in MW25 appears to have increased modestly in thickness (Section 4.2.5), with the brighter particles at its boundary with Layer 3 also potentially having increased in average diameter (to a few microns). Layer 3 has increased in thickness, but in a discontinuous manner – extending instead as penetrating ‘fingers’ with an oblong or spire-shape. Protrusions appear to reach a maximum distance (~25 μm by dissolution day 56) into the glass. Those protrusions with an oblong-shape typically have a penetration depth equal to the maximum value, whilst those which are more ‘pointed’ at their termination penetrate a lesser distance, potentially implying that features initially ‘grow’ in length until they reach a maximum depth and then they grow ‘outwards’ (in width). By day 56 an additional layer, evident from day 112 onwards at the scale shown in Figure 4.9, is evident on the outer-

surface of Layer 2 (i.e. at the once interface between the dissolved glass layer and the leachate). This layer, termed **Layer 1**, appears darker in BSE images than the pristine glass – a similar greyscale intensity to Layer 3. Layer 1 appears laterally continuous, but is too thin by dissolution day 56 to comment any further on its internal features or characteristics.

No new features or layers are evident after 112 days of dissolution, however some have become more pronounced. Layer 1 has increased in thickness, with Layer 2 relatively constant and Layer 3 now penetrating to a maximum ‘depth’ of  $\sim 50 \mu\text{m}$  into the pristine glass (as measured from the alteration layer/epoxy boundary). The bright particles at the Layer 2/3 boundary show some evidence of having increased minimally in average radius, with many of these now appearing to ‘fan’ inwards (towards the pristine glass) in a deltaic manner.

Micrographs taken after 224 days of dissolution show Layer 1 has continued to increase in depth (Section 4.2.5), with this layer now observably fibrous in morphology. Between Layer 1 and Layer 2 an additional sub-layer is becoming increasingly evident – comprised of sub-micron ( $< 0.5 \mu\text{m}$ ) micro-spheres of brighter material, far below the resolution of EDS. Layer 2 remains relatively unchanged in depth, though the bright features at the Layer 2-3 boundary may have increased in maximum diameter. Layer 3 now penetrates a maximum of  $\sim 60 \mu\text{m}$  into the glass (10  $\mu\text{m}$  more than at 112 days), and the apparent boundary from where the protrusions originate shows some evidence of migrating inwards. In other words, the *minimum* thickness of Layer 3 increases.

Similar trends are evident from 224 to 468 days. Layer 1, by 468 days of dissolution, has grown in depth considerably and now appears ‘cotton wool’-like, with roughly clumps or clusters of fibrous materials. Bright spheres at the Layer 2-3 interface appear to have increased in average size, with the maximum penetration depth of Layer 3 potentially now only  $\sim 5 \mu\text{m}$  greater than it was at 224 days. The only significant change by 672 days of dissolution is that the maximum penetration depth of Layer 3 has increased to  $\sim 90 \mu\text{m}$ .

Quantitative analysis of the bright ‘white’ globular features at the boundary between Layer 2 and Layer 3 reveal an imperfect, and only very approximate logarithmic increase in the maximum diameter of these with dissolution duration (Figure 4.10). However, no trend is evident in *mean* sphere diameters.

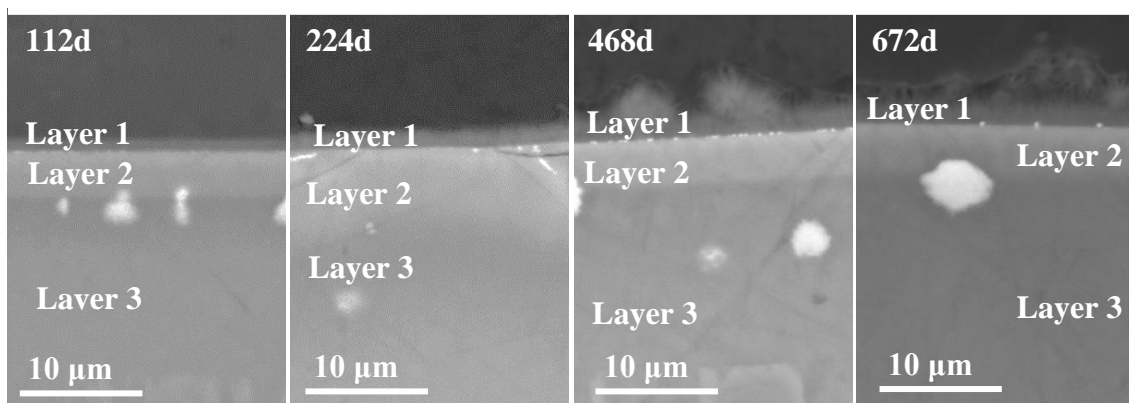


**Figure 4.9.** High magnification BSE-SEM images of MW25 after MCC-1 dissolution for various durations (indicated, in days, in top right). All images of same scale to aid comparison.

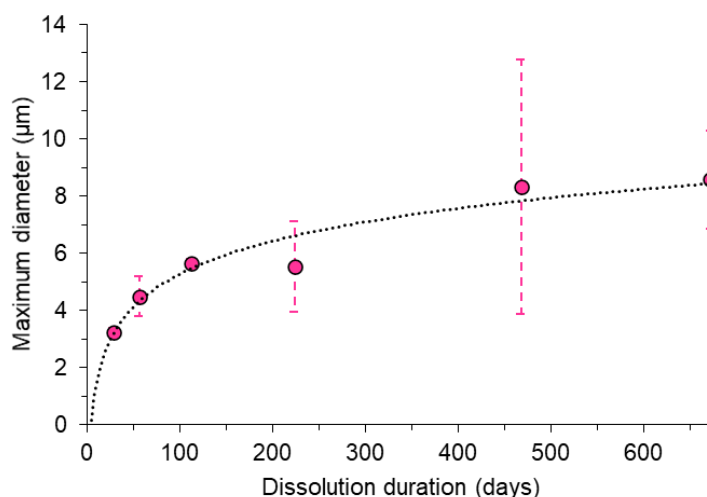


**Figure 4.10.** Change in maximum diameter of ‘bright’ features at the interface between Layers 2-3 in MW25 with dissolution duration, as determined via SEM-BSE image analysis. Logarithmic trend (dotted black line) shown as guide to the eye.

#### MCC-1/EDS

The ‘raw’ compositions, as estimated using SEM-EDS, of surface layers 1-3 developed on ISG are shown for various dissolution durations in Table 4.2a-c respectively. Note that Layer 1 could not be quantified before dissolution day 112, and layer 3 could not be measured until day 56. Further note that due to its low atomic number, boron cannot be measured in EDS, however it is not expected to be retained in surface layers in significant quantities [25], [70], [220].

Data show that Layer 1 comprises predominantly silicon and zirconium, with minor calcium and aluminium and only a trace of sodium. No consistent trends with dissolution duration were noted. Layer 2 is similar but with much less zirconium; instead predominantly comprising mostly silica, with minor aluminium, calcium and zirconium and only a trace of sodium. No large or consistent trends with dissolution duration were noted, though sodium sharply decreases between 28 to 56 days of dissolution, whilst aluminium and zirconium may show increasing influence with experiment duration. Layer 3 is similar to layer 2.

Recalculating surface layer composition as a proportion of elemental abundance in pristine glass (Figure 4.11) highlights these trends. Layer 1, has a strong enrichment in zirconium (up to four times that in pristine), with a significant depletion in sodium and only slight calcium and aluminium enrichment (maximum 1.5 times original).

Layer 2 shows an aluminium enrichment up to 2.5 times higher than the pristine composition, with this enrichment showing some evidence of increasing with dissolution duration. Calcium may show a similar increasing enrichment trend (up to twice that of pristine) with experiment duration. A modest (max 1.5-2 times) enrichment in zirconium is observed, with a significant depletion in sodium. Silicon is typically depleted modestly (0.7-0.8 times pristine) for the first 468 days of dissolution, with a moderate enrichment (1.2 to 1.3 times pristine) beyond this.

The innermost layer (Layer 3) appears consistently enriched in all elements except sodium (typically depleted to 0.05-0.1 times that of pristine glass). This is most notable for zirconium (1.5-2× enrichment) and aluminium (typically ~1.7-2×), with calcium close behind (mostly 1.5-1.8×). Silica is typically present in similar quantities to the pristine glass (0.85-1.15×).

<b>a) ISG Layer 1</b>					
<b>Duration (days)</b>	<b>Element weight %</b>				
	<b>112</b>	<b>224</b>	<b>468</b>	<b>672</b>	
<b>Al</b>	1.91 (0.11)	3.71 (0.2)	3.85 (0.2)	2.09 (0.12)	
<b>B</b>	-	-	-	-	
<b>Ca</b>	3.72 (0.14)	4.55 (0.16)	6.08 (0.21)	6.03 (0.2)	
<b>Si</b>	10.12 (0.44)	21.67 (0.92)	22.84 (0.97)	17.32 (0.74)	
<b>Na</b>	0.48 (0.05)	1.76 (0.13)	0.7 (0.07)	1.01 (0.09)	
<b>Zr</b>	10.94 (0.43)	11.76 (0.46)	6.25 (0.26)	14.07 (0.55)	

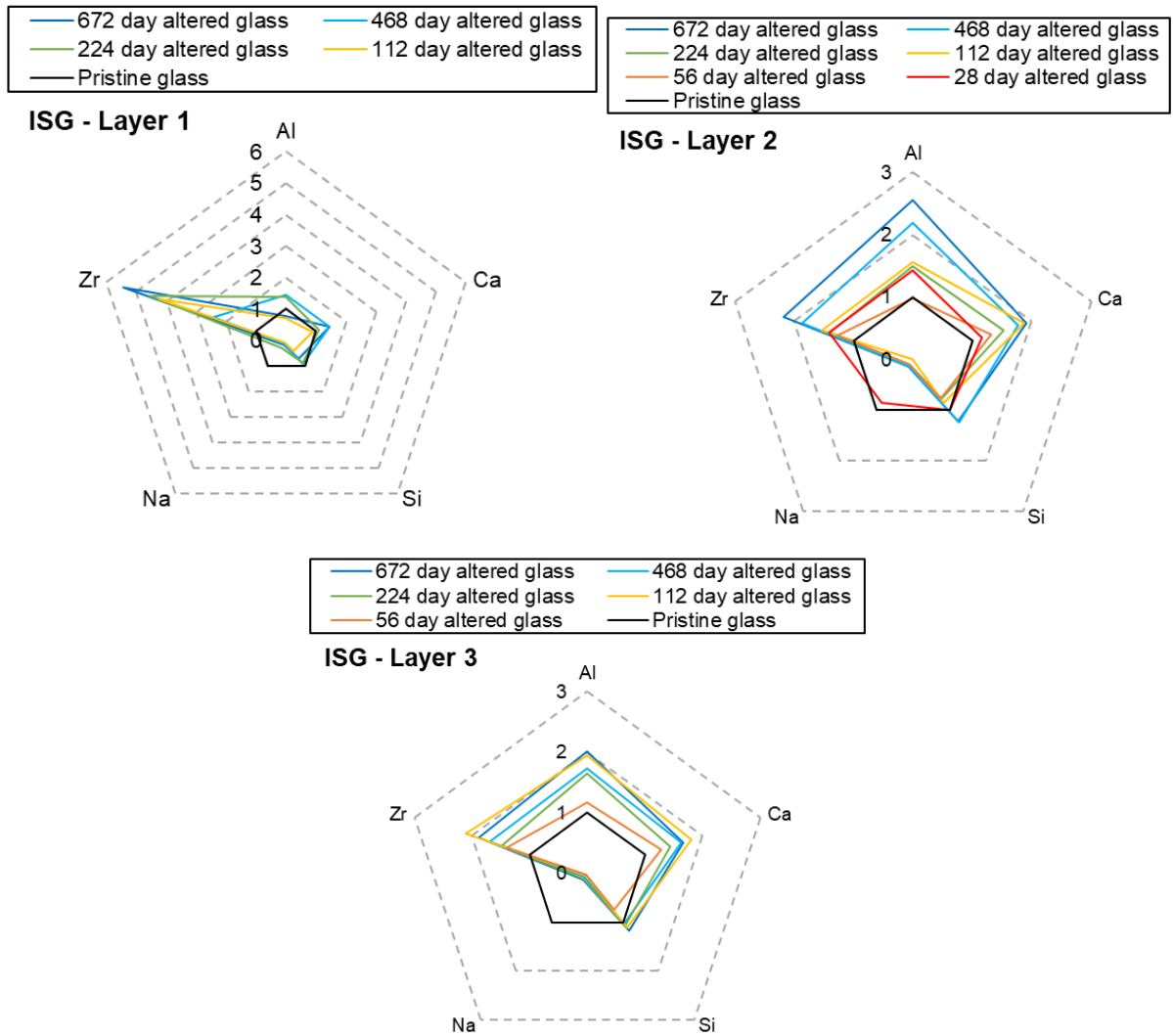
  

<b>b) ISG Layer 2</b>						
<b>Duration (days)</b>	<b>Element weight %</b>					
	<b>28</b>	<b>56</b>	<b>112</b>	<b>224</b>	<b>468</b>	<b>672</b>
<b>Al</b>	3.83 (0.2)	2.63 (0.15)	4.16 (0.22)	4.01 (0.21)	5.83 (0.29)	6.81 (0.34)
<b>B</b>	-	-	-	-	-	-
<b>Ca</b>	4.91 (0.17)	5.58 (0.19)	7.86 (0.26)	6.46 (0.22)	7.44 (0.25)	8.05 (0.26)
<b>Si</b>	24.82 (1.05)	18.89 (0.81)	20.86 (0.89)	19.05 (0.81)	30.77 (1.3)	30.19 (1.28)
<b>Na</b>	5.62 (0.37)	0.65 (0.06)	0 (0)	0.62 (0.06)	0.86 (0.08)	0.87 (0.08)
<b>Zr</b>	3.65 (0.16)	3.28 (0.15)	3.98 (0.17)	3.6 (0.16)	4.83 (0.2)	5.66 (0.24)

<b>c) ISG Layer 3</b>					
<b>Duration (days)</b>	<b>Element weight %</b>				
	<b>56</b>	<b>112</b>	<b>224</b>	<b>468</b>	<b>672</b>
<b>Al</b>	3.13 (0.17)	5.2 (0.27)	4.39 (0.23)	4.62 (0.24)	5.35 (0.27)
<b>B</b>	-	-	-	-	-
<b>Ca</b>	5.42 (0.19)	7.63 (0.25)	6.04 (0.2)	6.84 (0.23)	6.99 (0.23)
<b>Si</b>	18.31 (0.78)	27.33 (1.16)	26.26 (1.11)	25.29 (1.07)	28.79 (1.22)
<b>Na</b>	0.25 (0.04)	0.26 (0.04)	0.75 (0.07)	0.51 (0.06)	0.8 (0.07)
<b>Zr</b>	3.58 (0.16)	5.43 (0.23)	3.84 (0.17)	4.36 (0.19)	4.87 (0.21)

**Table 4.2.** SEM-EDS estimated compositions of the surface layers developed during MCC-1 testing of ISG: Layer 1 (a, top); Layer 2 (b, middle) and Layer 3 (c, bottom). Values stated are elemental weight percent with absolute measurement error in parathesis.



**Figure 4.11.** Surface layer compositions (as in Table 4.2) recalculated as a proportion of the pristine ISG glass composition for Layer 1 (top left), Layer 2 (top right) and Layer 3 (bottom).

Surface layer compositions for MW25 and prior to further processing are presented in Table 4.3a-c. Only major elements (present in more than one weight percentage in the pristine glass) excluding boron (unmeasurable via this technique) are shown for brevity and not all layers could be measured at all dissolution durations.

Layer 1 mostly comprises silicon, with variable magnesium and potentially decreasing sodium contributions with dissolution duration. Minor amounts of aluminium and iron are also present. Layer 2 is also predominantly silicon with some magnesium. This layer, however, contains more iron, zirconium and aluminium compared to Layer 1, with less sodium. The innermost layer (Layer 3) is compositionally similar to Layer 2, again mostly comprising silicon, but here magnesium shows lesser contribution. Layer 3 also contains less iron than Layer 2 until day 672, with comparable zirconium throughout. All layers contain negligible calcium.

Comparisons with pristine glass compositions (Figure 4.12) show Layer 1 is highly enriched in magnesium, containing up to six times (but more typically four times) that present in the pristine glass. All other elements appear depleted, relative to pristine, except for aluminium and silicon which are present in similar quantities to the pristine glass. No consistent variation in this with dissolution duration was noted for either Layer 1 or 2. Layer 2 also appears enriched in magnesium – typically containing two to three times more of this element than pristine glasses. Sodium in this layer is highly depleted, with silicon in similar (if not slightly lower) quantities as the pristine glass. Iron, zirconium and aluminium are modestly enriched by a factor of 1.1 to 2. Layer 3 is highly depleted in sodium, with a lesser depletion in magnesium. Silicon is present in this layer in quantities comparable to, or slightly below, the concentration in pristine glass; with zirconium similar although more variable with dissolution duration. Iron is typically modestly depleted until dissolution day 672 where it shows some evidence of modest enrichment. Aluminium is consistently enriched by a factor of 1.1 to 1.9, though this factor shows no consistent trend with dissolution duration.

Average EDS-estimated compositions of the “bright globules” at the Layer 2/Layer 3 boundary are shown in Table 4.4 (for constituents > 1%), alongside a decimal comparison with unaltered glass compositions. This material predominantly comprises silicon and phosphorous, with the latter element enriched by a factor of more than 150 compared to pristine material. Molybdenum and nickel (minor components of the bright globules) are also enriched, though only by a factor of circa two. All other elements including Zr appear depleted, though elemental maps imply the latter element can be enriched.

<b>a) MW25 Layer 1 Elemental weight %</b>			
<b>Duration (days)</b>	<b>224</b>	<b>468</b>	<b>672</b>
<b>Si</b>	8.5 (-)	26.97 (5.52)	21.32 (0.48)
<b>Na</b>	1.58 (-)	0.56 (0.71)	0 (0)
<b>Mg</b>	0.44 (-)	15.21 (3.64)	9.78 (0.41)
<b>Al</b>	0.67 (-)	2.08 (1.5)	1.97 (0.85)
<b>Fe</b>	0 (-)	1.06 (1.36)	2.19 (0.98)
<b>Zr</b>	0 (-)	0.98 (0.51)	0.49 (0.43)
<b>Ca</b>	0.29 (-)	0.2 (0.21)	0.06 (0.1)

<b>b) MW25 Layer 2 Elemental weight %</b>						
<b>Duration (days)</b>	<b>28</b>	<b>56</b>	<b>112</b>	<b>224</b>	<b>468</b>	<b>672</b>
<b>Si</b>	14.27 (0.01)	19.83 (3.52)	17.57 (5.38)	18.69 (0.52)	17.06 (2.53)	19.95 (0.97)
<b>Na</b>	0 (0)	0 (0)	0 (0)	0.51 (0.88)	0.58 (0.6)	0.36 (0.33)
<b>Mg</b>	3.51 (0.08)	6.54 (2.27)	5.51 (0.32)	5.78 (0.88)	5.22 (0.57)	5.29 (0.6)
<b>Al</b>	2.82 (0.08)	4.44 (1.51)	3.13 (0.15)	3.23 (0.84)	3.54 (0.77)	3.07 (0.57)
<b>Fe</b>	4.29 (0.13)	5.42 (0.11)	3.62 (0.86)	4.3 (1.16)	3.03 (0.43)	2.54 (0.96)
<b>Zr</b>	2.91 (0.08)	2.86 (0.83)	2.16 (0.19)	2.52 (0.7)	1.9 (0.59)	2.14 (0.26)
<b>Ca</b>	0.06 (0.04)	0.09 (0.13)	0.04 (0.05)	0.15 (0.23)	0.06 (0.1)	0.08 (0.12)

<b>c) MW25 Layer 3 Elemental weight %</b>						
<b>Duration (days)</b>	<b>28</b>	<b>56</b>	<b>112</b>	<b>224</b>	<b>468</b>	<b>672</b>
<b>Si</b>	15.09 (-)	21.05 (4.69)	17.14 (3.64)	19.15 (4.05)	23.92 (3.9)	20.29 (7.15)
<b>Na</b>	0.13 (-)	0.55 (0.95)	0.09 (0.12)	0.24 (0.41)	1.86 (1.03)	0.45 (0.79)
<b>Mg</b>	0.98 (-)	1.48 (0.74)	1.1 (0.45)	1.64 (1.23)	1.65 (0.4)	1.15 (0.47)
<b>Al</b>	2.46 (-)	3.1 (1.44)	2.33 (0.75)	2.44 (0.94)	4.22 (0.82)	3.27 (1.34)
<b>Fe</b>	2.38 (-)	2.54 (0.47)	2.27 (0.29)	2.98 (0.78)	2.54 (0.6)	4.18 (0.61)
<b>Zr</b>	2.23 (-)	1.95 (0.36)	1.24 (0.43)	1.7 (1.15)	2.7 (0.77)	2.19 (1)
<b>Ca</b>	0.32 (-)	0.15 (0.25)	0 (0)	0.04 (0.08)	0.29 (0.1)	0.02 (0.03)

**Table 4.3.** SEM-EDS estimated compositions of the layers developed after MCC-1 of MW25: Layer 1 (a, top); Layer 2 (b, middle) and Layer 3 (c, bottom). Values are average elemental weight percent, with standard deviation in parathesis (unless only one measurement possible). Where standard deviation is as large as measurement, value can be assumed to be zero

	<b>Wt. %</b>	<b>Pristine diff</b>
<b>Si</b>	9.74 (2.62)	0.44
<b>P</b>	3.36 (0.86)	168
<b>Fe</b>	1.89 (0.3)	0.63
<b>Mg</b>	1.67 (0.26)	0.69
<b>Zr</b>	1.59 (0.88)	0.84
<b>Al</b>	1.38 (0.51)	0.62
<b>Mo</b>	1.19 (0.35)	1.97
<b>Ni</b>	1.11 (0.32)	1.83

**Table 4.4.** SEM-EDS estimated composition of the 'bright' material at the Layer 2/Layer 3 boundary of dissolved MW25. Values stated as: Average elemental weight percent ('Wt. %') with standard deviation from average shown in parenthesis and as a fraction of pristine glass ('Pristine diff') where 'pristine' compositions are as measured via the same technique.

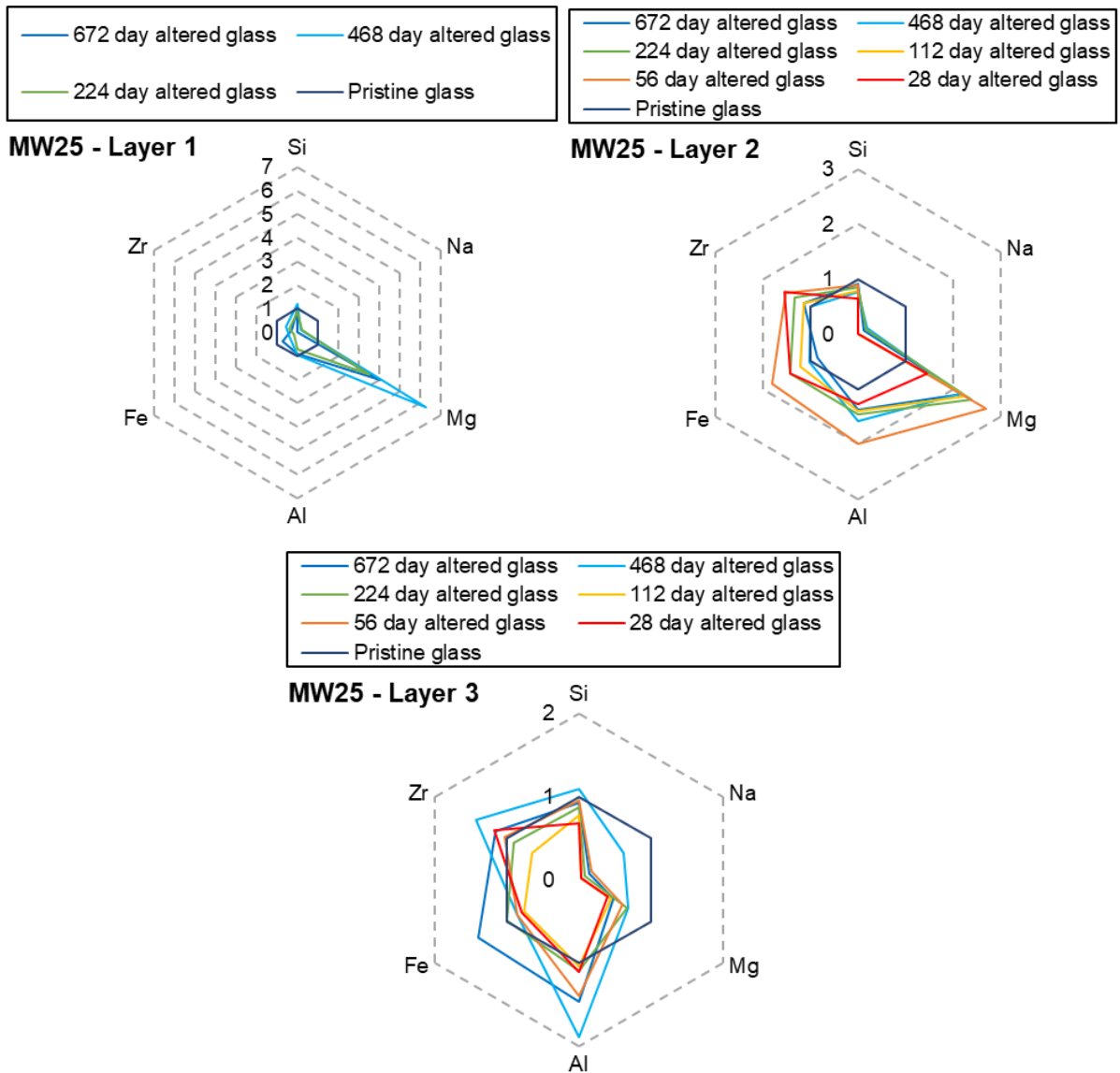


**Figure 4.12.** Surface layer compositions (as in Table 4.3) recalculated as a proportion of the pristine MW25 composition for Layer 1 (top left), Layer 2 (top right) and Layer 3 (bottom).

### *PCT-B/BSE*

Figure 4.13 shows representative BSE images taken after all experimental durations conducted in the PCT-B method. As noted for pristine powders, the powder particles exhibit fracturing within a few microns of the surface.

Few striking differences, relative to pristine samples, are noted for ISG until 224 days of dissolution. By this point, ISG powders show evidence of contracting inwards from the epoxy to leave an air-filled void. This void separates the bulk sample and a highly-discontinuous (~1  $\mu\text{m}$  thickness) surface layer, not always present, of similar greyscale to the pristine sample.

MW25 appears near-identical to pristine powders for at least the first 28 days. By experiment day 56, MW25 occasionally shows evidence of a thin (~1  $\mu\text{m}$ ) discontinuous surface layer which is slightly darker in greyscale than the pristine glass (Figure 4.14a). Similarly, images taken after 224 days show evidence of darker (relative to pristine glass) roughly semi-circular regions surrounding the precipitates within the pristine glass where these are in the vicinity of particle surfaces (Figure 4.14b). By experiment day 224, MW25 powders are surrounded by a void (either epoxy or air filled and <1  $\mu\text{m}$  wide) which separates a continuous dark surface layer of minimal thickness ( $\ll$  1  $\mu\text{m}$ ) from otherwise pristine glass (Figure 4.14c-d). In one instance this darker surface layer appears as a significantly thicker (up to ~5  $\mu\text{m}$ ) layer. This is accompanied by ‘agglomerations’ of similar-appearing material that may have detached from the particle surface (Figure 4.14e). This material appears somewhat ‘fluffy’ and contains bright ‘flecks’ of acicular material ( $\ll$  1  $\mu\text{m}$  wide and 1-3  $\mu\text{m}$  long; Figure 4.14e inset). These bright flecks resemble the bright dendritic features (Figure 4.14f-g), of up to 5  $\mu\text{m}$  in size, that are occasionally observed elsewhere at 224 days of experiment duration.

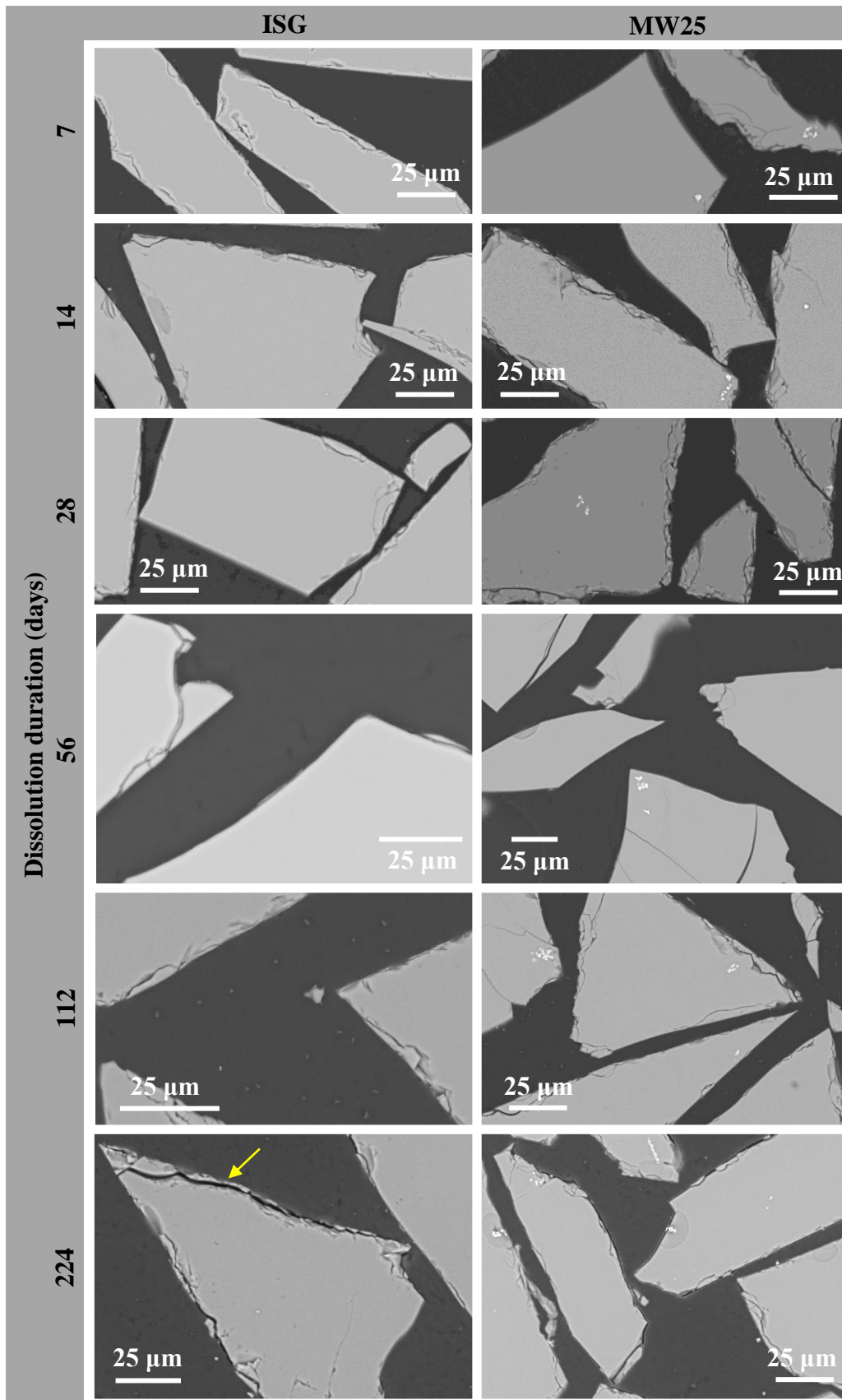
### *PCT-B/EDS*

Compositional maps and ‘line-scans’ intersecting ISG powder surfaces showed no compositional variations at any magnification or dissolution duration. EDS of speculative surface layers tentatively highlighted in Figure 4.13 was not possible given the layer’s size and the achievable EDS resolution. Regardless, compositional deviation of this layer from pristine glass was not expected given its strong greyscale resemblance to the pristine sample in BSE.

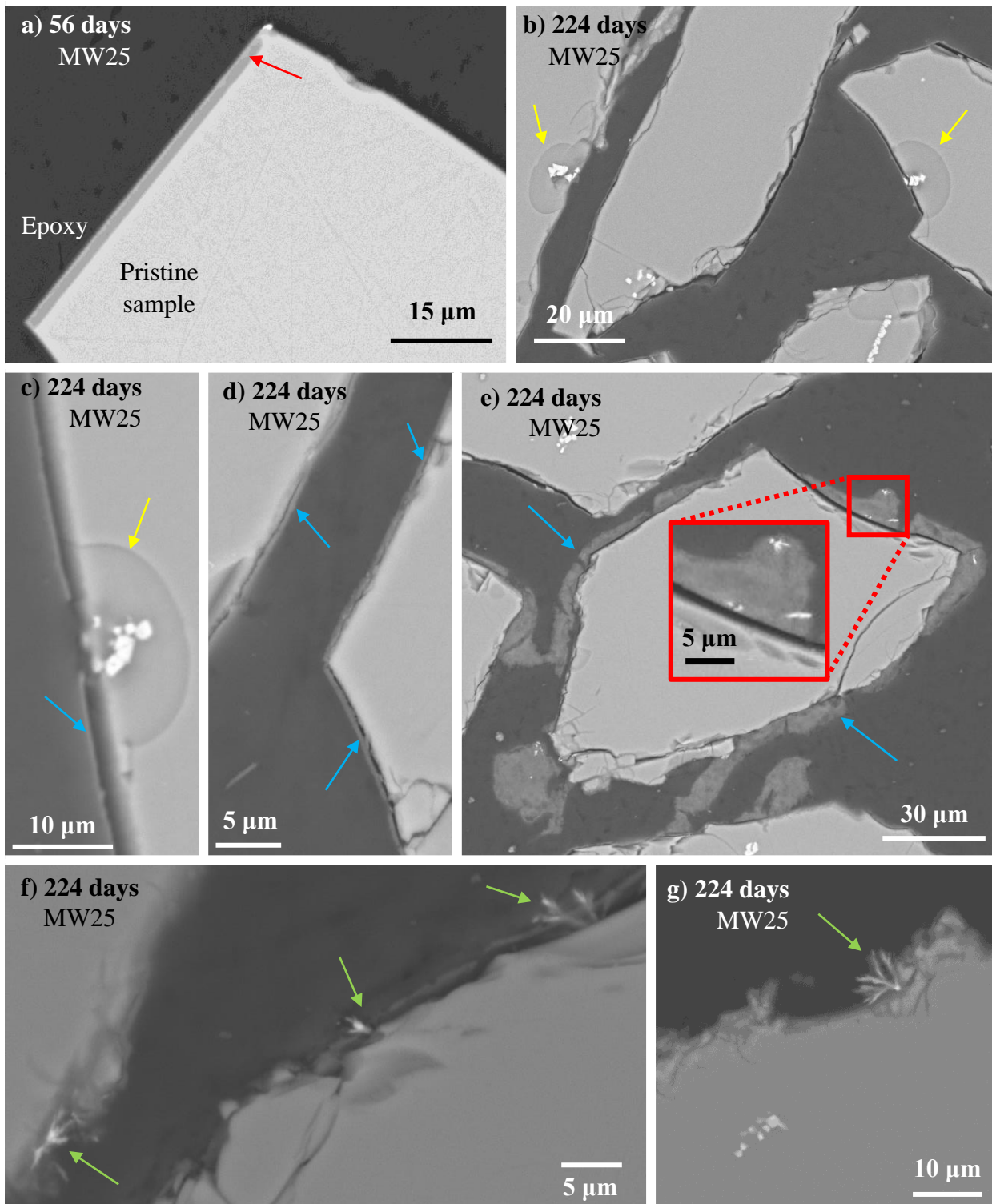
In comparison, EDS of the dark material surrounding surface-proximal precipitates in MW25 shows this region is depleted in magnesium, sodium and silicon relative to pristine values (Figure 4.15). This region may be enriched in zirconium and iron, however this is not evident in qualitative elemental ‘maps’ and this quantification may lack accuracy due to the feature size, the inability to measure boron, and the quantities of these elements in the pristine glass.

EDS of the MW25 surface layer was only possible in the few instances where it’s thickness was sufficient (Figure 4.16). Here, this material comprises silicon, magnesium and aluminium, with minor zirconium. Compared to pristine glass, the layer is highly enriched in magnesium (up to 800% of the pristine glass), with a lesser enrichment of silicon (~230%). The small enrichment in aluminium (~150% of pristine) and zirconium (up to ~200% pristine values) is less convincing given they are only minor constituents of the pristine glass or the altered region.

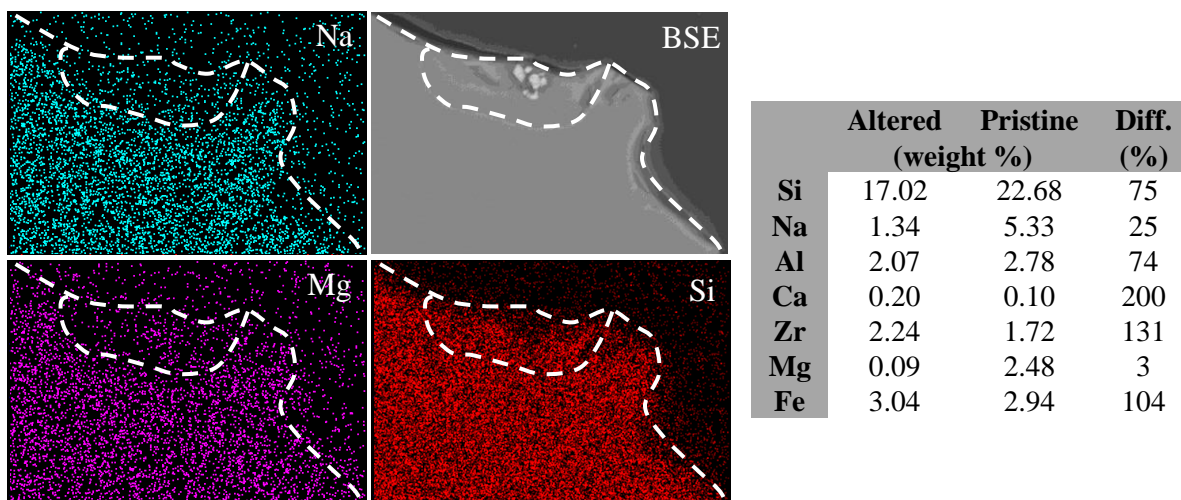
EDS of the ‘bright’ dendritic forms on the surface of MW25 (Figure 4.14f/g) and within the darker layer (Figure 4.14e) was not possible because their size was below the resolution of EDS. However, their bright appearance in BSE implies they may be enriched in somewhat heavier elements than the pristine glass.



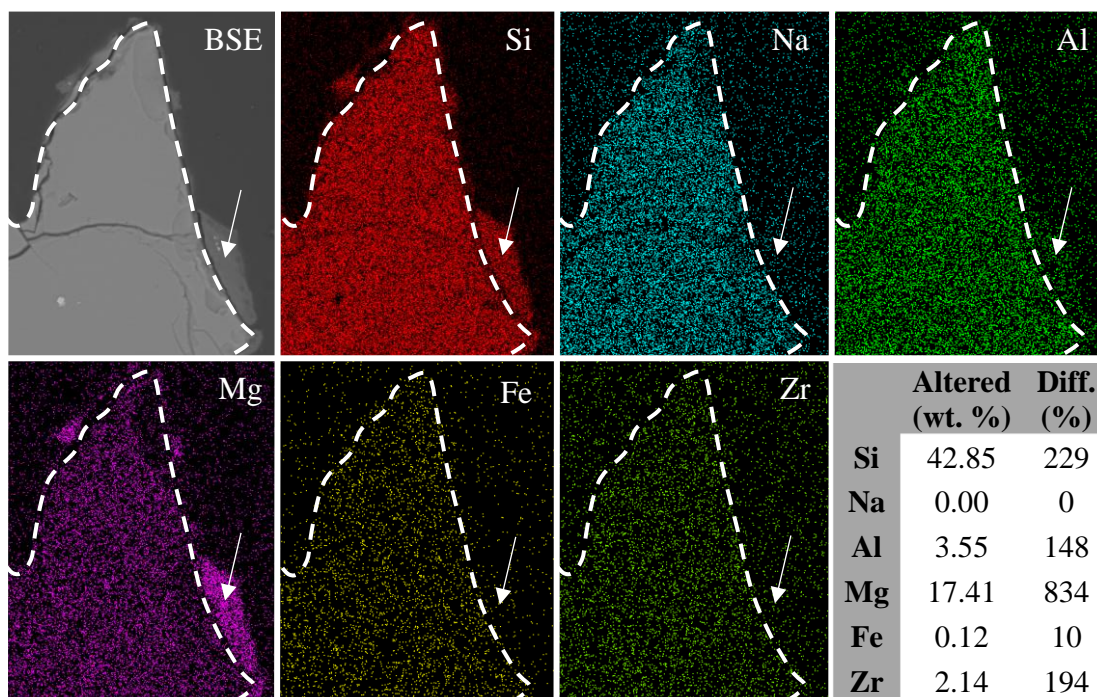
**Figure 4.13.** BSE images of ISG and MW25 after given durations of PCT-B experiments. Features formed on MW25 are illustrated at higher magnification in Figure 4.14, with the only observable difference (compared to pristine) for ISG described in-text and arrowed in yellow.



**Figure 4.14.** BSE images of features formed on MW25 after various durations (as indicated) of PCT-B experimentation. a) Thin surface layer evident by day 56, arrowed in red; b) dark semi-circles formed by day 224 where precipitates in pristine glass are in vicinity of powder surface, arrowed in yellow; c), d), and e) dark surface layer, arrowed in blue, evident at experiment day 224, with inset showing bright 'flecks' within this; f) and g) bright flecks at day 224 evidencing dendritic form, arrowed in green.



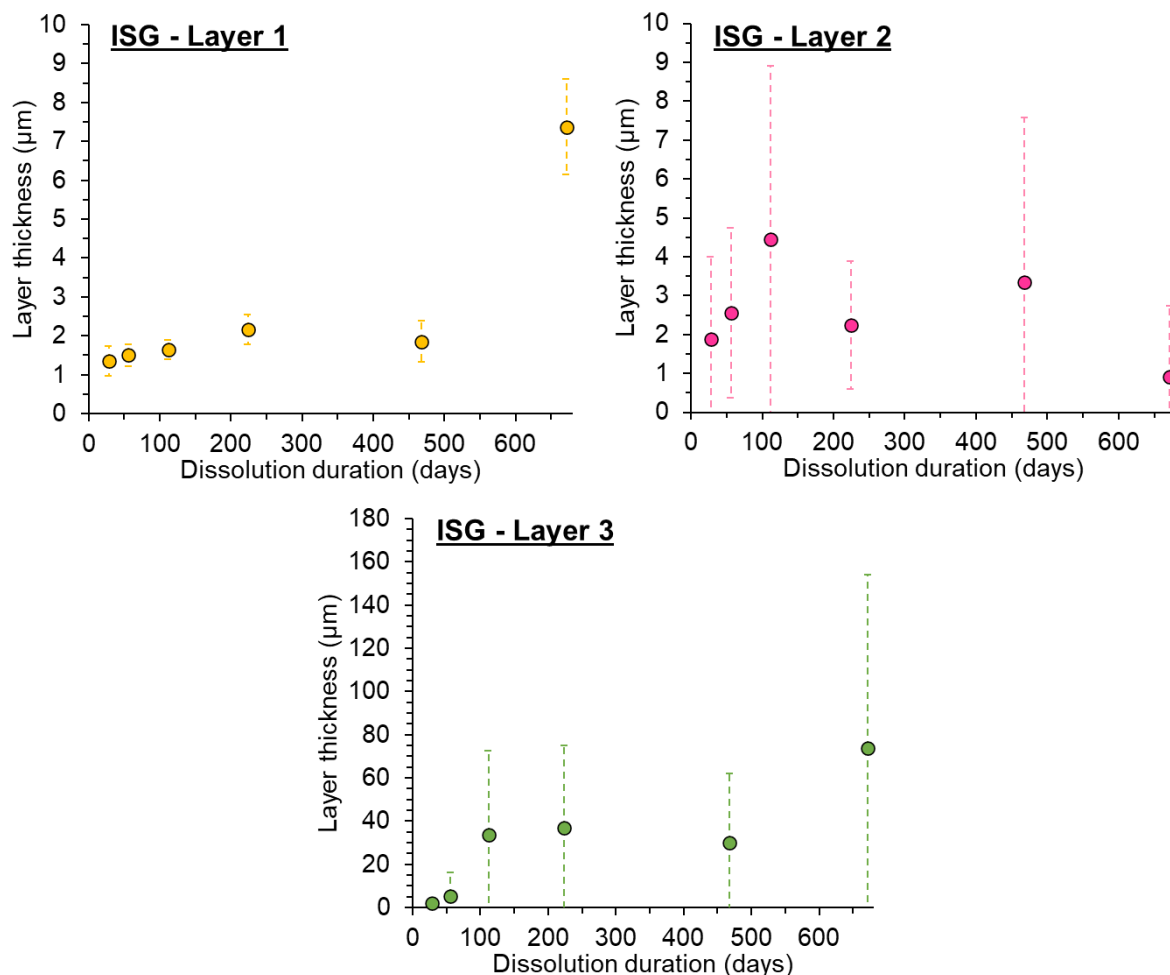
**Figure 4.15.** EDS images (left) and estimated quantification (right) of dark material surrounding surface-proximal precipitates in MW25 after 224 days of dissolution via PCT-B. Difference (“Diff.”) between pristine (as measured via EDS) and altered compositions shown.



**Figure 4.16.** BSE & EDS images, with estimated quantification of “Altered” dark layer surrounding MW25 powders after 224 days of dissolution via PCT-B. Difference (“Diff.”) between pristine (as measured via EDS) and altered compositions shown in percent.

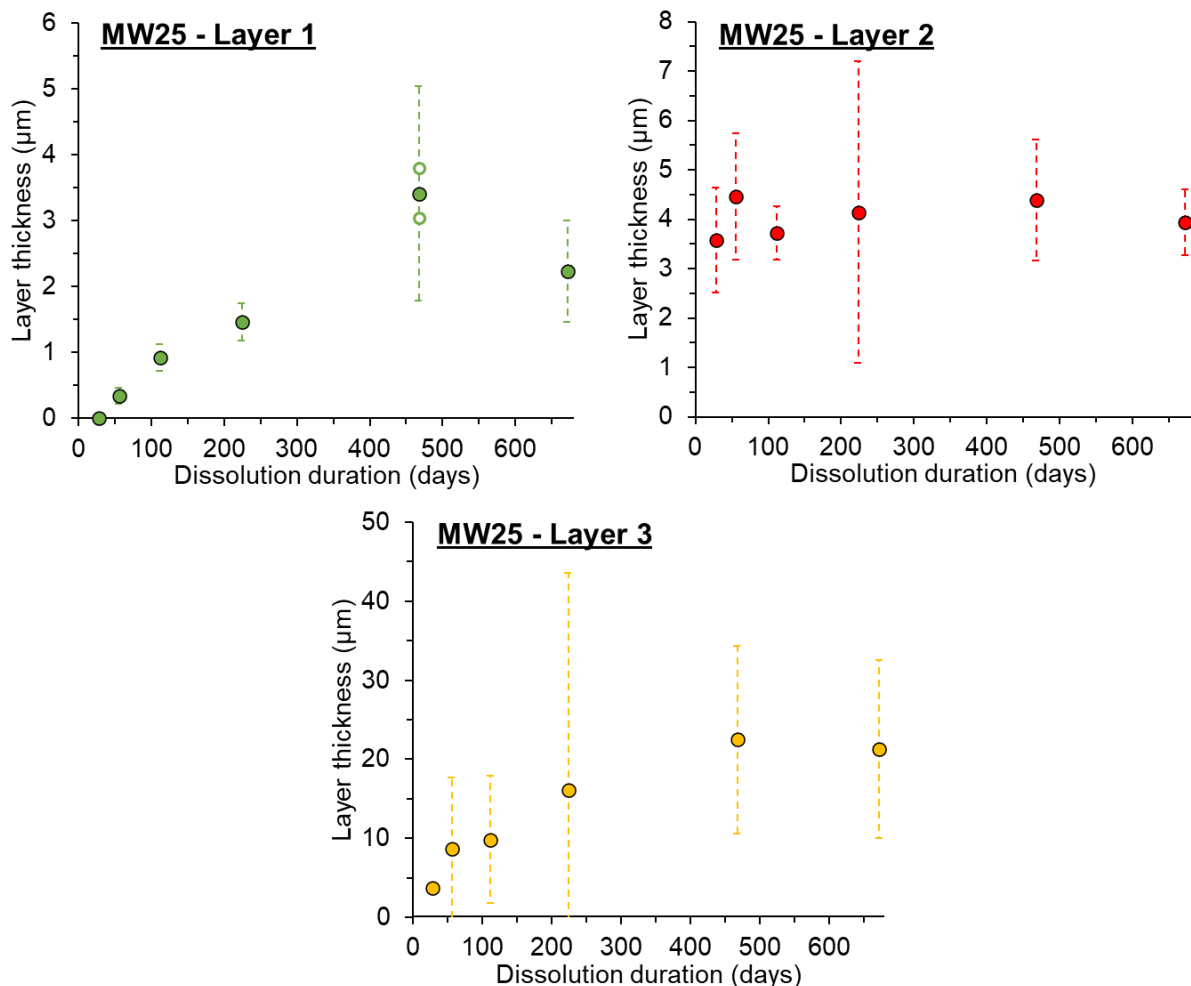
#### 4.2.5. MCC-1 surface layer thickness analysis

Figure 4.17 shows the results from ISG surface layer thickness analysis, as performed via the method outlined in Chapter 6. Layer 1 thickness increases approximately linearly with time from day 28 (1.3  $\mu\text{m}$ ) to 224 (2.2  $\mu\text{m}$ ). However, by day 468 this layer thickness has fallen (to 1.8  $\mu\text{m}$ ), before it sharply re-increases (to 7.4  $\mu\text{m}$ ) by dissolution day 672. In contrast, Layer 2 shows little such consistent trend in thickness with dissolution duration, with all thicknesses (ranging from 0.9  $\mu\text{m}$  to 4.4  $\mu\text{m}$ ) within error of each other. Absolute average values may increase linearly up to a maximum thickness (of 4.4  $\mu\text{m}$ ) by day 112, but beyond this averages decrease (to 2.2  $\mu\text{m}$  by day 224), then re-increase (to 3.3  $\mu\text{m}$  by 468 days) and finally re-decrease (to 0.91  $\mu\text{m}$  at 672 days). Layer 3 thickness measurements are similarly all within error of each other; however absolute (average) values in this case may show a step-like trend of increasing with dissolution duration: Thicknesses range from 1.9  $\mu\text{m}$  to 5.5  $\mu\text{m}$  between 28 and 56 days, before they show a stepped increase to  $33 \pm 3 \mu\text{m}$  between days 112-468 and a further step-increase to thicknesses of 73.7  $\mu\text{m}$  by day 672.



**Figure 4.17.** Development of surface layer thicknesses with experimental duration for ISG dissolved via the MCC-1 method. Measured via SEM/BSE combined and the method outlined in Chapter 6. Datapoints show average of two measurements, with error bars representing standard deviation on this.

MW25 surface layer thickness development is shown in Figure 4.18. For Layer 1, thickness appears to increase logarithmically with experiment duration. Data from the penultimate timestep represent the only significant deviation from this, however these data are considered anomalous. Though individual datapoints at this 468 day timestep are self-consistent (see Figure 4.18), these have a large associated error and lack consistency with data from solution analysis and other layer thicknesses. By removing these data, as may be considered valid based on these inconsistencies, a logarithmic fit with a correlation factor of 0.99 can be fitted to Layer 1 growth. Layer 2 shows no such clear trend, with its thickness instead appearing to fluctuate around  $4.0 \pm 0.5 \mu\text{m}$  throughout the experiment. In contrast, Layer 3 appears to increase in thickness approximately logarithmically (or with a power law function) with dissolution duration. However, the latter cannot be argued with certainty given the high standard deviations. Considering these, a linear or power-law increase of Layer 3 thickness with dissolution duration is also possible; however a constant thickness with dissolution duration is not feasible (within error).



**Figure 4.18.** Surface layer thicknesses development for MW25 dissolved via the MCC-1 method, as measured via SEM/BSE and the method outlined in Chapter 6. Filled datapoints show average of two measurements, with error bars representing whichever is higher: the standard deviation on this average, or the standard deviation on either measurement. For MW25 Layer 1, individual datapoints are shown (as open symbols) at dissolution day 468.

Total surface layer thicknesses for both ISG and MW25 are shown in Figure 4.19. MW25 shows an increase in total surface thickness with dissolution, with this increase relatively rapid for the first 112 days ( $\sim 0.32 \pm 0.06 \mu\text{m day}^{-1}$ ), before slowing for the remainder of the experiment ( $\sim 0.12 \pm 0.00 \mu\text{m day}^{-1}$  from 224 – 672 days). For ISG, layer thicknesses initially increase similarly to MW25 from 28 – 112 days, before potentially plateauing or modestly decreasing from 112 - 468 days and then rapidly re-increasing by 672 days. Comparison indicate similar total thicknesses and growth rates for MW25 and ISG from 28 – 112 days, beyond which MW25 surface layer thickness consistently exceeds that of ISG.

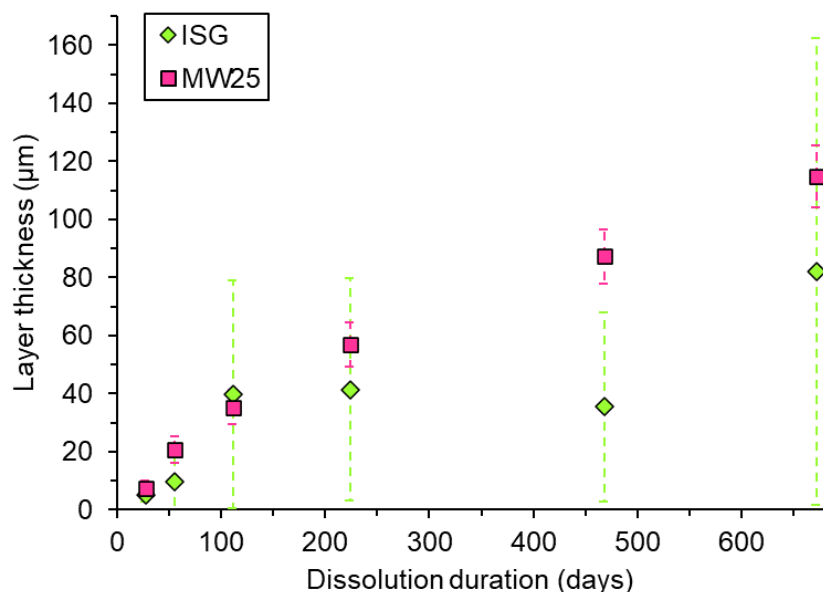


**Figure 4.19.** Total surface layer thicknesses for ISG and MW25 dissolved via MCC-1 method

#### 4.2.6. XRD

Diffraction data collected from ISG and MW25 PCT-B samples dissolved for 224 days is shown in Figure 4.20. Neither show evidence of crystalline peaks. Instead, diffuse scattering is evident both from 15 to 40  $^{\circ}2\theta$  and more weakly from 40 to 50  $^{\circ}2\theta$ . Comparison with XRD of ‘pristine’ MW25 samples (Figure 4.2) reveals no significant differences post-dissolution.

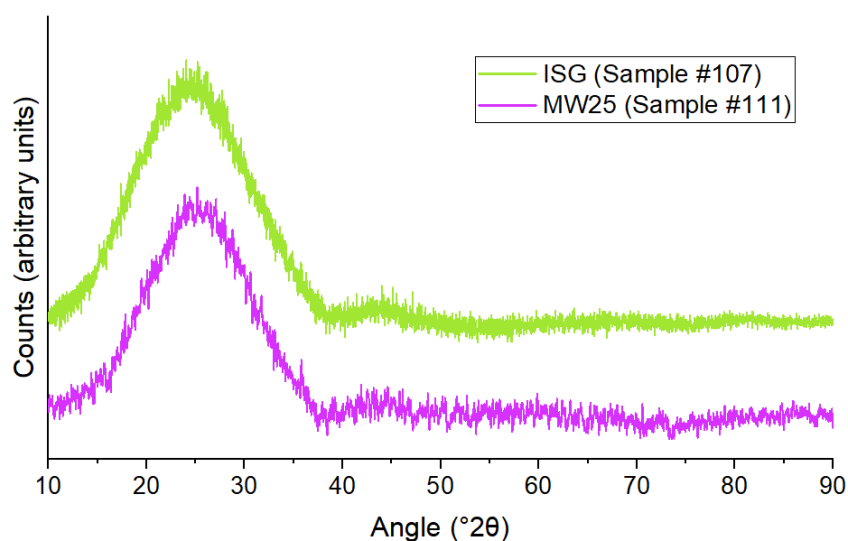


**Figure 4.20.** XRD of MW25 (pink) and ISG (blue) PCT-B samples after 224 days of dissolution.

### 4.3. Discussion of Results

#### 4.3.1. Pre-dissolution characterisation

XRD shows glasses are predominantly amorphous, with acid digest and ICP-OES indicating their composition is as-expected. However, SEM and Raman spectroscopy indicate the presence of a minor (< 5 wt.%) crystalline precipitate component in MW25.

The precipitates observed in pristine MW25 are hypothesised to be chromium-containing spinel [(Fe,Mg)(Cr,Fe)<sub>2</sub>O<sub>4</sub>], as are commonly observed in HLW glasses including MW25 [192], [196], [221]–[224]. This hypothesis is consistent with the dominant peak, at ~694 cm<sup>-1</sup>, evident in Raman data collected from the crystallites (Figure 4.3). This peak is assignable to the symmetric breathing mode of the AO<sub>4</sub> unit within spinel lattice, which typically occurs at ~690 - 700 cm<sup>-1</sup> [223], [225], [226]. These phases typically have minimal effect on HLW glass durability (as tested via accelerated leaching [227]) because they are highly durable and have a high degree of symmetry which minimises grain boundary effects [51], [228], [229].

Surface fracturing of pristine ISG and MW25 powders must result from sample preparation and *not* dissolution. This damage may have arisen during powder production (via aggressive and repetitive impact of glass fragments within a percussion pestle and mortar) and/or during epoxy-mounting (which involved vigorously mixing a viscous slurry comprising powder and epoxy resin). The damage resulting from this may have been further amplified during epoxy curing and via dehydration.

#### 4.3.2. MCC-1 experiments

The rapid initial pH increase inferred from Figure 4.4 (if a starting pH of 7 is assumed) is to be expected given the alkali/alkaline contents of the glasses. Rapid early release of these elements during Stage I dissolution is expected to increase leachant pH, which will remain high as these elements remain in the solution. Differences in pH may be accounted for by the differences in glass composition and alteration products/rates.

Boron is widely used as a ‘tracer’ element to indicate overall glass dissolution trends as it is assumed that it is not involved with the formation of secondary precipitates or alteration layers [25], [70], [220]. On the basis of the normalised mass losses of this element, ISG shows evidence of Stage I initial dissolution from 0-112 days, with steady Stage II dissolution beyond this. MW25 shows a similar trend, though with a less clear (or at least more rapid) residual rate from 112 days of experiment duration onwards. No rate resumption is seen for either glass. On these bases, dissolution rates can be calculated as in Figure 4.21.

Comparisons of these with published values is shown in Table 4.5, however comparisons are challenging due to the range of test conditions (predominantly temperature and leachant composition). Considering these differences, initial ISG and MW25 dissolution rates are consistently circa twice the equivalent rates calculated at lower temperatures (50°C compared to 90 °C) in alkaline leachants. These differences are consistent with the lower dissolution rates expected for both lower temperatures [224], [230], [231] and HLW glass dissolution in a saturated Ca(OH)<sub>2</sub> compared to pure water leachant [232], [233]. Residual rates for ISG calculated under the same (lower temperature alkaline) conditions differ from zero by the same magnitude as the rates here-calculated (approximately -0.005 g m<sup>-2</sup> d<sup>-1</sup> herein and +0.005 g m<sup>-2</sup> d<sup>-1</sup> in [60]). Residual rates for MW25 in these studies differ by an order of magnitude (approximately 0.004 g m<sup>-2</sup> d<sup>-1</sup> herein and 0.04 g m<sup>-2</sup> d<sup>-1</sup> in [60]).

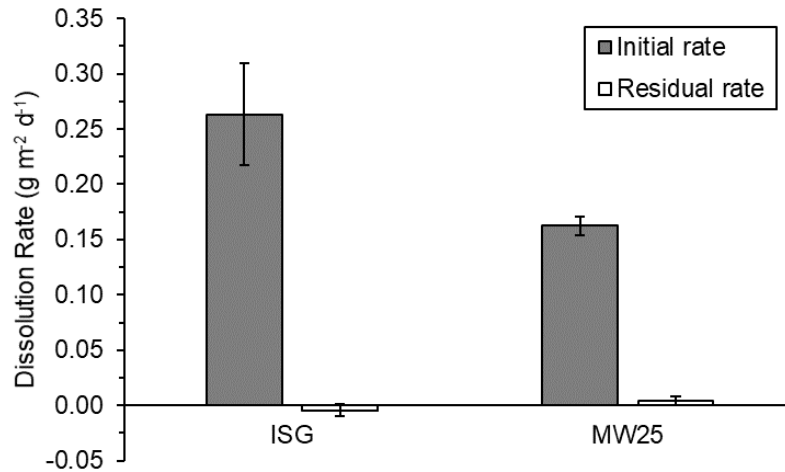


**Figure 4.21.** Initial and residual dissolution rates in grams per metre squared per day ( $\text{g m}^{-2} \text{d}^{-1}$ ); calculated for MCC-1 on the basis of  $NL_B$  and an initial rate of 112 days duration.

Glass	Leachant	Temp. (°C)	Initial and residual dissolution rates ( $\text{g m}^{-2} \text{d}^{-1}$ )	Author
MW25	H <sub>2</sub> O	90	Initial = $0.162 \pm 0.008$ Residual = $0.004 \pm 0.004$	This work
MW25*	H <sub>2</sub> O	90	Initial = $\sim 1.2$ Residual rate not stated	Brookes et al. [234]; Zwicky et al. [235]
MW25	Ca(OH) <sub>2</sub>	50	Initial = $0.168 \pm 0.02^{**}$ Res = $0.0544 \pm 0.007^{**}$	Corkhill et al. [233]
MW25	Ca(OH) <sub>2</sub>	50	Initial = $0.087 \pm 0.013$ Residual = $-0.047 \pm 0.007$	Backhouse [60]
ISG	H <sub>2</sub> O	90	Initial = $0.263 \pm 0.046$ Residual = $-0.005 \pm 0.006$	This work
ISG	Ca(OH) <sub>2</sub>	50	Initial = $0.146 \pm 0.022$ Res. = $-0.0025 \pm 0.0004$	Backhouse [60]
ISG	Ca(OH) <sub>2</sub>	40	Initial = $0.075 \pm 0.000$ Residual = $0.031 \pm 0.000$	Fisher & Corkhill [236]

**Table 4.5.** Comparison of dissolution conditions and calculated rates from this study (shaded rows) and others using the MCC-1 method ( $SA/V = 10 \text{ m}^{-1}$ ) and boron as a tracer. Note that: \* Monolith used “as cut” without polishing; \*\* Values initially published (in [233]) were two orders of magnitude lower, however this was subsequently identified as erroneous and corrected by Fisher & Corkhill [236].

The reliability of both initial and residual rates calculated for ISG may be questioned. Initial rates for ISG appear greater than those for MW25 – an unexpected result given PCT-B experiment results and given previous studies have found the reverse trend [31], [60]. These high rates may result from the high  $NL_B$  value at 112 days (Figure 4.5). This datapoint is identified as anomalous given the trend indicated by the two prior datapoints and the lower  $NL_B$  value at later timepoints. Rates instead calculated for only the 28-0.13 56 day data ( $0.130 \text{ g m}^{-2} \text{d}^{-1}$ ) may be more reliable. Unrealistic residual rates for ISG may similarly be caused by this anomalously high  $NL_B$  value at 112 days, with rates calculated from 224-672 days ( $-0.0027 \pm 0.0099 \text{ g m}^{-2} \text{d}^{-1}$ ) potentially more reliable, although still negative. Stating a ‘near-zero’ residual rate for ISG is perhaps more prudent.

## ISG

ISG shows evidence of an alteration layer within 28 days of dissolution; with Layer 1 and Layer 2 both evident by this time. Which layer formed first is challenging to determine, however it may be hypothesised that Layer 2 formed initially and uniformly across the glass surface as soluble network modifying cations (particularly sodium) are preferentially released via ion-exchange compared to network forming elements (such as Al, Si and Zr) [237].

Layer 1 may then have formed above Layer 2 and within 28 days of dissolution, as illustrated in Figure 4.22. Zirconium, highly enriched in this layer, is often retained (along with Al, Ca and Si [64], [87], [122]) and enriched in ISG alteration layers formed in alkaline conditions [60], [64], [122]. However, the formation mechanism of this layer is much debated. In the dissolution-precipitation method, Zr-containing phases precipitate from the leachate after Zr in the leachate reaches saturation [60]. This formation mechanism is supported by the heterogenous distribution of Zr within alteration layers formed on ISG in highly-alkaline (pH >11) solutions [60], [68]; however is less compatible with observations of low Zr solubility at pHs below 10.5 [34], [87], [238]. Instead, at lower pHs, the zirconia-enriched layer may form via glass network reorganisation following the release of more readily dissolved elements (B, Na, Ca) [86]. The latter mechanism, however, is contrary to findings that Zr hinders silicate network hydrolysis and gel restructuring due to the greater cross-linking it allows through its high coordination number [34], [87], [239]. Although Figure 4.4 shows pH values some authors have correlated with low Zr solubility, the heterogenous distribution of zirconium throughout the alteration layer shown in Table 4.2 and the continued growth of Layer 1 at later timepoints implies this layer most likely formed by reprecipitation, however this cannot be definitely concluded.

The onset of Layer 1 formation may have triggered formation of the sub-layer at the base of Layer 2, however this is difficult to interpret without compositional analysis. This layer may have formed at the inward-migrating diffusion/dissolution front (at the base of Layer 2) via elemental precipitation or a reduction in the driving force for a specific chemical's removal.

Regardless of which formed first, the calcium within these earliest-formed layers ( $5.9 \pm 2.2$  weight percent calcium across both layers) likely gives these alteration layers a highly protective effect [54], [70], [240]; significantly passivating further dissolution. This variable passivation may account for the slower initial dissolution of ISG compared to MW25 (<0.5 weight percent calcium in the alteration layer).

Dissolution rates remain in the rapid forward rate regime by day 56, with Layer 1 increasing in thickness as hypothesised precipitation continues. Layer 2 remains unchanged as the elements required for Layer 1 growth are now supplied by dissolution of the glass to form Layer 3. This dissolution is hypothesised to be via the same interdiffusion and ion-exchange mechanism as Layer 2 (hence the similarities in compositions shown in in Table 4.2 and Figure 4.11). However, by 56 days this process has become increasingly localised, leading to the distinctive scallop morphology observed. Given the semi-circular shape of these features, it may be speculated that their formation is around loci either within the alteration layer or at the glass/solution interface. This 'scalped' interface is widely observed in other studies [15], [74], [122], [236] and has been proposed to occur due to preparation-induced defects on the original glass surface [236]. Similarly, lateral alteration layer heterogeneities have been speculated [11] and observed [15] in other studies. A combination of any or all of these factors

may have caused the scalloped interfaces observed in Figure 4.7: Layer 1 and/or 2 may contain structural or compositional heterogeneities which disrupt their passivation ability; or sample preparation may have led to micro-weaknesses/cracks on the sample surface. Preferential dissolution below these features could conceivably lead to a scalloped morphology.

Layer 3 shows limited evidence of continued growth between day 56-112; with Layer 1 and 2 remaining a constant thickness as dissolution continues in the forward rate regime. This is consistent with dissolution continuing only around localised heterogeneities. The approximate increase in radii of the scallop features and the resulting coalescence of these to form a continuous layer, as illustrated in Figure 4.22 is consistent with continued localised attack.

Normalised mass loss data indicate that the system transitions into the residual regime between experiment days 112 and 224. It may be hypothesised that this was due to an increase in alteration layer passivation – potentially caused by pore closure and/or restructuring of one or more of the alteration layer components [22], [33], [241], [242]. This is coincident with a termination in Layer 3 growth, potentially after Layer 3 penetration reached a critical depth - beyond which lateral growth was more favourable than growth in thickness. This would explain the increase in horizontal layer continuity. Growth beyond this depth may have remained possible but unfavourable, allowing formation of rare trapezoid fingers penetrating from the otherwise laterally continuous layer.

Between 224-468 days, dissolution remains in the residual regime and alteration layers remain broadly unchanged in thickness. However, Layer 3 now shows clear zonation and internal heterogeneity, as may be further evidence of continued alteration layer restructuring.

Residual rates are maintained, according to  $NL_B$  data, between 468 and 672 days of dissolution. However the alteration layer during this time appears much less stable or consistent with other observations/datasets. Which layers remain evident by 672 days varies across the monolith surface, and classification of the observed layers is challenging. However it is probable that significant restructuring has occurred: Layer 1 and Layer 2 may have combined, potentially via formation (speculatively precipitation) of an additional ‘sub-layer’ of Layer 1. Dissolution and reprecipitation of Layer 1 during this time is supported by the doubling of  $NL_{Zr}$  values between 468 days ( $0.09 \text{ g}^{-1} \text{ cm}^{-2}$ ) to 672 days ( $0.18 \text{ g}^{-1} \text{ cm}^{-2}$ ). PHREEQC geochemical modelling also indicates that at 468 and 672 days of dissolution calcium zirconate ( $\text{CaZrO}_3$ ) is highly saturated in the solution, potentially after calcium and zirconium were released into the leachate due to loss/restructuring of Layer 1/2. Layer 3 remain unchanged, or may show evidence of entering a renewed period of thickening/growth.

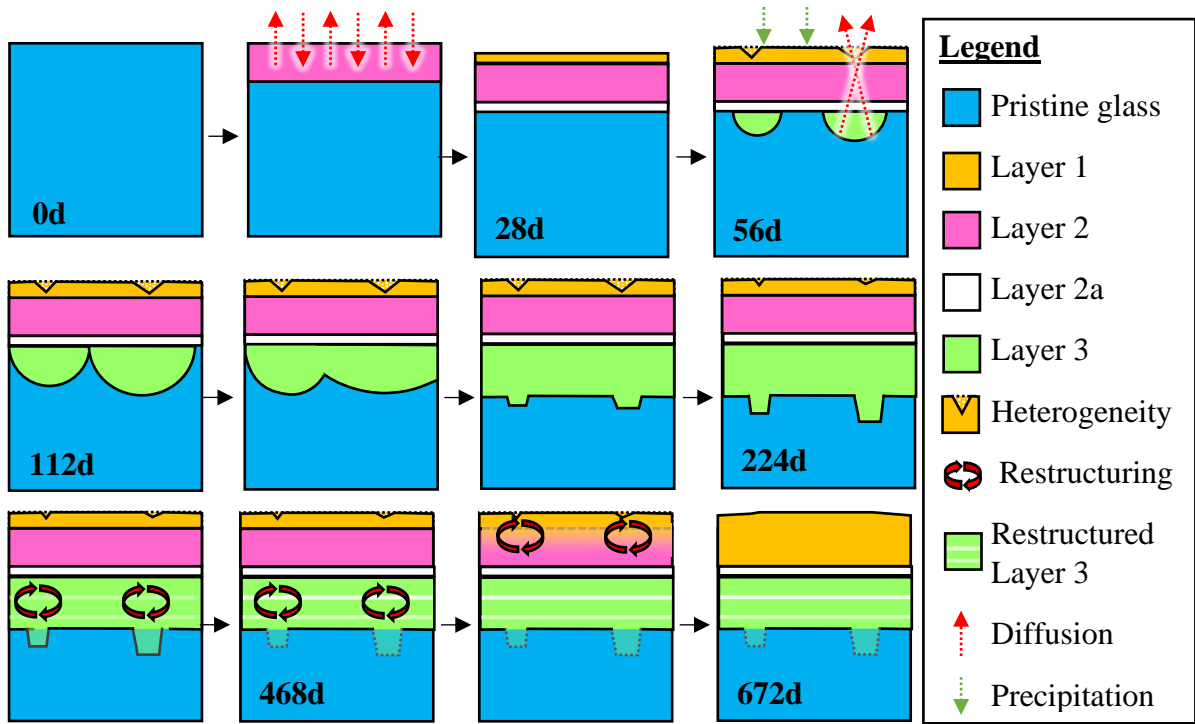


Figure 4.22. Schematic illustration of ISG dissolution in MCC-1 experiments.

## MW25

Two surface layers have formed on MW25 within 28 days of experiment duration; however neither is hypothesised to be significantly passivating given the rapid forward dissolution rates shown in  $NL_B$  data. Both Layer 2 and Layer 3 are compositionally similar (notably depleted in sodium), however Layer 2 is enriched in magnesium whilst Layer 3 is depleted in this. The sodium depletion and early dissolution stage supports formation of both layers via interdiffusion as the inward migration of protonated water species is allowed by outward diffusion of weakly-bound network modifiers [69]. However, which layer formed first, if formation was not synchronous, is impossible to confidently state. Synchronous formation is possible as sodium is leached into the solution from both layers whilst magnesium effectively migrates outwards from Layer 3 into Layer 2.

Alternatively, the logarithmic growth trend of Layer 3 (Figure 4.18) can be back-projected to intercept the y-axis at ~13 days of experiment duration. Based on these data it may be speculated that Layer 2 formed prior to Layer 3. However, back-projection in this manner is unreliable and Layer 3 thickness measurements are distorted by its distinct ‘finger’-like morphology (the circle-fitting method often falsely identifies the narrower ‘finger’ width as the ‘layer thickness’; as further discussed in Chapter 6). However, this unique morphology may also provide some chronological evidence.

The finger-like penetrations of Layer 3, also observed in other studies [235], are likely evidence of non-uniform (‘localised’) attack and thus may imply the presence of local heterogeneities. These heterogeneities appear to interact minimally with Layer 2, potentially implying the heterogeneity results from or formed after Layer 2. As discussed for ISG, these heterogeneities may be surface defects or the alteration layer heterogeneities speculated/observed in other studies [11] [15]. It thus may be hypothesised that the first-formed Layer 2 contains structural and/or compositional heterogeneities which disrupt its passivation ability and allow the unique morphological development of Layer 3.

The ‘bright’ phosphorous-enriched particles separating Layer 2 and Layer 3 are challenging to identify. PHREEQC modelling indicates no phosphorous-containing phases would be saturated at 28 days and post-dissolution XRD shows no crystalline peaks. However, previous studies (of Magnox glass dissolved via MCC-1 in UHQ water) identified rare-earth/Zr phosphate nanoparticles at the glass/alteration layer interface [31], [91]. Alternatively, apatite has also been identified as a glass alteration product [243] and was saturated (though only beyond 56 days) in geochemical modelling. These phases may be highly beneficial in a GDF environment because they can act as a sink for some long-lived fission products [31]. Their continued growth with dissolution duration, also potentially beneficial, is likely via Ostwald ripening.

Layer 1, with a magnesio-aluminosilicate composition, is evident in SEM-BSE from day 56. Magnesium-enriched alteration layers such as these are typically interpreted as secondary phases or M-S-H (Magnesium-Silicate Hydrate) phases in other MW-glass dissolution studies [60], [82], [91], [233]. However, here the presence of aluminium in Layer 1 (Table 4.2) and the crystal-like morphologies shown in Figure 4.23 imply this layer comprises crystalline phases. These minerals likely started precipitating after a silicon and/or magnesium reached saturation [240]. These are observed to rest atop gel layers (Layer 2-3), as is widely seen elsewhere [36], [244], [245]. Alignment of these fibrous clays perpendicular to the glass surface (Figure 4.23) is also widely observed in natural systems [246], [247] and an analogous “fuzzy blanket” of phyllosilicates has also been identified following PCT-B dissolution of other HLW glasses [248, p. 197].

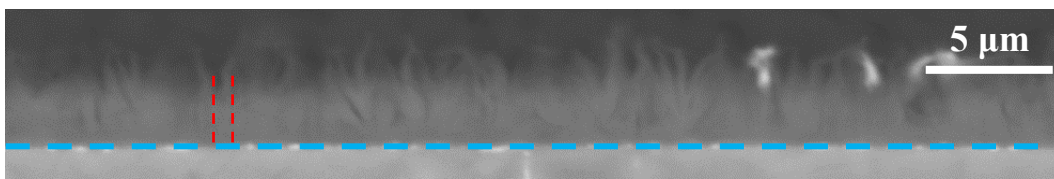


**Figure 4.23.** Alignment of crystalline phases (highlighted in red) perpendicular to the surface of MW25 glass (delineated in blue) dissolved under MCC-1 conditions for 468 days.

Geochemical modelling (Table 4.6) implies these phases are most likely saponite and/or nontronite. Smectites such as these have been similarly identified after comparable aqueous dissolution of MW [31], [82], [91] and other HLW glasses [54], [246], [248], [249]. SEM-EDS compositions (Figure 4.24) support this identification, indicating some nontronite-like minerals and some intermediaries between saponites and hectorites. All are broadly compositionally comparable to those in other aqueous MW25 dissolution studies [31].

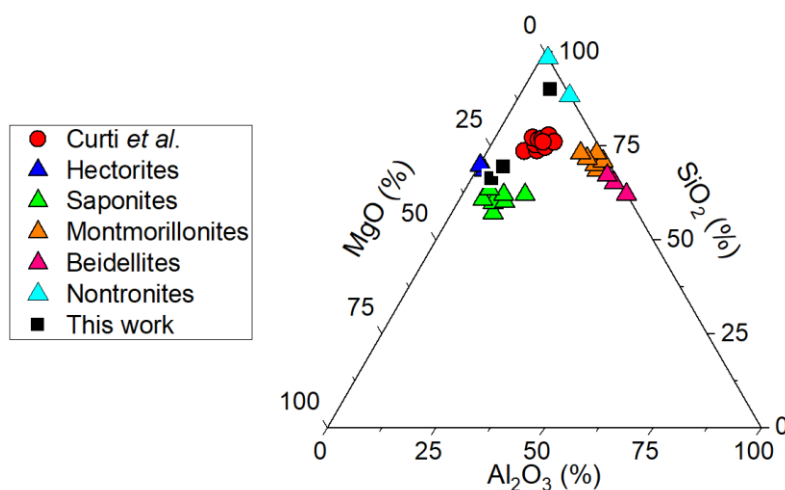


**Figure 4.24.** Ternary diagram comparing composition of clays observed on MW25 (measured using SEM-EDS), in comparable works (Curti *et al.* [31]) and in other works (Newman [250] and references therein).

Phase	Formula	Saturation Index (SI) at day #					
		28	56	112	224	468	672
Amesite	Mg <sub>4</sub> Al <sub>4</sub> Si <sub>2</sub> O <sub>10</sub> (OH) <sub>8</sub>	+	+	+	+	+	+
Celadonite	KMgAlSi <sub>4</sub> O <sub>10</sub> (OH) <sub>2</sub>	+	-	-	-	+	+
Clinochlore	Mg <sub>5</sub> Al <sub>2</sub> Si <sub>3</sub> O <sub>10</sub> (OH) <sub>8</sub>	+	+	+	+	+	+
<b>Montmorillonite</b> (Ca/Mg)	Ca <sub>0.165</sub> Mg <sub>0.33</sub> Al <sub>1.67</sub> Si <sub>4</sub> O <sub>10</sub> (OH) <sub>2</sub> / Mg <sub>0.495</sub> Al <sub>1.67</sub> Si <sub>4</sub> O <sub>10</sub> (OH) <sub>2</sub>	+	-	-	-	-	-
<b>Nontronite</b> (Ca/H/K/Mg/Na)	Ca <sub>0.165</sub> Fe <sub>2</sub> Al <sub>0.33</sub> Si <sub>3.67</sub> H <sub>2</sub> O <sub>12</sub>	/	+	+	+	+	+
	H <sub>0.33</sub> Fe <sub>2</sub> Al <sub>0.33</sub> Si <sub>3.67</sub> H <sub>2</sub> O <sub>12</sub>						
	K <sub>0.33</sub> Fe <sub>2</sub> Al <sub>0.33</sub> Si <sub>3.67</sub> H <sub>2</sub> O <sub>12</sub>						
	Mg <sub>0.165</sub> Fe <sub>2</sub> Al <sub>0.33</sub> Si <sub>3.67</sub> H <sub>2</sub> O <sub>12</sub>						
	Na <sub>0.33</sub> Fe <sub>2</sub> Al <sub>0.33</sub> Si <sub>3.67</sub> H <sub>2</sub> O <sub>12</sub>						
Phlogopite	KAlMg <sub>3</sub> Si <sub>3</sub> O <sub>10</sub> (OH) <sub>2</sub>	+	+	+	+	+	+
<b>Saponite</b> (Ca/H/K/Mg/Na)	Ca <sub>0.165</sub> Mg <sub>3</sub> Al <sub>0.33</sub> Si <sub>3.67</sub> O <sub>10</sub> (OH) <sub>2</sub>	+	+	+	+	+	+
	H <sub>0.33</sub> Mg <sub>3</sub> Al <sub>0.33</sub> Si <sub>3.67</sub> O <sub>10</sub> (OH) <sub>2</sub>						
	K <sub>0.33</sub> Mg <sub>3</sub> Al <sub>0.33</sub> Si <sub>3.67</sub> O <sub>10</sub> (OH) <sub>2</sub>						
	Mg <sub>3.165</sub> Al <sub>0.33</sub> Si <sub>3.67</sub> O <sub>10</sub> (OH) <sub>2</sub>						
	Na <sub>0.33</sub> Mg <sub>3</sub> Al <sub>0.33</sub> Si <sub>3.67</sub> O <sub>10</sub> (OH) <sub>2</sub>						

**Table 4.6.** Potential magnesio-aluminosilicate silicate phases precipitated during MW25 dissolution, as identified using PHREEQC modelling. Common smectites identified in **bold**. Saturation index calculated for each experiment timestep based on the measured elemental abundances and pHs of the leachate at the time of sampling. “+” indicates a potentially saturated phase, “-” a phase unlikely to be saturated and “/” indicates a lack of data.

The precipitation of these minerals can explain the stepped decrease in leachate Mg contents between 28 days (0.203 ppm Mg) and 56 days (0.107 ppm Mg) and the onset of a pH decrease comparable in magnitude to that noted elsewhere during magnesio-aluminosilicate mineral precipitation [54], [251]. The formation of these phases may also explain the rapid (not -plateauing) residual dissolution rates. The consumption of silicon and magnesium required for secondary precipitate formation is expected to increase the driving force for further hydrolysis of the glass network [12], [224], [240]; thereby increasing dissolution rates. This effect is widely reported for MW-glass dissolution studies performed in both pure aqueous [31], [52], [234], [252] and more complex leachates [82]. Aggressive Stage II dissolution of other borosilicate glasses, including ISG [91], has also been correlated with phyllosilicate precipitation [55], [84], [240].

Secondary phase precipitation has also been hypothesised to hinder gel layer growth; as both alteration products compete for the same dissolved glass constituents [82]. This may explain why the magnesium-rich Layer 2 remains a constant thickness from 56 days (Figure 4.18). Magnesium and silicon sourced from dissolution (to form Si/Mg-depleted Layer 3) is no longer consumed to form (gel) Layer 2, as it is now utilised in precipitation of Layer 1. The alteration layer destruction hypothesised as the source of these elements in other studies [240] was not evident as a decrease in Layer 2 silica content (Table 4.3) or in layer thickness (Figure 4.18).

Residual dissolution rates are maintained during and following this mineral precipitation, without evidence of rate resumption by 672 days. Continuation of residual dissolution rates in spite on mineral precipitation is similarly observed in other HLW glass corrosion studies [248]. Residual rates are often maintained during phyllosilicate (smectite) phase formation, with the precipitation instead of zeolite-type phases implicated with rate resumption [248].

### 4.3.3. PCT-B experiments

Continuing the use of boron as a tracer element, MW25 shows Stage I (initial) rate behaviour in PCT-B experiments from 0-28 days, with Stage 2 beyond this. Stage II continues until at least 112 days, with the next and final datapoint potentially indicating rate resumption (Stage III), although this cannot be confidently asserted without further data. ISG shows a similar trend, though qualitatively the initial rates (approximately from 0-28 days) appear less distinct from residual rates. Again, for ISG, the final datapoint may indicate the occurrence of rate resumption, although further data is required to verify this. On these bases, and assuming no rate resumption, the dissolution rates presented in Figure 4.25 can be calculated.

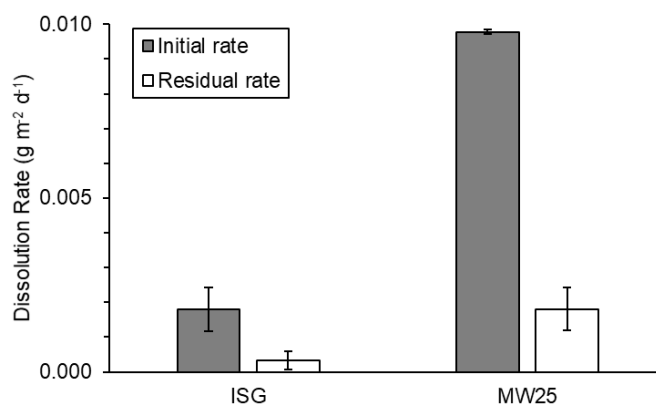


**Figure 4.25.** Dissolution rates in grams per metre squared per day ( $\text{g m}^{-2} \text{d}^{-1}$ ) calculated using  $NL_B$  data and an initial rate regime from 7-28 days with residual rates from 28-112 days

These values can be compared to others in Table 4.7; however caution is again required as parameters including temperature, SA/V and leachant type vary, and dissolution rates are highly dependent on these [231]. Caution is also necessary given that some particle coalescence was observed in the present PCT-B experiments. Though  $NL_i$  data appears minimally impacted by this and coalescence was lesser than for basaltic glasses (Chapter 5), this may adversely affect  $NL_i$  data by reducing the effective surface area in contact with leachate and thus leading to a discrepancy between assumed and actual SA/V values. Rates presented in Figure 4.25 may thus be underestimated. This coalescence has similarly been observed by authors studying comparable systems (within a few days of MW25 corrosion via PCT-B in UHQ water [235]).

For MW25, initial and residual rates appear consistent with the most reliable comparable studies using UHQ water at 40-90 °C [30], [31], [252], [253]. Though in some cases rates from these (40-90°C UHQ) studies appear an order of magnitude greater than those measured herein, the authors of these studies recognise their own values are likely overestimates due to the measurement period and powder coalescence. Correcting their measurements for these factors would likely bring them to comparable orders of magnitude to the rates measured in this work.

Rates calculated in Table 4.7 are also lower, by a factor of 2-8, than those elsewhere calculated for more aggressive ( $\text{Ca}[\text{OH}]_2$ ) leachates [53], [60], [252]. For ISG, initial rates are of a similar magnitude to those calculated for dissolution in UHQ water between 25-90 °C [254], [255], with no comparisons between residual rates available. Rates here-calculated for UHQ are a factor of 15-35 lower than those calculated for aggressive alkali leachates [53], [60], [236], [252]. These differences are consistent with other studies comparing HLW glass dissolution in a saturated  $\text{Ca}(\text{OH})_2$  and pure water leachant [232], [233].

Experimental pH values (Figure 4.4) initially rapidly rise, if a near-neutral start is assumed, to 9.1 and 9.3 for ISG and MW25 dissolved for 7 days respectively. As in MCC-1 experiments, this is likely a characteristic of the initial dissolution regime, as alkali/alkaline earth elements in the glass are rapidly exchange with protonated water species in the solution [69].

<i>Glass type</i>	<i>Leachant type</i>	<i>Temp. (°C)</i>	<i>SA/V (m<sup>-1</sup>)</i>	<i>Initial and residual dissolution rate (g m<sup>-2</sup> d<sup>-1</sup>)</i>	<i>Author</i>
MW25	H <sub>2</sub> O	50	2000	Initial = 0.010 ± 0.000 Residual = 0.002 ± 0.001	This work
MW25	H <sub>2</sub> O	90	1200	<i>Initial rate not stated</i> Residual = 0.001 ± 0.001	Curti et al. [30], [31]
MW25	H <sub>2</sub> O	40	1200	Initial = 0.024 ± 0.004 Residual = 0.003 + 0.000	Schofield et al. [53], [252]
MW25	H <sub>2</sub> O	90	2000	<i>Initial rate not stated</i> Residual = ~ 0.12*	Brookes et al. [234]
MW25	H <sub>2</sub> O	90	1200	Initial note stated Residual = ~ 0.01**	Zwicky et al. [235]
MW25	Ca(OH) <sub>2</sub>	40	1200	Initial = 0.023 ± 0.002 Residual = not stated	Schofield et al. [53], [252]
MW25	Ca(OH) <sub>2</sub>	50	1200	Initial = 0.062 ± 0.008 Residual = 0.017 ± 0.002	Backhouse [60]
ISG	H <sub>2</sub> O	50	2000	Initial = 0.002 ± 0.000 Residual = 0.000 ± 0.000	This work
ISG	H <sub>2</sub> O	40	1200	Initial = 0.016 ± 0.002 <i>Residual rate not stated</i>	Schofield et al. [53], [252]
ISG	H <sub>2</sub> O	25	2000	Initial 0.005 ± 0.0002 <i>Residual rate not stated</i>	Thorpe et al. [254]
ISG	H <sub>2</sub> O	90	2000	Initial 0.039 ± 0.005 <i>Residual not achieved</i>	Calculated from Smith [255]
ISG	Ca(OH) <sub>2</sub>	50	1200	Initial = 0.051 ± 0.007 Residual = 0.0034 ± 0.001	Backhouse [60]
ISG	Ca(OH) <sub>2</sub>	40	1200	Initial = 0.0329 ± 0.0047 <i>Residual rate not stated</i>	Schofield et al. [53], [252]
ISG	Ca(OH) <sub>2</sub>	40	1200	Initial = 0.0356 ± 0.000 Residual = 0.002 ± 0.000	Fisher & Corkhill [236]

**Table 4.7.** Comparison of dissolution conditions and calculated rates from this study (shaded rows) and others using the PCT-B method and boron as a tracer. Readers should note that: \* Brookes et al. [234] identified residual rates as probable over-estimates because they were calculated from the earliest (hypothesised fastest) stages of residual dissolution and \*\* Zwicky et al. [235] observed significant powder coalescence within days of the experiment, leading the authors to identify these rates as probable overestimates.

ISG and MW25 NL<sub>B</sub> data indicate initial dissolution continues until experiment day 28 and little evidence of alteration layer formation during this time is observed. Though leachate magnesium content drops (from 2.3 to 1.0 ppm) for MW25 from 7 to 14 days, no other element concentrations notably decrease, as might be expected during alteration layer formation. Similarly, no distinguishable alteration layer is evident in SEM. However, the degree of surface fracturing (relative to that observed in pristine samples; Figure 4.1) may have increased. These fractures are often associated with sample preparation [82] and are readily correlated with the

drying of a hydrated layer [74], [75], [256]–[258]. Increased fracturing may thus imply the formation of a hydrated layer via the aforementioned migration of water species into the glass. De/hydration is known to cause fracturing of rhyolitic [259] and basaltic [260] glasses [261].

Within 56 days  $NL_B$  data imply both glasses have entered residual dissolution. From this duration onwards,  $NL_i$  data also imply the drawdown of elements to form an alteration layer.

For MW25,  $NL_{Mg}$  and  $NL_{Al}$  decreases constantly from this point until the experiment termination, with  $NL_{Si}$  decreasing until at least 112 days. EDS analysis of the layers formed on MW25 MCC-1 monoliths (Table 4.3) implicate these elements in alteration layer formation, supporting the hypothesis of alteration layer formation over this time in PCT-B. SEM of post-dissolution powders also show an alteration layer on MW25 from 56 days onwards. Though significantly thinner (likely due to the less aggressive conditions), these layers appear consistent with Layers 2/3 in MCC-1 experiments; with both appearing slightly darker in BSE than pristine glass. Further comparisons or identifications is impossible due to EDS resolution.

$NL_i$  data for ISG similarly implies alteration layer formation, though this alteration layer is not observed in SEM until after 224 days. Decreasing  $NL_{Al}$  and  $NL_{Si}$  from day 56 until at least day 112 is consistent with formation of layers with a comparable composition to those formed in the equivalent MCC-1 experiments (Table 4.2). These hypothesised surface layers may not be evident in SEM due to instrument resolution and the lesser thickness generally of ISG surface layers compared to MW25 (as observed for MCC-1 surface layer thicknesses in Figure 4.19).

Residual dissolution continues for both experiments until at least day 112; with no noteworthy changes observed in  $NL_i$  or SEM from 56-112 days. By 224 days of dissolution, most observations imply both glasses are in the residual rate regime, however this cannot be verified with certainty without further data. Both glasses show a significant increase in  $NL_B$  from 112-224 days, with the rate of increase particularly high for MW25, however this is not hypothesised to be rate resumption. This interpretation is supported by the lack of observed zeolite phases (typically associated with rate resumption [43], [248]) and SEM indications of alteration layer growth over this time (contrary to the expected alteration loss/damage during rate resumption). The high leachant pH (>11) required for zeolite precipitation and rate resumption [16], [43] was also not observed in Figure 4.4. Instead, for MW25 at least, magnesio-aluminosilicate precipitation is hypothesised to sustain relatively rapid residual dissolution rates via silica consumption [31], [54], [262], as observed in MCC-1.

Within 224 days of experimental duration, the alteration layer hypothesised to have started forming on ISG from day 56 of dissolution is now evident in SEM. This layer is highlighted by the increased dehydration associated with sample-preparation by this stage; however why dehydration is more pronounced can only be speculated. Samples may have been air-dried for longer or in more aggressive conditions after test termination (sample drying was uncontrolled and variable), or samples may have become increasingly hydrated (pre-drying) with dissolution duration. Elucidation of the formation mechanism or identification of this layer is challenging due to lack of available EDS and limited observations, however comparisons with layers formed in MCC-1 experiments may offer some insight. Comparison of the single layer observed in PCT-B with MCC Layer 3 are least plausible given this layer was last-formed and had a unique scallop-morphology never observed in PCT-B. Comparison with Layer 2 in MCC-1 experiments are supported by the previous hypothesis of this layer's early formation via a process, ion exchange, that would make it highly susceptible to the dehydration observed

in PCT-B. However, in MCC-1, Layer 2 appeared darker than pristine glass in BSE - which was not observed for PCT-B. Instead, MCC-1 Layer 1 *was* of comparable greyscale to the pristine glass, however this layer occurred only in tandem with a second layer which was never seen in PCT-B. Furthermore, Layer 1 in MCC-1 was consistently thicker than Layer 2, so why Layer 2 would now, in PCT-B, be thicker or more readily observed remains unclear. EDS and  $NL_i$  data are unable to provide further insight: EDS of MCC-1 Layers 1 and 2 indicate a predominantly aluminosilicate composition (consistent with  $NL_{Si}$  and  $NL_{Al}$  PCT-B decreases), with the only notable difference being the greater zirconium content of Layer 1. However, in PCT-B,  $NL_{Zr}$  shows no consistent trend from the onset of hypothesised layer formation. In summary, if this layer is not solely the result of variable sample preparation then it appears most comparable to Layer 1 or 2 in MCC; however any comparison is at-best speculative.

MW25 shows multiple notable features in SEM by 224 days. The first is a  $\sim 5 \mu\text{m}$  thick surface layer which appears fibrous ('fluffy') and darker than pristine glass (in BSE). This magnesian-aluminosilicate layer appears comparable to the hypothesised precipitate layer (Layer 1) formed in MW25 MCC-1. Both have a similar mineral habit, magnesium enrichment, and chemical composition. Geochemical modelling again indicates saponite precipitation is possible from day 7 onwards, with potential nontronite precipitation from day 28 onwards. As previously stated, the precipitation of these phases can explain the rapid residual dissolution rates, as the dissolution driving force is increased by consumption of silicon and magnesium [12], [224], [240]. Identification of the brighter dendritic forms within this precipitate layer is more challenging owing to their size, absence in post-dissolution XRD, and the lack of EDS data. However, geochemical modelling indicates manganese, iron and zirconium-containing phases become increasingly saturated beyond 28 days of dissolution and rare-earth/Zr phosphates have previously been identified during aqueous Magnox glass dissolution [31], [91].

The arcuate depleted zones surrounding near-surface spinel crystallites in MW25 are also notable in 224 day dissolved samples. The magnesium, sodium and silicon depletion in these, as well as their delayed formation, implies formation via dissolution. Similar preferential dissolution around crystallites has been observed in previous HLW glass corrosion studies [236]; however explanations are elusive. Multiple possibilities exist: crystallite formation may have locally depleted the glass in network forming/strengthening elements (e.g. Fe), or crystallite dissolution may have generated local leachate zones that were more aggressive to glasses. However, no chemical variation in the glass surrounding the crystallites was noted pre-dissolution, and spinel phases are relatively durable [51], [228], [229], so should minimally influence local leachate chemistry. Alternatively, the crystallite/glass boundary may have contained more dangling bonds and structural defects than elsewhere in the glass; or crystallite formation may have increased localised glass stresses, thereby promoting dissolution. However, glass/spinel grain boundary effects have previously been considered minimal [51], [228], [229] and samples were annealed to minimise stresses post-casting. Regardless of their cause, the overall effect of these features is likely low given their rarity (<5 % of sample volume), particularly at powder surfaces. However, they may offer insight into formation of the scalloped boundary observed in MCC-1. Alteration layers may contain crystallites or local precipitate clusters [60] which may promote dissolution of the underlying glass in a comparable way to the spinel in MW25 PCT-B experiments. This localised dissolution requires further investigation to establish the causes and magnitude of any effects.

#### 4.4. Summary

Glasses formulated to simulate the behaviour of nuclear waste glasses have been dissolved in simplified aqueous conditions via the MCC-1 and PCT-B procedures. Dissolution rates and alteration products were found to differ, both between glasses and between test methods.

In MCC-1 experiments, MW25 likely dissolves more rapidly than ISG during the initial dissolution period, however an anomalous datapoint may mask this trend (Figure 4.26). In this period (“Stage I”) behaviour is associated with formation, via interdiffusion and ion exchange, of two sodium-depleted layers in each glass within 28 days of dissolution. The outer of these layers is notably enriched in magnesium for MW25, with the equivalent outer layer for ISG showing a zirconium enrichment. Both glasses develop an additional third layer within 56 days. For ISG this new innermost layer is compositionally comparable to its neighbouring sodium-depleted layer, though now with a distinctive scallop-morphology. For MW25, this third layer comprises crystalline smectites (probable saponites/nontronites) formed at the leachate interface. The scalloped boundary of altered layers with pristine glass for ISG is thought to result from localised attack comparable to that which forms the ‘finger’-like morphology between pristine MW25 glass and the alteration layer. “Stage II” behaviour is achieved within 224 days of alteration for both glasses. Rapid (residual) dissolution rates for MW25 over this period are linked to consumption of elements from the leachate in order to precipitate the aforementioned clays. These magnesian-aluminosilicate minerals did not form on ISG potentially because this glass composition lacks the required magnesium for their formation. Rate resumption (“Stage III”) was not observed for either glass, however ISG alteration layers show evidence of significant instability and restructuring between 468-672 days of dissolution and the rapid residual rates shown by MW25 could be interpreted as rate resumption if  $NL_B$  values were the exclusive consideration.

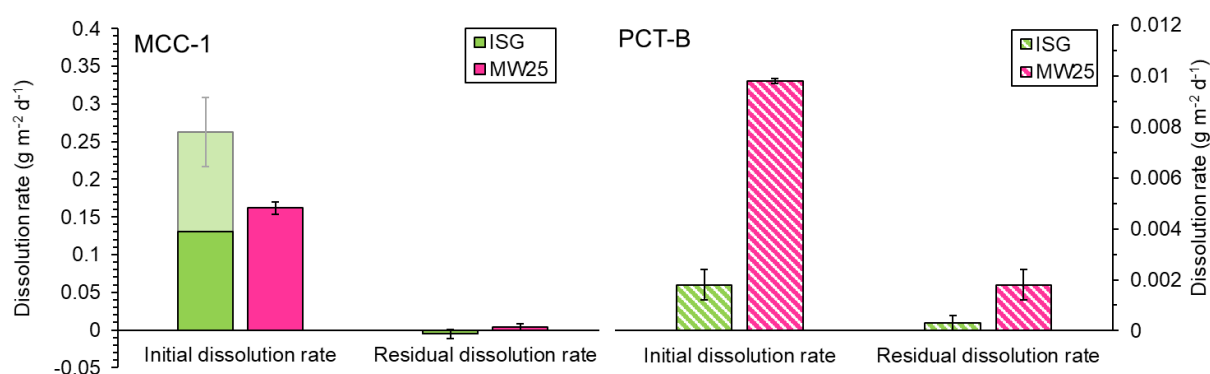


**Figure 4.26.** Comparison of dissolution rates (calculated using  $NL_B$  data) for ISG (green) and MW25 (pink) in both MCC-1 (left; solid bars) and PCT-B (right; striped bars) experiments. Note that MCC-1 initial rates calculated for ISG from 28-112 days appear anomalous (faded) relative to the more-reliable (unfaded) rates calculated from 28-56 days.

In PCT-B experiments, initial dissolution appears again more rapid for MW25 than ISG (Figure 4.26). Neither glass shows persuasive evidence of alteration layer formation for at least the first 56 days, however leachate pH increases and normalised mass losses indicate dissolution via the expected “Stage I” behaviour (interdiffusion and ion exchange) and alteration layers may be below the achievable instrument resolution. This may have formed a hydrated layer which readily fractured during sample preparation (drying) of both glasses. Solution data imply alteration product formation and “Stage II” dissolution behaviour for both glass compositions

from 56 days onwards. Higher residual dissolution rates for MW25 than ISG over this time are hypothesised to, again, result from precipitation of saponite clay products in MW25 but not ISG. These clay alteration products were observable in SEM by 224 days of dissolution, the same time at which alteration layers on ISG are hypothesised to also become evident at the available resolution. Preferential glass dissolution was observed surrounding spinel crystals within MW25 samples, however the cause of this can only be speculated. Interpretations of rate resumption for either glass were not supported by pH or SEM observations, however as for MCC-1 experiments, this cannot be categorically rejected without longer term dissolution data.

Overall, the aqueous dissolution behaviours of ISG and MW25 are partially comparable albeit with some notable and potentially significant differences. Both glasses dissolve via the same expected mechanism, with transitions between the stages of this occurring at approximately the same times. However, the alteration products formed during these stages differ depending on the elemental constituents of the parent glass. The rates of dissolution during these stages also differ: a probable result of the differing alteration product development. These differences may limit the value of ISG in studies seeking to elucidate the dissolution of UK nuclear waste glass.

# 5. The Role of Magnesium in Basaltic Glass Dissolution

## 5.1. Introduction

A comprehensive understanding of the impact of magnesium on glass dissolution processes and rates is crucial if scientists and engineers are to prove the safety case for geological disposal of the UK's HLW. Without this, the UK may see limited benefit from the international knowledge accrued on the dissolution of other HLW glasses, which are typically lower in this element, as international comparisons will remain overshadowed by uncertainty concerning the effect of magnesium on any observed trends. Elevated magnesium contents are already hypothesised to limit UK HLW glass durability [52], [53], however, the mechanistic causes and the magnitude of this effect requires further research.

Natural 'analogue' glasses offer useful insight into long-term durability in both natural and laboratory environments. Basaltic glasses are considered some of the most useful glasses for this purpose [151], however the role of magnesium in the dissolution of basaltic glasses remains poorly understood.

To gain insight into this, basaltic glasses with a variable magnesium to calcium ratio have been synthesised and dissolved (in pure water) via the methodology outlined in Chapter 3. MCC-1 experiments, utilising glass monoliths, were completed on the mid- and end-members of the basaltic glass series; with PCT-B experiments conducted on all synthesised basaltic glasses including the intermediary compositions. This chapter presents a comparison of the undissolved glasses, their dissolution rates and behaviours and the alteration layers developed during dissolution. A comparison and discussion of the reliability of results from the differing test methodologies is also offered.

## 5.2. Results

### 5.2.1. Pristine glass characterisation

#### SEM-EDS

Micrographs of all samples prior to their dissolution (but after their mounting in epoxy resin) shows all glasses to be uniform and homogenous (Figure 5.1). All powders appear equally highly fractured and fragmented within a 1-3  $\mu\text{m}$  perimeter of their surface.

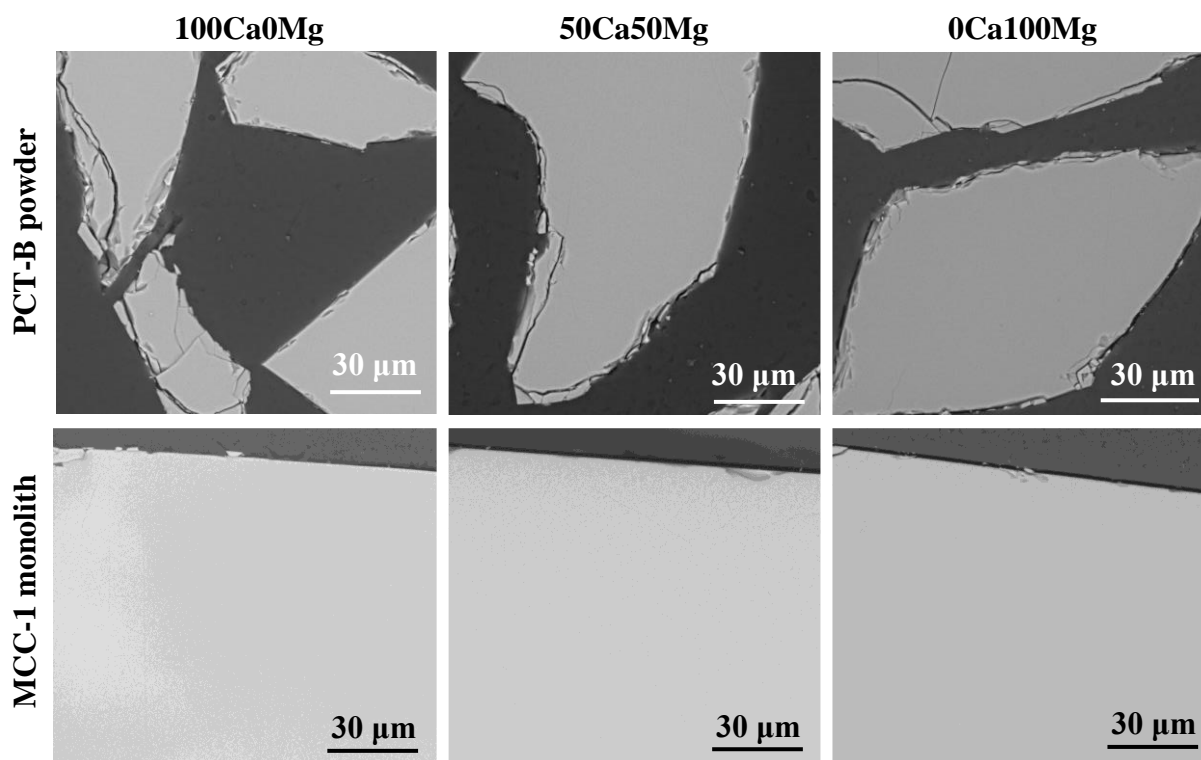


**Figure 5.1.** BSE images of samples prior to dissolution. 30Ca70Mg and 70Ca30Mg samples, (only prepared as powders) not shown for brevity, but exhibit surface fracturing as above.

#### Acid-digest & ICP-OES

Pristine glass compositions, as measured via external acid-digest & ICP-OES are stated in Table 5.1. All were within tolerance of the ‘target’ (batched) compositions shown in brackets.

Mol. %	0Ca100Mg	30Ca70Mg	50Ca50Mg	70Ca30Mg	100Ca0Mg
SiO <sub>2</sub>	55.5 (53.3)	55.06 (53.3)	54.7 (53.3)	56.95 (53.3)	55.86 (53.3)
Al <sub>2</sub> O <sub>3</sub>	9.13 (9.4)	9.2 (9.4)	7.62 (9.4)	8.27 (9.4)	7.9 (9.4)
Fe <sub>2</sub> O <sub>3</sub>	4.56 (4.4)	4.43 (4.4)	4.56 (4.4)	4.37 (4.4)	4.51 (4.4)
Na <sub>2</sub> O	3.08 (2.8)	3.01 (2.8)	3.26 (2.8)	2.94 (2.8)	3.05 (2.8)
Li <sub>2</sub> O	1.81 (2.2)	1.75 (2.2)	1.81 (2.2)	1.74 (2.2)	1.78 (2.2)
CaO	0.36 (0)	8.12 (7.8)	11.8 (10.8)	17.04 (18.2)	24.8 (25.9)
MgO	23.44 (25.9)	16.34 (18.2)	14.13 (15.1)	6.67 (7.8)	0 (0)
P <sub>2</sub> O <sub>5</sub>	0.08 (0)	0.08 (0)	0.09 (0)	0.08 (0)	0.12 (0)
SrO	0.35 (0.2)	0.34 (0.2)	0.36 (0.2)	0.33 (0.2)	0.34 (0.2)
MnO	0.16 (0.1)	0.15 (0.1)	0.16 (0.1)	0.15 (0.1)	0.15 (0.1)
TiO <sub>2</sub>	1.53 (1.4)	1.5 (1.4)	1.51 (1.4)	1.45 (1.4)	1.49 (1.4)

**Table 5.1.** Compositions, as measured (and as batched, in parathesis) in oxide molar percent, of basaltic glasses. Errors not originally stated, but assumed to be circa  $\pm 3\%$ .

### XRD

Figure 5.2 shows XRD of the synthesised basaltic glasses prior to their dissolution. A region of diffuse scattering is evident from 15 to 40 °2 $\theta$ . In addition to this, higher magnesium glasses (0Ca100Mg and 30Ca70Mg) also show evidence of narrower, though not sharp, peaks at circa 36, 44 and 63 °2 $\theta$ . The intensity of these peaks decreases with decreasing magnesium content.

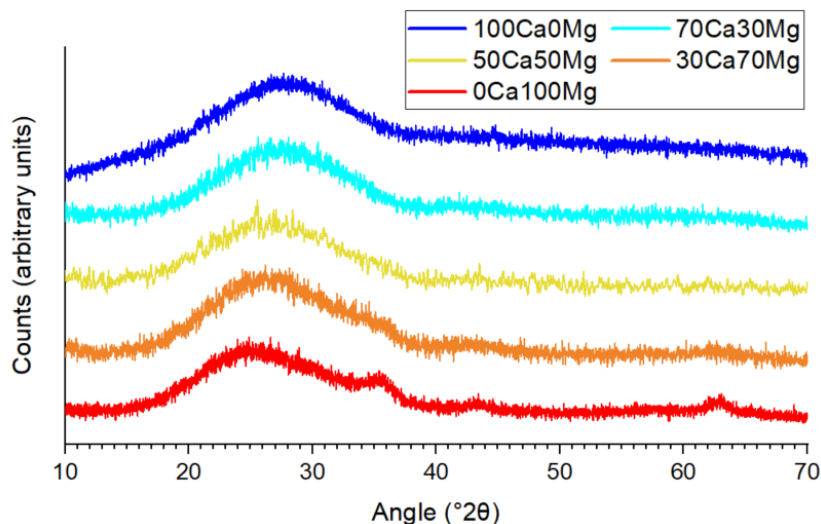


**Figure 5.2.** XRD patterns of the pristine basaltic glasses, with variable Mg:Ca contents, synthesised in this study.

### Raman

Raman spectra (Figure 5.3) from all glasses show two broad peaks centred around 510  $\text{cm}^{-1}$  (with a width of circa 280  $\text{cm}^{-1}$ ) and centred around 970  $\text{cm}^{-1}$  (with a slightly larger width at circa 330  $\text{cm}^{-1}$ ). In higher magnesium glasses (Ca:Mg  $\geq$  70:30) these broad peaks appear subdued due to the presence of a more dominant peak at 672  $\text{cm}^{-1}$  (with a width of  $\sim$ 150  $\text{cm}^{-1}$ ). High magnesium glasses also show low intensity peaks at 320 and 460  $\text{cm}^{-1}$ , both with widths of circa 100  $\text{cm}^{-1}$ .

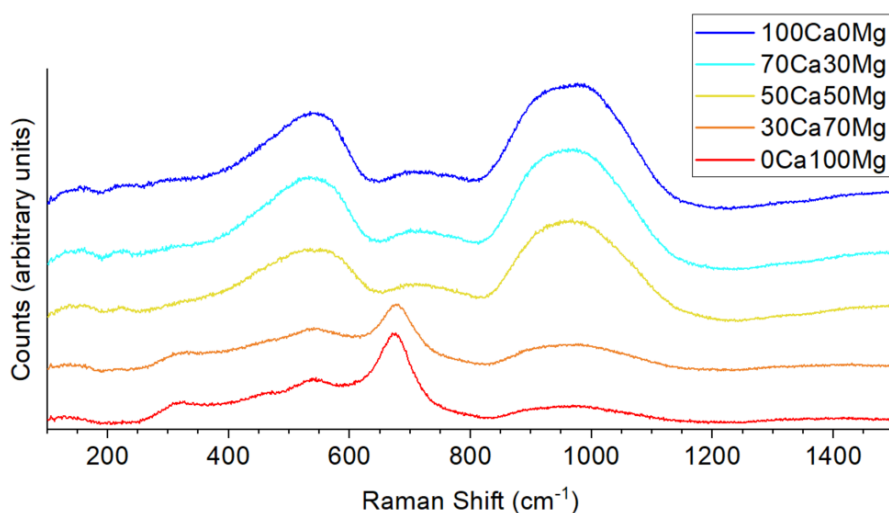


**Figure 5.3.** Raman spectra of pristine basaltic glass series containing variable Mg:Ca.

### 5.2.2. pH

Figure 5.4 shows the evolution of leachate pH in basaltic glasses dissolved via the PCT-B and MCC-1 methodologies. Error bars indicate measurement repeatability error (standard deviation between triplicate samples), *not* the instrument error which some users estimate to be as large as one pH unit (Colleen Mann, personal communication). Trends in the pH of blank vessels are as described in Section 4.2.2, but are also shown here for completeness.

In MCC-1 experiments, leachate pH appears high (pH 9.0 to 9.5) for the first 28-56 days, before falling modestly (to pH 8.5 to 9) for the remainder of the test. A compositional dependency may also be evident: in most cases the 100Ca0Mg and 0Ca100Mg leachates have the highest and lowest mean pH values respectively. This implies a negative correlation between leachate pH and magnesium content of the pristine basaltic glass. However, exceptions to this occur at the 468 and 672 day timesteps where the 50Ca50Mg leachate appears to have an anomalously low and high pH respectively.

PCT-B leachates may show a similar trend, with a higher pH (8.5 – 9.5) for the first 14 days falling to lower (pH 8 - 8.5) values from 14 to 112 days. Leachate pH may then re-rise (to 8.5 – 9) by day 224. No consistent trend with magnesium/calcium ratio is evident: at a given timestep all values are approximately within error and mean values show no trend.

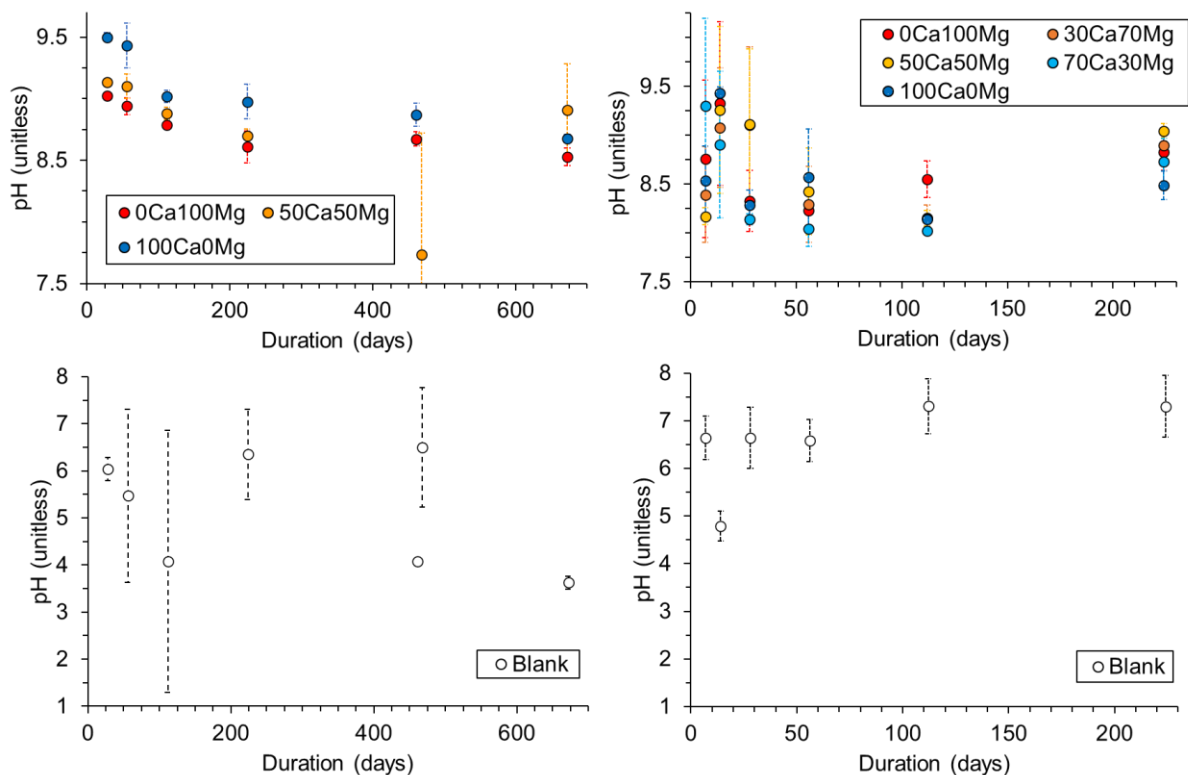


**Figure 5.4.** pH measurements of blank (below) and experimental (above) leachates derived from MCC-1 (left) and PCT-B (right) experiments of the basaltic glass series.

### 5.2.3. Normalised mass losses

Normalised mass loss ( $NL_i$ ) values calculated for MCC-1 and PCT-B experiments are shown in Figure 5.5 and Figure 5.6 respectively. Values for some elements (Fe, K, Mn, Ti) are omitted for brevity, but only where normalised mass loss values for the element are less than  $0.5 \text{ g m}^{-2}$  for all samples and for the entire experiment duration. Lithium, sodium and silicon typically show similar trends in these data, so are described together below.

In MCC-1 experiments lithium, sodium and silicon normalised mass losses generally show an approximately logarithmic increases with dissolution duration until 468 days of dissolution. Beyond this,  $NL_i$  values for these elements appear to decrease, particularly for the end members. However this  $NL_i$  decrease is notably dependant on a single timestep (672 days), so may lack significance. Compositional dependencies are consistent and clear in  $NL_{Li}$ ,  $NL_{Na}$  and  $NL_{Si}$  values: for a given timestep, and where values are not within error of each other, 0Ca100Mg consistently shows the largest normalised mass losses, with 100Ca0Mg having the lowest.

In contrast,  $NL_{Al}$  decreases with dissolution duration for all compositions, though with an approximately exponential decrease for 0Ca100Mg basaltic glasses and an approximately linear decrease for 100Ca0Mg samples.  $NL_{Na}$  values for the latter samples (100Ca0Mg) are also approximately twice those for 0Ca100Mg and 50Ca50Mg glasses. Magnesium, where present, shows a decrease in normalised mass loss with duration – with an approximate inverse logarithm trend for 0Ca100Mg and 50Ca50Mg (if the first two timesteps are ignored as outliers for the latter composition). Normalised mass loss of strontium and phosphorous remains low but constant until the final (672 day) timepoint, where  $NL_{Sr}$  sharply rises for 100Ca0Mg and  $NL_P$  sharply increases for 0Ca100Mg.

In PCT-B experiments  $NL_{Li}$ ,  $NL_{Na}$  and  $NL_{Si}$  again all show similar trends: values appear constant for all composition between 7-14 days (for  $NL_{Li}$ ) or between 7-56 days (for  $NL_{Na}$ ) before increasing approximately linearly for the remainder of the test duration. For  $NL_{Li}$  values, the rate of this increase appears to be compositionally-dependent, with high/mid magnesium compositions (0Ca100Mg, 30Ca70Mg, 50Ca50Mg) showing the largest rate of increase. These compositions also consistently show higher normalised mass loss values for a lithium, sodium and silicon at a given timepoint than lower magnesium glasses (70Ca30Mg, 100Ca0Mg). However this compositional dependence is less clear in the  $NL_{Si}$  and  $NL_{Na}$  data where all values are within error for a given timestep.

The trend of high/mid magnesium compositions (0Ca100Mg, 30Ca70Mg, 50Ca50Mg) showing the largest normalised mass losses, holds similarly true for  $NL_P$  values. However, for  $NL_{Sr}$  this compositional-dependency trend appears reversed: the highest magnesium glass (0Ca100Mg) consistently has the lowest  $NL_{Sr}$ . Compositional dependency of the  $NL_{Mg}$  and  $NL_{Ca}$  data is indiscernible as most values are within error of each other.

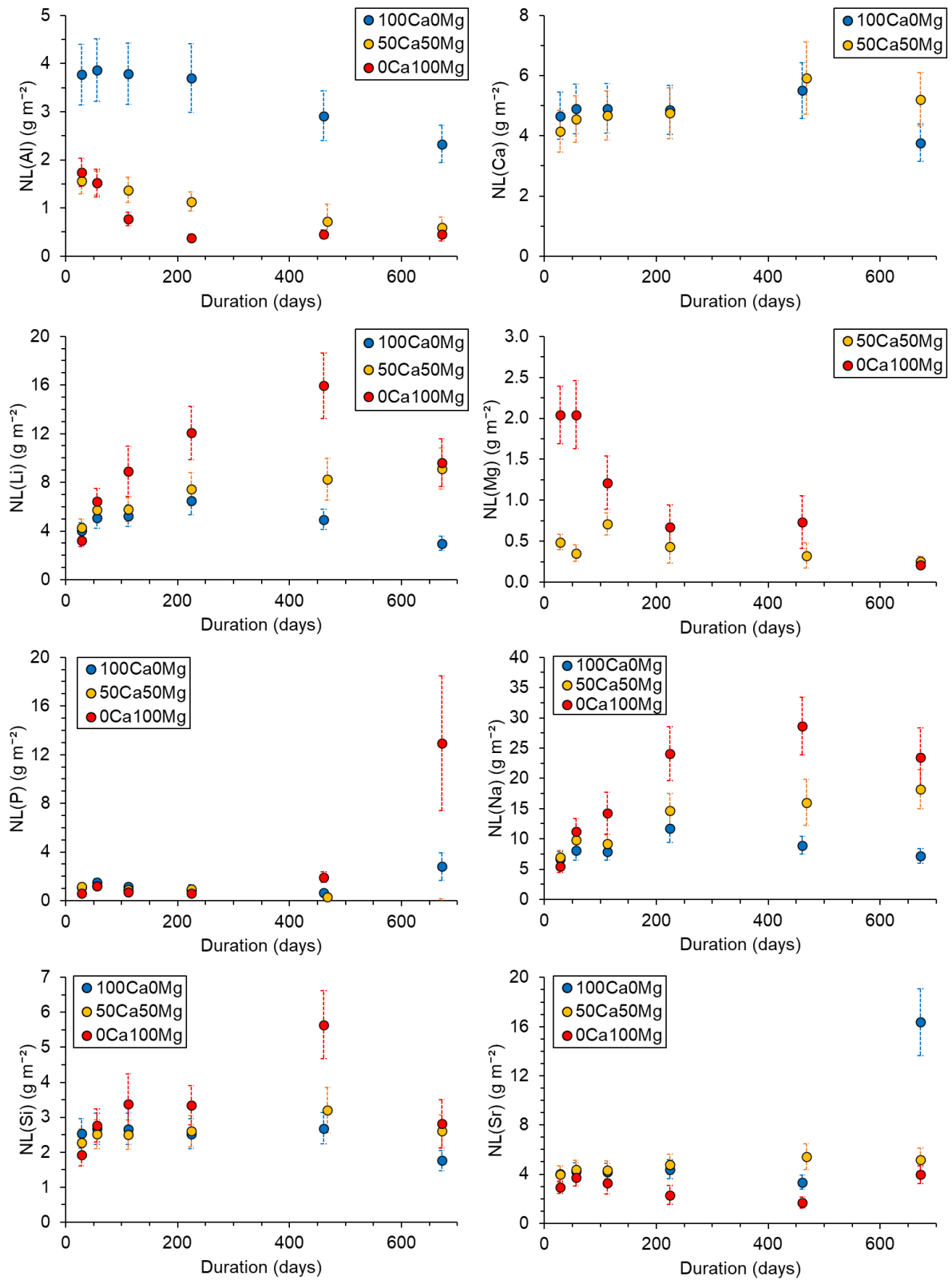


**Figure 5.5.** Normalised mass loss values calculated for the MCC-1 experiments completed on basaltic glasses with a range of MgO:CaO ratio.

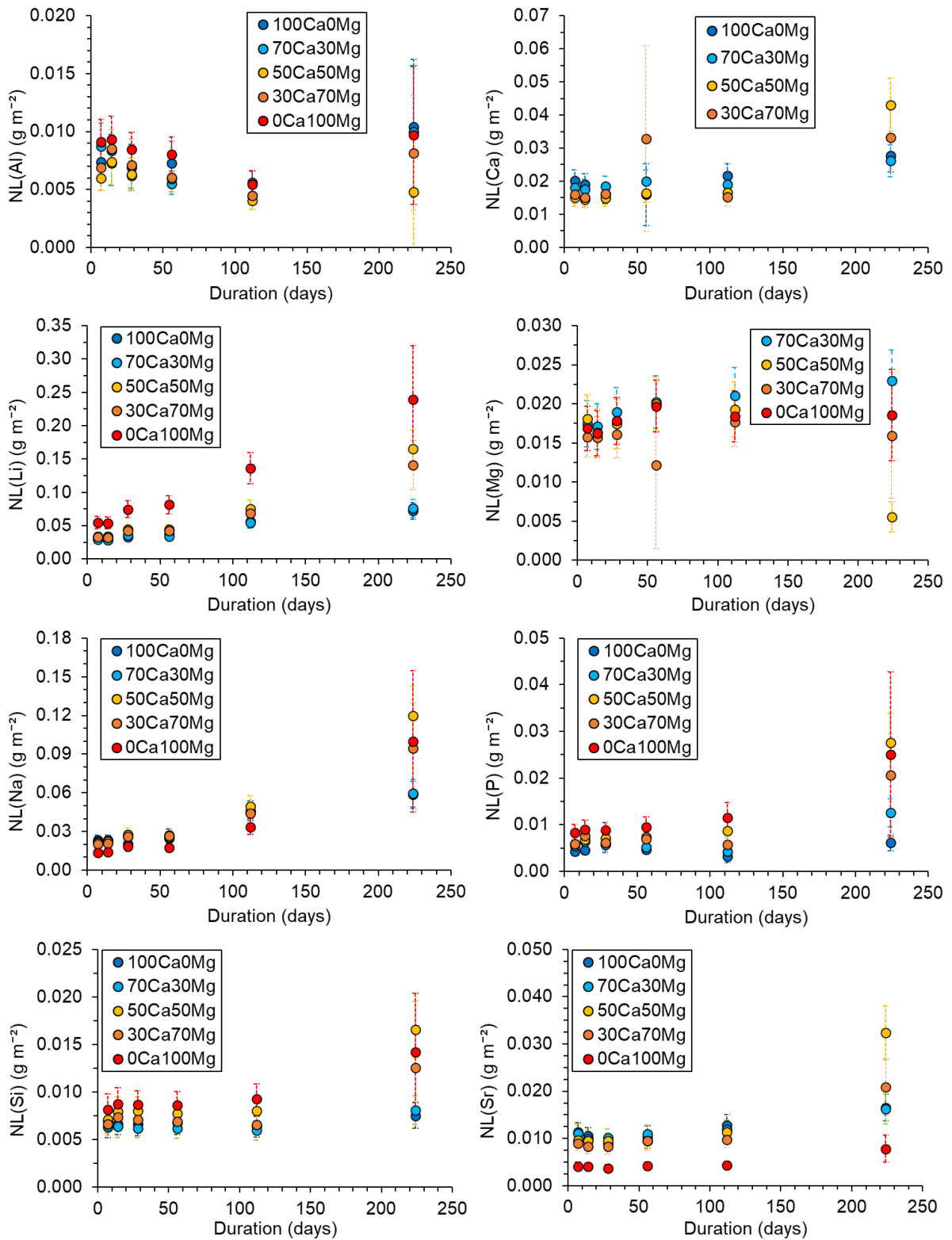


**Figure 5.6.** Normalised mass loss values calculated for the PCT-B experiments completed on basaltic glasses with a range of MgO:CaO ratio.

#### 5.2.4. SEM EDS analysis

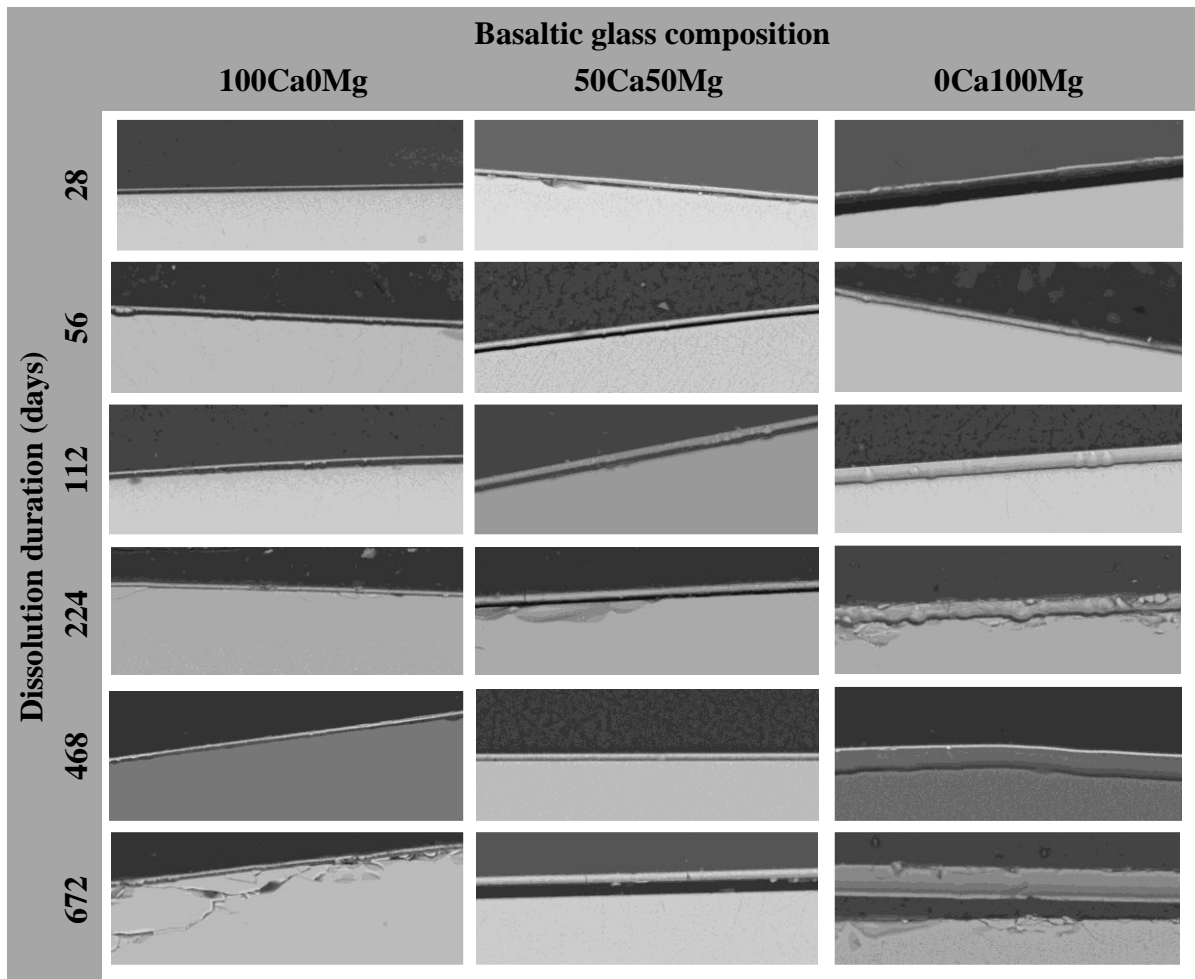
##### *MCC-1/BSE*

Figure 5.7 shows representative SEM-BSE images from each basaltic glass composition at each MCC-1 timestep. To aid comparison all images were taken at an identical magnification and are from areas which are relatively unaffected by vermiform features (see Chapter 6).

All compositions, at all timesteps, show the presence of a surface layer of variable thickness. This layer is highly heterogeneous, varying considerably across even a single monolith. The layer is occasionally broken into block-like segments by fractures that are approximately perpendicular to the surface. In places, this surface layer can cleave into sub-layers (Figure 5.8): with two layers evident by 28 days and three layers emerging after 468 days. These sub-layers are frequently separated by a (layer of) fluffy material, and are evident in both 100Ca0Mg and 50Ca50Mg glasses. The epoxy-filled void that separates the alteration layer from the pristine glass and the sub-layers from each other is presumed to arise during sample preparation and as a result of dehydration shrinkage.

The surface layer is also highly heterogeneous in greyscale intensity, as indicates internal compositional non-uniformity. Though the bulk surface layer is typically of similar greyscale intensity to the unaltered glass, a 'brighter' sub-layer (Figure 5.9) within this is also evident. This bright region, typically of 0.5-2  $\mu\text{m}$  in thickness, is evident within the surface layer developed on 0Ca100Mg and 50Ca50Mg basaltic glasses by 112 days of dissolution. This sub-layer is particularly evident within vermiform features where it is typically centrally located within the features. Away from these areas, the layer may be located proximally to either layer surface: near the contact with the leachate or nearest to the pristine glass (e.g. compare 0Ca100Mg at 468 and 672 days in Figure 5.7).

Resting atop this layer, situated at the layer/leachate interface during dissolution, are less sharply-defined globular, equant, acicular, fibrous or bladed occurrences (Figure 5.10). These are evident after 56 days of dissolution in all compositions and generally become larger and more numerous with dissolution duration. Though noted to occur in all compositions, these precipitates may be marginally more abundant in high-magnesium glasses; however a statistical comparison to verify this has not been completed.



**Figure 5.7.** Representative SEM-BSE images of a cross section made through basaltic glass monoliths (with variable Mg:Ca ratios) after dissolution via the MCC-1 procedure. All images are 115µm across, with the pristine glass oriented towards the bottom of the image.

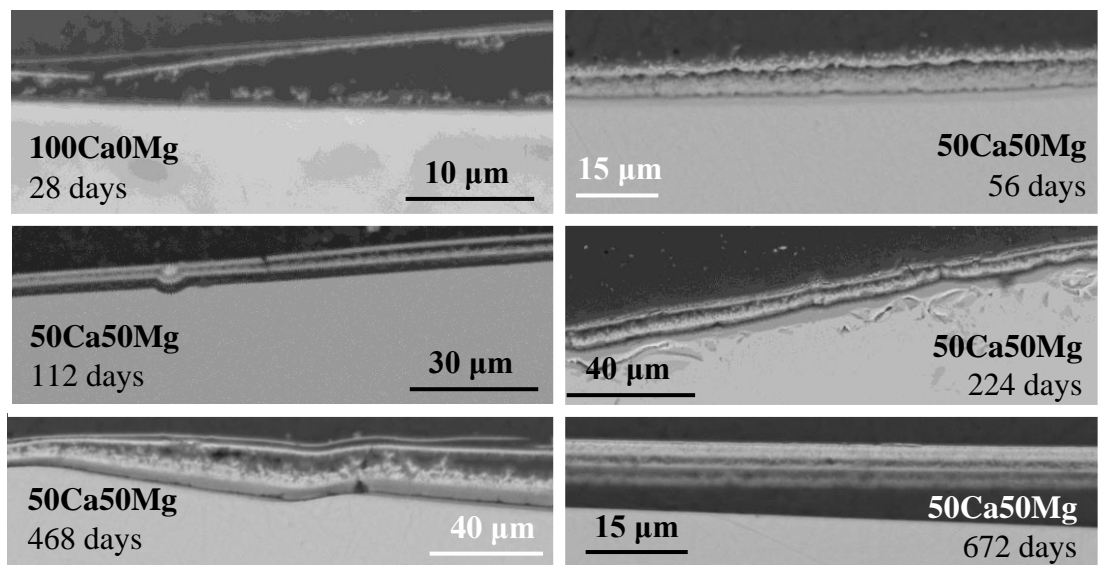


**Figure 5.8.** SEM-BSE images to show cleaving of the surface layer evident in 50Ca50Mg and 100Ca0Mg basaltic glasses after dissolution via the MCC-1 procedure for various durations. Glass composition and dissolution duration specified in text insets.

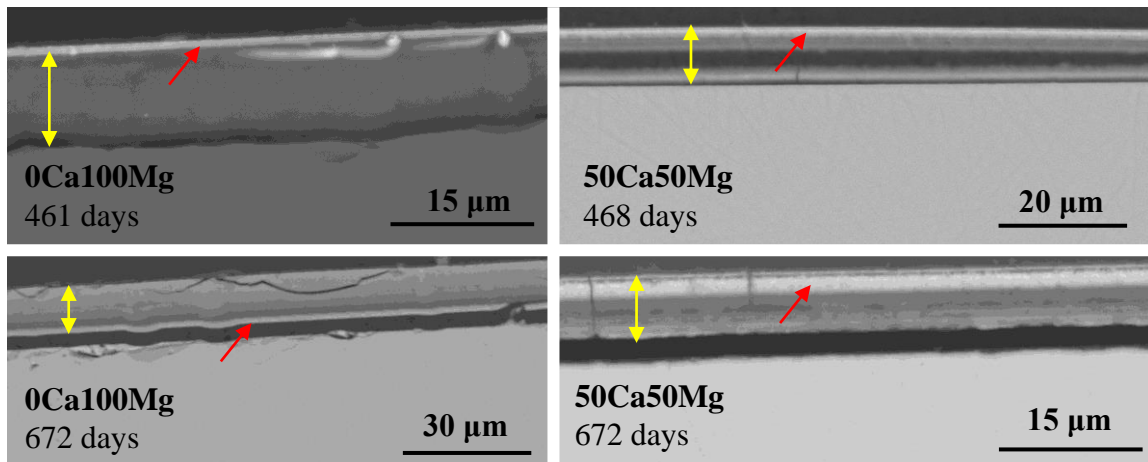


**Figure 5.9.** SEM-BSE images of 'brighter' sub-layer (arrowed in red) within the surface layer (bound by yellow arrow) developed on basaltic glasses, with variable Mg:Ca, after dissolution via the MCC-1 procedure

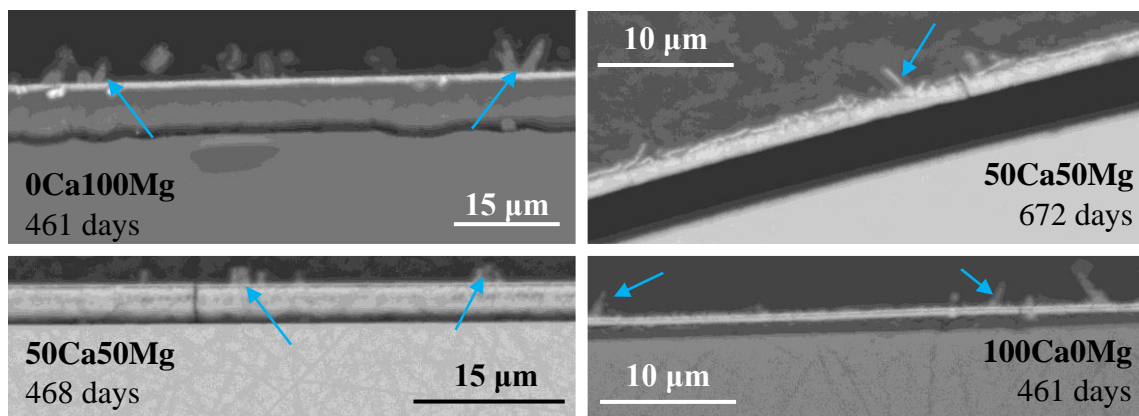


**Figure 5.10.** SEM-BSE images of particles (arrowed) resting atop the more continuous surface layer developed on all glass compositions after > 56 days of dissolution via MCC-1.

*MCC-1/EDS*

The unprocessed composition of surface layers measured on all basaltic glass composition at all timesteps are presented in Table 5.2a-c. All layers comprise silicon, iron, aluminium and titanium, whilst the layer developed on the end-member glasses also contain their calcium or magnesium constituent and the mid-member contains both. Sodium content was negligible.

<b>a) 100Ca0Mg</b>		<b>Element weight%</b>			
	<b>56 days</b>	<b>112 days</b>	<b>468 days</b>	<b>672 days</b>	
<b>Si</b>	14.1 (0.6)	15.6 (0.7)	23.6 (1)	12.1 (0.5)	
<b>Fe</b>	20.4 (0.6)	13.9 (0.4)	3.4 (0.1)	12.1 (0.4)	
<b>Mg</b>	0.2 (0)	0.3 (0)	0 (0)	0.8 (0.1)	
<b>Al</b>	5.6 (0.3)	6.6 (0.3)	6.4 (0.3)	5.2 (0.3)	
<b>Ti</b>	2.7 (0.1)	2.3 (0.1)	0.9 (0.1)	1.3 (0.1)	
<b>Ca</b>	7.7 (0.3)	9.6 (0.3)	3 (0.1)	4 (0.1)	
<b>Na</b>	1 (0.1)	0.7 (0.1)	0.2 (0)	0.8 (0.1)	

<b>b) 50Ca50Mg</b>		<b>Element weight%</b>			
	<b>56 days</b>	<b>112 days</b>	<b>224 days</b>	<b>468 days</b>	<b>672 days</b>
<b>Si</b>	10.2 (0.4)	16.6 (0.7)	15.9 (0.7)	18.7 (0.8)	17 (0.7)
<b>Fe</b>	13.9 (0.4)	10.5 (0.3)	18.1 (0.6)	16.4 (0.5)	13.2 (0.4)
<b>Mg</b>	5.8 (0.3)	6.9 (0.4)	5.3 (0.3)	7.9 (0.4)	3.9 (0.2)
<b>Al</b>	5.6 (0.3)	8.4 (0.4)	6.3 (0.3)	7.5 (0.4)	6.1 (0.3)
<b>Ti</b>	0.5 (0)	1.8 (0.1)	2.3 (0.1)	2 (0.1)	1.6 (0.1)
<b>Ca</b>	1.6 (0.1)	1.8 (0.1)	4.4 (0.2)	3.1 (0.1)	4.6 (0.2)
<b>Na</b>	0.2 (0)	0.7 (0.1)	0 (0)	0.4 (0)	0.3 (0)

<b>c) 0Ca100Mg</b>		<b>Element weight%</b>			
	<b>56 days</b>	<b>112 days</b>	<b>224 days</b>	<b>468 days</b>	<b>672 days</b>
<b>Si</b>	15.8 (0.7)	16.1 (0.7)	13.6 (0.6)	18.4 (0.8)	12.8 (0.6)
<b>Fe</b>	14.8 (0.5)	18.5 (0.6)	14.5 (0.4)	20.9 (0.6)	20.1 (0.6)
<b>Mg</b>	9.3 (0.5)	7.3 (0.4)	9 (0.5)	8.5 (0.5)	6.6 (0.4)
<b>Al</b>	10.5 (0.5)	7.2 (0.4)	8.5 (0.4)	9.3 (0.5)	7.3 (0.4)
<b>Ti</b>	2.5 (0.1)	3.9 (0.1)	3.1 (0.1)	2.8 (0.1)	2.9 (0.1)
<b>Ca</b>	0.3 (0)	0.1 (0)	0 (0)	0.3 (0)	0.1 (0)
<b>Na</b>	0.5 (0.1)	0.8 (0.1)	0.3 (0)	0.2 (0)	0.3 (0)

**Table 5.2.** SEM-EDS estimated compositions of the surface layers developed during MCC-1 testing of basaltic glasses with variable magnesium/calcium contents: 100Ca0Mg (a, top table), 50Ca50Mg (b, middle table) and 0Ca100Mg (c, bottom table). Values stated are mean elemental weight percent, as measured from two or more locations, and the standard deviation on this mean (in parentheses).

Figure 5.11 shows surface layer compositions recalculated as a proportion of elemental abundances in each respective pristine glass. All surface layers were enriched in titanium and iron; with a depletion in silicon. No consistent trends with dissolution duration were noted, and compositional dependencies appear weak. Titanium enrichment was marginally more pronounced in high-magnesium glasses (Ti enriched by a factor of 2-4 in 0Ca100Mg, compared to an enrichment factor of two for 50Ca50Mg and a factor of 2-3 for 100Ca0Mg). Iron was enriched by a factor of circa two in 0Ca100Mg and 50Ca50Mg glasses, and by a factor of 2-3 in magnesium-free glasses. Silicon, on average (across all compositions/timesteps), was depleted by ~70% relative to parent glass compositions.

Aluminium was present in all layers in quantities comparable to parent glasses ( $100 \pm 30\%$ ). Where present in the parent glass, magnesium appears in the surface layer in quantities comparable to parent glasses (100-110%) for 0Ca100Mg glasses but in larger quantities (100-200%) for 50Ca50Mg glasses. Sodium was on average present in quantities 30% of the parent glass (though this ranged from sodium-free to 70% of pristine glass values).

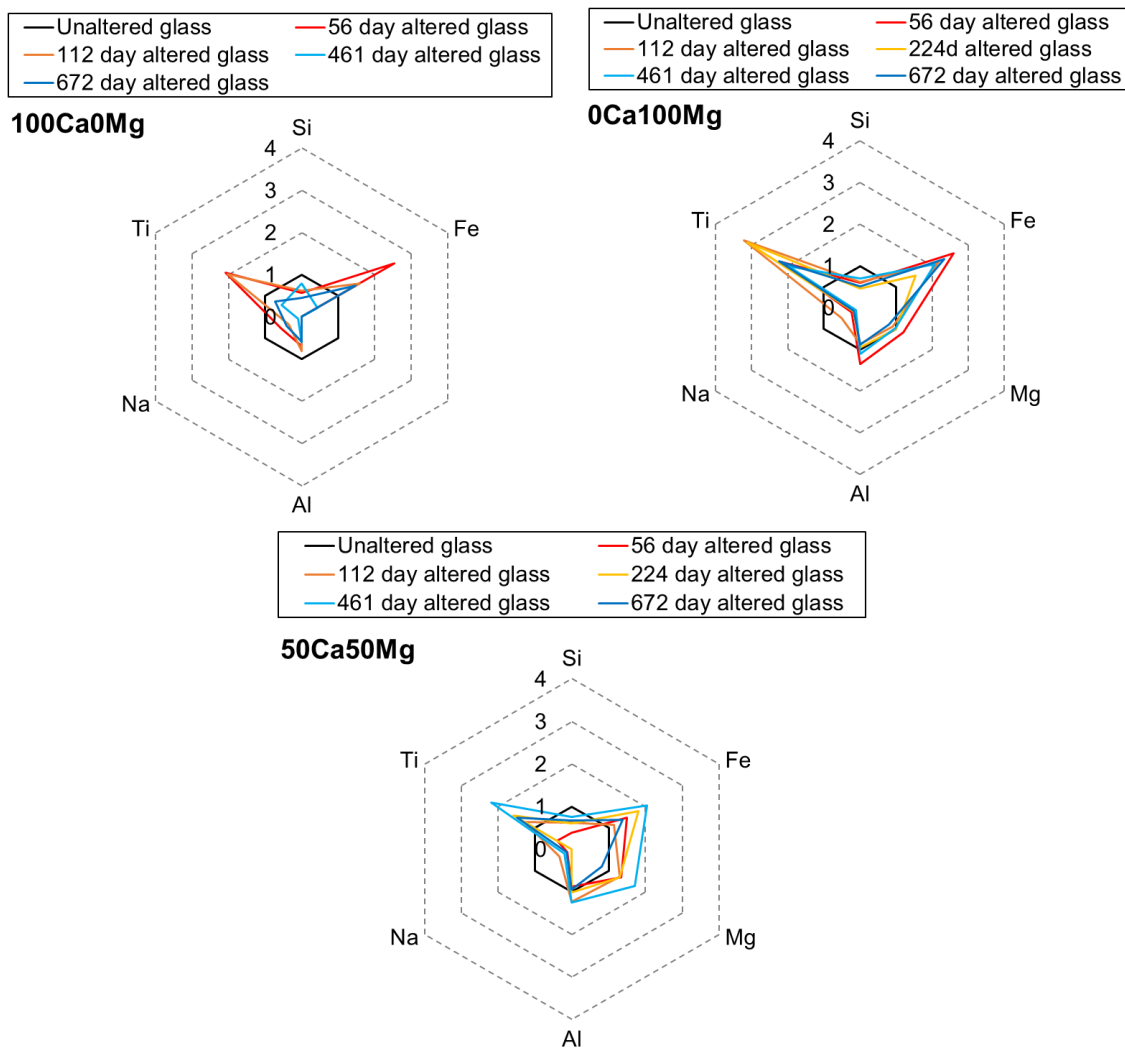


**Figure 5.11.** Surface layer compositions, as outlined in Table 5.2, recalculated as a proportion of the pristine glass: 100Ca0Mg (top left), 50Ca50Mg (bottom) and 0Ca100Mg (top right). Note that 100Ca0Mg glass contains no magnesium.

EDS maps of the ‘bright’ sub-layer observed in BSE reveal this to be further enriched in iron and titanium (Figure 5.12). Compositional quantification of this sub-layer was not possible owing to its slender nature and limited imaging resolution, however line scans (Figure 5.13) imply this region may contain up to 300% of the Fe and Ti content of the pristine glass (compared to ~200% of pristine values for the surface layer more generally). Figure 5.13 also indicates that there may be an additional sublayer, closest to the outer-edge of the main layer. This second sub-layer can be defined by a modest (~0.25%) enrichment in aluminium and magnesium relative to the surface layer as a whole.

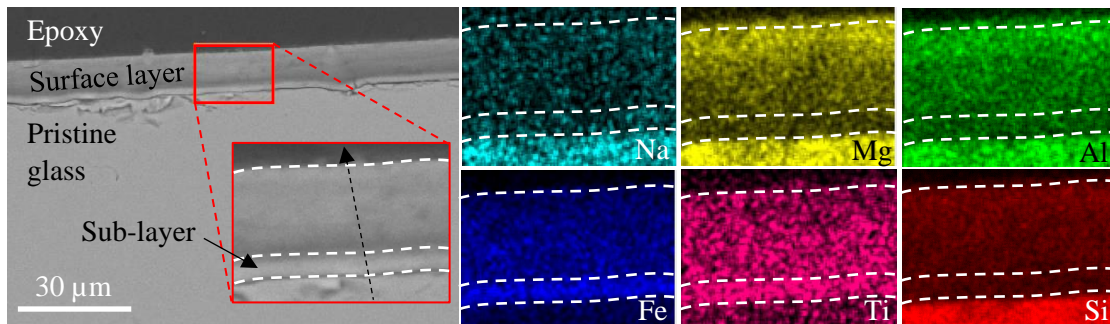


**Figure 5.12.** SEM-EDS map of a 0Ca100Mg basaltic glass monolith dissolved for 672 days. Note the presence of a thin Fe- and Ti-rich sub-layer proximal to the surface layer/pristine glass interface. Dashed arrow shows location of linescan shown in Figure 5.13.

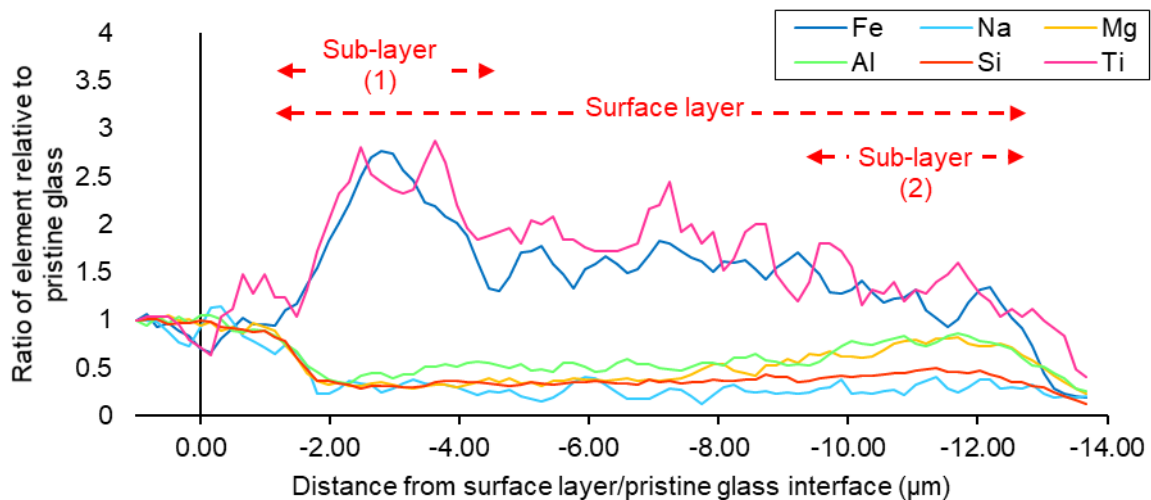


**Figure 5.13.** SEM-EDS line scan across the 672 day dissolved 0Ca100Mg basaltic glass monolith shown in Figure 5.12. Note the presence of a thin sublayer containing 250 - 300 % of the Fe and Ti content of the pristine glass.

EDS of the particles resting atop this layer (Figure 5.14) show these to be highly enriched in aluminium relative to the parent glass. SEM-EDS maps further reveal that these particles can penetrate *into* the surface layer. As well as aluminium, particles contain appreciable iron, silicon, magnesium and titanium in quantities estimated in Table 5.3.

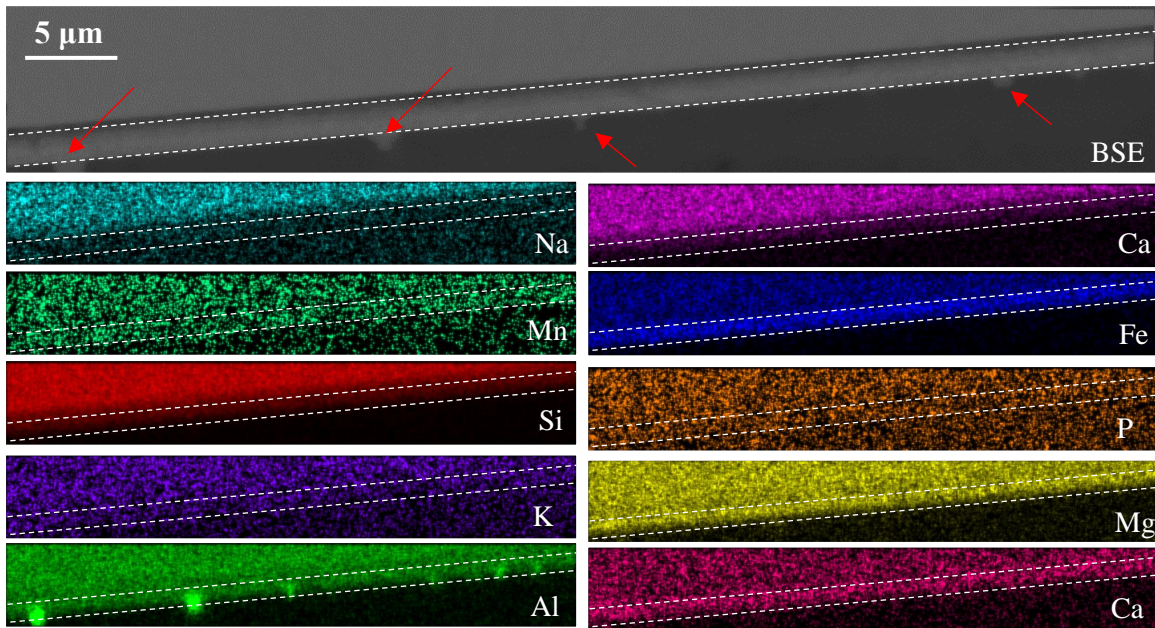


**Figure 5.14.** SEM-EDS image of a 50Ca50Mg basaltic glass monolith dissolved via the MCC-1 methodology for 112 days to show the aluminium enrichment and elemental contents of surface particles (arrowed in red).

Element	Wt. % (SD)
Al	14.02 (0.7)
Si	4.44 (1.06)
Fe	4.63 (2.06)
Mg	1.46 (0.93)
Ti	0.27 (0.15)

**Table 5.3.** Composition of particles shown in Figure 5.14. These particles are approximately representative of all other similar particles.

#### PCT-B/BSE

Figure 5.15 shows representative images from each basaltic glass composition dissolved via PCT-B. No continuous surface layer was observed on any composition, at any dissolution duration. Powders remain highly fractured, as also observed for pristine (undissolved) samples (Figure 4.1). Fractures are now also occasionally filled by fine fragments of a lower contrast ('darker') material, which also appears on some powder surfaces as shown in Figure 5.16. These particles are never present in laterally continuous layers thicker than 1 μm (the approximate resolution of EDS imaging). Aside from these darker discontinuous surface (or fracture-filling) layers, on some particles a discontinuous surface layer (~1-3 μm in width) was observed with a greyscale comparable to that of the glass is (Figure 5.17).

#### PCT-B/EDS

EDS of PCT-B powders revealed no significant compositional variation towards exposed surfaces and no compositionally significant features at the achievable resolution.

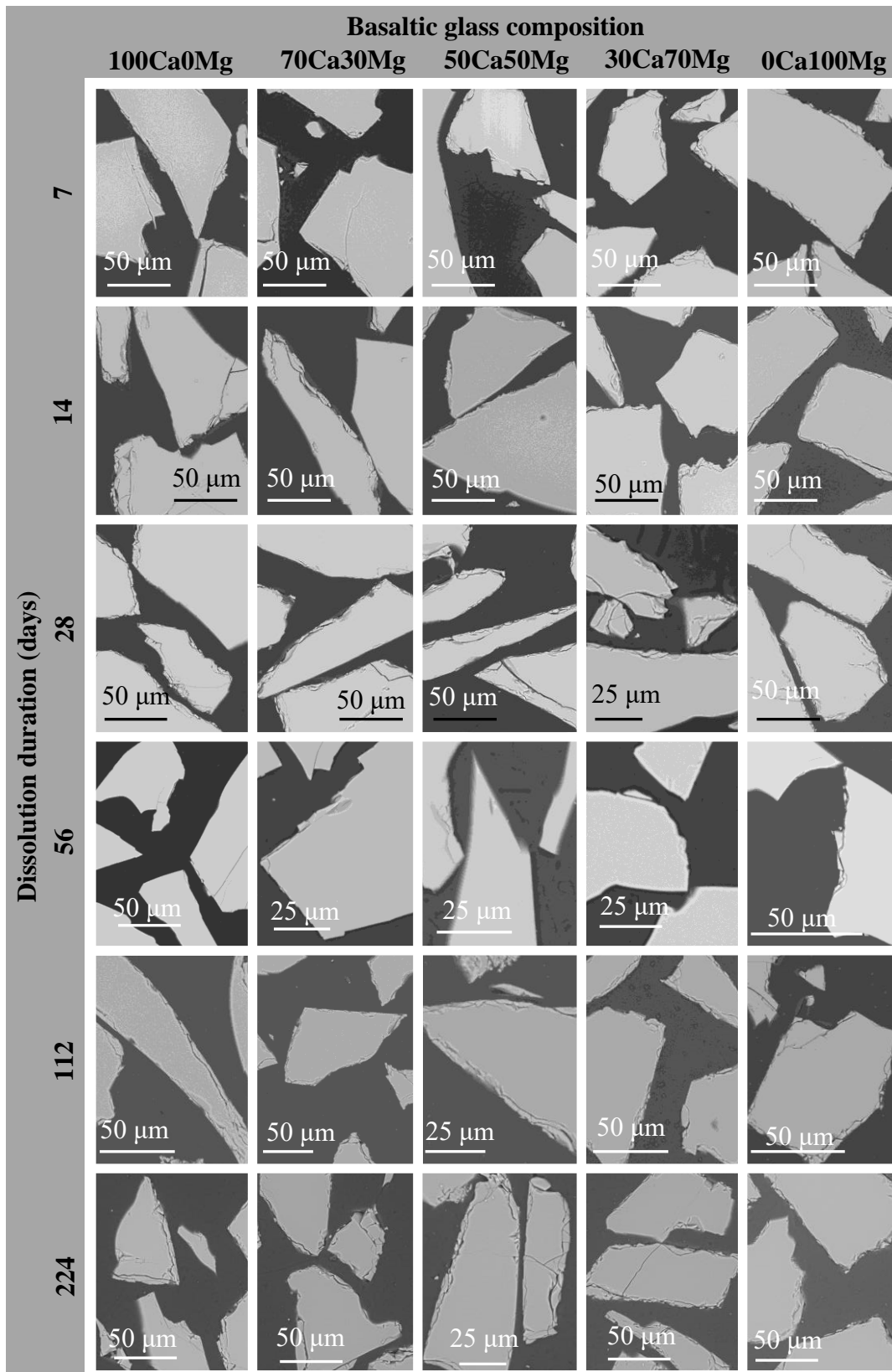


*Figure 5.15. SEM-BSE images of a basaltic glass samples after dissolution via PCT-B.*

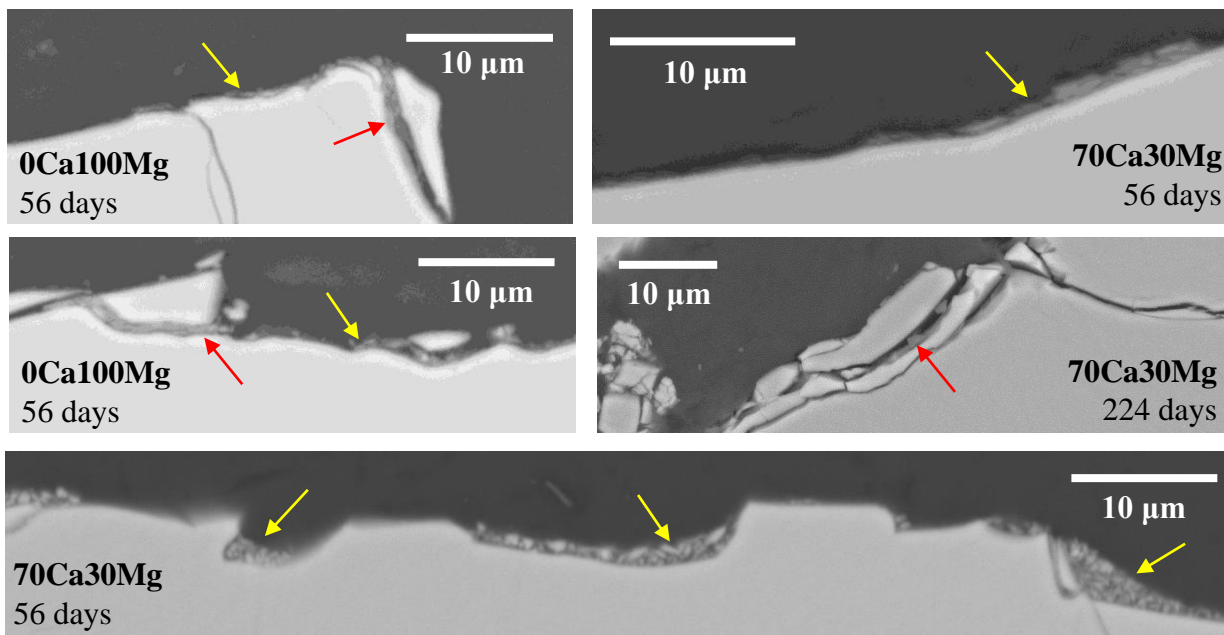


**Figure 5.16.** SEM-BSE images showing ‘darker’ material than the pristine glass in fractures (arrowed in red) and on surfaces (arrowed in yellow) of dissolved PCT-B powders from various timesteps and in various basaltic glass compositions.

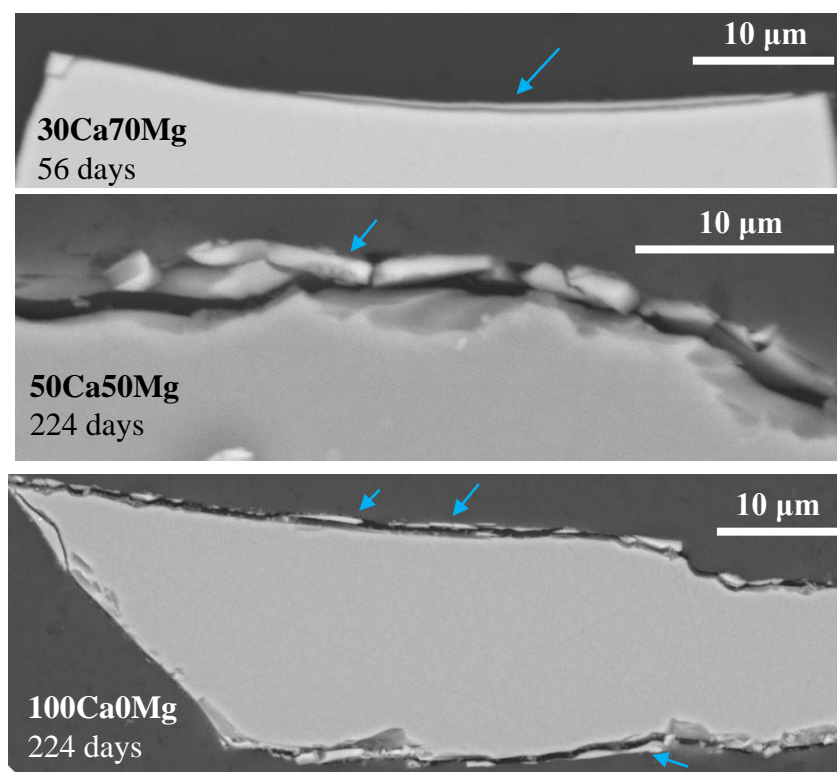


**Figure 5.17.** SEM-BSE images showing rare thin surface layer (arrowed in blue), with a similar greyscale to pristine glass, on some basaltic glasses (identified in inset text).

### 5.2.5. MCC-1 surface layer thickness analysis

Results from the analysis of surface layer thickness via the method outlined in Chapter 6 are shown in Figure 5.18. Low magnesium samples consistently have the lowest layer thicknesses, with this layer remaining approximately the same thickness (0.8 – 1.8  $\mu\text{m}$ ) for the entire test duration. The highest magnesium samples (0Ca100Mg) typically have the thickest surface layers, with this thickness increasing approximately logarithmically or potentially linearly to  $\sim 10 \mu\text{m}$  after 672 days of dissolution. The 50Ca50Mg samples typically have intermediate thicknesses, however the thickness of this layer is closer to (and often within error of) the magnesium-free end member. These 50Ca50Mg samples also show relatively constant surface layer thickness (of 1.5 to 2.6  $\mu\text{m}$ ) with dissolution duration. This implies that after formation, further growth of the surface layer only occurs when the pristine glass contains magnesium and does not contain calcium.

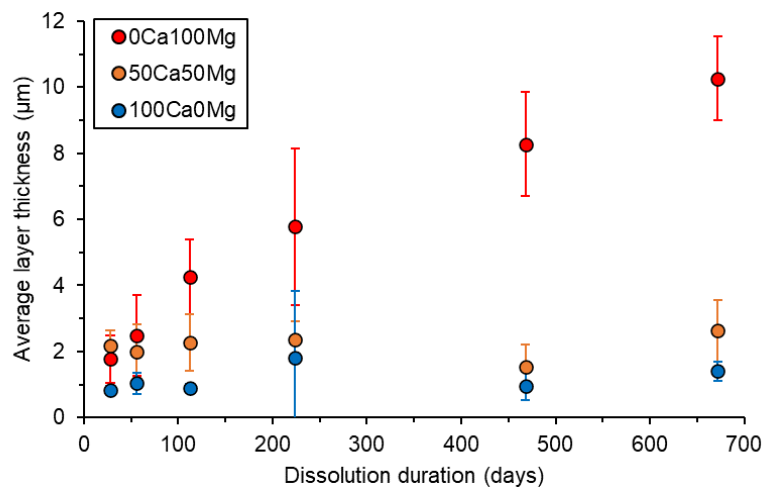


**Figure 5.18.** Observed trends in surface layer thickness in SEM-BSE images taken following of basaltic glass dissolution via the MCC-1 procedure.

### 5.2.6. XRD

XRD of basaltic glasses dissolved via the PCT-B method for 224 days (Figure 5.19) show the same broad peaks and region of diffuse scattering as observed in undissolved glasses (compare to Figure 3.1). No new peaks or features were observed in any post-dissolution XRD.

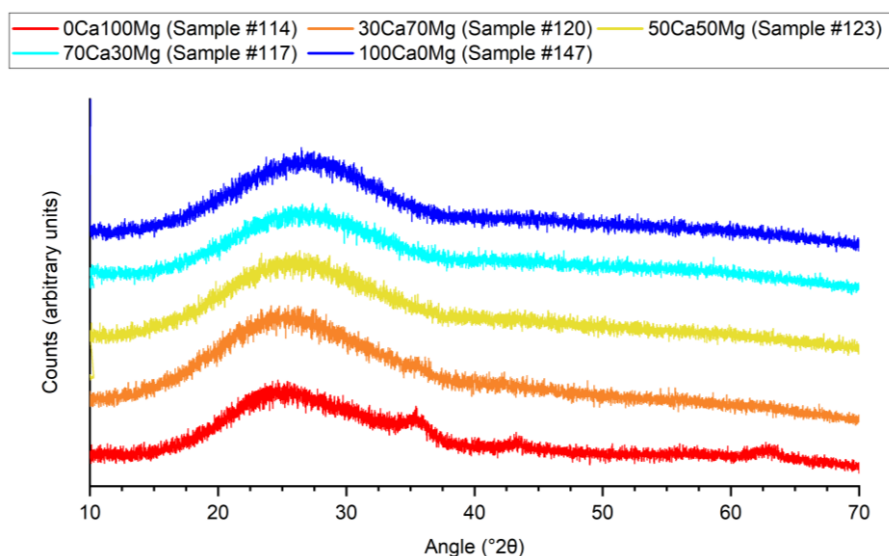


**Figure 5.19.** XRD of variable Mg:Ca basaltic glasses after 224 days of PCT-B dissolution.

### 5.2.7. XCT

#### *MCC*

In some localities, a surface layer was observed to have detached from the dissolved basaltic glass monoliths in XCT images (Figure 5.20). This layer was similarly or occasionally slightly less attenuating than the ‘parent’ glass, implying it was a similar if not lower density than the glass itself. Only a single basaltic glass composition (50Ca50Mg) was studied in XCT, so no compositional dependency in alteration layers properties can be determined from these data.

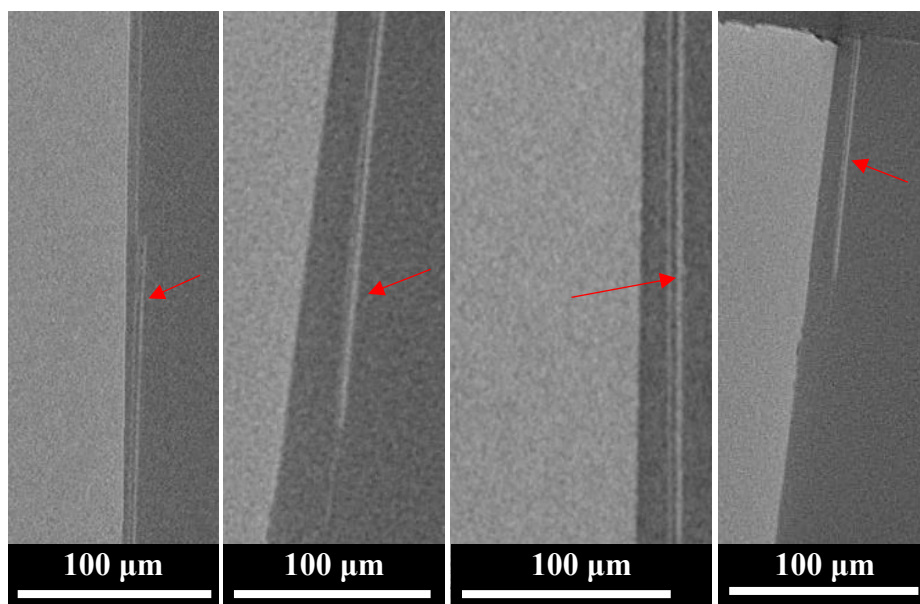


*Figure 5.20. XCT of a 50Ca50Mg basaltic glass monolith dissolved via the MCC-1 procedure for 672 days. Note the surface layer (arrowed in red).*

#### *PCT*

No significant surface features were observed in XCT of dissolved PCT-B powders (including those dissolved at elevated temperatures of 90 °C for almost one year, as in Figure 5.21). No alteration layers were found and no evidence of significant fracturing at the grain edges (as observed in SEM) was observed. In some datasets a subtle increase in attenuation (i.e. an increase in voxel brightness and inferred density) may be tentatively observed towards particle surfaces, however this is extremely subtle and is interpreted as a phase-contrast-like artefact.

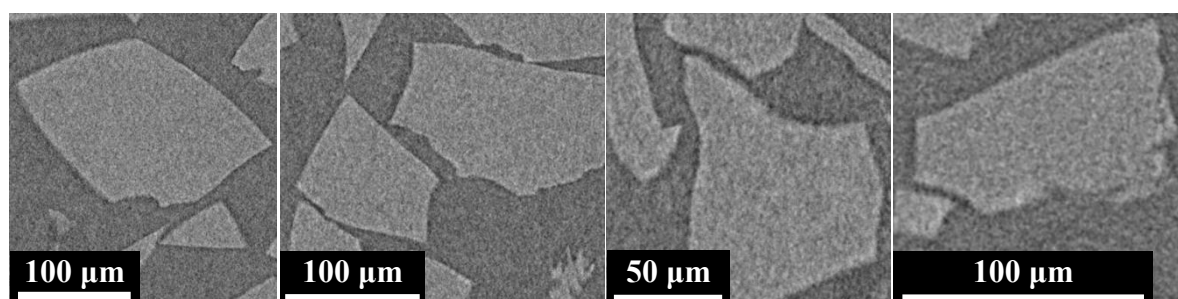


*Figure 5.21. XCT of 50Ca50Mg basaltic glass dissolved for 353 days via the PCT-B procedure at 90 °C. A similar lack of notable features was observed in all other scanned PCT-B samples.*

## 5.3. Discussion of Results

### 5.3.1. Pre-dissolution characterisation

XRD shows all glasses to be predominantly amorphous prior to dissolution. However, both XRD and Raman data imply the presence of an additional (partially-)crystalline component in magnesium-rich glasses. Analysis of Raman and XRD data (Figure 5.22) imply this component may be a pyroxene-type mineral similar to diopside.

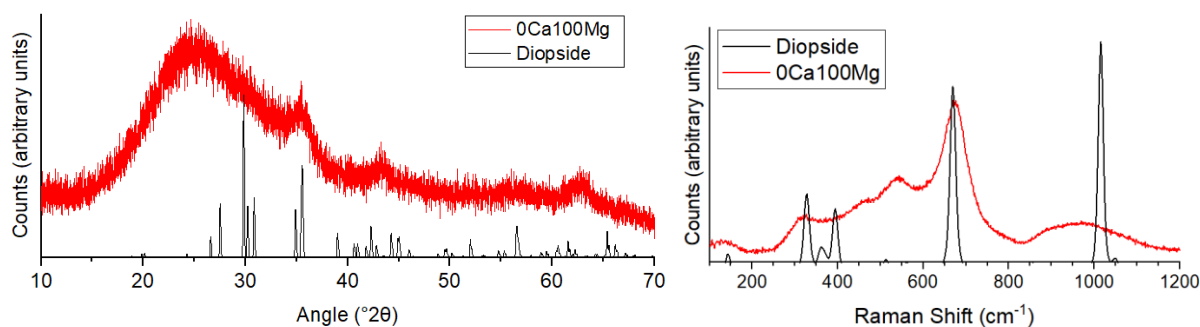


**Figure 5.22.** Comparison of undissolved 0Ca100Mg basaltic glass and diopside in XRD (left) and Raman spectroscopy (right).

The dominant Raman peak evident at  $675\text{ cm}^{-1}$  is commonly associated with the Si-O bending mode (at  $600 \pm 90\text{ cm}^{-1}$ ) and/or the Si-O stretching modes (at  $650\text{-}750\text{ cm}^{-1}$ ) of bridging oxygen atoms in pyroxene minerals [263], [264]. Though this is not the highest intensity peak typically evident in Raman of pyroxenes, relative peak intensities of the basaltic glass samples may be distorted by the more dominant amorphous contribution resulting from the glass. Similarly, otherwise sharp crystalline peaks evident in XRD and Raman data may be broadened by the limited crystallinity of this additional phase.

Pyroxenes (including diopside) have similarly been observed in XRD of the geological basaltic glass used as ‘base-glass’ herein [265]. Glass-ceramics containing diopside, known as *sitalls*, are also commonly used as an inexpensive though durable construction materials derived from blast furnace slags [266]. These minerals may be unresolvable in pre-dissolution SEM images owing to their limited size, as has also been noted to occur in electron microprobe analysis of other basaltic glasses containing pyroxenes [267].

The presence of this mineral, even in micro-crystalline form, may affect dissolution rates. However, the low peak intensities suggest that the amount of crystalline material present is very small and thus its affect is also likely to be small.

The significant damage observed around the perimeter of undissolved (Figure 4.1) and dissolved (Figure 5.15) powder samples must result from sample preparation and not dissolution. As for HLW glasses (Section 4.3.1), this may have arisen during powder production (by percussion) and/or during epoxy-mounting (involving potentially abrasive mixing). XCT data of powders which were produced via the same method but were *not* mounted in epoxy showed no surface fracturing, supporting the hypothesis that these features must result from the epoxy mounting process.

### 5.3.2. MCC-1 experiments

Observed trends in the pH data (Figure 5.4) are to be expected for dissolution of glasses containing appreciable alkali/alkaline elements. During the initial stage of glass dissolution, these ions are rapidly released into the leachate, increasing its pH, in order to preserve charge neutrality as water species diffuse into the glass. This pH rise can be inferred from pH data if it is assumed that leachant pH prior to dissolution was circa neutral, as expected for pure water. This pH is expected to remain high, as observed, as alkali elements remain in the leachate.

In the normalised mass loss data, sodium values are hypothesised to be a reliable marker of glass dissolution given that EDS evidence suggests it is not significantly retained within the alteration layer. Furthermore, sodium normalised mass losses show similar trends to lithium which is similarly unretained in alteration products. Sodium is also frequently used as a so-called ‘tracer’ element, in the absence of boron, in other studies [232].

Based on sodium normalised mass loss data, all basaltic glasses (regardless of magnesium content) are interpreted to show the same dissolution behaviour: a period of initial rapid dissolution lasting up to 224 days is followed by slower ‘residual’ dissolution that continues until the test termination. No rate resumption is observed for any glass. Based on this  $NL_{Na}$  data and an ‘initial rate’ duration of 224 days, initial and residual dissolution rates can be calculated as in Table 5.4 and Figure 5.23. However, these values do not represent true forward dissolution rates, given that alteration layers were observed in SEM images of these timesteps, and the potential for solution feedback effects. In the latter, the solution chemistry adjacent to monolith can be altered by dissolution and this altered solution may impact further dissolution and therefore solution chemistry etc. Regardless of this, rates are of comparable magnitude to those calculated for basaltic glasses dissolved, via MCC-1, in highly alkaline conditions [60].

	$(g\ m^{-2}\ d^{-1})$		
	100Ca0Mg	50Ca50Mg	0Ca100Mg
<b>Initial dissolution rate</b>	0.0222	0.0344	0.101
	$\pm 0.0065$	$\pm 0.0109$	$\pm 0.0202$
<b>Residual dissolution rate</b>	-0.00968	0.00787	$-3.28 \times 10^{-4}$
	$\pm 0.00107$	$\pm 0.00127$	$\pm 0.0123$

**Table 5.4.** Dissolution rates (in  $g\ m^{-2}\ d^{-1}$ ) calculated on the basis of  $NL_{Na}$  data and an ‘initial rate’ duration of 224 days. Negative rates are effectively zero within experimental uncertainty.

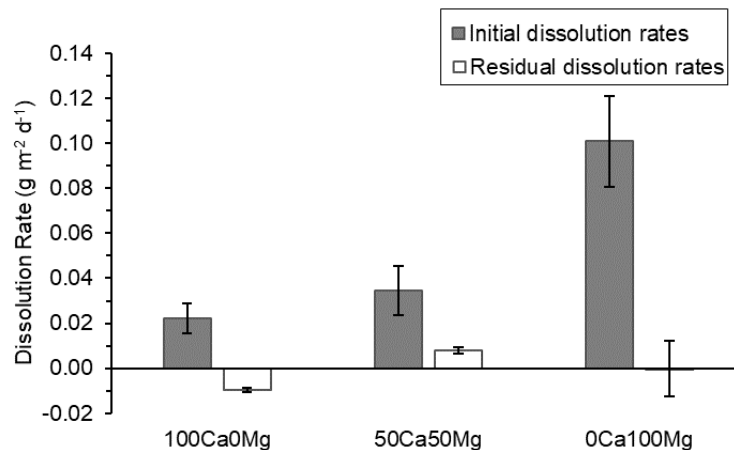


**Figure 5.23.** Comparison of initial and residual rates calculated for this study. Negative rates are considered to be effectively zero within experimental uncertainty.

These data suggest that increasing magnesium content (and/or decreasing calcium content) may increase initial dissolution rates; decreasing glass durability overall. This correlation is widely reported in other studies [31], [42], [48], [54], [60], however is more commonly observed at higher SA:V (e.g. PCT-B experiments) [64].

The observed positive correlation between magnesium content and dissolution rates may result from increased propensity for mineral precipitation in magnesium-rich leachates [31], [42], [48], [54], [60]. Aluminous hectorites have been identified by other authors as one such mineral which is more likely to precipitate more readily with increasing magnesium contents [54]. Hectorite is also often observed as secondary alteration product of (crystalline) basaltic lava flows [268].

A greater propensity for precipitation of aluminous minerals, such as aluminous hectorites, in magnesium-rich glass compositions may be seen in the normalised mass loss data.  $NL_{Al}$  values decrease more rapidly and earlier for high-magnesium basaltic glasses and  $NL_{Mg}$  values also imply the consumption of magnesium from the solution, potentially in order to form precipitates. Normalised mass loss values for silicon do not show the same decreasing trend potentially as the release of silicon into solution, caused by dissolution, is more dominant than the consumption of silicon to form precipitates.

Compositional analysis of the surface particles (via SEM-EDS; Table 5.3), revealed an enrichment of aluminium alongside the presence of silicon, iron, magnesium and titanium. This would also support the interpretation of hectorite precipitates given the typical compositions of this mineral shown in Table 5.5. Similarly, optical observations made during sampling are also consistent with aluminous hectorite precipitation: A translucent, white/cream foliated material with an earthy to waxy lustre was observed at the waterline of vessels containing 0Ca100Mg basaltic glass. This was notably absent in vessels containing lower-magnesium glasses. This material conforms to the mineralogical description of hectorite [269], but was not present in sufficient quantities and was too delicate to allow XRD or further analysis.

Oxide	Wt. %
SiO <sub>2</sub>	53.95
TiO <sub>2</sub>	Trace
Al <sub>2</sub> O <sub>3</sub>	0.14
Fe <sub>2</sub> O <sub>3</sub>	0.03
MgO	25.89
CaO	0.16
Li <sub>2</sub> O	1.22
Na <sub>2</sub> O	3.04
K <sub>2</sub> O	0.23
H <sub>2</sub> O	14.9

**Table 5.5.** The composition of (non-aluminous) hectorite [269]. Aluminous hectorite is:  $Na_{0.52}(Mg_{2.47}Li_{0.12}Al_{0.11}Fe_{0.01}M_{0.29})(Si_{3.45}Al_{0.55}O)_{10}(OH)_2$ , where  $M = \text{trace cation}$  [54].

This hypothesised difference in mineral precipitation propensity with differing Mg:Ca ratios may also be evident in SEM data, however insufficient occurrences were observed to allow statistical analysis and verification of this. Though geochemical modelling could possibly provide support for the formation of this mineral, the solubility product and other relevant data for hectorite is absent from many thermodynamic databases, as lamented by other authors [270].

The precipitation of hectorite or any other mineral requires elemental consumption from the solution, glass and/or alteration layer. The latter seems plausible given that EDS quantification of surface layer compositions show a subtle decrease in aluminium contents with dissolution duration for 0Ca100Mg samples, but not for 100Ca0Mg samples. Such aluminium consumption may degrade the alteration layer's passivation ability and thereby allow the greater dissolution rates observed for higher magnesium glasses. As a cross-linking element within glass alteration layers [271]–[273], increased aluminium within the gel layer is known to be able to enhance passivation [274]. This may occur as the tetrahedral bonding [62], [273] and charge balancing requirements of aluminium in glass alteration layers hinders alkali motion through the gel [275]. Decreased aluminium within the alteration layer may also prevent restructuring of the altered layer which would otherwise lead to increased passivation [275].

The silicon required for secondary phase precipitation may also be sourced from the gel layer, degrading its passivation ability [61]. Silicon might also be gained from the leachate – increasing the chemical driving force for dissolution [42]. The  $NL_{Si}$  values actually imply *higher* silicon concentrations in the leachates of high-magnesium (0Ca100Mg) glasses. This may be because the increased release of silicon into solution, caused by increased dissolution, is more dominant than the consumption of silicon to form precipitates. Silicon may also be sourced from the glass itself – directly catalysing its dissolution [31].

The role of calcium content variability in these experiments must also be considered. The decrease in dissolution rates with decreasing magnesium content may result from the coincident *increase* in calcium. Though the role of calcium on glass dissolution is highly dependent on alteration conditions [71], studies suggest that in high-pH systems, calcium promotes the formation of a protective calcium-silicate film during the initial phases of dissolution [71], [276]–[279]. In aluminoborosilicate glasses, increased calcium is similarly correlated with decreased residual dissolution rates via the resulting increased propensity for calcium-silica gel layer formation [70], [232], [280]. Calcium incorporation into this layer is often associated with a gel layer densification (decrease in pore size) and thus increased passivation ability [82], [91], [223], [232], [233], [280], [281]. These effects may be evident in the present experiments. A calcium-containing film was observed to form within 28 days of dissolution (via the MCC-1) of the high-calcium basaltic glass. This layer may be absent in other compositions and may be more passivating, thanks to a greater density, than the thicker (lower density) alteration layer developed on high-magnesium glasses.

### 5.3.3. PCT-B experiments

Trends in the pH data for PCT-B experiments (Figure 5.4) are comparable to those observed for MCC-1, with an initial rapid rise inferred to occur prior to the earliest sampling duration as alkali/alkaline ions are rapidly released into the leachate.

Continuing the use of sodium or lithium as an indicator of glass dissolution allows assessment of the behaviour of glasses dissolved via the PCT-B method. Assuming normalised mass losses are initially zero reveals an initial rapid increase, which cannot be characterised due to lack of shorter duration experiments, to a plateau. This constant normalised mass loss continues until day 56 or day 14 depending on if sodium or lithium is utilised as the ‘tracer’ respectively. Beyond this, normalised mass losses then re-increase approximately linearly from 14/56 days to the test termination. This behaviour is characteristic of transition from Stage I dissolution (forward dissolution rates; from zero to seven days of experiment duration) through Stage II (residual rates; from 7 to 14/56 days of dissolution) and into Stage III (resumption rates; from 14/56 to 224 days of dissolution). This allows the calculation of the rates shown in Table 5.6 and Figure 5.24.

	Dur- ation	100Ca 0Mg	70Ca 30Mg	50Ca 50Mg	30Ca 70Mg	0Ca 100Mg
<b>NL<sub>Na</sub> residual rate</b>	7-56 days	7.33E-05 (7.49E-05)	5.28E-05 (4.39E-05)	8.69E-05 (7.07E-05)	1.42E-04 (5.52E-05)	7.73E-05 (4.95E-05)
<b>NL<sub>Li</sub> residual rate</b>	7-14 days	-1.76E-05 (N/A)	-1.20E-04 (N/A)	-7.15E-05 (N/A)	-1.06E-04 (N/A)	-1.51E-04 (N/A)
<b>NL<sub>Na</sub> resumption rate</b>	56-224 days	1.76E-04 (5.65E-05)	1.96E-04 (5.29E-05)	5.69E-04 (4.93E-05)	4.10E-04 (3.39E-05)	5.05E-04 (7.44E-05)
<b>NL<sub>Li</sub> resumption rate</b>	14-224 days	2.09E-04 (2.10E-05)	2.26E-04 (2.29E-05)	6.20E-04 (6.73E-05)	5.12E-04 (5.30E-05)	8.74E-04 (4.39E-05)

**Table 5.6.** Dissolution rates (and errors on these values) calculated on the basis of sodium (NL<sub>Na</sub>) and lithium (NL<sub>Li</sub>) normalised mass losses in PCT-B experiments. Negative rates are considered to be effectively zero within experimental uncertainty.

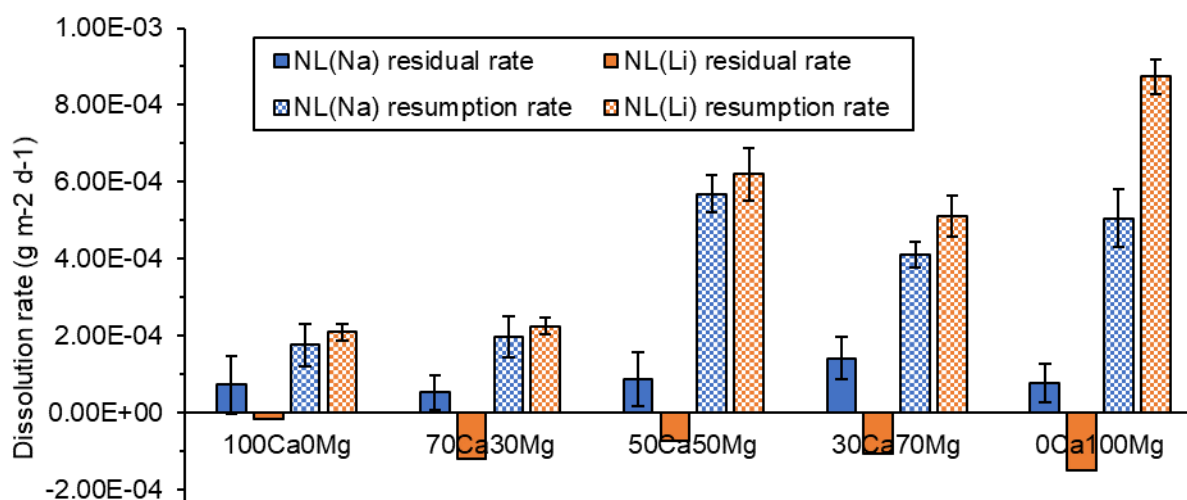


**Figure 5.24.** Dissolution rates as calculated in Table 5.6. Negative rates are considered to be effectively zero within experimental uncertainty.

The calculation of differing rates on the basis of sodium than lithium normalised mass losses may imply that one or both of these elements is a poor tracer of overall glass dissolution. Lower rates calculated on the basis of  $NL_{Na}$  compared to rates based on  $NL_{Li}$ , as consistently observed for resumption rates herein, have also been observed elsewhere [232]. In the latter study, lithium was deemed to be more reliable given that rates based on lithium were similar to those based on the  $NL_B$ , which is widely considered more reliable. However, boron cannot be used as a benchmark in basaltic glasses. Given the clarity of trends based on lithium and sodium in MCC-1 experiments and the compositions of likely precipitates/surface layers discussed previously, these elements likely remain the most representatives of overall glass dissolution in PCT-B.

Little to no consistent trend is observed between residual dissolution rates and magnesium-to-calcium ratio in basaltic glasses, though rates appear highly-dependant on which tracer element is used. However the reliability of this data may be questioned given the magnitude of errors compared to absolute values (for  $NL_{Na}$  data), the reliance on just two data points (for  $NL_{Li}$ ) data and the inconsistencies in Stage II duration depending on tracer element. This high uncertainty may aid in explaining why residual rates based on sodium normalised mass losses are one to two orders of magnitude lower than the equivalent rates estimated for basaltic glasses dissolved via PCT-B in alkaline conditions [60]. Regardless of this, residual rates appear to remain at or around zero regardless of magnesium to calcium ratio. This is consistent with results from MCC-1, where residual dissolution rates fluctuated around zero (though fluctuations in MCC-1 were of two orders of magnitude greater than those in PCT-B) with no consistent compositional dependence observed. In terms of *absolute values*, residual rates for PCT-B appear one to two orders of magnitude lower than the equivalent residual rates calculated for MCC-1 experiments. This discrepancy has similarly been noted by others [60], [82] and occurs in spite of normalisation to the differing SA:V values for both experiments. This may result from the lower temperatures used in PCT-B (50°C for PCT-B compared to 90°C for MCC-1), or may be related to differing feedbacks in both experiments.

Resumption rates calculated on the basis of  $NL_{Na}$  are generally within error of those calculated for  $NL_{Li}$  (for all except the 0Ca100Mg samples), arguably providing these data a greater reliability. These data show a consistent increase in Stage III dissolution rates (decrease in durability) with increasing magnesium contents. This is similar to the trend observed more clearly and for *initial* dissolution rates in MCC-1 experiments and is consistent with higher  $NL_{Li}$  values with increasing magnesium content for any given timestep. Resumption and initial rates are known to be comparable to data elsewhere [38], [39], so similar compositionally-dependant trends are not unexpected.

The only exception to this negative correlation between magnesium content and basaltic glass durability is evident in the 30Ca70Mg sample, which unexpectedly appears modestly *more* durable (with a lower resumption rate) than the 50Ca50Mg composition. Such a subtle trend, if true, would not be evident in MCC-1 data where intermediary compositions (30Ca70Mg and 70Ca30Mg) were not studied. However, this detailed trend may lack significance in PCT-B data: with many of the high-magnesium glasses having  $NL_{Na}$  values for a given timestep within error of each other.

Though the similarity with trends in MCC-1 data makes it tempting to invoke similar explanative mechanisms for the observed decrease in durability with increasing magnesium content, caution is required. Similar results are not necessarily expected given the different SA/V ratio of both techniques and the previously-noted reversal of the effect of magnesium depending on this (see Figure 2.2). Furthermore, little persuasive evidence exists for the presence of alteration layers in these PCT-B experiments.

The reliability of this PCT-B method must be carefully evaluated given that previous studies have noted intended SA/V values may differ from the *achieved* SA/V in these tests [53]. This may arise due to particle agglomeration during testing, as noted by many other investigators [64], [232], [236] and as may be under-reported given it can be noted purely anecdotally [53]. This effect was likely significant in the present study, where powders were observed to have coalesced into a solid puck mirroring the size/shape of the test vessel upon drying post-dissolution. This agglomeration may result from the growth of secondary alteration products (including precipitates or gel layers) between particles [53], [236].

Such particle agglomeration will partially-invalidate normalised mass loss data. The reduced surface area exposed to the leachate, relative to the intended surface area, would result in lower dissolution rates and normalised mass losses [232]; as the available surface for attack is reduced and both values are normalised to SA/V values which are assumed to be higher than they truly are. This effect is hypothesised to be the dominant source of  $NL_i$  error in other PCT-B tests [64] and may explain why the present data is order of magnitude lower than that in [60]. Particle agglomeration may also hinder equilibration of interstitial water with the bulk leachate as intergranular porosity is reduced [53].

Particle adhesion may also explain the conspicuous absence of alteration layers in SEM data. The majority of imaged particles may have been within the core of the adhered mass, inaccessible to the bulk leachate. Furthermore, any alteration products developed before appreciable agglomeration or on exposed particles may have been disintegrated and removed during particle separation post-dissolution. This destructive process may have also disturbed, displaced or destroyed the secondary precipitates expected given the inferred rate resumption (typically associated with zeolite precipitation [16], [41]). Such damaged alteration layer fragments may explain the finely fragmented particles observed on grain surfaces/in fractures in Figure 5.16.

Though undocumented, speculated variability in the degree of agglomeration with magnesium content may further complicate result interpretation. Other studies imply particle agglomeration may be more problematic in calcium-rich solutions [53], [232], [253], implying lower magnesium basaltic glasses, with their corresponding higher calcium contents, may be more adversely affected by particle agglomeration than their higher magnesium counterparts. This could result from the morphology of the secondary precipitates developed: calcium-rich precipitates including Calcium-Silicate-Hydrates (C-S-H phases) may have longer more fibrous habits that are more prone to agglomeration than the equivalent Magnesium-Silicate-Hydrate (M-S-H) phases [60], [82].

## 5.4. Summary

Basaltic glass generally exhibits a dissolution behaviour dependant on experimental conditions. In monolith tests at high temperature and low SA/V values (MCC-1 experiments), all glasses show transition from the rapid Stage I dissolution to the more subdued Stage II of glass dissolution after ~224 days of dissolution. Subsequently, this ‘Residual Rate’ stage continues until at least 672 days of alteration. Contrastingly, in lower temperature and higher SA/V experiments (PCT-B), all glasses reach Stage II of glass dissolution within seven days of alteration and remain in this stage until somewhere between 14-56 days. Beyond this, basaltic glasses in PCT-B tests are hypothesised to enter an aggressive third stage of dissolution, sometimes known as “Rate Resumption”.

In MCC-1 experiments, magnesium-rich basaltic glasses appear to be less durable than their lower-magnesium counterparts. This is thought to be because the gel layer developed on magnesium-rich basaltic glasses, though thicker, is less protective than that developed on calcium-rich basaltic glasses. Such decreased passivation *may* result from a reduced aluminium content in the gel layer developed on higher magnesium glasses. Aluminium in these layers may be being consumed to form the secondary precipitates, potentially including hectorites, that are hypothesised to form more readily on higher-magnesium glasses. Consumption of the aluminium and silicon required to form these precipitates may also increase the chemical driving force for dissolution and/or directly catalyse degradation of the glass network. The higher calcium content in low magnesium basaltic glasses may also allow formation of a thin but higher-density and more passivating layer on low-magnesium basaltic glasses.

Results from PCT-B experiments were likely adversely affected by agglomeration of glass particles. Hence, any results from this experiment should be interpreted with caution, with results from MCC-1 tests deemed more reliable and informative. Regardless of this, the same trend was observed in PCT-B and MCC-1: Magnesium-rich glasses generally have a lower durability than their lower magnesium counterparts despite the differing (assumed) surface area to volume ratio of these experimental methods.

# 6. Surface Layer Thickness Quantification

## 6.1. Introduction

Alteration layers may be a crucial control in residual glass dissolution rates and processes [15], [20]–[23]. To allow comparison of these layers between samples and to gain insight into their growth, researchers often measure ‘alteration layer thicknesses’. However, identifying alteration layer boundaries can be highly subjective and measurement techniques can be time consuming, unreliable and variably ambiguous.

This chapter reviews previous layer thickness measurement techniques and presents a new methodology for surface layer thickness measurement. This new method is comprehensively described and evaluated, before results from this method and others are compared. Comparisons with longer-term natural experiments are also made in an effort to validate the extent to which laboratory methods can simulate natural processes.

## 6.2. Review of previous techniques and literature

Surface layer thickness is a crucial parameter in many studies [282], however the term “thickness” is so ubiquitous that rarely is it precisely defined. Definitions are, however, crucial and variability in these should be highlighted if only to emphasise the ambiguity in its usage. In technical drawing ‘thickness’ can be defined as the distance between points on two opposite *parallel* surfaces [283], whilst in more general dictionaries it may be defined as the minimum distance between two (opposite) surfaces [284]. Though the latter definition is broader (in that it does not stipulate the surfaces must be parallel), both definitions are ambiguous or even non-applicable to features with complex morphologies (e.g. tapered objects, or those with curved surfaces). Instead, perhaps the best definition for application to such morphologically complex objects (including glass alteration layers) is that thickness is “*the dimension through an object, as opposed to its length or width*” [285]. This definition appears most relevant in the current context, as it is movement (diffusion) of elements *through* the alteration layer that many believe controls residual glass dissolution rates [15], [20]–[23].

Regardless of definition, alteration layer thickness can be estimated or measured using either leachate (solution) data and/or direct observation of monoliths or samples.

### 6.2.1. Alteration layer thickness estimation via leachate analysis

Elements that are not involved in secondary phase or alteration layer formation (so called ‘tracer elements’) can be used to estimate alteration layer thicknesses via many proposed equations. For example, alteration layer thicknesses can be estimated directly from the concentration of these elements in the leachate [60], [286] using

$$AL_{Ci} = \frac{c_i}{\rho \times (SA/V) \times x_i} \quad \text{Equation 6.1}$$

where  $AL_{Ci}$  (in metres) is the alteration layer thickness,  $c_i$  is the (average) concentration of element  $i$  in solution (in  $\text{g m}^{-3}$ ),  $x_i$  is the elemental fraction of  $i$  in the initial glass composition (as a decimal-expressed percentage),  $\rho$  is the glass density (in  $\text{g m}^{-3}$ ) and  $SA/V$  is the sample Surface Area ( $\text{m}^2$ ) to leachant Volume ( $\text{m}^3$ ) ratio ( $\text{m}^{-1}$ ).

This equation can be derived by dividing the Normalised Mass Loss equation (Equation 3.5) by the alteration layer density ( $\rho$ ); a derivation that works on the basis that the mass per unit area ( $NL_i$ ) is divided by the mass per unit volume (density) to output a thickness (volume divided by area).

Alternatively, if leachate element concentration are unstated then alteration layer thicknesses ( $AL_{Ri}$ ; in  $\mu\text{m}$ ) can also be estimated using initial dissolution rates [82] via

$$AL_{Ri} = \frac{R_{initial}}{\rho} \times t \quad \text{Equation 6.2}$$

where  $R_{initial}$  is the initial dissolution rate ( $\text{g m}^{-2} \text{d}^{-1}$ ),  $\rho$  is the density of the glass ( $\text{g cm}^{-3}$ ) and  $t$  is the dissolution duration (in days).

All of the aforementioned methods crucially assume that no tracer element is retained in the alteration layer. Where this is untrue, these methods inevitably underestimate alteration layer thicknesses [60]. Equation 6.1 and Equation 6.2 further assume that the volume of the gel is the same as the volume of the altered glass and that both the glass and alteration layer is the same density [286]. This assumption has previously been shown unreliable [11], [47].

These techniques require only mathematical reprocessing of data necessarily collected for other purposes, so estimations can often be made rapidly with minimal difficulty. However, these methods also require assumptions that may appear to be rarely entirely true.

### 6.2.2. Alteration layer thickness estimation via imaging techniques

Alternatively, alteration layer measurement can be made by imaging dissolved glasses using microscopy or other imaging techniques (including XCT). As for techniques estimating thicknesses via leachate analysis, these techniques require various assumptions and do have limitations. For example, two dimensional imaging techniques (including SEM) require production of a sample cross-section which, in order to achieve accurate measurement, must be taken perfectly perpendicular to the sample surface being observed. Where this is not true, as presumably in many cases, alteration layer thicknesses measured via this technique will be overestimated [287], as shown in Figure 6.1. Though the overestimated alteration layer thickness ( $AL_{\hat{t}}$ ) can be corrected to provide the true thickness ( $AL_t$ ) using

$$AL_t = AL_{\hat{t}} \times \cos \theta \quad \text{Equation 6.3}$$

if the angle between the monolith surface and plane of section ( $\theta$ ) is known. In practice this is never performed because reliably determining the angle is near-impossible. These techniques are also limited by microscope resolution, much as leachate analysis techniques are limited by measurement sensitivity.

This assumption of a perfectly perpendicular cross section rarely holds true when powders (with inevitably irregular morphologies) are analysed, as in PCT-B experiments. Whether alteration layers generated in such experiments can be reliably measured and analysed remains debated. Some authors argue these layers cannot be accurately measured because of uncertainty in particle orientation [91], however others assume this is resolved by calculating an *average* layer thickness from multiple (randomly orientated) grains [82].

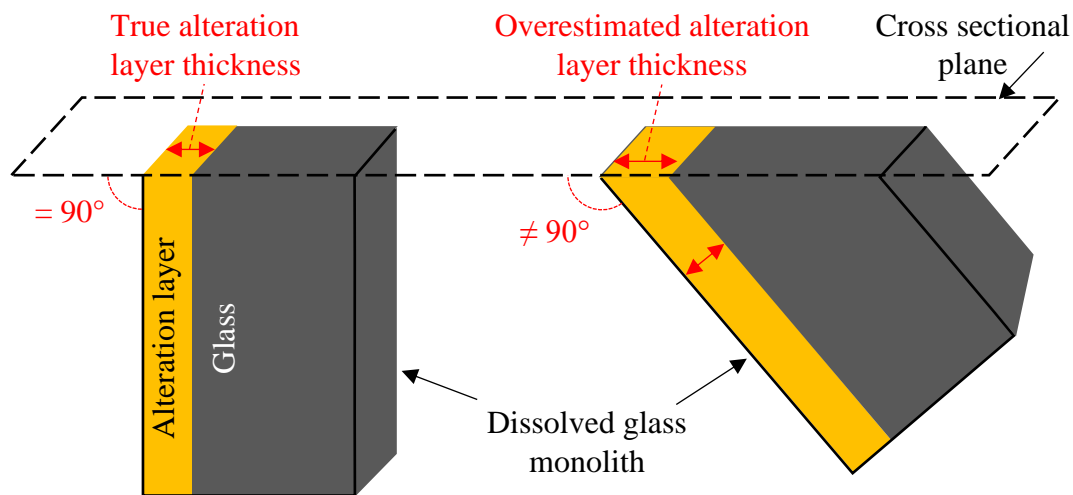


**Figure 6.1.** Overestimation of apparent alteration layer thickness where cross sections are not made perfectly perpendicular to monolith faces.

#### *Optical microscopy*

Direct alteration layer thickness measurement has been of interest to scientists and archaeologists since at least 1960 [288], when it was first recognised that these values may offer insight into the age of naturally dissolved glass samples [289]. Initially, measurements were made from petrographic thin sections of dissolved glasses using optical microscopy and a ‘filr micrometer ocular’ [289]. Even these earliest practitioners noted the challenges in this process – including in preparing sections, identifying the alteration layer/glass boundary and operator bias/inconsistencies in boundary identification [289]. These challenges remained even with advancements via the use of cross-polarized light, interference plates and split image micrometers [288].

Though many authors state measurement accuracies, using the above techniques, of circa 0.1  $\mu\text{m}$  [289]–[291] (down to 0.07  $\mu\text{m}$  in one case [292]) and that measurement errors may cancel out via the averaging of multiple measurements [293]; many argue these techniques have much more limited precision and accuracy [287], [294]. Sources of inaccuracies stem from variable microscope resolution, sample preparation methods [287], operator variability and variation in the optical properties of the layer [295]. Image analysis techniques, based on photodensitometry, have also been applied to optical photomicrographs [296], including as an attempt to minimise user-associated errors [297]; however even these techniques are adversely impacted by gradational (“fuzzy”) diffusion fronts [287], [297].

#### *Scanning Electron Microscopy*

Imaging via Scanning Electron Microscopy (SEM) overcomes many of these issues by allowing increased magnification and resolution along with the ability to analyse chemical variations indicative of the alteration layer/pristine glass boundary.

Authors, however give variably detailed descriptions of how thickness measurements are actually obtained from SEM images – ranging from next to no detail (e.g. [60]), through a detailed measurement methodology [91], and finally a full methodology including statistical

and sensitivity analyses [82]. This variation in detail can undermine result repeatability and can lead to ambiguity during reader interpretation.

In recognition that alteration layer varies across a single MCC-1 monolith face, multiple measurements are typically made on multiple images. For a single monolith edge, with a cross sectional distance of  $\sim 10$  mm, anywhere from ten [91] to more than fifteen [82] images can be considered to give representative results; with anywhere from 5 [91] to 40 [82] measurements taken from *each* image. However, the scale, magnification or field view of each images is never stated or even said to remain constant; with this instead implicitly assumed to be irrelevant.

Once images have been selected for analysis and the number of measurements per image chosen, alteration layers are identified (presumably subjectively and by eye). The thickness of these is then typically measured using image analysis software, such as *ImageJ*, to draw and measure a ‘line’ drawn from one edge of the layer to the other. Each ‘line’ is presumably orientated approximately perpendicular to either the alteration layer/epoxy boundary or the alteration layer/pristine glass boundary, however this orientation is never stated or verified as remaining constant. Further ambiguity is evident in the spacing of these ‘lines’, with no consistency stated.

#### *The Sphere and Ray Methods*

The aforementioned investigators implicitly use the ‘*Ray Method*’ of thickness quantification (Figure 6.2). In this, an imagined ‘ray’ (line) is passed (drawn) from one surface of an object to the other, with the Euclidean (straight line) distance between the two points where this lines intersects the object defined as its ‘thickness’ [284], [298]. To ensure accuracy, this ray must always be passed through the object in a direction precisely *opposite to the local outward normal* (i.e. *perpendicular* to the surface) [283]. In previous alteration layer measurement methods it is unclear as to whether this strict definition was consistently used, with ray orientations never stated or verifiably constant. Even if these rays *are* assumed to be consistently passed through the object perpendicular to a surface, further ambiguity arises when the two surfaces of this object are not parallel [283]. In this case, thicknesses will differ depending on which surface the measurement is taken perpendicular to as in Figure 6.2 [284]. This ambiguity and the variability allowed in user interpretations when applying the method, particularly when combined with the limited stated methodology detail, limit the repeatability and thus usefulness of the Ray Method, potentially undermining inter-study comparison.

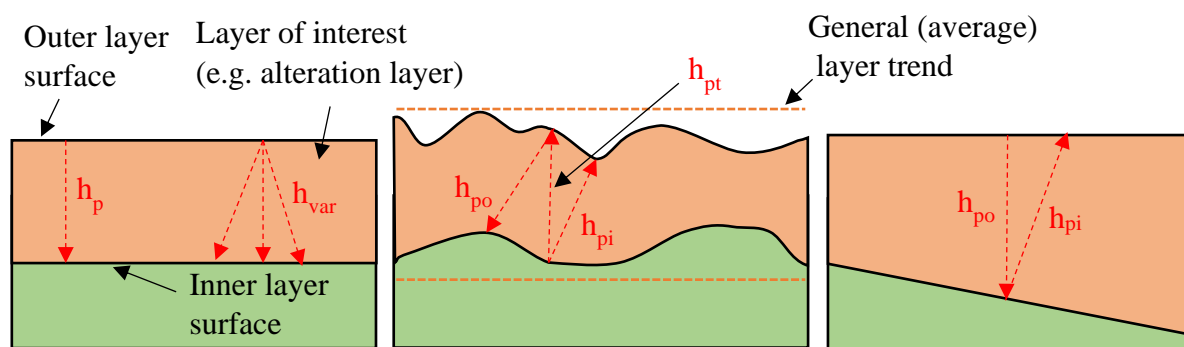


**Figure 6.2.** Variability in the thickness ( $h$ ) of a layer measured via the Ray Method with variable ray orientation ( $h_{var}$ ); or with rays orientated perpendicular to the inner surface ( $h_{pi}$ ), outer surface ( $h_{po}$ ) or general layer trend ( $h_{pt}$ )

The ‘*Sphere Method*’ of thickness definition (technically a ‘*Circle Method*’ when applied to 2D images; but nevertheless referred to as the sphere method for consistency throughout) resolves many of these ambiguities: returning consistent results regardless of operators. This method, shown in Figure 6.3, defines the thickness at a point as the diameter of the maximum inscribed sphere contacting both surfaces of the layer [283]. Ambiguity concerning ray orientations is removed because a sphere (or circle in 2D) will have an equal diameter in all directions. This further resolves complications arising when layers have non-parallel surfaces.

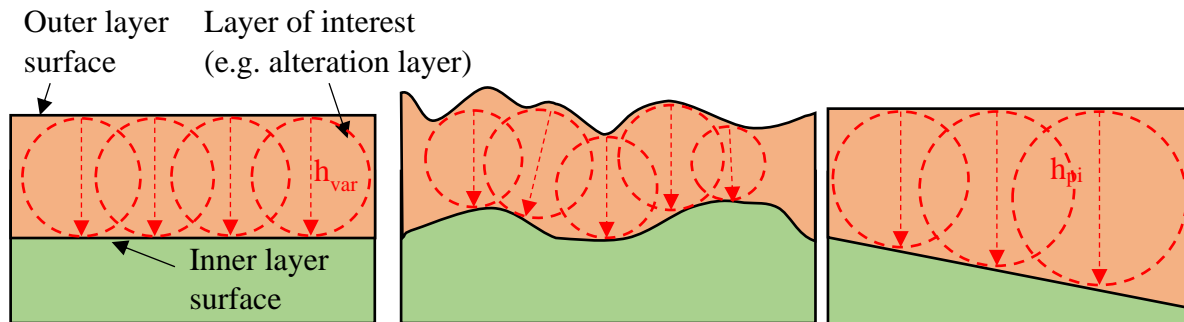


**Figure 6.3.** *The Sphere Method of layer thickness measurement resolves many of the ambiguities within the Ray Method (Figure 6.2)*

### 6.2.3. Alternative alteration layer thickness measurement techniques

Various other techniques have also been applied to measuring the thickness of altered layers. For example, Time-of-Flight Secondary Ion Mass Spectrometry (ToF-SIMS) and X-ray Photoelectron Spectroscopy (XPS) [13], [299], [300] can provide elemental profiles which are used to measure alteration layer thickness. Spectroscopic Ellipsometry (SE), can provide alteration layer thicknesses via the polarisation change that occurs as a beam is reflected from the surface or interface of a layer [301], whilst grazing incidence X-Ray Reflectometry (XRR) estimates alteration layer thickness using the phase difference/interferences between X-rays reflected from the alteration layer’s upper and lower surfaces [286], [302], [303].

Nearly all of these techniques use comparison with SEM-measured alteration layer thicknesses for either verification or calibration, potentially implying the latter is the most effective/reliable technique. Despite this, methods for measuring alteration layer thickness from SEM cross sections remain variable, unreviewed and often inadequately detailed to allow reproducibility.

### 6.3. Methods

*Dragonfly* software (produced by Object Research Systems) was utilised to implement the *Sphere Method* outlined in Section 6.2.2 in a semi-automated manner. Data segmentation and analysis was completed as below, with further image processing (optimisation of equalisation, brightness and contrast etc.) deemed unnecessary given the quality of ‘raw’ SEM images.

SEM photomicrographs were imported into *Dragonfly* as a single greyscale channel (i.e. with RGB channels assumed identical) with an 8-bit colour depth. Each pixel was thus automatically assigned a greyscale value from zero (black in SEM images, indicative of low atomic numbers) to 256 ( $2^8$ ; white in images, indicative of high Z elements). Pixel dimensions were manually entered to match the original image scale, with an image depth (Z) value arbitrarily set to 1  $\mu\text{m}$  for 2D SEM data. X-Ray computer tomography data were imported as a 16-bit greyscale TIFF stack with voxel dimensions automatically imported from accompanying metadata.

XCT and SEM images were segmented into between one and six discrete regions, as outlined in Table 6.1. Regions corresponding to surface layers were measured in terms of area and/or thickness, with the latter as measured via the Sphere and/or Ray methods. Area measurements were made for all regions in datasets where any single surface layer showed significant morphological complexity, because the Sphere Method was observed to show questionable reliability when measuring such complexity. The Ray Method was applied only to a single composition from a single MCC-1 dissolution duration (Table 6.1), because prior discussions revealed this to be time consuming and inconsistent/ambiguous; however comparisons to this method were still deemed worthwhile given its ubiquitous use elsewhere. XCT was only collected for a single composition at two timesteps because of the limited experiment time available and the challenges (and time) associated with sample preparation. Only the Sphere Method could be applied to these data because ambiguity in the Ray Method preclude its automated application and manual application would have been debilitatingly time consuming given the dimensions of the three dimensional dataset. Two-dimensional area measurements could not meaningfully be made for 3D XCT datasets.

	No. of regions	Measurement method	Data source	Dissolution duration (days)					
				28	56	112	224	468	672
3 Basaltic glasses	1 (1SL)	Sphere thick.	XCT	/	/	/	/	50Ca50Mg corner edge	
		Sphere thick.	SEM	--- One corner and one edge for each of three --- ----- compositions at each of six timesteps -----					
		Ray thick.	SEM	/	2x 50Ca	/	/	/	/
ISG	4 (3SL + 1P)	Sphere thick. Area	SEM	One image from corner and one image from edge ----- at each of six timesteps -----					
MW	6 (3SL + 25 1P, 2B)	Sphere thick. Area	SEM	Two images from two separate corners at each of ----- six timesteps -----					

**Table 6.1.** Collected surface layer thickness data for each glass type, including the number of regions segmented. SL refers to the number of individual Surface Layers identified, P refers to Pristine glass which was segmented and B refers to Bright regions. Sphere and Ray thickness measurement methods are described in-text.

### 6.3.1. Image segmentation

Segmentation involves partitioning an image/dataset into regions (referred to as “Regions Of Interest” or ROIs) which often correspond to different phases [304], [305]. This was achieved by thresholding: identifying a greyscale range (bound by ‘threshold values’) which entirely and exclusively encompasses all of the pixels within a region of interest. Thresholds for this were determined by scrutinising both raw SEM/XCT images and a histogram of the greyscale intensities contained in those images. More advanced (e.g. algorithmic) segmentation methods were also trialled, but these were not considered sufficiently robust or reliable to implement globally.

After thresholding, segmented regions were ‘pruned’ to remove anomalous (mis)identifications that arose due to edge blurring and image noise. So-called “data islands” of less than circa five pixels were filtered out as in Figure 6.4, with the boundaries of all segmented areas scrutinised and refined manually. Where multiple layers were present within a single image (e.g. for ISG and MW25 analysis), Boolean operations were also used to ensure no pixel was assigned to more than one ROI. Each pixel was thus only ever classified as one region, with no overlap.

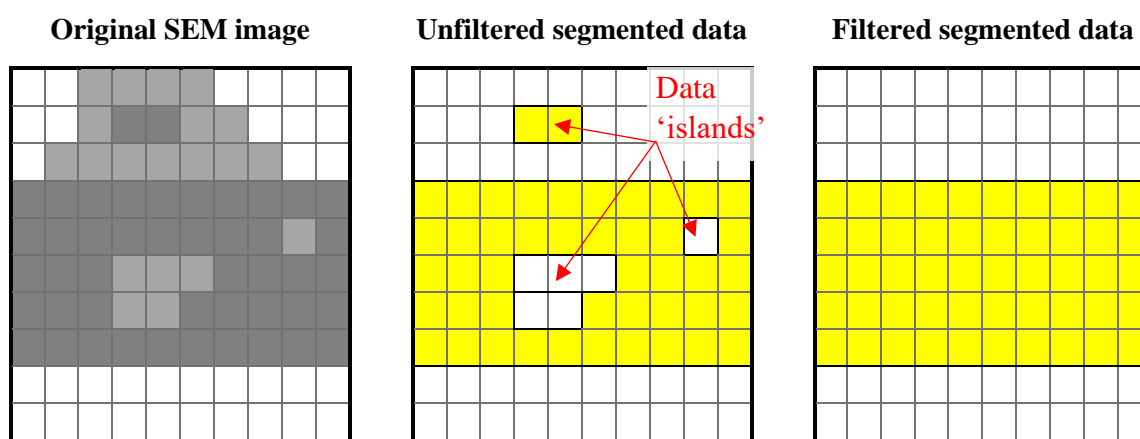


**Figure 6.4.** Schematic illustrating automated “island removal” process used to refine (filter) segmented regions

### 6.3.2. Image analysis

Image analysis involves measuring the constituent phases within an image [305]. Based on the above literature review, the Sphere Method of layer thickness quantification was deemed most reliable and consistent, hence this method was utilised in surface layer quantification for all datasets. Layer thicknesses were calculated by generating a ‘*Volume Thickness Map*’ for each ROI. This generates a dataset (with a bit-depth of six) displaying each ROI as a series of overlapping circles/spheres, with the greyscale value of each circle/sphere set to be proportional to the “local thickness”. The latter term is defined as the diameter of the largest sphere which both encloses the point and is entirely bound within the solid surfaces of a ROI [306]. A histogram of local thicknesses can be generated from this data.

This histogram, generated from a six-bit dataset, inevitably comprises 64 data bins with each ‘bin’ corresponding to a single greyscale (or ‘local thickness’) value. Occurrence frequency is, by default, expressed as a percentage of the total number of pixels within the ROI. This histogram is exported (as a .csv file) to allow further data processing as in Section 6.3.3.

Data concerning layer area (in 2D cross sections) was collected with ease from *Dragonfly*’s Graphical User Interphase (GUI). The number of segmented pixels within a ROI was noted and later processed to give absolute (cross sectional) area values as below. Use of this value, as opposed to software-calculated ‘volumes’ avoids any assumption of image depth.

### 6.3.3. Data treatment/analysis

To calculate surface layer areas, the number of pixels in a ROI was processed and re-expressed as a percentage of *all* labelled pixels (belonging to any ROI). Data were thus normalised to the total sample area visible in SEM (the total image area minus the area occupied by voids and epoxy). Areas were also re-expressed as cross sectional areas in microns by multiplying the number of pixels by the area of each pixel.

For the Sphere Method, the average diameter of fitted spheres (i.e. the average local thickness) was calculated from the local thickness histogram using:

$$\bar{x} = \frac{\sum(y_n \times \bar{y})}{y_n} \quad \text{Equation 6.4}$$

where  $\bar{x}$  is average layer thickness,  $y_n$  is the number of observations in data bin  $y$  and  $\bar{y}$  is the mid-point (mean) of bin  $y$ . The standard deviation on this value ( $\sigma$ ) is calculated as

$$\sigma = \sqrt{\frac{\sum[(\bar{x} - \bar{y})^2 \times (y_n \times \bar{y})]}{\sum(y_n \times \bar{y})}} \quad \text{Equation 6.5}$$

## 6.4. Results

### 6.4.1. Measurement location

Figure 6.5 shows a moderately strong one-to-one relationship between alteration layer thickness measurements made (via the Sphere Method) at the corners and edges of both ISG and basaltic glass monoliths. Standard deviations are relatively high for both measurement locations, particularly for ISG and at corners.

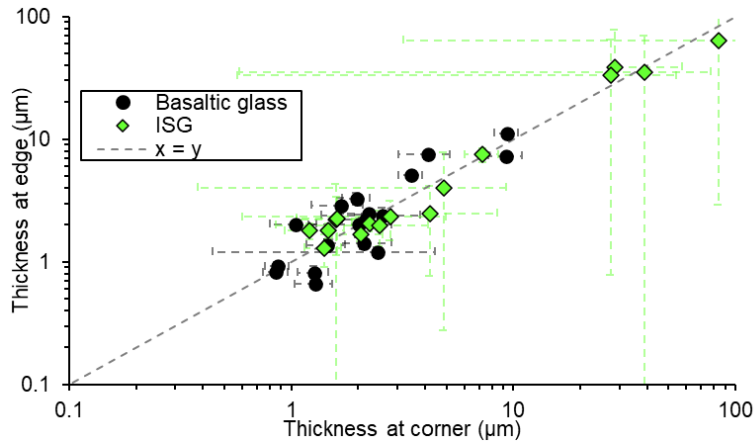


**Figure 6.5.** Comparison of alteration layer thicknesses as measured (via the Sphere Method) from the corner and edge of a single MCC-1 monolith. Data for basaltic glasses includes all compositions (0Ca100Mg, 50Ca50Mg, and 100Ca0Mg) and data for ISG encompasses all surface layers (Layer 1, 2, and 3); with all timesteps (28-672 days) included for both

### 6.4.2. Method comparison

#### Leachate vs. Sphere method

A comparison between alteration layer thicknesses estimated using leachate sodium data (Equation 6.1) and the Sphere Method is presented in Figure 6.6. Results from other leachate-based methods (Equation 6.2) are not shown for brevity, however near-identical trends are observed as both methods are based on the same raw ICP-OES data. Data are well fitted by a straight line on a log-log plot which implies a power law relationship as described by the equation in Figure 6.6. This deviates from the perhaps expected 1:1 trend.

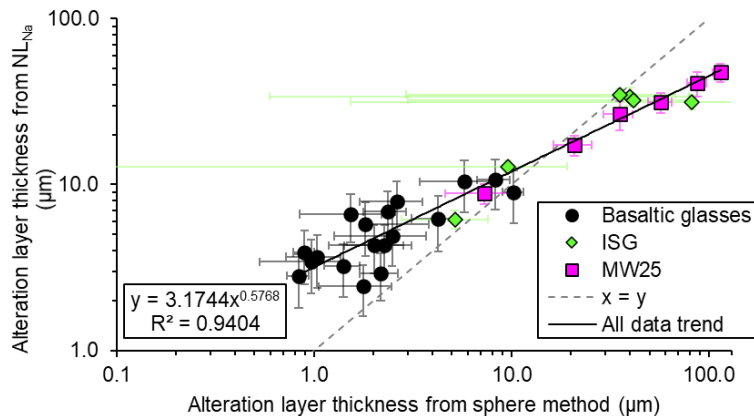


**Figure 6.6.** Comparison of alteration layer thicknesses measured via leachate data (Equation 6.1) and via the Sphere Method. All basaltic glass compositions from all timesteps are represented using identical symbols. Data for ISG and MW25 (from all timesteps) show cumulative surface layer thickness (i.e. Layer 1 + Layer 2 + Layer 3 thickness)

### Sphere method (XCT vs SEM) vs Ray method

Figure 6.7 compares results obtained from both the Ray and Sphere method, as applied to SEM and XCT data. Measurements made via the Ray Method are within error of those made via the Sphere Method; though the Sphere Method shows a larger standard deviation ('error') than the Ray Method. Alteration layer thickness measurements made (via the Sphere Method) using XCT data are not within error of those measured from SEM data; with XCT measurements typically larger (by ~ 2.8  $\mu\text{m}$ ) than those made via SEM.

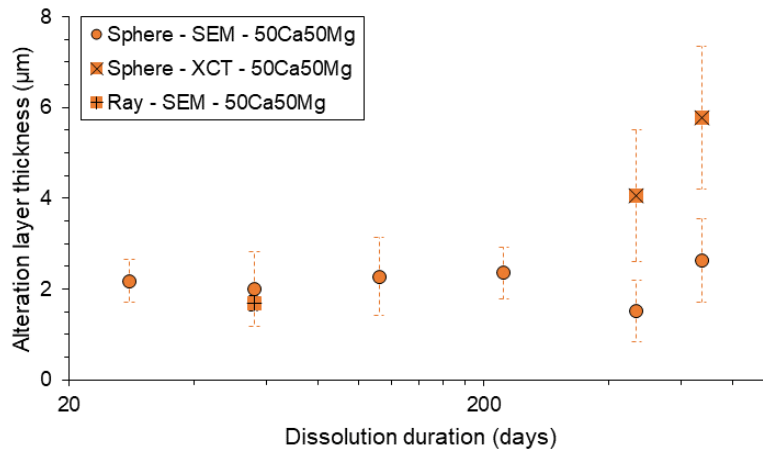


**Figure 6.7.** Comparison of alteration layer thicknesses measured via the SEM/Sphere method with measurements made via the SEM/Ray Method and XCT/Sphere method. All were measured from 50Ca50Mg basaltic glasses, with Sphere Method data taken from corners and edges.

### Sphere vs Area measurement

A comparison of the sphere and area-based measurement methods for individual ISG and MW25 surface layers is shown in Figure 6.8. Surface layer thicknesses measured via the Sphere Method are shown to approximately increase as a power of the same values measured in terms of area. Specific trends appear distinct for ISG and MW25, with the ISG showing a trend with both a lower constant and exponent compared to that of MW25. Data for MW25 Layer 3 may show a very subtle deviation from this trend beyond durations of 28 days. The latter data subset may be better-described by a logarithmic trend as shown in Figure 6.9.

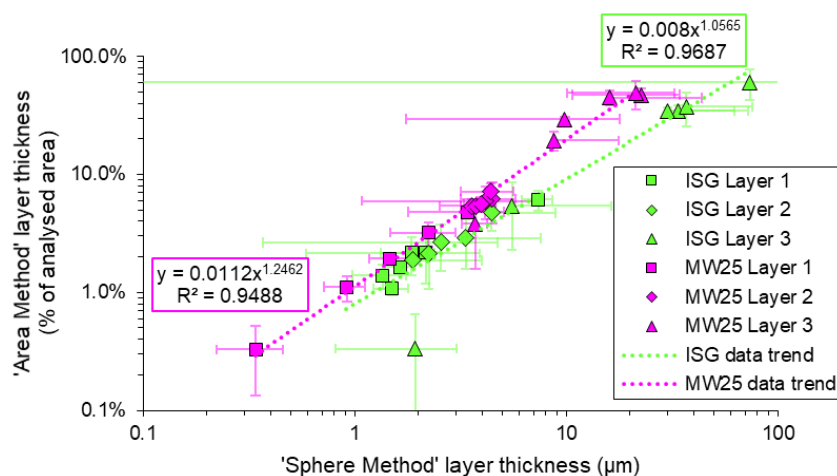


**Figure 6.8.** ISG and MW25 surface layers measured as thickness (via the sphere method) and area (as a percentage of total analysed area). Dotted lines show trendline fitted to all ISG and MW25 data in green and pink respectively.

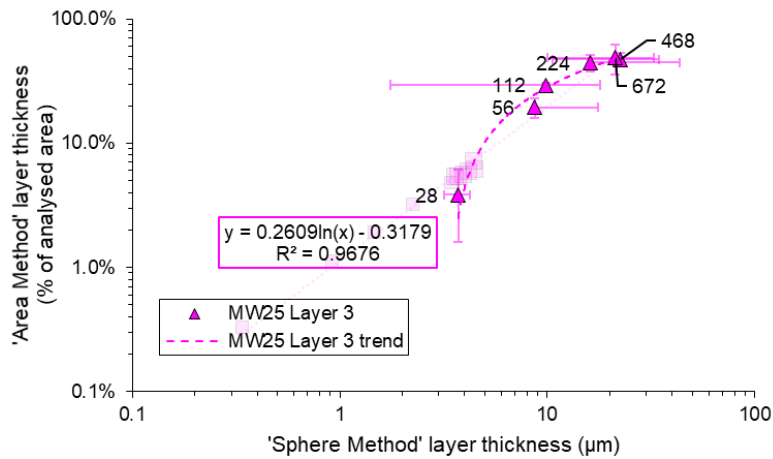


**Figure 6.9.** Comparisons of measurements made via the Sphere and Area measurement for MW25 Layer 3 (unfaded data) can be described by a logarithmic trend (plotted), whilst all other data (faded) can be described by power law relationships as in Figure 6.8. Numerical annotations show datapoint dissolution duration (in days).

Plotting area and sphere-based measurements against dissolution duration (Figure 6.10) indicates that both measurement methods show similar trends – with a plateau in growth beyond 224 days of dissolution.

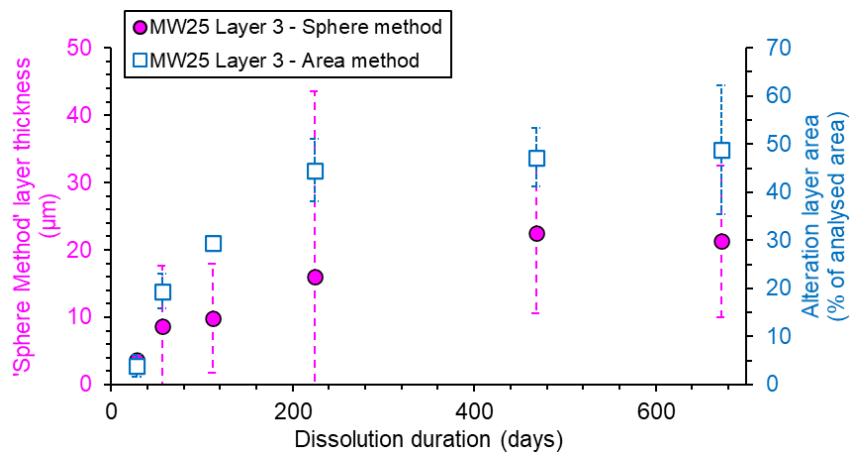


**Figure 6.10.** Comparison of MW25 Layer 3 thickness as measured by Sphere Method (pink; left axis) and as proxied by surface layer area (blue; right axis).

### 6.4.3. Comparison with other works

Figure 6.11 compiles various alteration layer thickness measurements. Data from the current study (including HLW glasses) are shown alongside basaltic glass alteration layer thicknesses measured from naturally-dissolved archaeological tools and basaltic lava flows [260] and from basaltic glasses dissolved in oceanic and continental environments [157]. All data subsets individually exhibit power law trends, though the specificities of these trends differ depending on data type/source as further outlined in Section 6.5.6. Taken collectively, all basaltic glass dissolution data further exhibit the broad (fairly weak) power law trend shown in Figure 6.12.

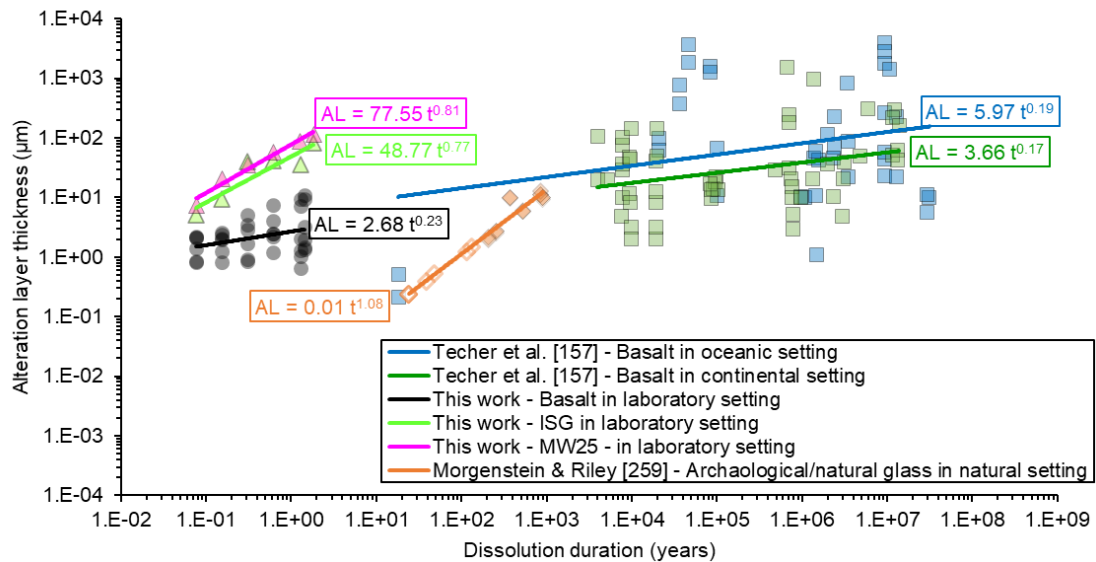


**Figure 6.11.** Comparison of alteration layer thickness development with time for various works, including laboratory investigations from this work and natural experiments compiled by Techer et al. [157] and completed by Morgenstein & Riley [260]. Note that thicknesses for ISG and MW25 are cumulative (i.e. include all three surface layers).

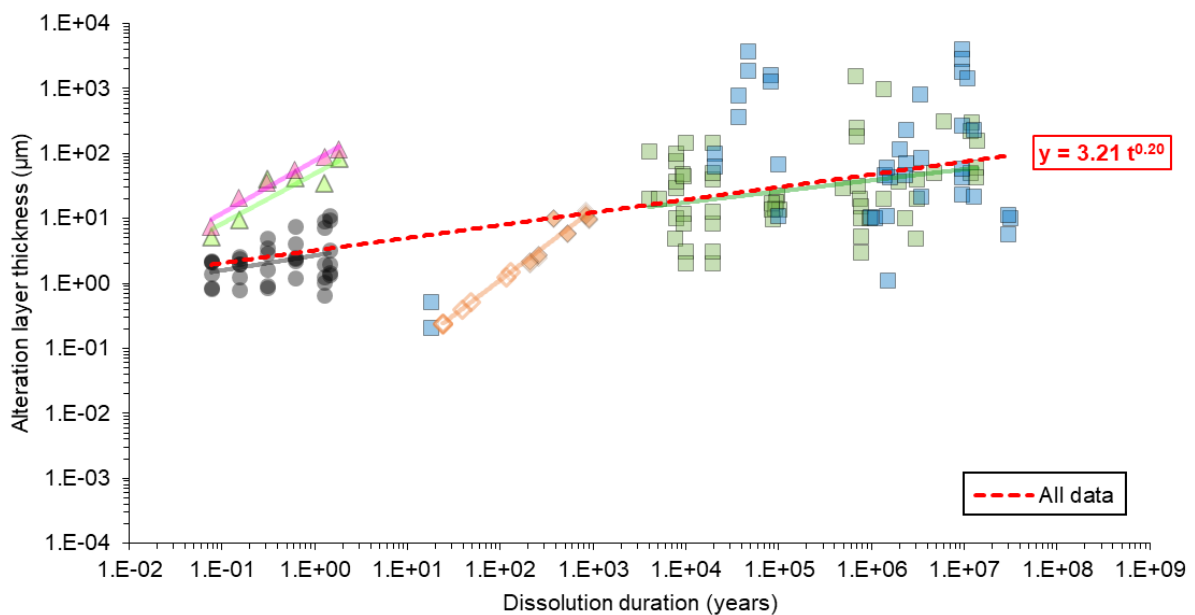


**Figure 6.12.** Power law fitted to all visible datasets (bold dashed line in red). Datapoints as identified and cited in Figure 6.11.

Basaltic glass alteration layers are consistently thinner than the equivalent layers formed on HLW glasses, with this difference increasing with increasing dissolution duration (from a thickness difference of ~300% with reference to basaltic glass alteration layer thickness at 28 days to a difference of ~3000% by 672 days). Basaltic glasses also show a larger spread of alteration layer thickness compared to HLW, however this is associated with the variable Mg:Ca ratio of these samples (see Chapter 5). Of the data from this work, HLW glasses show the steepest (highest exponent) power law trends.

Data for basaltic glasses dissolved over timescales of 10 to 1,000 years and by a single author [260] show the steepest (highest exponent) power law trend in alteration layer thickness development for any data subset, with glasses from more 'recent' (15 – 150 year old) basaltic lava flows showing thinner alteration layers than those formed on archaeological glasses dissolved for longer durations (250 – 1,000 years). Over longer timescales, basaltic glasses dissolved in oceanic and continental settings develop similar alteration layer thickness [157], with a slightly higher constant for oceanic values trendline but similar exponents for both. Broadly, data from basaltic glasses dissolved in natural (continental and oceanic) settings show a similar (power law) trend to basaltic glasses dissolved in a laboratory setting; though a large spread of data is observed in the former.

## 6.5. Discussion

### 6.5.1. Measurement location

Figure 6.5 indicates that ISG and basaltic glass alteration layers appear similarly thick regardless of whether measurements are made from the edge or corner of a single monolith. Verification of this was necessary given previous studies noted that alteration layers may be thicker at corners due to preferential damage in these areas during sample preparation [91], and given that stress intensity factors are increased around corner geometries [307].

Given this, alteration layer thicknesses were only measured from monolith corners for MW25. Corners were favoured for analysis efficiency because photomicrographs containing monolith corners encompass circa twice the cross sectional perimeter of images containing only an edge. Micrographs of corners also include a monolith surface orientated both vertically and horizontally during dissolution (i.e. images from corner include a surface facing vessel walls and either the top or bottom of the vessel during dissolution).

### 6.5.2. Alteration layer thickness estimation via leachate and monolith analysis

Alteration layers measured via leachate analysis and monolith analysis generally show a strong correlation, supporting the reliability of both methods. However, this correlation is of a power law type (described in Figure 6.6), not the linear (one-to-one) equivalence that may initially be expected. This non-direct equivalence may result from the differences in what the methods measure: Leachate-based methods provide the thickness of material that must have been dissolved to source the observed quantity of tracer element in solution (assuming that none was retained in alteration products). This does not *directly* take into account the efficiency of drawdown of other elements to form alteration products. The latter would only be considered *indirectly* and if these alteration products were to have a passivating effect (which would allow their influence of dissolution rates and thus provision of elements into the leachate). Monolith analysis methods however, *do* directly consider the efficiency of elemental drawdown to form alteration products. Hence, the difference between these methods must result from the fact they do and do not consider the efficiency of elemental drawdown to form alteration layers.

The exponent of the trend shown in Figure 6.6 may warrant further discussion. When applied to time-dependant data, power law relationships with exponents of  $\sim 0.5$ , as in Figure 6.6, are often associated with diffusional processes [300]. Dissolution fronts have previously been assumed to progress inwards proportionally to the square root of time [122]: a result of their dependence on diffusion/ion exchange processes [22], [26], [300], [308]. This may imply that the difference between the two alteration layer measurement methods may relate to a diffusional process – for example alteration layer passivation via diffusion.

Replotting data as a function of time (Figure 6.13) shows both methods output layer thicknesses increasing, approximately, with the square root of the dissolution duration. This is particularly true of alteration layer thicknesses inferred from leachate data. Hence, given alteration layer thickness can proxy dissolution duration (which is valid given alteration layer thickness increases with increasing time), if diffusion dominates a power-law relationship with an exponent of 0.5 is expected when methods are plotted as a function of each other (Figure 6.6).

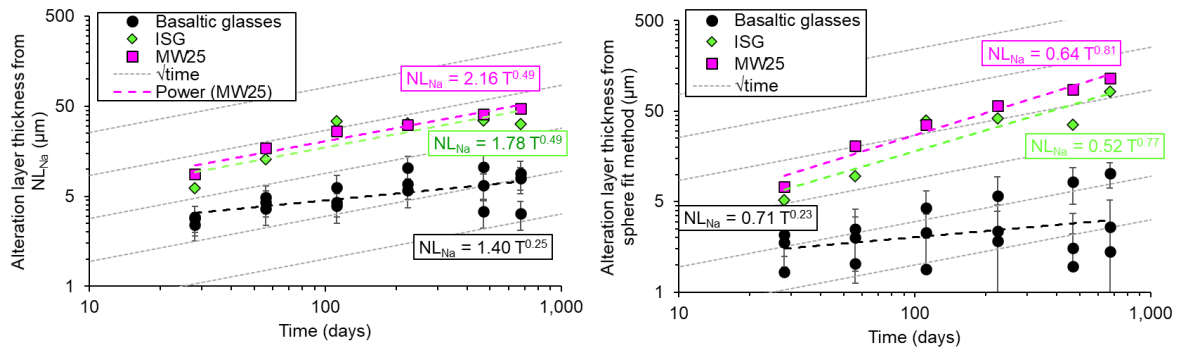


**Figure 6.13.** Alteration layer thicknesses from sodium normalised mass losses ( $NL_{Na}$ ; left) and as measured via sphere method (right) in comparison to square root time ( $\sqrt{\text{time}}$ ) trends.

### 6.5.3. Application of the Sphere Method to XCT and SEM

Comparison of alteration layer thicknesses (as measured via the Sphere Method) measured from XCT and SEM datasets reveals some discrepancy. Layer thicknesses measured using XCT data appear 2.5 - 3 $\mu\text{m}$  thicker than the equivalent layer measured from SEM data; with values from the two data sources not within error. This may be due to challenges segmenting the larger 3D XCT datasets. During segmentation, a single threshold may provide good results in one region, but poorer in another. Larger datasets inevitably contain more ‘regions’ and thus higher potential for this to happen, with a greater impact if it does. More time must thus also be spent scrutinising data to prevent or mitigate this, potentially increasing the likelihood that insufficient time was spent refining segmentation parameters. Furthermore, XCT data contained considerably more noise (that was more challenging to remove) than the SEM data. Some of the measurement difference may also be non-artefactual: though data were collected from the same sample *type* (50Ca50Mg basaltic glass) dissolved for the same durations (468 and 672 days), data were from separate individual monolith triplicates.

Application of the Ray Method to XCT data cannot be automated within *Dragonfly*’s GUI. However, such automation is conceivable and could be relatively robust if a ray was defined as being perpendicular (in all directions) to a confined region of a given face. Ambiguity would, however, be introduced in arbitrary definitions of the size and dimensions of the planar region used to define ‘perpendicular’ relative to. Which face (the upper or lower alteration layer face) this was measured from would also have to be decided upon.

### 6.5.4. The Sphere and Ray Methods

Alteration layer thickness measured via the Sphere and Ray Methods (both applied to SEM data) are within error (Figure 6.7). This supports the reliability of inter-study comparisons with works utilising the more widely used Ray Method. The Sphere Method is shown to have a higher associated ‘error’ than the Ray Method, however this might be considered a more accurate representation of the true variability in alteration layer thicknesses. Errors provided for the Ray Method in Figure 6.7 (which show the standard deviation within ~60 measurements) are also likely underestimated; especially when compared to other works where standard deviations were taken on hundreds of measurements per monolith [82], [91].

Though results are comparable, the Sphere Method of alteration layer thickness measurements may be considered preferential compared to The Ray Method. Defining layer thickness in this way would align alteration layer thickness analysis with the measurement methods used in equivalent engineering and technical drawing disciplines [283], [298]. Automatic image analysis, as allowed by this technique, is also already applied to cement- [309], ceramic- [310], metal- [311] and even wood- [312] science; hence application to glass science appears overdue.

Similarly, automated techniques can offer more statistically-robust and repeatable results [313] and improved efficiency. Though both the Ray Method and Sphere Methods are currently similarly time consuming (requiring 1 - 3 hours per monolith), the Sphere Method offers considerable scope for improvements in this; whereas few efficiency improvements are possible for the Ray Method. Segmentation as part of the Sphere Method may, in the future, be accelerated by artificial intelligence or machine-learning; with both of these implementable within the *Dragonfly* GUI. Algorithmic segmentation may also be explored, with algorithms based on thresholds (including edge, region and watershed detection methods) potentially most promising; though clustering techniques (based on pattern recognition) or deformable models (based on modelling curve evolution or object class variability) may also be worthwhile exploring [314], [315].

However, the semi-automated Sphere Method has some disadvantages relative to the Ray Method. The former method, for example, requires slightly more advanced software usage (though both could be applied using the same open-source software) and subjectivity remains in both methods. Though alteration layer thicknesses are always somewhat subjective [254], subjectivity is arguably lesser where a single quantifiable threshold is applied to consistently identify an alteration layer within a single image.

The potential impact of anomalies may also be greater in the Sphere Method where regions of contamination or localised attack are *by default* included in analysis. These regions may be intuitively interpreted and excluded during the manual Ray Method where scrutiny and image interpretation is inherent within the technique. Furthermore, with increased automation comes increased risk of inadequate adequate scrutiny and ‘filtering’ of input datasets. Finally, analysis of localised attack zones may also output less meaningful results in the Sphere Method.

#### **6.5.5. Localised attack/the effect of perturbations**

Measuring Layer 3 protrusions in MW25 proved problematic in the Sphere Method. Here, the *width* of the ‘finger-like’ feature is often measured as opposed to either feature *length* or alteration *thickness* as defined intuitively by the Ray Method (Figure 6.14). This, the feature width, then contributes to calculations of average alteration layer thicknesses. Area-based measurement techniques were developed in an attempt to resolve this.

The strong correlation between area and sphere-based measurements in all available datasets excluding MW25 Layer 3 suggests both techniques are effective in characterising the thickness of uniform alteration layers (those without significant protrusions). The similarity of the trends in these data further implies these features formed via similar (likely diffusional) mechanisms. This diffusion, may occur at different rates for ISG and MW25, potentially accounting for the slight differences in trends shown by both glasses.

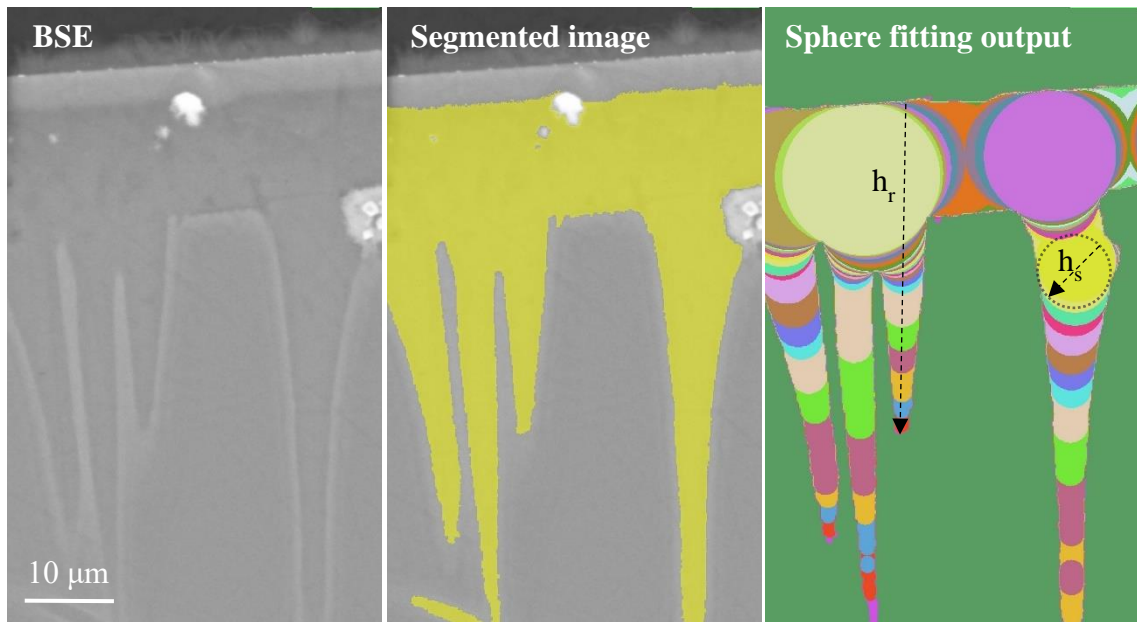


**Figure 6.14.** Localised alteration layer protrusions (viewed in SEM-BSE; left image) are segmented (middle image) and analysed via the sphere method (right). This leads to a discrepancy between thickness measurements made ‘intuitively’ or via the Ray Method ( $h_r$ ) and thickness outputted via the Sphere Method ( $h_s$ ).

In plotted comparisons of area and sphere-based techniques, MW25 Layer 3 (Figure 6.9) may show a subtly different trend compared to other datasets (which can be described by the power law trends shown in Figure 6.8). Though this difference is subtle, speculative and dependant on relatively few datapoints, the distinctiveness of this data subset would be consistent with the unique morphology of MW25 Layer 3 and may potentially imply these features are forming via a different (or modified) process compared to all other layers.

### 6.5.6. Comparison with other works

For basaltic glasses, alteration layer thicknesses generated via accelerated laboratory tests appear consistent those measured from continental and oceanic settings in nature. The minimal difference between values for oceanic and continental samples may be due to the subtly differing conditions (e.g. leachate chemistries) and natural phenomena operative in these environments [155].

The vast spread of alteration layer thicknesses developed on natural basalts is likely associated with a plethora of variables. Comparisons with laboratory data imply some of this variability may be associated with differences in glass composition, with varying only the Mg:Ca ratio in the present study also leading to considerable variation in alteration layer thickness. Significant uncertainty also exists in the dissolution duration of many of the natural basaltic glasses shown in Figure 6.11, as is often acknowledged by the original measuring authors [156]. Establishing this value can be challenging as aqueous exposure duration does not necessarily equate to sample age – even deep ocean samples can become disconnected from water supplies following cement precipitation [147]. Stated alteration layer thicknesses also likely contain error, as this value was noted to vary considerably across a single sample surface [156].

Comparing individual trends implies Morgenstein & Riley’s [260] data is perhaps anomalous. This may be associated with the sample dating challenges noted by the authors - as this involved the radiocarbon dating of stratigraphically equivalent specimens [260]. Thickness measurements may also be of limited accuracy because these appear to have been made manually using a relatively rudimentary petrographic microscope. Despite this, taken as part of the wider dataset, this subset may be less anomalous.

Alteration layer growth trends exhibited by HLW glasses may also differ somewhat from the equivalent trends of basaltic glasses, with exponents of 0.81 and 0.77 for MW25 and ISG comparing to more modest values of 0.16 to 0.26 for basaltic glasses. The more rapid or greater dissolution of HLW compared to basaltic glasses implied by this is consistent with leachate (NL<sub>i</sub>) data and other works [60], [151], [316]. However, given the unique morphology of the innermost layer (Layer 3) in these glasses, and the potential that this layer formed via modified or different mechanisms relative to other layers (see Section 6.5.2), data can be replotted with this layer *excluded* as in Figure 6.15. These data show trends more consistent with those shown by basaltic glasses, potentially further indicating that much of the difference between HLW and basaltic glass dissolution is attributable to the presence/formation of this “Layer 3”.

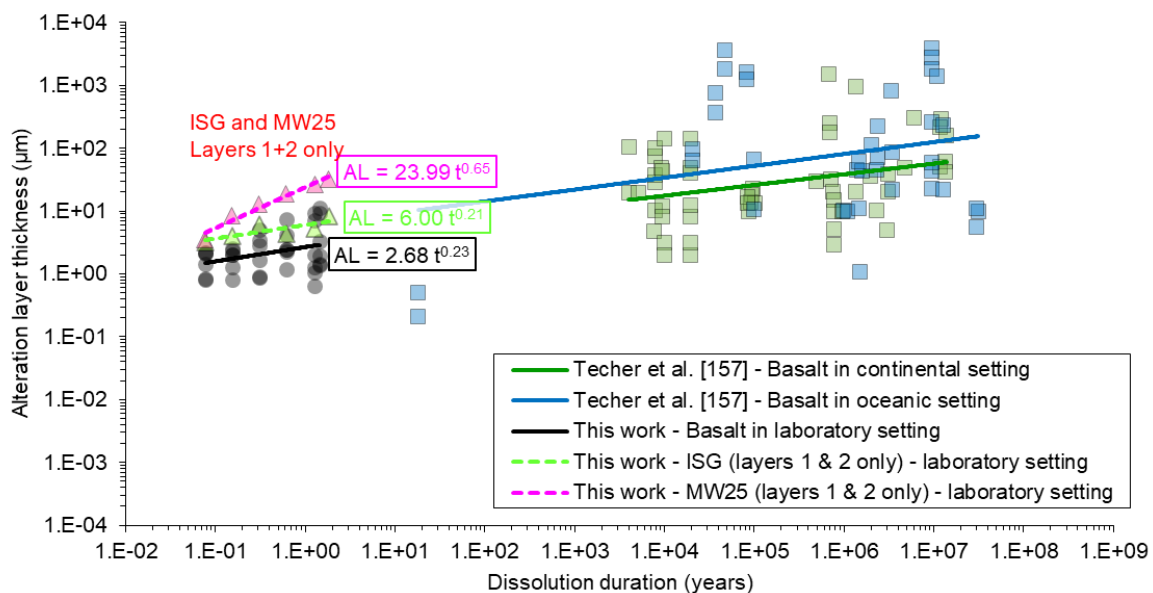


**Figure 6.15.** Alteration layer thicknesses and power-law trends for ISG and MW25 after the exclusion of thickness measurements from Layer 3.

Collectively, however the broad consistency of trends in all datasets is promising. A single power law relationship can adequately describe nearly all of the basaltic glass dissolution data subsets as in Figure 6.12. This, the consistency of trends observed for laboratory and natural experiments, may be used to support the case that laboratory data can be reliably extrapolated to geological timescales. The same mechanisms appear to control dissolution and alteration layer growth in both laboratory and natural experiments. This, if true, implies that the work of many researchers studying HLW glass alteration layers via accelerated laboratory techniques can be extrapolated to otherwise unreachable timescales – timescales with a direct relevance to the safety case for nuclear waste disposal.

## 6.6. Summary

Alteration layer thickness may be quantified via leachate or monolith analysis. Leachate-based methods estimate the thickness of material that must have dissolved to source observed concentrations of a tracer element in the leachate and are readily calculable from pre-existing data. However, these methods use assumed volumes and densities and, to be accurate, require no element retention within dissolution products. Alternatively, imaging of dissolved glasses (often monoliths) can be used to more directly measure alteration layer thicknesses. Though more advanced techniques are possible, measurement of alteration layer thickness is most often performed via microscopy of sample cross sections (which are assumed to be taken at exactly 90° relative to the sample face being analysed). These methods have been used for decades, with most investigators employing the Ray Method of thickness quantification. In this, the distance of a line (“Ray”) constructed through a layer is equated to its thickness. However, considerable ambiguity is possible, and often present, in the precise orientation and specificities of this “Ray” and this can lead to highly variable measurements and data irreproducibility. To resolve this, thickness can be redefined as the diameter of the largest sphere/circle which can be entirely enclosed by the layer. By resolving many of the aforementioned ambiguities, this method (the Sphere Method) can be readily applied to multiple data sources and via automated techniques. The only remaining ambiguity concerns the angle the cross section was taken from.

Thickness measurements made via SEM monolith analysis (via the Sphere Method) and leachate analysis appear to be relatable but not equal, potentially because the methods offer subtly different insight into dissolution process. Both methods, however, produce time-dependant trends indicative of a diffusional process. Generally, the Sphere and Ray Methods output similar alteration layer thicknesses when applied to SEM cross sections; however the Sphere Method can be more readily applied to 3D datasets. Comparisons between XCT and SEM measured alteration layer thicknesses imply XCT analysis may overestimate thicknesses, however this is hypothesised to result from segmentation challenges and sample differences.

The Sphere and Ray Methods can be compared as in Table 6.2. Generally, the Sphere Method produces more statistically robust and repeatable results. Furthermore, although both the Sphere and Ray Methods are similarly time consuming, the Sphere Method offers scope for improvement in this via further process automation. However, with this increased automation comes increased risk of inadequate scrutinization of input/output datasets. Furthermore, the Sphere Method provides unexpected results where layers are morphologically complex. If protrusions are present in a layer then the *width* of these features is (arguably incorrectly) considered in calculations of average alteration layer *thickness*. The Sphere Method is effectively unable to discriminate between alteration layer *thickness* and *width*. Resolving this is possible if alteration layers are measured in terms of area, however normalisation of these values is somewhat arbitrary.

Alteration layers generated by accelerated laboratory testing and measured via the aforementioned Sphere Method appear to develop at rates comparable to those shown by basaltic glasses dissolved in natural settings. Similarities are strongest where samples are directly equivalent (i.e. comparing basaltic glasses dissolved in the laboratory to basaltic glasses dissolved in nature), with spread in these data likely attributable compositional variability amongst other factors. This implies the same mechanisms are operative in both laboratory and natural experiments and thus supports the application of laboratory studies to the safety case for nuclear waste disposal.

HLW glasses show more rapid alteration layer growth than basaltic glasses (dissolved in the laboratory or in nature), as is consistent with leachate and other dissolution data. However, when contributions from the innermost HLW surface layer are removed, the remaining HLW trends show greatly improved similarity with data from natural experiments and basaltic glasses. The latter implies at least some of the differences in dissolution rate and behaviour between HLW and basaltic glasses may be attributable to this innermost surface layer. Logarithmic thickness development of this layer also implies that it may be associated with processes that differ from the (likely diffusional processes) associated with the power-law growth of the more outer surface layers in HLW glasses. These process may relate to or generate the protrusions observed in these layers.

	<b>The Sphere Method as applied in this study</b>	<b>The Ray Method as applied by others</b>
Measurements per image	Variable, though average ~35,000 with a range of 8,000 – 135,000	Variable, but typically 50 - 600
Automated outputs	Thickness statistics (histogram, mean etc.) and segmented images	Average thickness
Time required per monolith	1 – 3 hours of segmentation, but potential for efficiency increases	1 - 3 hours of ray drawing with little scope for improvement
Method robustness	Medium (terms well defined and little/no ambiguity)	Low (ambiguity in definitions of ‘thickness’ and ray orientations)
Required software knowledge	Low to medium	Minimal
Comparison with other disciplines	Comparable to techniques used in image processing and engineering	More primitive than techniques used in other related disciplines
Applicability to other datasets	Already proven for 2D (SEM), and 3D (XCT) datasets, with scope for wider application	Proven for 2D (SEM/TEM), but unproven/challenging to apply to 3D datasets
Potential for further work	High (AI/algorithmic segmentation possible)	None considered
Subjectivity	Medium (image segmentation is subjective, but the same threshold is applied to a single image)	Medium-high (ray direction subjective, with alteration layer boundaries variable)
Potential for anomalies	Medium (greater automation means less user intuition applied)	Low (images interpreted by eye individually, so anomalies can be intuitively identified & removed)

**Table 6.2.** Comparison of The Sphere Method and The Ray Method of thickness measurement, as applied herein and by other authors respectively.

# 7. Vermiform Features

## 7.1. Introduction

Features resembling ‘worms’ in 2D cross sections of dissolved glasses (so-called vermiform features) have been observed by many previous authors (see Section 2.4.2), however rarely are they comprehensively discussed. This is despite the possibility that these features may be coupled with alteration layer formation [92] and the potential impact of vermiform features on the exposed surface area [14], [47] and thus dissolution rates [90] of glasses.

This chapter characterises the vermiform features generated via MCC-1 (accelerated dissolution) testing of basaltic and HLW analogue glasses. SEM was used to observe features in two-dimensional cross sections, with XCT allowing extension of observations into the third dimension. Comparisons are drawn between the features generated on each glass type, before the impact of these features on surface areas is quantified and their potential formation mechanisms discussed.

## 7.2. Results

Vermiform features, as defined here, are elongate finite-length curvilinear structures that penetrate the pristine glass and have a well-rounded or arcuate termination (i.e. they do not sharpen to a point). These features are hypothesised as distinct from dissolved fractures or cracks in the glass. Compared to vermiform features, fractures or cracks typically follow more angular paths and either have an extended length (reaching from surface-to-surface) or a more angular/pointed termination which may taper into a conventional (undissolved) fracture. These distinctions are highlighted in Figure 7.1.

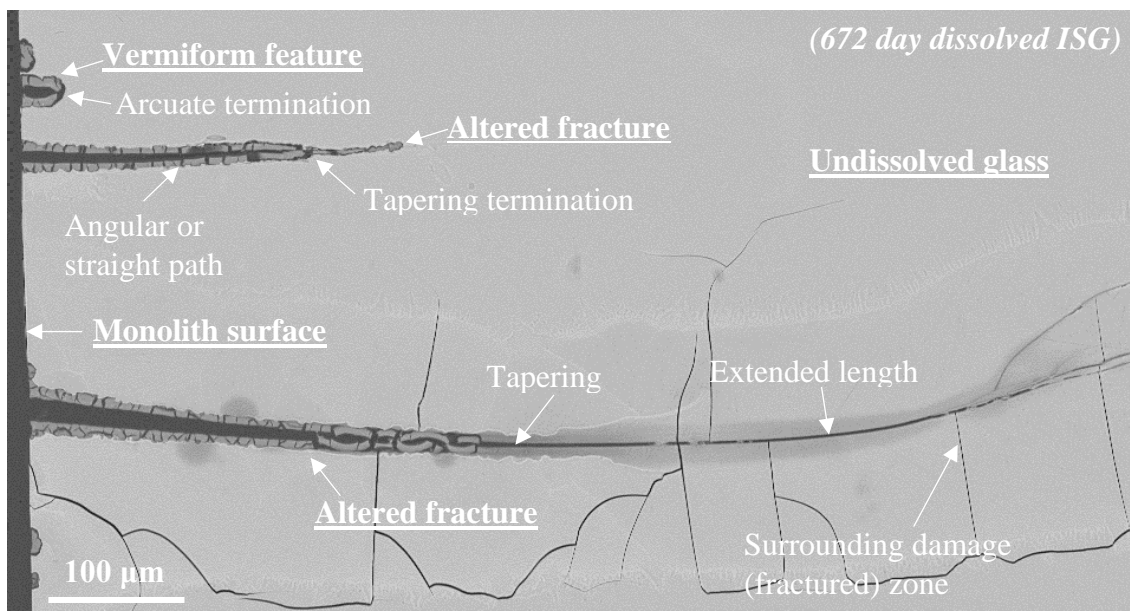


**Figure 7.1.** SEM-BSE image illustrating differences between vermiform features and dissolved fractures in dissolved MCC-1 monoliths.

### 7.2.1. SEM-BSE

#### *Basaltic glasses*

Vermiform features were observed on all basaltic glass compositions, with no noted compositional dependencies or differences across the variable Mg:Ca series. Per analysed cross section (~28 mm perimeter), 50 to 300 features were observed scattered randomly across the surface, with no evidence of abundance consistently varying with dissolution duration. Feature morphologies ranged from comparatively 'simple' to morphologically more complex varieties, with some evidence of increasing feature complexity with dissolution duration.

Simple solitary vermiform features (Figure 7.2) are the most abundant type of features in all basaltic glasses at all dissolution durations. These are 2 – 60  $\mu\text{m}$  in length, with a width which is typically a factor of 2-4 times that of the alteration layer width. These typically penetrate the glass at angles of  $\sim 90^\circ$ , though this can be significantly shallower. Solitary features often have relatively straight paths, however deviations from this are possible – with smooth curvilinear forms also noted. These vermiform cavities contain both a narrow void (comparable to that which separates the glass alteration layer from the sample elsewhere) and material resembling the alteration layer as observed distant from features. Vermiform features, however, contain a notably distinct central zone, no more than 0.5  $\mu\text{m}$  in width, of 'bright' material in BSE images.

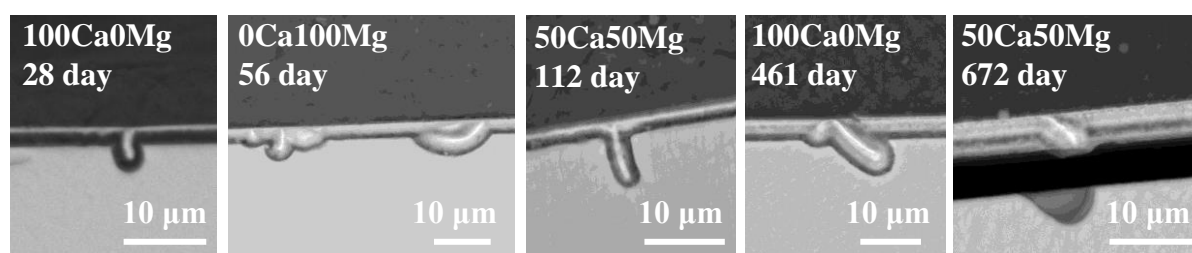


**Figure 7.2.** SEM-BSE images of typical simple vermiform features observed on basaltic glasses of all compositions after stated dissolution durations

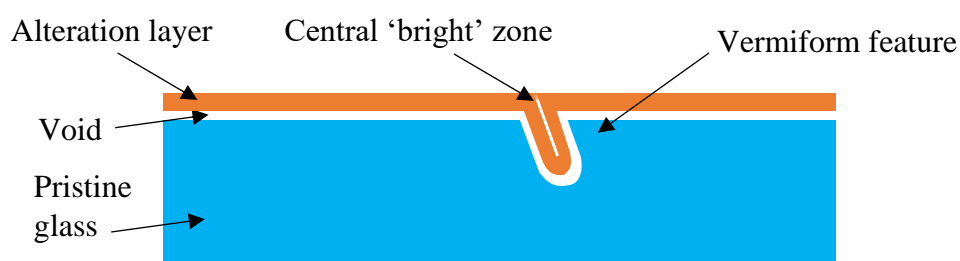


**Figure 7.3.** Schematic of simple solitary vermiform features formed on basaltic glasses

Single solitary features can show variation from those shown schematically in Figure 7.3. For example, vermiform features may widen towards the sample surface, or may appear entirely unconnected from the monolith surface as in Figure 7.4. The bright central 'thread' within these vermiform features was also occasionally observed to spiral around itself (Figure 7.4).

More complex features and clustering of vermiform features was also observed. Occasionally, 'clusters' of 5 - 20 closely spaced features are evident over a small distance (Figure 7.5, top), or multiple features can emanate from a single (near-)surface region (Figure 7.5, bottom). Vermiform features were also observed to branch after extending into the sample (Figure 7.6).

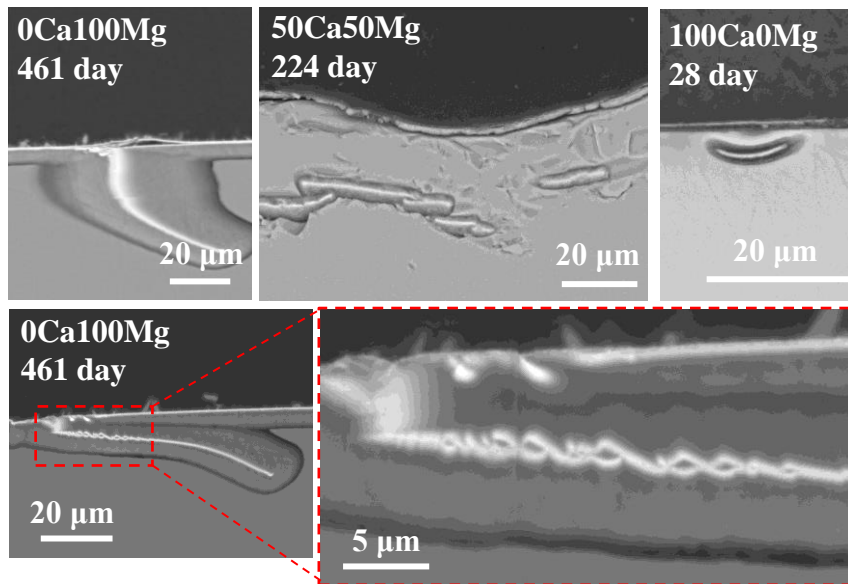


**Figure 7.4 (above).** SEM-BSE images showing rarely-observed characteristics of vermiform features formed on basaltic glasses of all compositions after the stated dissolution duration

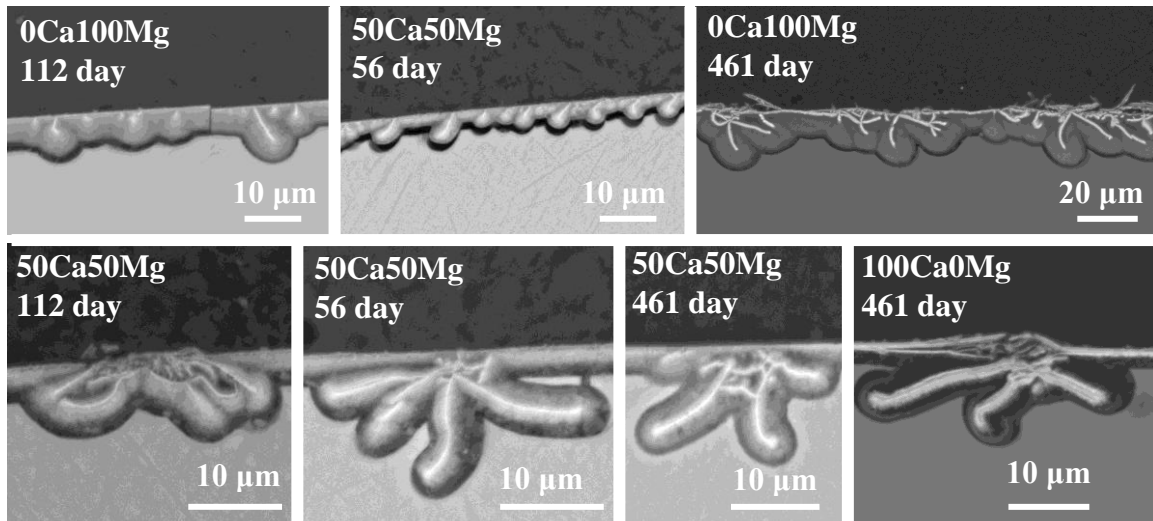


**Figure 7.5 (above).** SEM-BSE images showing clusters of vermiform features in basaltic glasses of all compositions after the stated dissolution durations.

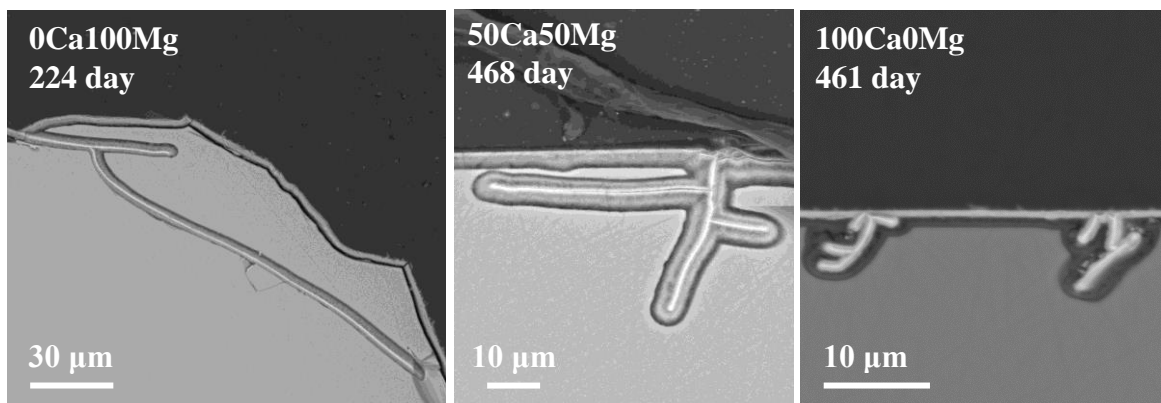


**Figure 7.6 (above).** SEM-BSE images showing branching of vermiform features in basaltic glasses of all compositions after the stated dissolution durations.

## MW25

Vermiform features within dissolved MW25 glasses are, at their simplest, single solitary occurrences (Figure 7.7) which are noted in quantities of 10-25 per cross sectional perimeter (28 mm). These are observed at all dissolution durations and appear unchanged with duration. ‘Simple’ type features occur in Layer 2, are 3 – 15  $\mu\text{m}$  in length, and protrude at angles of  $90^\circ$  ( $\pm 50^\circ$ ) to the glass-surface into Layer 3. Features are twice the thickness of Layer 2 and are demarcated down their centre by a thin ( $<0.5 \mu\text{m}$ ) high-contrast strand. Layer 2 is displaced inwards by vermiform features, arching around their terminations. The protrusions of Layer 3 into the pristine glass (see Section 4.2.4) notably never occur directly “below” the vermiform features, however the nearby finger-like elongations of Layer 3 are often splayed apart from the vermiform features, as illustrated schematically in Figure 7.8.

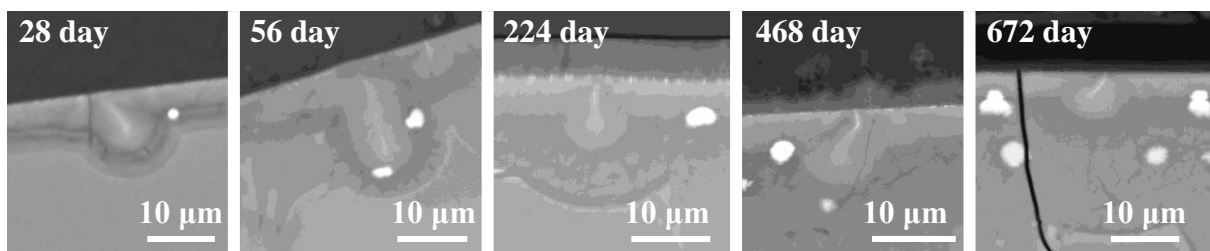


**Figure 7.7.** SEM-BSE images of simple solitary vermiform features formed on MW25 samples after various (indicated) dissolution durations

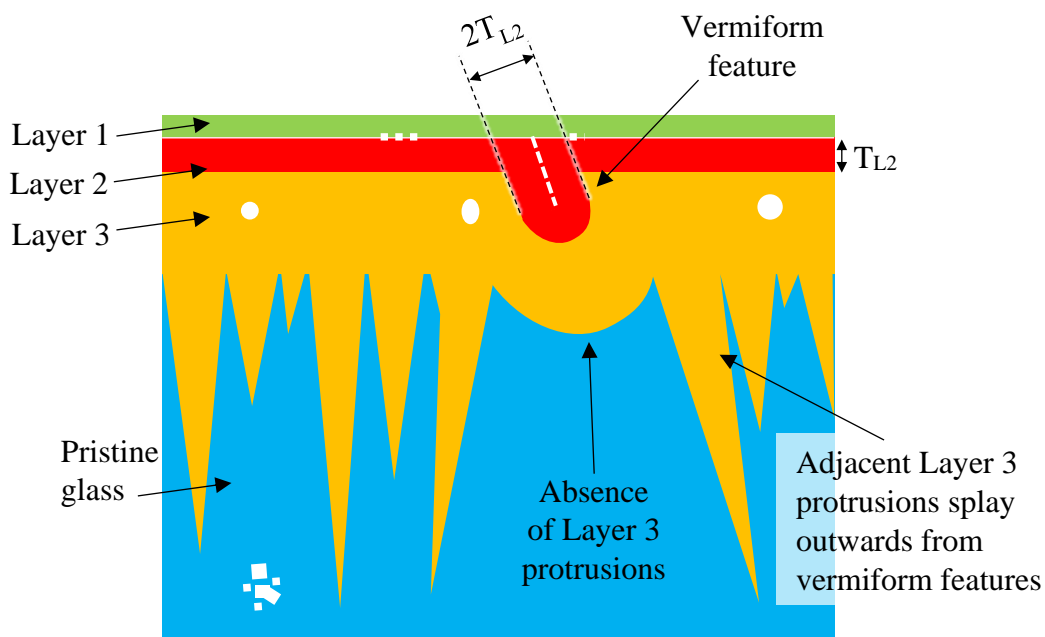


**Figure 7.8.** Schematic of simple solitary vermiform features formed on MW25 as in Figure 7.7

More complex and larger occurrences of similar features also occur. In one instance, a feature extended from a monolith corner  $\sim 100\ \mu\text{m}$  into the glass (Figure 7.9), as may be associated with a potential subtle increase in the abundance and/or length of these features towards monolith vertices. Elsewhere, features can be observed to branch (Figure 7.10a-d) or rapidly change course (Figure 7.10b,d) and in one instance a clustering of  $\sim 15$  small ( $\sim 1\ \mu\text{m}$  length) features was observed over a (cross sectional) distance  $\sim 35\ \mu\text{m}$  (Figure 7.10e).

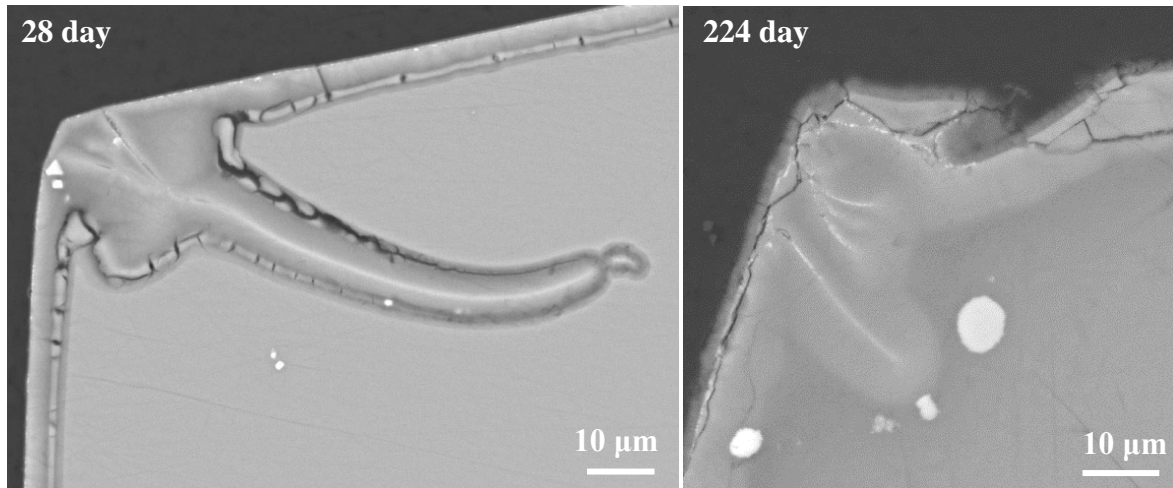


**Figure 7.9.** SEM-BSE images of vermiform features formed on/near MW25 sample vertices after indicated dissolution durations

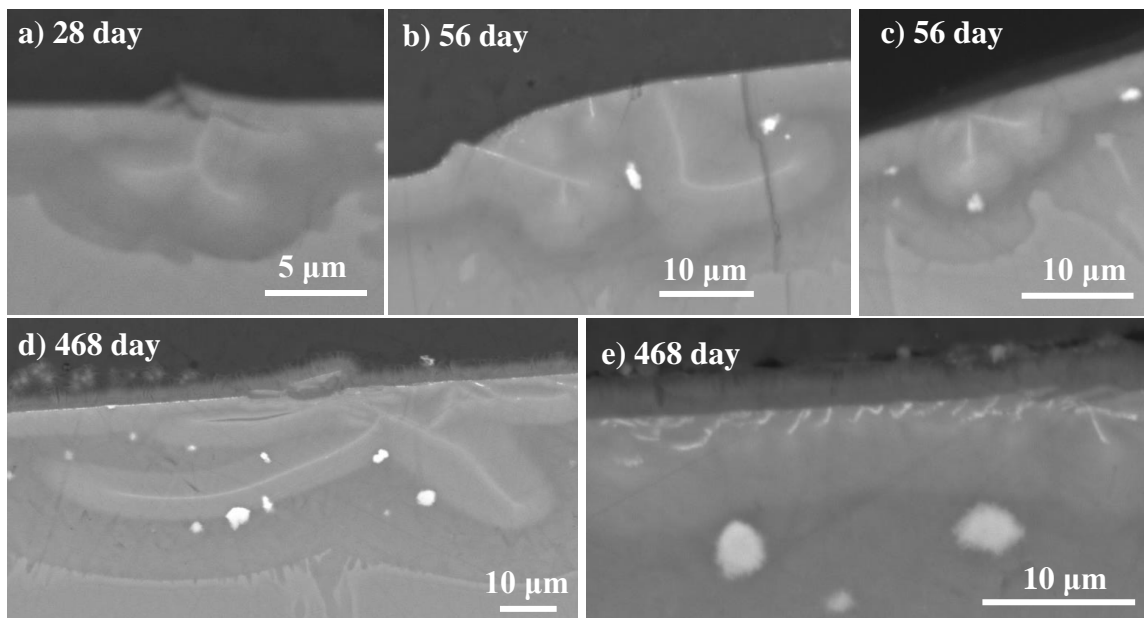


**Figure 7.10.** SEM-BSE images of vermiform features formed on MW25 samples after indicated dissolution durations show features branching, changing course and clustering

## ISG

Comparable features are also observed on dissolved ISG samples. Single solitary features, the most abundant type of features (at 10 – 30 occurrences per monolith cross section), penetrate 3 – 40  $\mu\text{m}$  into monoliths and are observed at all dissolution durations. These show some evidence of increasing in abundance with dissolution duration, however a comprehensive evaluation of this has not been completed. Distinct from the equivalent features in MW25, the 5  $\mu\text{m}$  width of these features is not *entirely* filled by alteration layers: Layer 1 outlines the feature walls (with a thickness comparable to the layer thickness elsewhere on the monolith); however, the majority of the vermiform feature is an unfilled void (see Figure 7.11). Layer 1, where it lines vermiform features, is cross-cut by abundant fractures and breakages to give a ‘blocky’ morphology as observed elsewhere. A breakage is nearly always observed at the feature tip. Whilst Layer 1 partially fills the features, Layer 2 appears displaced inwards by the vermiform features, effectively arches inwards in order to maintain a consistent layer thickness compared to Layer 2 thicknesses elsewhere. Vermiform features never cross-cut Layer 2. In contrast, Layer 3 appears unaffected by features – meaning that on occasion the feature extends beyond or ‘cross-cut’ Layer 3 (Figure 7.11b).

As in MW25, vermiform features in ISG can be observed to branch (Figure 7.13), however the point of furcation is always at or near the surface for ISG. Localised feature clustering was not observed for ISG.

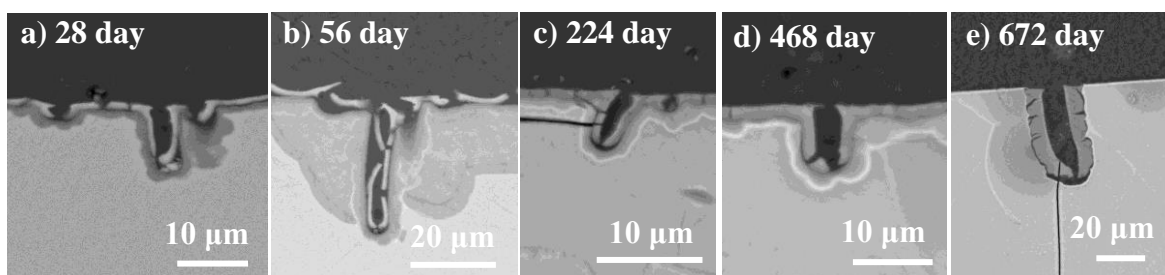


**Figure 7.11.** SEM-BSE images of simple solitary vermiform features formed on ISG samples after various (indicated) dissolution durations

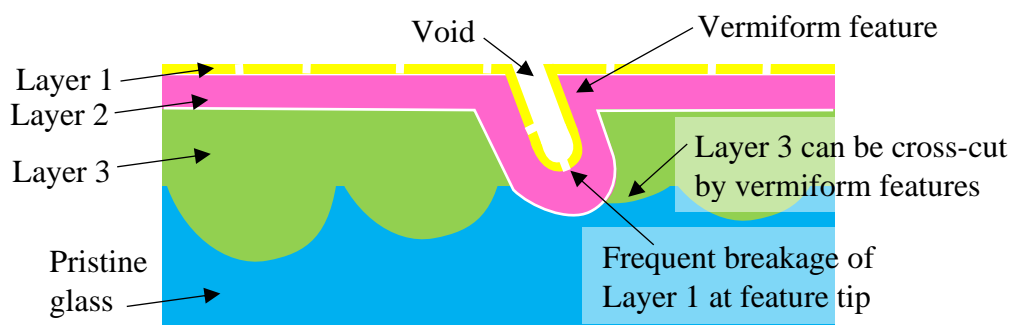


**Figure 7.12.** Schematic of simple solitary vermiform features formed on ISG

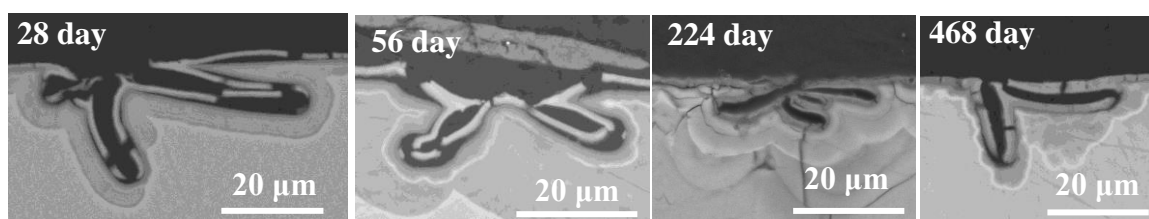


**Figure 7.13.** Branching of vermiform features in ISG

### 7.2.2. SEM-EDS

Qualitative EDS analysis showed the material within vermiform features on all glasses was compositionally consistent with the alteration layer observed elsewhere on the sample. The central ‘bright’ region within these features was unresolvable via EDS, however an enrichment in relatively high atomic number elements is suspected in these areas given the high brightness in BSE images.

### 7.2.3. XCT

Despite considerable efforts, vermiform features of comparable scale and abundance to those observed in SEM were not observed in XCT. However, some potentially related features were observed, and a singular vermiform feature may be speculatively identified.

In scans containing only dissolved glasses (with no attached alteration layers), basaltic glass samples were noted to contain multiple concavities. In surface views, the majority of these appear approximately circular, with diameters of less than 10  $\mu\text{m}$  (Figure 7.14). In cross section, these features are evident as symmetrical bowl-shaped pits with a depth of 1 – 5  $\mu\text{m}$  (Figure 7.14). In one instance, a feature appearing similarly circular in surface views was observed to potentially appear vermiform in profiles (Figure 7.15), however this was smaller than many of the vermiform features previously observed in SEM-BSE.

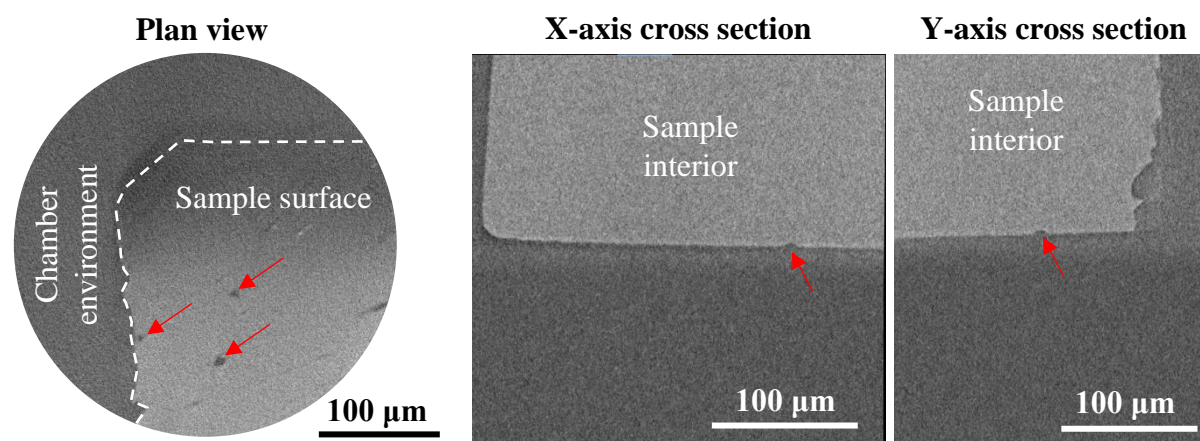


**Figure 7.14.** *XCT scans of 50Ca50Mg basaltic glass after 468 days of dissolution shows ‘pit-like’ features*

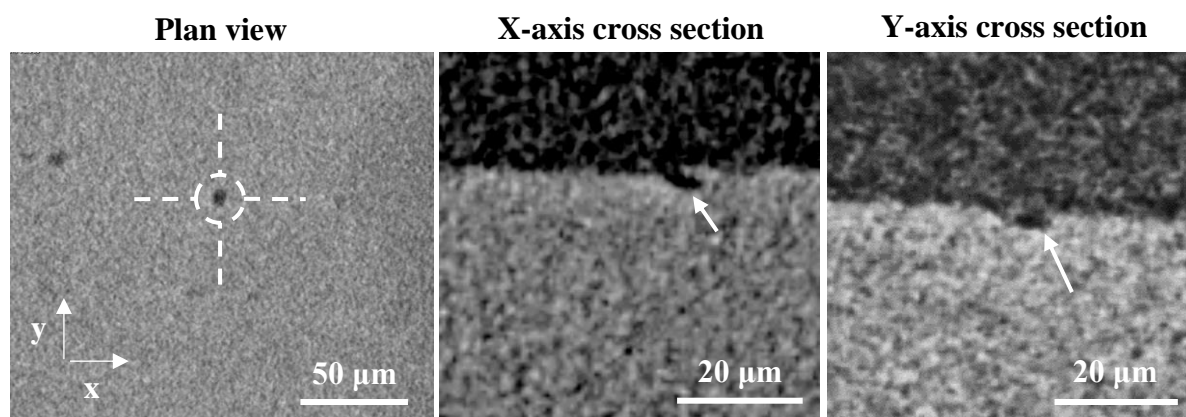


**Figure 7.15.** *XCT scans of potential smaller-scale vermiform feature in 50Ca50Mg basaltic glass after 468 days of dissolution*

Similar scans of glass samples where the alteration layer was detached show linear striations on the glass surfaces (Figure 7.16). These features were evident as multiple parallel lines spaced 20 – 100  $\mu\text{m}$  apart, with lengths of 20 – 120  $\mu\text{m}$  and widths of no more than five microns. Cross sections indicate these features penetrate only microns into the glass.

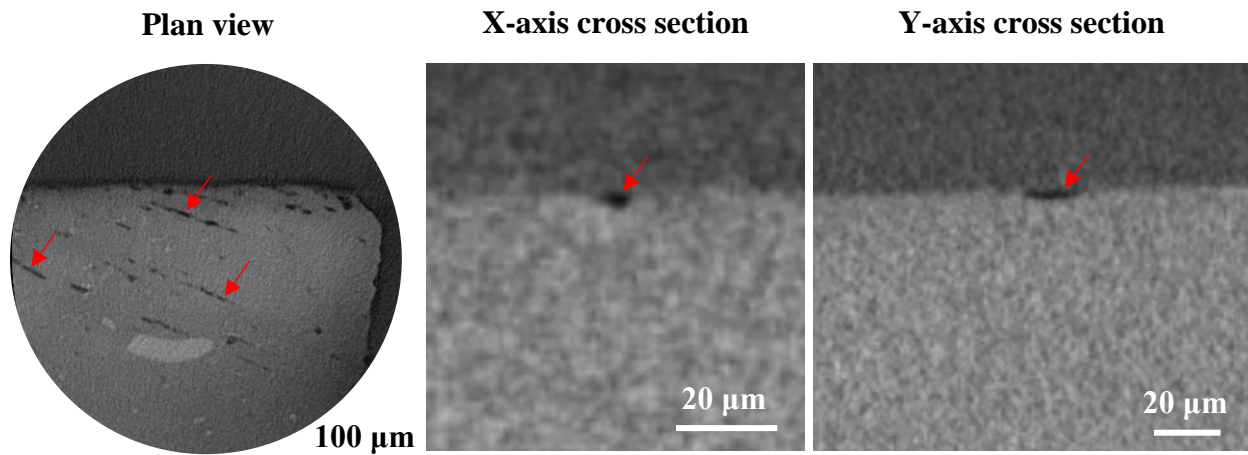


**Figure 7.16.** Striations evident on 50Ca50Mg basaltic glass after 468 days of dissolution

In scans containing both the dissolved glass and alteration layer, the alteration layer can be inferred to have once penetrated the aforementioned cavities. Figure 7.17 shows the underside of an alteration layer is characterised by high-density (bright) ‘ridges’, with a width of singular microns and a length of  $\sim 20 \mu\text{m}$ . These correspond to a featureless area on the upper alteration layer surface and approximately elliptical depressions in the glass surface below. In cross-sections, the alteration layer can be seen to penetrate these concave depressions in the glass.

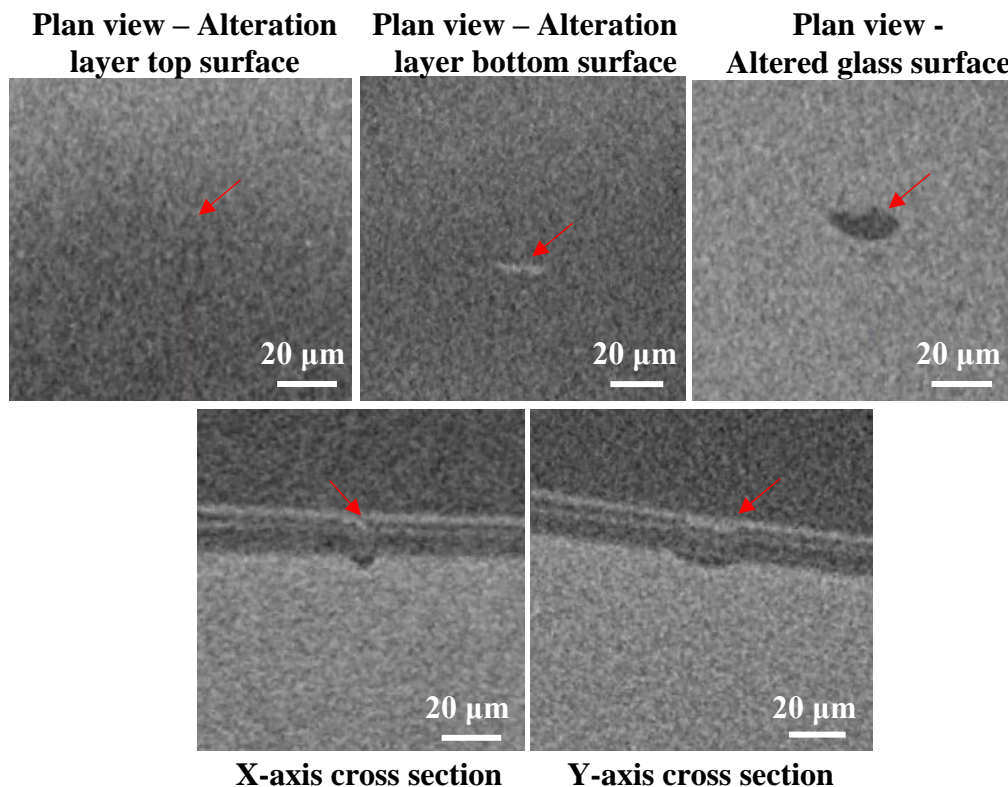


**Figure 7.17.** Alteration layers above concavity in 672-day dissolved 50Ca50Mg basaltic glass

## 7.3. Discussion

### 7.3.1. Feature comparison

Vermiform features were noted to vary in size, abundance and characteristics depending on the studied glass composition, as summarised in Table 7.1.

	Basaltic glasses	MW25	ISG
<b>Length / width</b>	2 – 60 $\mu\text{m}$ / 2-4 x alteration layer	3 - 15 $\mu\text{m}$ / twice Layer 2	3 – 40 $\mu\text{m}$ / 5 $\mu\text{m}$
<b>Features per cross section</b>	50 - 300	10 – 25 (increase at corners?)	10 – 30 (increase with dissolution duration?)
<b>Filled?</b>	Near-complete filling by single alteration layer protrusion with high-Z central enrichment, separated from glass by a void	Entirely filled by Surface Layer 2 which contains high-Z central enrichment	Mostly void, though Layer 1 present on either side of void (double alteration layer protrusion)
<b>Complexities</b>	Tapering, spiralling, disconnected from surface, branching, clustering	Branching (near surface only), angular redirections, clustering	Branching (near- surface only)
<b>Interaction with other layers</b>	N/A (only one surface layer present)	No Layer 1 interaction. Interacts with Layer 3 protrusions (absence immediately below feature and splaying adjacent to feature)	Interacts with Layer 2 (arches around feature)  No interaction with Layer 3 (can cross cut)

**Table 7.1.** Comparison of vermiform feature characteristics for all studied glasses

Perhaps the greatest difference evident in Table 7.1 is between the basaltic and HLW glasses. Basaltic glasses appear to contain more vermiform features, which can be significantly longer and show more evidence of complexity compared to HLW analogue glasses. These observations may be linked – it may be *because* more features are observed in basaltic glasses that more variation in complexity and size is noted. These variable abundances may reflect differing responses (e.g. due to differing intrinsic material properties) to the same external stimulus/factor in each glass composition. This implies that the formation and characteristics of these features is dependent on more than just sample preparation alone.

The increased feature abundance in basaltic glasses may indicate vermiform feature formation is more rapid or progressed in basaltic glasses. Features may initially preferentially form around monolith corners (consistent with observations made for ISG), before they begin to increasingly form elsewhere (hence the potential increase with time for MW25) until features become so widespread that no location or time dependence (at least beyond 28 days) is noted for basaltic glasses. This may also explain the increased complexity of features observed on basaltic glasses: complexity may develop with increasing progression through the vermiform feature formation process and progression may be more rapid in basaltic glasses. Preferential

or more rapid vermiform feature formation around monolith corners may be due to increased sample preparation-induced damage in these areas [91] or increased stress intensity factors here [307], as similarly discussed in relation to potential alteration layer thickening at monolith corners in Section 6.5.1. These hypotheses can only be speculated, however, as increasing abundance with dissolution duration (for ISG) or in the vicinity of corners (for MW25) has not been proven statistically.

The variable ‘filling’ of vermiform features may also be noted from Table 7.1. For basaltic glasses, the void separating the alteration layer from the bulk monolithic glass is hypothesised to result from desiccation during sample preparation (as in Section 5.3). Aside from this, the contents of vermiform features in both basaltic glasses and MW25 glasses is near-identical. Prior to drying, vermiform features in both would have been entirely filled by whichever surface layer underlies any precipitate layer (Layer 1 in MW25). In both MW25 and basaltic glasses, this vermiform infill also contains a central enrichment zone comprising apparently high atomic number elements. This may imply that the high contrast central zone is influential in or indicative of the feature generation mechanism. However, this similarity does not extend to ISG where only a thin layer (Layer 1) appears to penetrate the vermiform features as a sheath or coating which leaves most of the feature unfilled. This may simply result from the lower thickness of the infilling layer in ISG relative to MW25. Nevertheless, no central enrichment zone was noted for ISG, as may imply a modified casual mechanism if this central strand is considered influential in vermiform feature generation in MW25/basaltic glasses. The similarity in feature morphologies might imply that formation mechanisms were at least comparable, however, in all compositions. The absence of a central enrichment zone within vermiform features in ISG may thus detract from the importance of this characteristic in formation of vermiform features in other compositions. Absence of the central zone may also reflect the relative simplicity of the ISG composition.

The variable interaction of vermiform features with the surface layers in ISG and MW25 may provide useful chronological information regarding when these features and layers formed. Considering vermiform features as analogues to dikes or fractures in geology, it may be possible to determine relative ‘geochronologies’. For basaltic glasses, where only one surface layer is present, the penetration of this layer into vermiform features cannot be used to imply any sequence. Either the vermiform feature formed synchronously with the surface layer, or vermiform features predate the surface layer (the surface layer developed/formed within it) or the surface layer predates the vermiform feature (the vermiform feature formed below the surface layer, potentially as a result of a surface layer feature). The latter seems unlikely but it is possible. For MW25, the vermiform feature is infilled by Layer 2 and appears overcovered/overlain by Layer 1, with Layer 3 below. This may imply the vermiform feature grew during, or was present prior to formation of Layer 2, with Layer 1 forming sometime after (assuming the feature did not form after and beneath Layer 1). Layer 3 of MW25 shows a dependence on the vermiform features (deforming around them), potentially implying Layer 3 formed after or during the formation of the vermiform feature, or implying that the same mechanism which causes protrusions in Layer 3 is related to formation of vermiform features. For ISG vermiform features appear to “overprint” Layer 3, either implying that Layer 3 predates formation of the vermiform feature or implying that vermiform features continued growing in length quicker or for longer than Layer 3. However, these hypotheses do not consider what may be evident above and below the prepared cross section face.

### 7.3.2. XCT and 3D feature morphology

The three-dimensional morphology of these features may offer insight into their generation mechanism and is noted to be of interest by previous authors [317]. XCT data was collected in the hope of elucidating this and given that SEM offers only two-dimensional information.

As stated in Section 7.2.3, only a single vermiform features of a scale comparable to those observed in SEM were observed in XCT. This, though not entirely unexpected, was disappointing and may have occurred for two reasons: either the features were sparsely present in the scanned samples, or many of the features were indiscernible in XCT. The latter is plausible given that alteration layers were only evident in XCT images where layers had detached from their host-glass (Section 5.2.7). This means that should a vermiform feature be filled by an alteration layer, as is frequently observed to be the case in SEM images, this feature would be indistinguishable unless there was a *resolvable* cavity between the alteration layer and the vermiform feature. Such a cavity *is* evident in SEM, however it may be indistinguishable at the utilised XCT resolutions. Regarding the hypothesis that vermiform features are sparsely present in the scanned samples, SEM showed that vermiform features can be unequally distributed across monolith surfaces and thus locally sparse. The probability of observing such a feature may be reduced in XCT (relative to SEM) because in XCT the field of view is smaller, scouting and panning across wider areas is slower and the sample has already been size-reduced. It may, thus, be purely unfortunate that abundant features comparable to those noted in SEM were not observed in XCT. Remedying this may involve conducting high resolution XCT on an area where abundant vermiform features have already been observed in SEM cross sections, however cross sectioning inevitably involves the loss of some three-dimensional data.

A singular potentially comparable – though small-scale feature was observed in XCT (Figure 7.15). With a length of  $\sim 7\ \mu\text{m}$  and width of  $\sim 2\ \mu\text{m}$ , this is within the range of feature sizes observed for basaltic glasses in SEM (2 – 60  $\mu\text{m}$  in length and twice the alteration layer thickness in width). Virtual XCT ‘cross sections’ indicate the feature to be more tubular than planar. This may be pertinent to other studies where comparable features are considered to relate to planar structures such as crystallographic planes or grain boundaries (which are anyway notably absent in *amorphous* glasses). Furthermore, this may be used to strengthen the case that these features are not simply dissolved fractures. Such fractures would be expected to have more planar geometries in three dimensions – especially given the typical conchoidal fracture geometry shown by glasses.

Circular concavities observed in basaltic glass XCT are considered to be ‘micro-pits’ as are widely observed on dissolved archaeological and natural glasses elsewhere (see Section 2.4.1.). Combining or clustering of these to form “pitted troughs” (Figure 7.16) has similarly been noted in other studies [91], with alignment of these to form parallel rows also noted elsewhere [14], [47]. Discussions surrounding the cause of these pits is beyond the scope of this chapter–however readers are referred to Section 2.4.1 for a comprehensive list of possibilities. Some of the parallel striations may also indicate grinding/polishing defects which may have undergone preferential dissolution via similar mechanisms to those which form pits.

### 7.3.3. Significance of vermiform features

#### *Glass dissolution rates*

Vermiform features may impact glass dissolution rates by increasing the actual leachate-exposed sample surface area, however most authors and calculations assume that this surface area is constant and fixed (at the initial surface area value). Evaluating the potential impact on surface areas in MCC-1 experiments is, however, justified given similar vermiform features have elsewhere been found to increase surface areas by a factor of 2.4 [143].

Quantifying surface area increases associated with this effect is possible if various assumptions are made. For basaltic glasses cross sections, if 175 features per monolith perimeter are assumed, with each feature having a length and width of 31  $\mu\text{m}$  and 2  $\mu\text{m}$  respectively (the mid-range of values estimates in Section 7.2.1), then vermiform features can be estimated to cause an average *perimeter* increase of 1.4 times. If it is further assumed that one cross section is representative of a  $\sim 2 \mu\text{m}$  monolith thickness (i.e. that there are 5,000 of these cross sections per monolith) and if vermiform features are modelled as open-ended cylinders then a *surface area* increase of a similar quantity (1.4) can be calculated as in Figure 7.18.

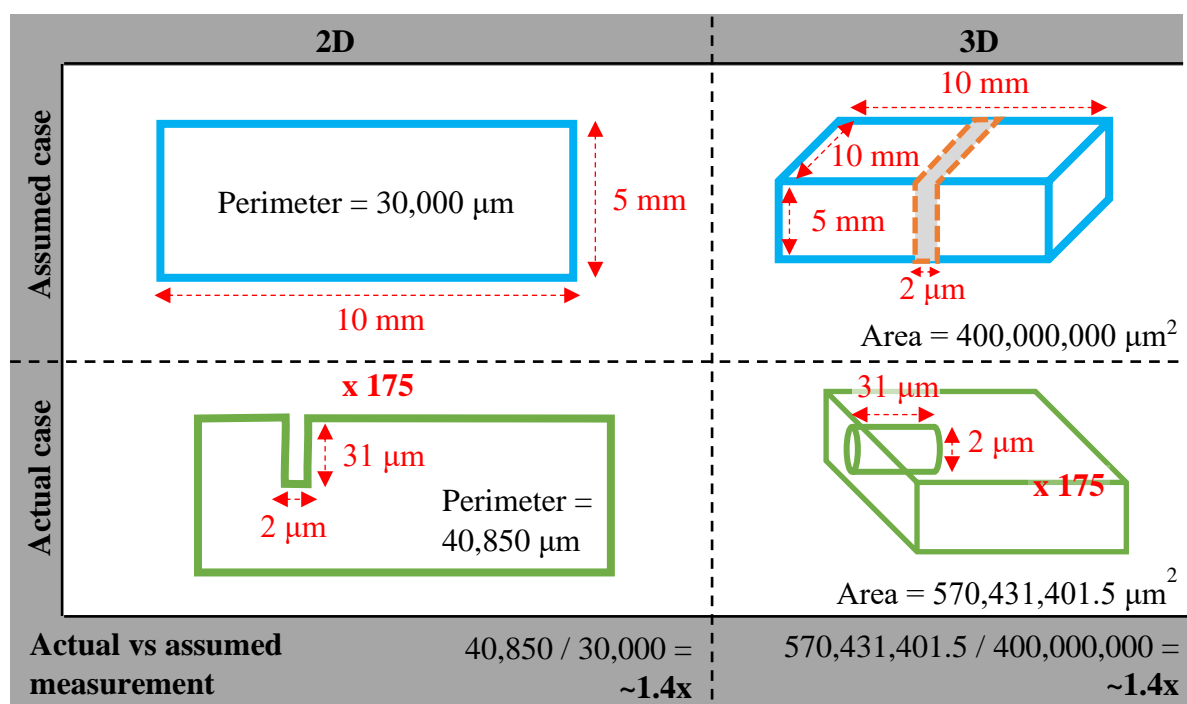


**Figure 7.18.** 2D and 3D methods of estimating the effect of vermiform features on sample surface areas

Applying these corrections would result in a surface area to volume ratio (SA:V) of 14-16  $\text{m}^{-1}$  for MCC-1 experiments, which differs considerably from the assumed value ( $10 \text{m}^{-1}$ ) used in normalised mass loss calculations. Inter/intra-study comparisons will not be devalued by this if these features are universal (in scale/abundance) across all experiments/studies – for example in Chapter 5 where the vermiform features appear relatively uniform across the variable Mg:Ca series. However if the features result from an extrinsic factor/process (e.g. sample preparation), then inter-study comparisons may be undermined. Significant further research, discussion and analysis of these features is nevertheless recommended before correction factors are applied; particularly given no other authors have previously considered them necessary.

### *Nuclear waste disposal*

MCC-1 tests are commonly used in nuclear waste glass durability assessments [254] and therefore play a crucial role in supporting the nuclear waste safety case. It is thus critical that any method limitations and (potentially false) assumptions are comprehensively evaluated such that the likelihood of adverse consequences can be estimated with a reliable uncertainty.

In MCC-1 experiments, surface areas are implicitly assumed to remain constant throughout. The ASTM C1220 standard states that surface areas should be calculated pre-dissolution and based on monolith dimensions [194]. In this protocol, every effort is made to ensure the reliability of this value by adequately polishing specimens and making corrections for sample porosity and ‘nicked’ edges [194]. However, no effort is made to account for any change in this value with dissolution duration. In reality surface areas may vary with dissolution duration – either decreasing as glass surfaces are dissolved/removed [102], or increasing as localised attack features (including vermiform features) are developed. Though these effects may counterbalance, this cannot be verified until a comprehensive study into the variability of surface area with dissolution duration has been conducted. Currently this surface area variability remains uncorrected, despite the comparable time-dependency in leachate volumes being corrected for via the use of leachate volumes measured at the *end* of experiments (after evaporative loss). Applying a comparable correction to surface areas (e.g. by multiplying values by 1.4) has a reciprocal effect on  $NL_i$  values (i.e. these decrease by a factor of  $\sim 1.4$ ).

### *Glass dissolution processes/kinetics/alteration layers*

As considered for other localised attack features [92], the formation of vermiform features may be coupled with alteration layer formation. Dissolution of vermiform features likely provides elements for alteration layer formation, but alteration layer formation may also infill and thus reduce the effect of vermiform features, potentially also ‘protecting’ them from further growth. This coupling is poorly understood, however further research in this area may provide insight into alteration layer development and characteristics (including potential layer heterogeneities).

Vermiform features also influence sample surface areas which have been found, for a given leachant volume, to strongly influence glass dissolution reaction kinetics [318]–[321] and alteration layer thickness [319]. For a set leachate volume, with increasing surface area there is comparatively less solvent to dilute any hydroxide/alkalis released during Stage I dissolution, so pH is able to increase more in higher SA/V experiments [318]. The less dilute conditions in higher surface area experiments also allows more rapid achievement of residual rates. Finally, with increasing surface area comes a potential decrease in alteration layer thickness (because less glass must react to attain the same level of saturation) and an increase in alteration layer growth rates (as saturation is more rapidly approached) [319]. Thus, if vermiform features can be shown to increase glass surface areas, they can also be inferred to impact alteration layer thickness and growth rates, as well as experimental pH values and dissolution stage durations.

### *Other perspectives*

Vermiform features also have a multidisciplinary significance. Geologists often use vermiform features to indicate biologically mediated weathering [119], whilst palaeontologists postulate that vermiform features (in basaltic glasses) evidence some of Earth’s earliest life [322] and astrobiologists hypothesise that worm-like features may, one day, become the first evidence of extra-terrestrial life that we obtain [144], [323]. However all of these relevancies require vermiform features to be exclusively caused by biological processes, which may be questioned.

### 7.3.4. Origin and formation of ‘typical’ (simple) vermiform features

#### *Biotic*

The resemblance of these features with plant roots and microbial borings necessitates a discussion surrounding a potential biological origin. Vermiform features with smooth edges, constant diameters and rounded ends are often used to suggest a biological origin [120], [324], [325]. To generate these ‘tunnels’, microbes can excrete glass-dissolving substances [102], whilst plant roots can extend via chemical attack or by exerting pressure after infiltrating micro-flaws [326], [327]. Both mechanisms could *theoretically* form the features observed in Section 7.2, however this appears highly unlikely.

This is because experiments were conducted in a clean laboratory where the likelihood of biological contamination is negligible. All reagents and solutions were of a laboratory grade and were stored appropriately to minimise potential biological influences. A source of carbon (other than that in the atmospheric air within the vessel) was also absent in experiments and no microbes were observed (or suspected) in SEM or XCT. Furthermore, no biological material was added to experiments and even if microbes were able to enter vessels during experiment initiation, these organisms would have been unlikely to be sufficiently adapted to survive the nutrient-poor, alkaline (pH 8.5 - 9.5) high temperature (90 °C) environment within vessels. Finally, it has been theorised that biological glass borings are near-impossible to generate in laboratory experiments (even if microbes are purposefully added) because the boring process is so unavoidably slow [102]. Given the latter, it seems highly unlikely that the vermiform features shown in Section 7.2 could be formed via biological processes.

Nonetheless, further attempts were made to refute a potential biological influence or origin. Evidence of living, or once-living, matter was sought by analysing leachates for the presence of DNA. Leachate samples were tested (by Dr. Victoria Workman at The University of Sheffield) for the presence of double-stranded DNA (dsDNA) via a Quant-iT™ PicoGreen™ dsDNA Assay test. This was performed on unacidified MCC-1 leachate aliquots which had been speculatively retained. Leachates from two experiments (0Ca100Mg basaltic glass dissolved for 461 days and ISG dissolved for 224 days) were tested and analysed in three forms: (1) without further processing, (2) after they had been concentrated and (3) after attempts were made to extract genomic DNA (gDNA) via the EtNa protocol [328]. No detectable DNA was identified in any samples. Though tests would have been unable to detect life at concentrations less than 5-200 million cells per millilitre and testing required DNA to be extractable from cells (questionable given the cell robustness required for life in the relatively harsh conditions within MCC-1 vessels), this null result is consistent with the aforementioned considerations.

#### *Abiotic*

Given that a biological cause is unlikely, various abiotic formation mechanisms for the simplest vermiform features may instead be considered. Such mechanisms typically involve preferential dissolution around a structural, morphological and/or chemical precursor. Chemical attack may progress quicker around these features via a positive feedback effect: dissolution of the precursor will generate an aggressive high-pH leachate which promotes further dissolution, especially if this leachate is retained in crevasses where diffusion with the bulk leachate may be reduced [46], [91], [92].

Structural precursors may include highly strained low angle bonds within the glass structure. However, glass structure analysis is beyond the scope of this work. Similarly, chemo-structural precursors may include alkali channels which may undergo preferential dissolution. The glass characterisation techniques used here would be unable to resolve these atom-scale features, however alkali channel features have been hypothesised in HLW glasses previously [128], [129]. Alkali channels may provide an initial precursor for vermiform feature growth (much like they have been proposed as the precursors to Griffiths flaws [329]), however further growth may then be independent of the alkali channel path.

Purely chemical precursors may include macro/micro-scale compositional variations, however phase separation or significant spatial compositional variations were not noted during pre-dissolution characterisation via SEM-EDS.

Finally, morphological precursors are also possible. Though every effort was made to thoroughly polish samples to a mirror-like (1  $\mu\text{m}$ ) surface finish, micro-scratches and other polishing remnants may, conceivably, have remained. Similarly, microfractures may have been present in the monoliths even if they were not evident optically or via SEM prior to dissolution experiments. This hypothesis is consistent with potential observations of increased vermiform feature abundance at monolith corners where preparation-induced damage is likely greatest. During sample preparation monolith corners were sometimes lost due to fracturing and, although monoliths with missing corners were not used in experiments, this illustrates that corner fracturing is common (as is also noted elsewhere [236]). Though this hypothesis may be less consistent with the observed compositional dependence of vermiform feature abundance (given all monoliths were prepared identically), this may be related to compositionally-dependant glass properties. Mechanical properties including the fracture toughness may have varied between compositions, potentially increasing the propensity for microfracture development in basaltic glasses. Any scratches/cracks may have promoted retention of the highly-aggressive high-pH leachate that forms during initial dissolution and may thus have promoted vermiform feature development [110], [130]. A cause related to sample preparation is also consistent with other studies [110], [130], [236].

The hypothesis that features result from polishing defects may explain why features, in some cases, cluster. Micro-scratches may cluster into a small area/region over which not all scratches from the previous polishing stage have been removed. Single scratches may also exist however, allowing generation of more solitary features. Features within clusters may be unequally spaced due to the random nature of polishing (diamond particles will be randomly distributed across polishing cloths) and potential contamination of grinding/polishing materials may allow introduction of rare 'deep' scratches that were not fully removed in later polishing stages.

Mechanisms able to generate the enigmatic morphologies of vermiform features can also be discussed. Even simple vermiform features were occasionally noted to have sinuous curvilinear paths. This may be associated with the lack of long-range order in glasses: preferential attack of strained bonds, which are located near randomly throughout the glass, may divert the course of vermiform features. The lack of long-range order means glass does not contain the crystallographic planes which preferentially dissolve to produce straight features in crystalline materials [330], [331]. Essentially, there are no reasons why vermiform features would generally be straight in glasses as no linear structural features are present in glasses.

### 7.3.5. Origin and generation of atypical vermiform features

Though only occasionally observed, the characteristics outlined in Section 7.2 (particularly Figure 7.4) may offer insight into how the more common features were formed, and they may also be used to illustrate why previous indicators of biogenicity must be reevaluated.

The widening of vermiform features towards the glass surface (Figure 7.4) may be indicative of biotic or abiotic processes. Funnel-shaped vermiform features, tapering in width from a materials surface inwards, have previously been used to suggest biological origins [116], [317], [332]. Such morphologies may develop as microorganisms initially spend a period of time inhabiting (and thus dissolving) the material surface before they later ‘tunnel’ into the substrate [102]. However, this tapering shape may also form via abiotic alteration of (micro-)fractures, as is occasionally overlooked in biological literature. Deeper areas within a fracture may have decreased fluid exchange with the bulk leachate, allowing accumulation (and increased saturation of) elements dissolved from the glass and thus decreased driving force for dissolution [333]. More rapid dissolution of fracture areas nearer the surfaces via this mechanism is expected to create a tapering vermiform feature morphology as in Figure 7.4. This may also explain the feature branching: Once vermiform features have achieved a critical length, growth at the ‘tip’ may slow, allowing the focus of attack to move up the fracture walls.

Similarly, helicoidal structures have previously been used as evidence of biogenicity [334]. Helical morphologies are commonly associated with living cells [335] including cyanobacteria (*Oscillatoria*, spirochaetes [144]), fungal hyphae (*Trichophyton mentagrophytes* var. *Mentagrophytes* [336]) and iron-oxidising bacteria (*Gallionella Mariprofundus* [337]). The evolutionary advantage provided by such spiral growth is unclear, however it may reflect a growth and/or feeding strategy [334]. Helical forms are also recognised in palaeontology – with the ichnospecies “*Tubulohyalichnus spiralis*” recently defined to encompass features [334] after their previous classification as ‘helical channels’ [335], ‘spiral structures’ [338], ‘helical tubes’ [115], [145] and ‘spiral tubes’ [339]. However, helical forms can also be generated via abiotic processes. For example, Ambient Inclusion Trails (AITs - formed via the propulsion of mineral crystals through a matrix) with helical morphologies have been reported [137], [340]. AITs are not considered a viable mechanism for vermiform features presently, however the ability for abiotic mechanisms to mimic biological forms (known as ‘biomimicry’) is of note. Crystallization and polycrystalline aggregate formation can also generate helical forms [144] including in experiments using organic gel media [341] and inorganic carbonates within alkaline silicate solutions [342]. Though these experiments involve organic matter or a carbon source, similar helical features (described as “pigtailed”) are hypothesised to form via self-organization during silicate glass corrosion [74] and in abiotic experiments of polymeric hydrogels [343]. The exact feedback mechanism responsible for this has not yet been identified, however it is thought to relate to pH-induced gel shrinkage and helical crack growth [74].

Vermiform features that appear unconnected from the monolith surface (Figure 7.4) are likely to be connected to the surface in three dimensions (outside of the plane of view). These features must relate to dissolution (as features were absent in equivalent micrographs from undissolved monoliths or monolith interiors) and dissolution is a *surface* process. Features also resemble forms which are observably connected to the surface (and hypothesised to be formed via dissolution) in most cases. Though features are hypothetically connected to the sample surface in other planes of view, this need not necessarily imply that the features themselves are planar. Tubular morphologies intersecting the plane of view may also generate this morphology.

### 7.3.6. Chemical garden experiments

Chemical garden experiments may provide an explanation or analogous system for vermiform feature growth. So called because they generate structures resembling plants, these experiments can *abiotically* generate tubular, helical, tapering, sinuously curvilinear and branching forms potentially comparable to vermiform features [144].

Chemical garden experiments typically involve a metal salt crystal dissolving in alkali silicate solutions (Figure 7.19). As the salt dissolves, the resulting acidic leachate reacts with the surrounding alkali medium to generate a semi-permeable silica gel membrane [144]. Inflow of water through this, a result of osmosis, subsequently increases the pressure contained by the membrane until its eventual rupture releases the acidic solution as a ‘column’ which rises buoyantly [344]. This column is rapidly ensheathed by a new gel membrane in the form of a thin tube which may remain open at the tip [345]. Growth of this, and potentially other tubes, will continue until the salt is wholly dissolved. Morphological complexity of features is widely reported and is considered a potential result of complex fluid dynamics [345]. Variation on this ‘classic’ experiments is also possible: solutions may be aluminates, borates, carbonates, chromates, cyanoferrates, phosphates, or silicates [346] and the metal salt need not be solid [345], [347].

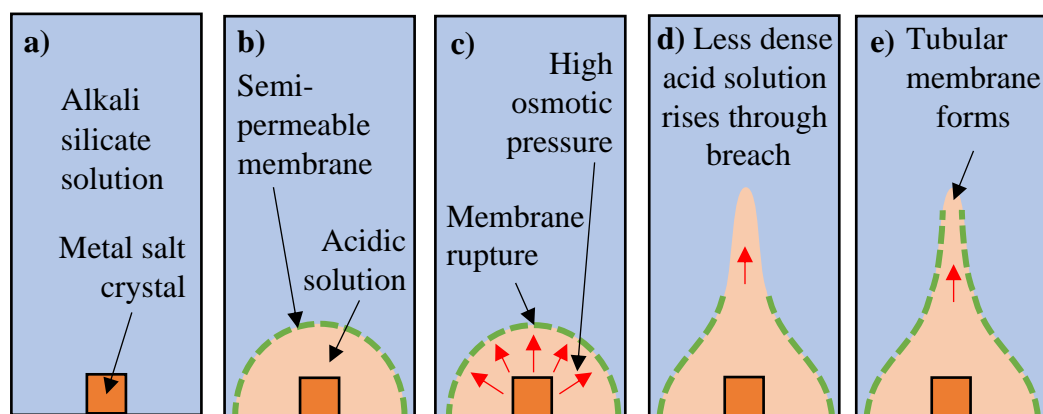


**Figure 7.19.** In chemical garden experiments, dissolution of metal salt within an alkali silicate solution (a), forms a semi-permeable membrane between basic and acidic solutions (b). Pressure confined by this membrane then increases (c) until rupture releases an acidic solution column (d) which is ensheathed by a new semi-permeable membrane tube. Figure after [345].

Chemical garden features grow as a result of an osmotic pressure gradient across a semi-permeable membrane separating two liquids. This phenomena cannot thus directly explain the formation of vermiform features which penetrate an apparently *solid* glass. An osmotic gradient simply does not exist between such a solid and a liquid. Notwithstanding that, chemical garden growth into a gel medium is reported [341], [348], [349] and glass alteration can form gel layers [66], [72], [73]. However, the vermiform features observed in Section 7.2 appear to penetrate pristine glass – not a gel layer. Hence, chemical garden experiments can only provide a potential analogy, not a direct explanation for the vermiform features observed in the present experiments.

Dissolution of a ‘seed’ feature at the glass surface remains a plausible mechanism of vermiform feature generation, however. This may generate a corrosive solution which encourages localised attack and the formation of a ‘tunnel’. The absence of such a ‘seed’ feature in SEM

observations may be because features are of a scale unresolvable via SEM or the seed has completely dissolved. The central high atomic number enrichment within some vermiform features may relate to the movement (or ‘digging down’) of this seed material. The seed, or at least central enrichment zone, is speculated to be iron-rich on the basis of the high contrast in BSE images, however EDS verification of this is not possible due to limited resolution. Potentially comparable preferential dissolution below crystallites (formed during glass cooling) at the surface of glasses has been tentatively speculated elsewhere [236] and was considered a potential mechanism for generation of depleted zone surrounding spinel crystallites in Chapter 4.

#### **7.4. Summary**

Vermiform features, distinct from dissolved fractures, have been observed in MCC-1 experiments and show variability across the studied glass compositions. Vermiform features are abundant on dissolved basaltic glasses, with features partially filled by the sole surface (alteration) layer present. This layer contains a high-atomic number central strand where it penetrates features. Vermiform features in basaltic glasses may be observed to taper, cluster or branch, with spiralling of the central strand also observed. The equivalent features on HLW glasses are less abundant, less complex and are typically shorter. Vermiform features on MW25 are entirely filled by surface Layer 2, which again shows a central zone enriched in high-atomic number elements. Vermiform features in MW25 do not interact with surface Layer 1 and are associated with a ‘splaying’ and absence of Layer 3 protrusions. Vermiform features in ISG are largely unfilled, containing only a thin ‘coating’ of Layer 1. Surface Layer 2 appears to arch around these features, whilst Layer 3 appears unaffected by the feature’s presence. XCT investigations imply features are tubular (not planar), but this cannot be stated conclusively as only a single feature was observed. This may result from limited instrument resolution and/or sample size and unequal feature distribution across the sample

Feature formation may be more progressed in basaltic glasses compared to HLW glasses, with this allowing greater abundance, complexity and length of features in the former. Variability in infilling may be correlated with variable alteration layer thicknesses, but may also indicate differing causal mechanisms. Regardless, features are estimated to increase sample surface areas by a factor of ~1.4, as may cause discrepancies in MCC-1 calculations (which assume a constant surface area measured geometrically and prior to dissolution). This may introduce previously unidentified uncertainty into models underpinning nuclear waste disposal.

Though comparable features are often considered to have exclusively biological origins, this is considered highly unlikely here given every effort was made to exclude organics. DNA, though sought, was also not found. Instead, preferential dissolution of a precursor feature is considered most likely – with plausible initiation points including alkali channels, highly strained bonds, and/or micro-scratch/fractures. Speculatively, the latter precursors are considered most plausible as these can explain feature clustering and potential abundance increases towards monolith vertices (which can become damaged during sample preparation). Preferential dissolution below/around a ‘seed’ material/crystal may also be possible, as inspired by analogue chemical garden systems. Whatever the mechanism(s), these appear able to abiotically generate novel vermiform feature characteristics (including funnel morphologies and helical forms) which have previously been used to infer biological processes. The use of such vermiform features in proving biogenicity can thus be called into question.

# 8. Potential Alteration Layers & Dissolution Features in Vitrified Hillfort Materials

## 8.1. Introduction

Materials from vitrified hillforts have unique advantages as HLW glass analogues [161], with samples from Dun Deardail vitrified hillfort particularly valuable from this perspective given the sites meteorological location (Figure 8.1). Vitrified samples from here were formed in ~310BC by burning, melting and quenching the fortification’s timber-laced stone ramparts to produce a glassy material which has since been exposed to high precipitation near-surface conditions (and thus potentially meteoric- and ground-waters) for almost 2,500 years. These materials may thus offer insight into glass dissolution behaviour.

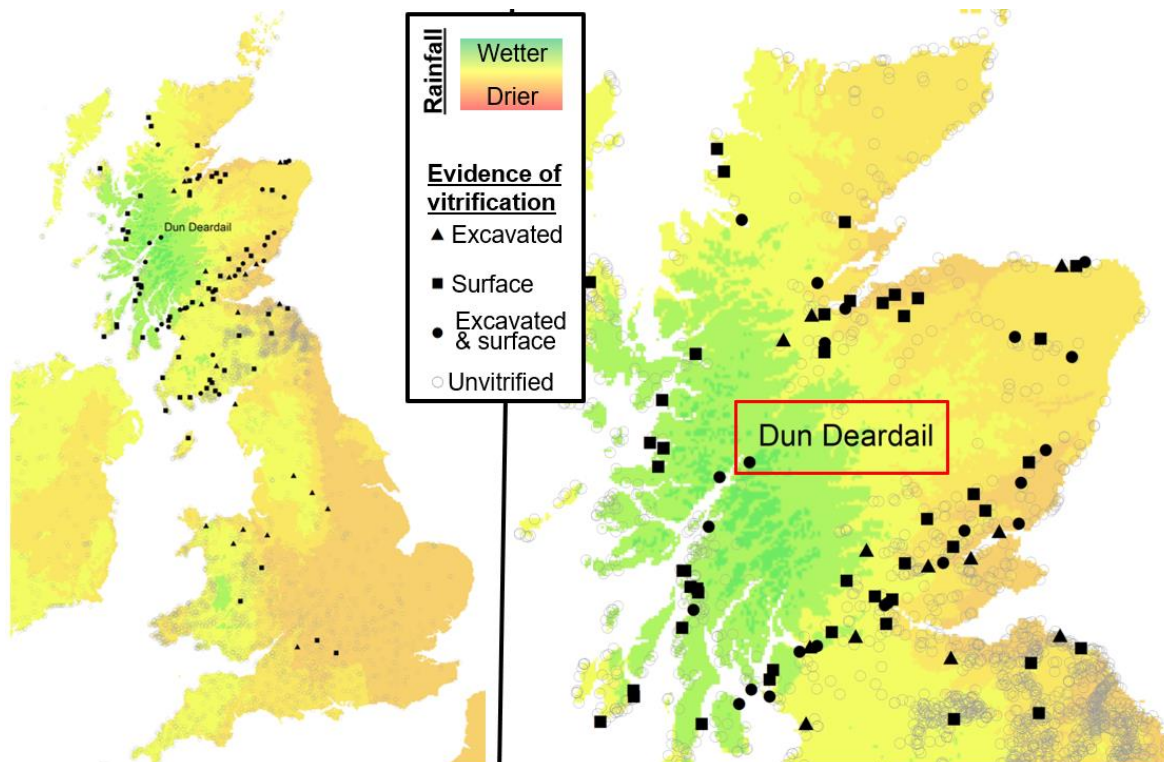


**Figure 8.1:** UK hillfort map, with vitrified hillforts assigned solid symbols – the shape of which indicates where vitrification evidence was found. Base map shows total annual precipitation from “wettest” (2,001-2,500 mm/yr; green) to “driest” (501-750 mm/yr; orange) with Dun Deardail located in the “wettest” category. Hillforts replotted after Lock & Ralston [175] and Kreston & Kreston [350]; base map and climate data from WorldClim [351].

In this chapter, samples collected from Dun Deardail vitrified hillfort (as in Section 3.1.2) are characterised to both probe the suitability of the materials from a glass analogue perspective and to seek evidence of dissolution. XRD was used to verify the presence of glassy material, before visual observations, SEM-EDS and XCT were used to infer the distribution and location of this material. Potential dissolution features were then identified via optical microscopy, SEM-EDS and XCT, before the likelihood that these features were formed via dissolution was assessed using comparisons with a synthesised replica glass, theoretical considerations and a qualitative analysis of material distributions across the sample surface.

## 8.2. Results

### 8.2.1. XRD

Figure 8.2 shows XRD patterns collected from a hillfort sample and the material synthesised to simulate the glass within this (see Section 3.1.4). In the hillfort sample, a subtle broad region of diffuse scattering is observed from 15-35 °2 $\theta$ , however this is diminished in relative intensity by multiple sharper and more intense peaks. In the synthesised simulant material, a similar region of diffuse scattering from 15-40 °2 $\theta$  is observed, with an additional single sharp peak at ~22 °2 $\theta$ .

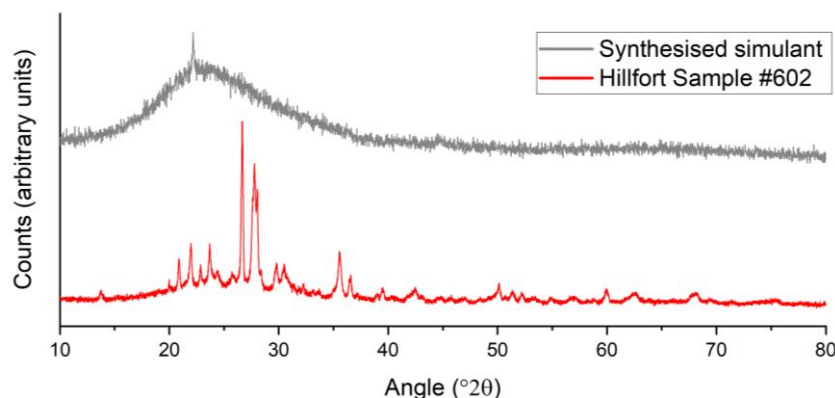


**Figure 8.2:** XRD trace of hillfort sample #601-602 and the synthesised replica material.

### 8.2.2. Visual sample inspection

Hillfort samples were visually inspected and catalogued prior to any analysis. Samples differed considerably in appearance, however broadly all samples contained vesiculated regions, often with a vitreous lustre, which separated more angular ‘clasts’. Flow textures were occasionally observed as bulbous protrusions, with some vitreous vesicle interiors appearing rusty-red/brown in places (Figure 8.3a). A patchy superficial coating of soil-like material and plant rootlets was also observed on some hillfort samples. Finally, the replica simulant hillfort glass was observed to contain abundant vesicles (Figure 8.3c).

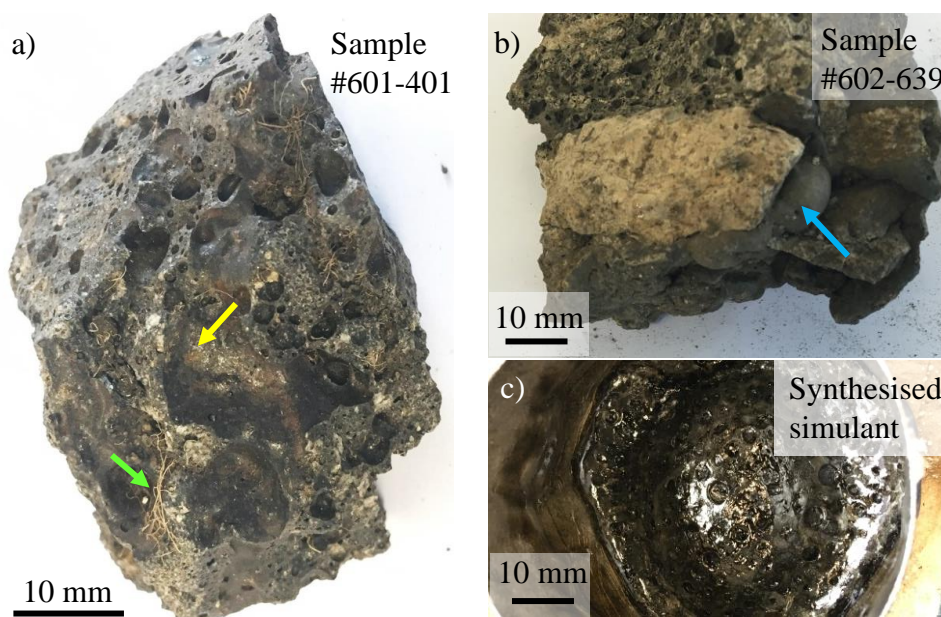


**Figure 8.3:** Hillfort sample photographs (a,b) show vitreous vesicle interiors occasionally with a rust-red surface coating (yellow arrow), plant rootlets (green arrow) and evidence of flow (arrowed in blue). Simulant replica material (c) noted to contain abundant vesicles.

### 8.2.3. SEM-EDS

SEM-EDS was used to estimate the composition of featureless (crystal-free) homogenous areas in hillfort samples. As outlined in Section 3.1.4, this alkali-aluminosilicate composition (Table 3.4) was used in synthesis of the replica glass. Which was observed to be homogenous and crystal-free in SEM. SEM-EDS elemental maps and line-scans revealed no consistent changes in the composition of hillfort samples towards potentially exposed sample surfaces, with no surface de-alkalisation found.

SEM-EDS analysis of the thin section from hillfort sample #410-401 reveal cavities (probable vesicles) were occasionally rimmed by iron-rich layers (of 2-10  $\mu\text{m}$  thickness; Figure 8.4). In one instance, an irregularly-shaped feature at the edge of a cavity (Figure 8.5) was observed to grade from iron/sulphur-rich (proximal to the sample surface) to more titanium/iron rich compositions moving from the vesicle surface into the glass. In many instances, remnants from sample preparation (completed externally as in Section 3.3.1) were observed in these cavities.

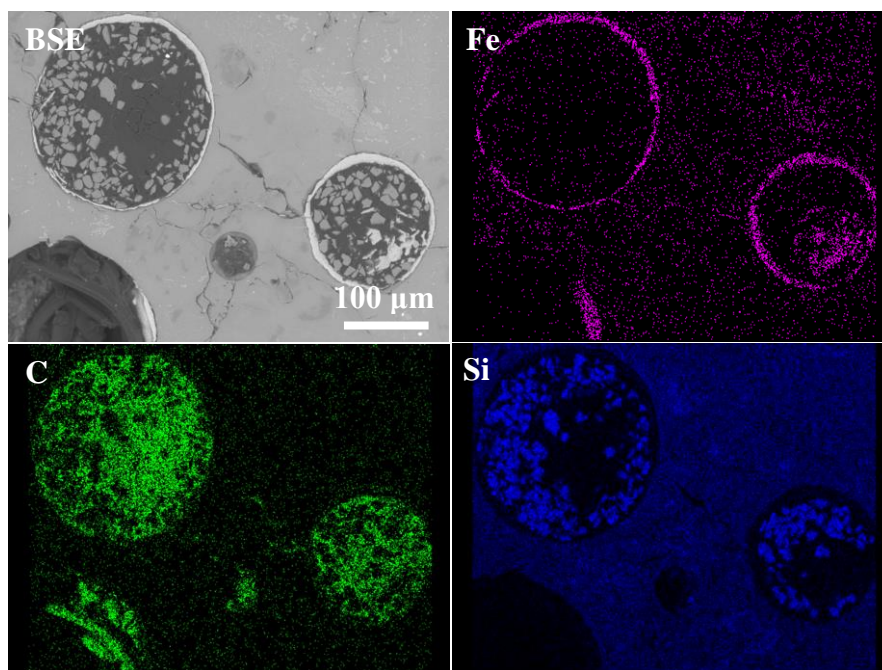


**Figure 8.4:** SEM-EDS of hillfort Sample #410-401 shows iron-rich cavity rim. Silicon-carbide grains within the cavity are remnants from sample grinding (conducted externally).

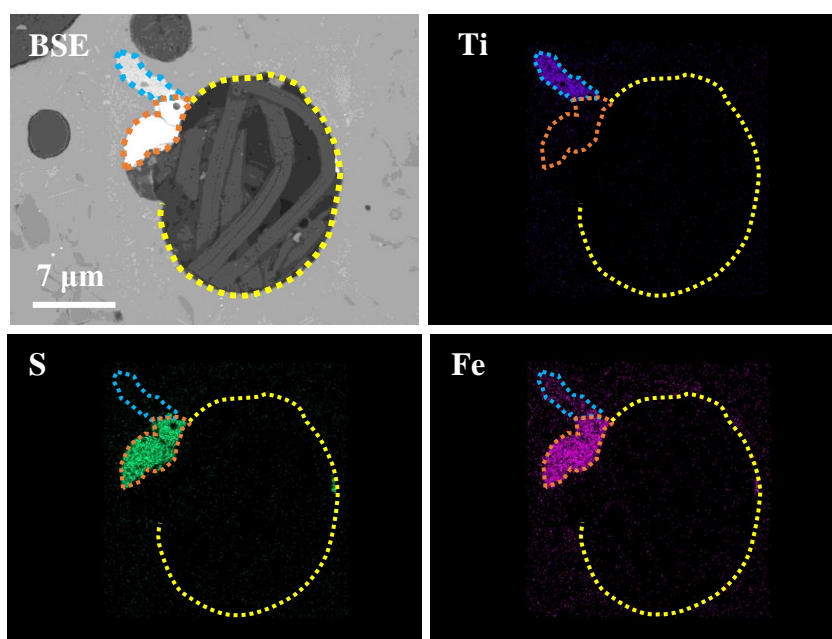


**Figure 8.5:** SEM-EDS of hillfort thin section (Sample #410-401) shows gradation of FeS area at the edge of a cavity into an FeTi area moving away from the vesicle. Note the (carbonaceous) strands within cavities (also evident in the lower right of Figure 8.4) are polishing cloth fibres.

#### 8.2.4. Optical microscopy

Optical micrographs of the synthesised hillfort replica material show iridescent areas containing abundant ( $<1 \mu\text{m}$  diameter) cavities. These cavities are also elsewhere observed to be filled by iridescent material (Figure 8.6).

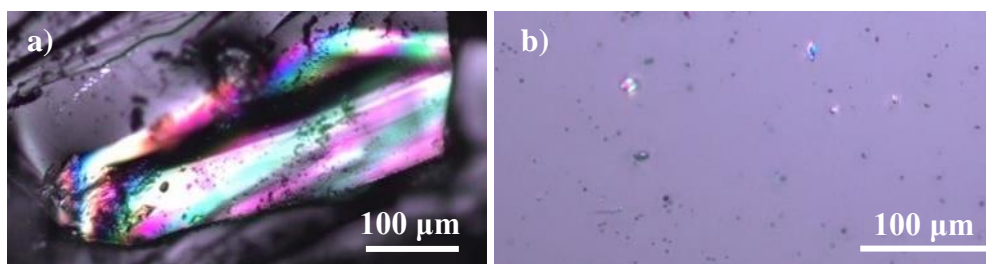


**Figure 8.6:** Simulant hillfort replica material micrographs show cavitated iridescent areas (a) and cavities filled by iridescent material (b).

Hillfort samples show similar circular cavities ( $\leq 1 \mu\text{m}$  in diameter) that are occasionally filled by iridescent material (Figure 8.7a-b). Entire areas of similarly cavitated iridescent material are also observed (Figure 8.7c) and larger cavities (probable vesicles of 100-300  $\mu\text{m}$  in diameter) are occasionally lined by (a 20-60  $\mu\text{m}$  thickness) rim of orange-brown material (Figure 8.7d).

Thin sections taken from hillfort samples also show abundant cavities (5  $\mu\text{m}$  to 3 mm in diameter) and fractures. Cavities are occasionally lined by material of a similar greyscale to the bulk sample (2-15  $\mu\text{m}$  in thickness; Figure 8.8a) or darker material which also contain multiple white, angular irregular polygons ( $\sim 10 \mu\text{m}$  diameter; Figure 8.8c). Similar ‘bright’ features were also observed within fractures in regions proximal to the sample surface (Figure 8.8d).

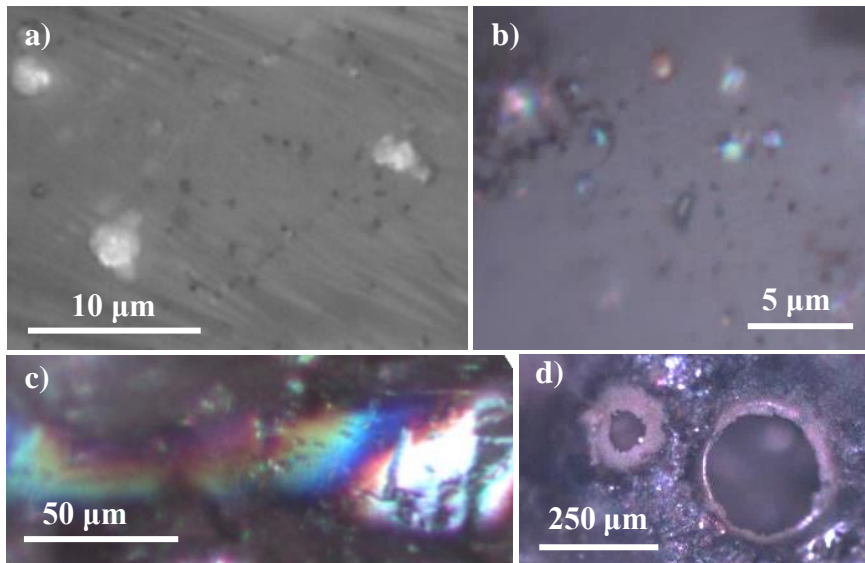


**Figure 8.7:** Hillfort sample #601-602 shows cavities (a), which are filled by iridescent material (b), coated by a rusty-brown material (c), and within iridescent areas (d).

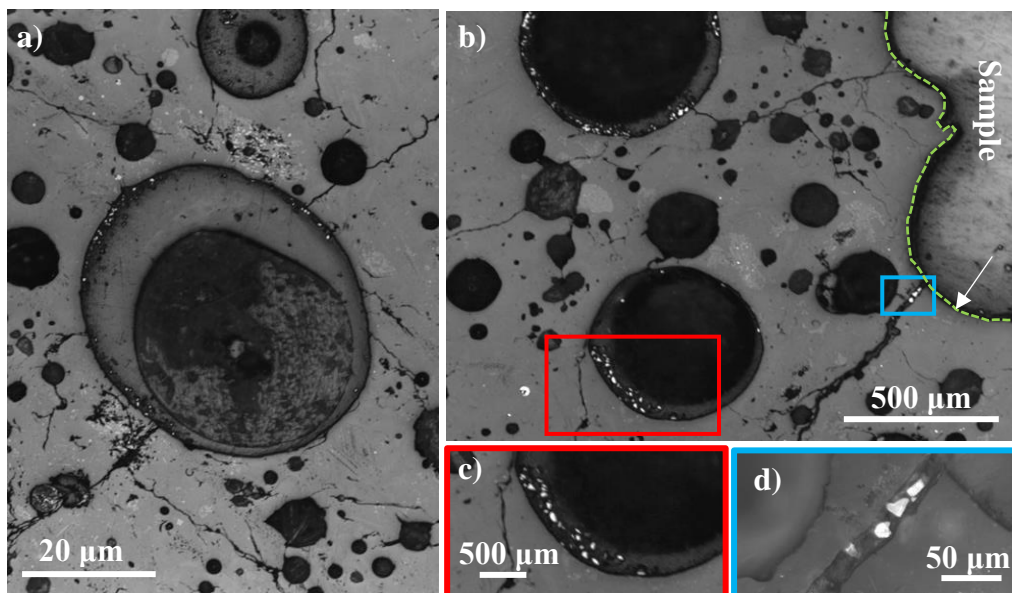


**Figure 8.8:** Hillfort thin section (Sample #410-401) shows cavities with lining which resembles the bulk material (a), cavities with a darker coating which contains bright white polygonal features (b, c) and bright polygonal features within fractures near the sample surface (b, d)

### 8.2.5. XCT

Initial observations indicated significant sample heterogeneity (Figure 8.9). However, all samples contained regions of cavity(vesicle)-rich material which comprised between ~5% and ~95% of the solid sample volume. These regions encompass angular to sub-angular clasts containing significantly fewer cavities and that are either internally homogenous (e.g. Figure 8.9d) or may show layering (Figure 8.9a). The boundary between these cavity rich/poor zones is sharp and well defined, often by contrast (density) variations or alignment of cavities (Figure 8.9). Samples may also contain internal fractures (e.g. Figure 8.9e) and Sample #601-602 showed significant layer deformation (e.g. Figure 8.9c).

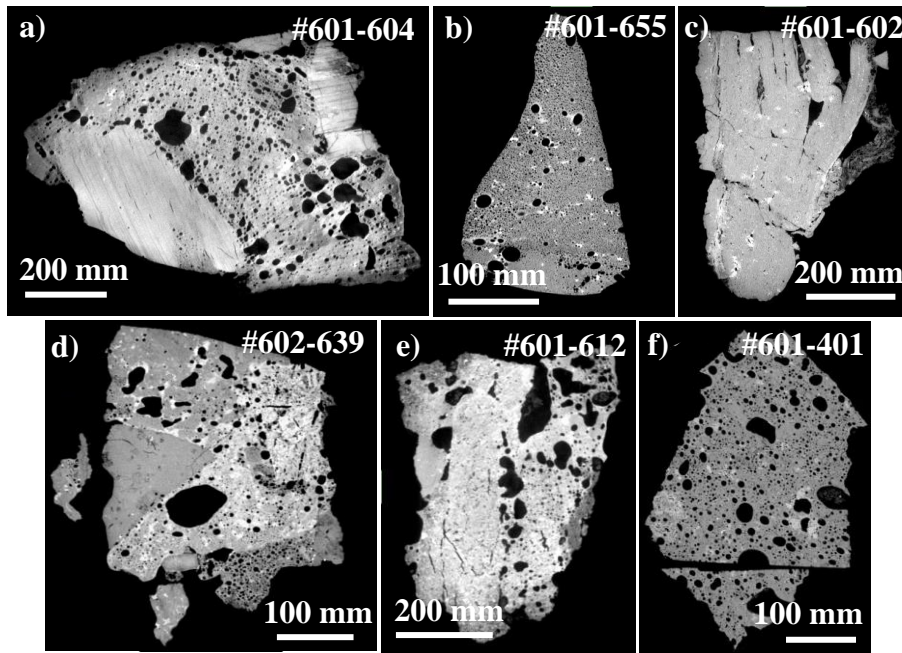


**Figure 8.9:** XCT images of hillfort samples (identified in figure). Note highly vesiculated regions separate poorly/non-vesiculated zones.

Surface-proximal regions with a darker appearance (lower density) than the bulk sample were identified as of potential interest. This material was evident as: (1) arcuate/crescent shape occurrences within vesicles (Figure 8.10a-c), (2) clusters of well-rounded particles at the sample surface (Figure 8.10d-f) and (3) fracture infilling (Figure 8.10g-i).

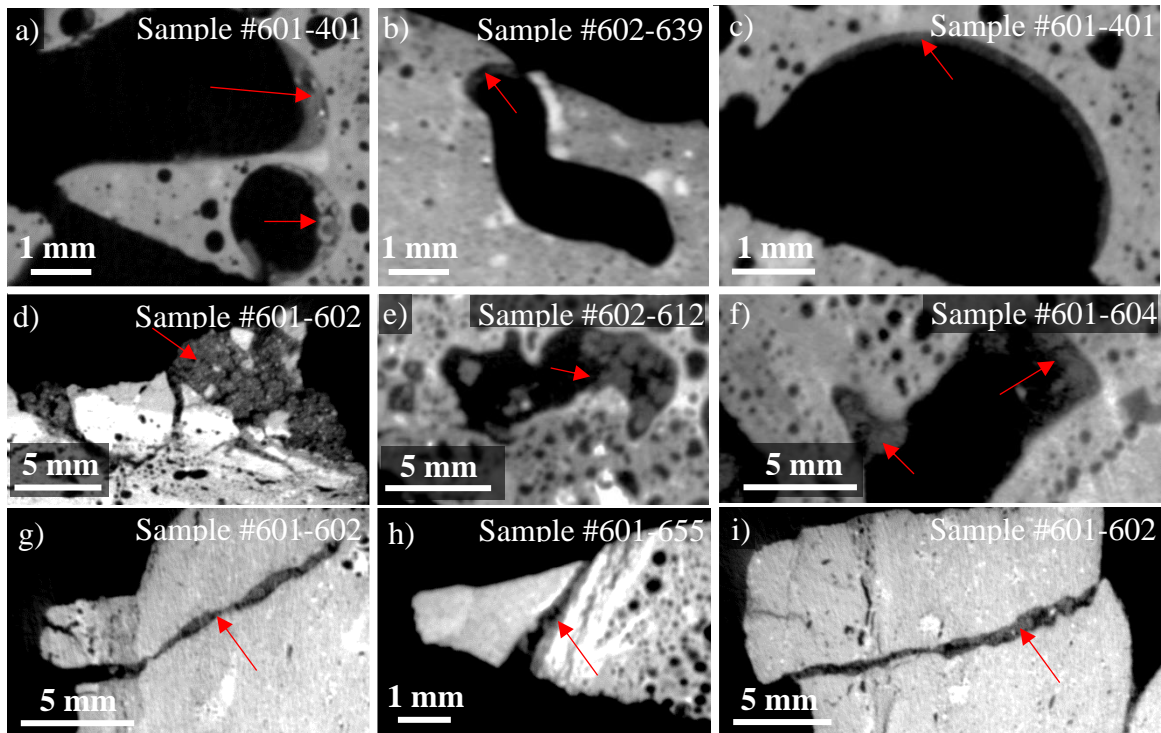


**Figure 8.10:** XCT images of hillfort samples (identified in figure) showing near-surface regions with a darker appearance than the surrounding/bulk material (arrowed in red).

A quantitative method was developed to analyse the distribution of this low density (i.e. ‘dark’) material relative to sample surfaces and the accessibility of those surfaces to the external environment. This method (described fully in Appendix I) involved segmenting the solid sample, ‘air’ and the Dark Regions Of Interest (DROI) via thresholding. The ‘air’ was then subdivided by accessibility (connectedness to the exterior environment) and a region within a given vicinity (200  $\mu\text{m}$ ) of in/inaccessible sample surfaces was generated. The intersections of these regions with the potential dissolution features (DROI) was then determined and expressed relative to values estimated by supposing a random DROI distribution.

Figure 8.11 shows that compared to a random distribution, there is a positive deviation in occurrence of these dark regions in the vicinity of accessible surfaces and a negative deviation for occurrence in the vicinity of inaccessible surfaces. Essentially, there are more dark regions of interest in the vicinity of accessible surfaces and less in the vicinity of inaccessible surfaces than could be expected from an entirely random distribution of material. Deviations appear large ( $\pm 30\text{-}60\%$ ) for datasets #602-639 and #601-655, but minimal ( $\sim \pm 10\%$ ) for datasets #601-612 and #601-604. Plotted error bars overlap in datasets #601-604 and come within 5% in datasets #601-612, #601-602 and #601-604. In these datasets the trend is thus deemed to be of negligible and minimal significance, respectively.

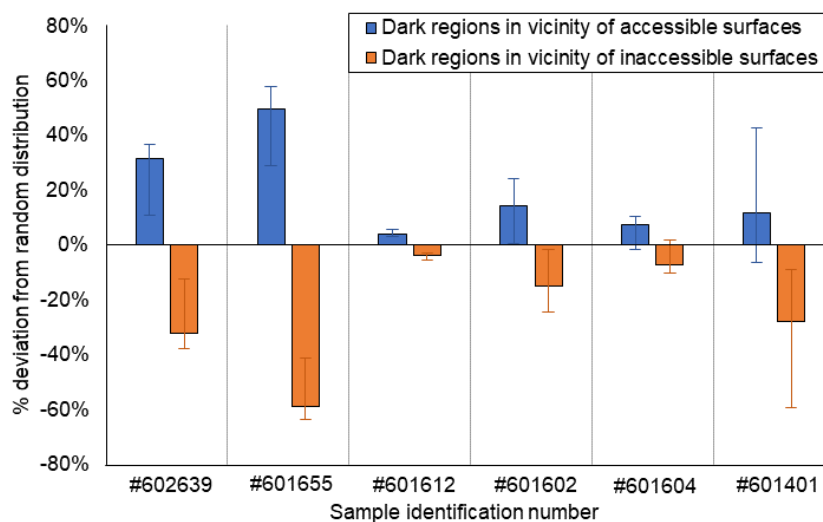


**Figure 8.11:** Results from qualitative analysis of dark region occurrence relative to surface accessibility for hillfort samples. Values show deviation from random surface distribution, with error bars produced by varying thresholding values (by  $\pm 1SD$ ) as outlined in Appendix I.

## 8.3. Discussion

### 8.3.1. Bulk sample characterisation

#### *Hillfort samples*

XRD (Figure 2.3) indicates the presence of amorphous material in hillfort samples, implying the presence of glassy matrix. This is hypothesised to correspond to the highly vesiculated material evident in SEM-EDS, XCT and optical microscopy. This material preserves evidence of molten flow (Figure 8.3) and must have been rapidly quenched in order to retain its vesicularity, hence formation of a glass seems probable. Hypothesising vesiculated regions are glassy is also consistent with other vitrified hillfort studies, [352], [81], [164], [353]–[358], observations of vitreous vesicle interiors (Figure 8.3) and the highly vesiculated appearance of the synthesised replica glass.

Crystalline peaks within the XRD pattern are attributable to minerals (identified in Figure 8.12) either from un-melted protoliths, or which were precipitated from the melt or incompletely melted in the first instance. Magnetite and quartz are likely derived from the pelite/schist protolith used in wall construction [175], with plagioclase feldspars either similarly originating from (diorite) protolith and/or crystallised from the melt [175]. These minerals have been similarly identified in other vitrified hillfort samples [81], but are of negligible interest to glass dissolution studies. None of the minerals identified in Figure 8.12 are thought to result from hydrothermal-type or dissolution reactions.

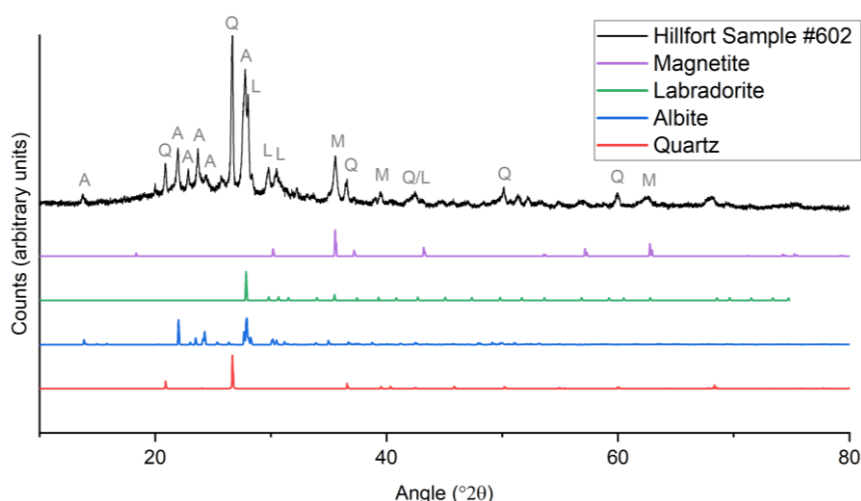


**Figure 8.12:** XRD trace of hillfort sample #602 showing crystalline peaks which can be attributed to magnetite, plagioclase feldspars (labradorite and albite) and quartz

Un-melted protolith is evident as the poorly vesiculated angular regions in XCT and SEM. These regions frequently retain their original geological features (e.g. bedding/lamination, mineralogical phenocrysts) and show minimal evidence of vitrification/melting. However, significant heat exposure of these is preserved as sample fracturing, delamination and warping [173], [176], [356], [358]. The few vesicles within these regions may indicate original geological features, or may show early-stage partial melting [358].

Sample heterogeneity likely results from differing protolith compositions [175] and sample collection from many contextual locations, each with differing melting conditions [164], [173], [176]. Despite this heterogeneity in appearance, glass compositions are fairly consistent and closely resemble the local aluminosilicate-rich geology [175]. The latter supports previous theories that no exotic materials/fluxes were added to Celtic forts [164].

### *Synthesised replica glass*

XRD of the synthesised simulant hillfort material showed this is predominantly amorphous – verifying that the glass element of the hillfort samples had been replicated in this respect. Figure 8.13 shows the single sharp XRD peak can be assigned to un-melted silica from the batch.

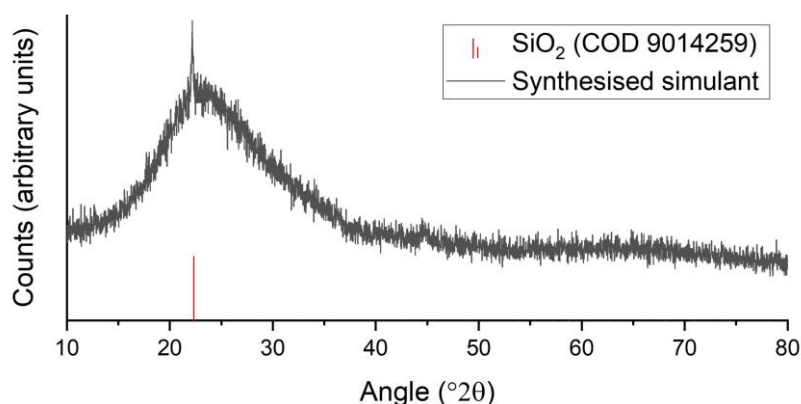


**Figure 8.13:** XRD of hillfort replica/simulant material and silica used in the materials production.

The synthesised replica glass also resembled the hypothesised glass component of vitrified hillfort samples in other ways. Viscosities appeared comparable, with the synthesised replica glass too viscous to pour on melting and actual hillfort glass evidencing viscous flow behaviour visually. Glasses were also similarly vesiculated (see Figure 8.3) and were, as intended, near-identical in composition. This implies that the hillfort glass was successfully replicated despite the differences in starting materials (reagents in the simulant vs rocks in the hillfort samples) and melting conditions (e.g. melting likely occurred over a more prolonged period in actual hillfort samples). Given this, the synthesised simulant can be reliably used in comparisons aiming to elucidate the likely causes of suspected/potential dissolution features in hillfort materials.

### **8.3.2. Identification and evaluation of potential dissolution features**

#### *Surface cavities*

Cavities resembling those in Figure 8.7 are often interpreted as pits formed via preferential glass dissolution (Section 2.4.1). However, these features were also evident in the synthesised replica glasses (which was never exposed to liquid water), implying they are unrelated to aqueous processes. Instead they are interpreted as micro-vesicles. This is consistent with the vesicle size variability in samples from other hillforts [355] and the macroscopic observations of vesicles in both hillfort samples from Dun Deardail and the synthesised replica material.

#### *Iridescence*

Glass alteration layers are often observed to be iridescent [76], [94], [359], [360], however this is not the hypothesised caused of iridescence in hillfort samples because this iridescence was again also observed in the *undissolved* replica glass. Instead, iridescence may result from potential phase-separation (as observed at Broborg hillfort [166]) or from a fine sub-surface fracture that effectively generates an additional glass layer which interacts with light to generate thin film interference patterns. Of these, the latter micro-fracture hypothesis appears most plausible given that no evidence of phase separation was observed in SEM-EDS. Why either phase separation or micro-fracturing may occur preferentially in vesicles remains unclear, although fracturing might arise from surface temperature gradients between the molten material and the surrounding atmosphere.

### Surface layers

Surface layers (often evident within vesicles) are considered potentially the most plausible evidence of aqueous dissolution as they may represent glass alteration layers. However, whilst this interpretation is consistent with many results, it cannot explain all surface layers.

In XCT, comparatively low-density surface layers were found to consistently occur more frequently on accessible surfaces than expected from a random surface distribution. The consistency of this observation across all samples implies it is not due to chance, with the low significance in some individual datasets speculated to result from segmentation difficulties, sample heterogeneity or differences in the dominant origin of the material between samples. This implies that a process requiring surface-accessibility (e.g. water flow) may control the distribution or formation of the majority of these low density surface coatings.

Features resembling surface layers but observed on *inaccessible* surfaces are considered to be methodological artefacts and misidentifications. Examining segmented images revealed some ‘blurred’ sample surfaces (Figure 8.14a-c) had been misidentified as low density surface layers. These may have resulted from sample motion during scanning [213], [361], post-processing operations [315], artefact correction [362], [363], or the partial volume effect/limited data resolution [362]. Similarly, some low density highly vesiculated veins within un-melted protoliths (Figure 8.14d-f) were also misidentified as low-density surface layers. Veins are reported to occur in the lithologies used to construct the hillfort [173] and may have melted and/or vesiculated preferentially upon vitrification to form these features.

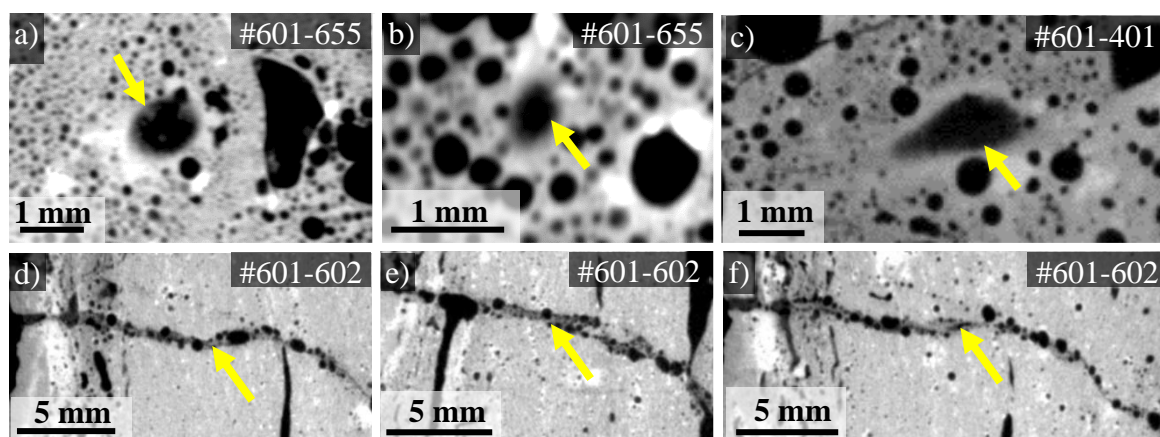


**Figure 8.14:** Areas anomalously identified as low density surface layers in quantitative XCT analysis (arrowed in yellow) of hillfort samples are more likely blurred sample edges (a-c) and low-density veins within the protolith (d-f). Sample numbers as identified.

The surface accessibility-dependant process(es) considered to control the formation and/or distribution of the correctly identified low-density surface layers all involve water. For example, some of these regions likely represent soil deposited from a groundwater. This is consistent with initial visual observations of soil on samples (Figure 8.3), particulate clusters identified in XCT (Figure 8.10d-f) and observations of particles within surface layers in optical micrographs (e.g. Figure 8.8). Typical dry soil density ( $1.1-1.6\text{g/cm}^3$  [364]) is significantly less than the density of the synthesised simulant hillfort glass ( $2.4\text{g/cm}^3$ ; determined by pycnometry), explaining the contrast variation in XCT images. Finally, the grain sizes estimated from SEM and optical microscopy (circa  $5-15\text{ }\mu\text{m}$ ) also resemble those for the topsoil at the Dun Deardail site (predominantly silty at  $2-50\text{ }\mu\text{m}$  [365]).

Surface layers may also have formed via reaction between the sample and groundwater, for example via aqueous corrosion. In optical microscopy, some vesicle linings and surface layers (e.g. Figure 8.7c and Figure 8.3a) were observed to superficially resemble the earthy or clay-like orange/brown appearance of palagonite rinds (basaltic glass alteration layers) [158]. Similarly, some surface layers observed in XCT data appear similar (in morphology and relative density) to the gel layer observed in XCT of other dissolved glasses [366]. The “dark” appearance of these features in XCT implies a low density, as is generally consistent with alteration layers relative to the glasses they form on [11], [47], [286]. Glass alteration layers typically have reduced density relative to the glasses on which they formed due to their micro-porosity [47] and/or the replacement of alkalis with less dense protons [286].

The iron-rich vesicle linings revealed in SEM-EDS are also consistent with the glass alteration layers. Iron oxides have elsewhere been reported on the surface [367] and within the vesicles of natural dissolved basaltic glass [368]; and were also replicated in laboratory basaltic glass dissolution experiments in Chapter 5. Formation and preservation of this material particularly within vesicles is to be expected. Precipitates (including palagonite rinds, clays and zeolites) are widely reported within the vesicles of dissolving basalts [98], [157], [369]–[371] and are often interpreted to result from redeposition of dissolved glass constituents [367]. The lower flow-rate in vesicles (particularly those only connected to potential water sources by fine cracks) is thought to allow preferential precipitation in these areas [369]. The low and/or sporadic flow here also allows porewater pH fluctuations from lower values (< 3) where glass dissolution is dominant to higher values (> 3) where reprecipitation of iron-oxide minerals is favourable [368]. Not only is alteration layer formation within vesicles likely, but as too is preferential preservation of these layers (relative to those on external surfaces) because interior vesicles are more protected from mechanical erosion or sample handling damage.

Low density surface layers within fractures may similarly be soil or glass alteration layers. Optical microscopy (Figure 8.8) revealed these areas can contain particles consistent with soil contamination, however glass alteration phases concentrated within microcracks have been observed by other authors [170]. As in vesicles, the lower flow rates in these fractures relative to external sample faces may promote development of alteration layers/secondary minerals by allowing solutions to more rapidly/readily reach saturation [171].

Interpreting low density surface layers as both soil and alteration layers is further consistent with other studies which noted the greyscale resemblance of glass alteration layers and adhered soil in XCT data [372]. Distinguishing between soil and alteration layers in XCT is challenging because analysis of the soil at Dun Deardail [365] implies up to 54% of the soil particles are likely indiscernible as discrete grains at the utilised resolution. If adhered to sample surfaces, this soil (with a grain size less than image resolution) would be indistinguishable from alteration layers because its fine grain size would preclude morphological distinction.

Regardless of whether a given surface layer is soil or a glass alteration layer, both imply that there was a groundwater solution in contact with glassy areas for sufficient time and in sufficient quantities to cause either dissolution and/or soil deposition. Further characterisation of these areas could thus offer insight into glass dissolution processes. Of particular interest is the material within fractures because the lower fluid replenishment rates here potentially best-replicate the conditions within/surrounding a GDF (where water flow is likely similarly limited by fracture networks [373]).

### *Other features*

The iron/sulphur-rich and titanium-rich features observed in Figure 8.5 are likely ilmenite and pyrite respectively. Ilmenite can be interpreted as a relic or quench crystal (as in other hillfort studies [354]), whilst pyrite is known to form during meteoric water interaction with basaltic glasses [97], [374], or during ilmenite reaction with dissolved sulphide [375], [376]. Given the proximity to observed ilmenite, the latter formation method seems most plausible. However, either method requires the presence of a (pore-) fluid containing sulphur. Though the source of this sulphur is unclear, this implies an aqueous medium was present within this vesicle (which is assumed to be glassy) for sufficient durations to allow mineralogical transformation. This area, thus, remains of interest from a glass aqueous durability perspective.

### **8.3.3. Absence of dissolution evidence is not evidence of dissolution absence**

Dissolution may not be evident in SEM surface profiles and XRD for many reasons and should not be used to infer that dissolution in other regions of the sample has not occurred.

#### *SEM*

Though sought, no evidence of surface de-alkalisation or other chemical evidence of glass dissolution was found in SEM-EDS surface profiles. Given the evidence of dissolution from other methods, glass compositions and leachates should have allowed dissolution. This may not have been evident in the limited probed areas due to methodological limitations and/or not all sample regions being exposed to groundwater for sufficient durations. Results from other chapters imply methodological limitations should not have hindered detection of dissolution-associated surface depletions (though re-collecting data using a longer acquisition time and higher magnification may be prudent). Instead, it is hypothesised that the small areas mapped by SEM-EDS may not have been exposed to groundwater/leachates for sufficient durations to allow dissolution. Observations of plant rootlets and soil in these areas imply that regions were likely exposed to groundwater at some point, however the duration of this exposure cannot be verified and may have been inadequate to allow sample dissolution there.

#### *XRD*

XRD similarly showed no evidence of glass alteration, however this is not unexpected given XRD of dissolved glasses from PCT-B experiments (Chapters 4 and 5) also did not reveal any glass dissolution products. Glass dissolution products may have been absent from the small region of hillfort sample removed for XRD powder production, potentially because this locality was not exposed to groundwater for sufficient durations to allow dissolution (as above for SEM). Alternatively, dissolution products may have been present but *undetected* by the methodology. The latter is consistent with results from laboratory experiments (PCT-B) conducted in Chapters 4 and 5, where dissolution products were observed in SEM but not XRD. Detection may also not have been possible if alteration products were amorphous or if dissolution products were present in minimal quantities relative to the undissolved glass.

## 8.4. Summary

Samples from Dun Deardail vitrified hillfort have been identified as of potential value from a nuclear waste glass analogue perspective and were characterised via a range of techniques from this perspective. Samples were observed to comprise vesiculated areas with a vitreous lustre that surround more angular clasts of un-melted geological clasts. Theoretical considerations, results from other studies, and evidence of diffuse scattering in XRD imply the vesiculated regions are glassy, with EDS showing this glass to be aluminosilicate in composition. Synthesis of a replica glass based on this composition was completed to allow comparisons with a verifiably undissolved equivalent.

Both the undissolved replica and the potentially dissolved hillfort glasses contained micro-cavities and iridescent regions, indicating these features were not dissolution pits or alteration layers respectively. Instead, these may represent micro-vesicles and fine sub-surface fracturing. Surface layers show much greater potential as dissolution features. In XCT these layers, of a lower density than the bulk sample, were found to occur preferentially on surfaces which were accessible to the external environment. The resemblance of these features with both soil and alteration layers in XCT data is in agreement with results from other techniques and studies.

SEM-EDS showed iron-rich layers on vesicle surfaces that are consistent with alteration layers observed in other works and in laboratory experiments in Chapter 5. Theoretical considerations also indicate dissolution and reprecipitation may be most favourable within these low flow rate vesicles, and optical microscopy revealed vesicle coatings superficially resembled naturally-formed basaltic glass alteration layers (palagonite rinds). However, equally, soil particles were observed visually on sample surfaces, with microscopy revealing this material had in some cases adhered to vesicle walls. Both the presence of soil and of potential glass alteration layers is nevertheless of interest from a glass durability perspective because both imply a glassy material was in contact with an aqueous solution for extended durations. Evidence of mineralogical phase transformation (from ilmenite to pyrite) similarly imply that an aqueous solution with the potential to cause dissolution was present on at least some sample surfaces.

## 9. Concluding Remarks and Future Work

### 9.1. Conclusions of work to date

A literature review established that glass dissolution can be described in three stages: In Stage I, rapid dissolution occurs as interdiffusion and network hydrolysis provide elements for alteration layer formation; in Stage II, dissolution is slow as solutions reach saturation and/or the alteration layer impedes diffusion; finally, occasionally Stage III occurs as alteration layer breakdown (often related to mineral precipitation) allows resumption of rapid dissolution. Magnesium has previously been found to increase Stage II rates by either entering the alteration layer and thereby hindering diffusion through it, or by promoting mineral precipitation at the expense of the glass, alteration layer or solution saturation. Localised attack features were identified as ubiquitous, but poorly understood despite their impact on surface areas and thus dissolution rates. These features include those resembling ‘worms’ (vermiform features) which were found to be particularly poorly understood in their formation mechanism and impact on glass dissolution, perhaps because of inconsistencies in nomenclature and inadequate consideration of work in other disciplines. Analogue materials (including basaltic glasses and vitrified hillforts materials) were identified as valuable in HLW glass dissolution studies due to their long-term exposure to water in the natural environment.

Two HLW glasses, MW25 and ISG, were dissolved in pure water via the MCC-1 and PCT-B procedures. These glasses transitioned between dissolution stages at similar times, however Stage II dissolution rates were higher for MW25 than ISG. This is thought to be associated with precipitation of clay during MW25 dissolution, which was not possible in the case of ISG because the latter did not contain the required magnesium. The alteration layers formed on these glasses during MCC-1 experiments also differ. Though dissolution of both glasses initially forms two sodium-depleted layers, the outer of these was enriched in magnesium for MW25 but zirconium-enriched for ISG. Furthermore, for MW25, the last-formed (third) layer comprised magnesium clays deposited on the sample exterior, whilst for ISG this final layer formed internally (below other layers) and was sodium-depleted with a scalloped morphology. Again, these differences are deemed attributable to the presence of magnesium in MW25 but not ISG. The role of magnesium in glass dissolution is thus reiterated as highly important to the UK nuclear waste disposal safety case, as the abundance of this element in UK HLW may allow this glass to differ in dissolution behaviour compared to other international glasses.

To further elucidate the role of magnesium, basaltic glasses with a variable magnesium-to-calcium ratio were synthesised and dissolved in identical experiments to those above. In these experiments, magnesium-rich basaltic glasses are generally less durable than their lower-magnesium counterparts. This may be because the thicker gel layer developed on high magnesium basaltic glasses is less passivating- a result of decreased aluminium within the layer, as this element is instead preferentially incorporated into the secondary precipitates (e.g. hectorites) which more readily form during dissolution of high-magnesium basaltic glasses. These trends were observed in MCC-1 and PCT-B experiments, though are considered less reliable in the latter because particle agglomeration may have adversely affected results. These results again highlight the potential impact of the elevated magnesium within the UK’s HLW.

Alteration layer thickness measurement methods previously relied on leachate analysis and various assumptions, or monolith cross section analysis and ambiguously constructed ‘lines’ (or ‘rays’). To improve rigour in cross section analysis, thickness can be redefined as the

diameter of the largest sphere/circle which can be entirely enclosed by the alteration layer. This “Sphere Method” provides improved result repeatability, decreased ambiguity, greater potential for 3D measurement, and increased automation potential. Though this Sphere Method performs poorly when characterising morphologically complex layers (due to its inability to discriminate ‘thickness’ and ‘width’), applying it to SEM data generated in this work provides layer thicknesses which are relatable to those from leachate analysis methods and comparable to those measured via previous cross section analysis techniques. Application of the method to XCT data was found to be possible, but could be undermined by imperfect image segmentation. Regardless, alteration layer thicknesses determined by applying the Sphere Method to SEM cross sections of laboratory-dissolved basaltic glasses are consistent with those made by applying other techniques to naturally dissolved basaltic glasses. This provides confidence that laboratory methods can recreate natural processes, supporting application of laboratory studies to the nuclear waste disposal safety case. With further regard to the latter, it was determined that basaltic glasses and HLW glasses show similar alteration layer growth rates *if* contributions from the innermost HLW surface layer component are removed. This inner HLW alteration layer component, which is also distinct in its morphology and growth trend, may thus account for many of the differences between basaltic glass and HLW glass dissolution behaviours.

Vermiform features were observed following aqueous MCC-1 dissolution of HLW and basaltic glasses. Features were most abundant and complex (tapering, clustering and/or branching) on basaltic glasses, where the tubular forms were partially filled by the alteration layer. The high atomic number central strand within these features, which was occasionally observed to spiral around itself, was similarly observed within vermiform features on MW25. Vermiform features formed on MW25 glasses were entirely filled by the central/middle surface layer (Layer 2) and were associated with the absence or splaying of protrusions of the innermost MW25 surface layer. Vermiform features on ISG contained only the thin outermost surface layer component, with the central layer (Layer 2) deforming or arching around the features which appear to ‘overprint’ the innermost layer (Layer 3). Across all glasses, variations in abundance and complexity may be due to increased feature formation progression in basaltic glasses; with the variable infilling due to differences in alteration layers. Formation of these features via biological mechanisms seems highly improbable, with preferential dissolution around a precursor flaw (most likely a micro-scratch or fracture) more probable. Regardless of their cause, these features were estimated to cause a 40% increase in glass surface area, which may undermine dissolution rates calculated using assumed surface areas and may introduce previously unidentified uncertainty into the nuclear waste disposal safety case.

Evidence of glassy material was found within materials from Dun Deardail vitrified hillfort, verifying the promise of these materials as nuclear waste glass analogues. This glass was hypothesised to form the vesicle-rich aluminosilicate sample regions which encompass the relatively less-melted geological clasts. By comparisons of the speculated glass regions with a glass synthesised to replicate these in composition but *not* the potential for dissolution, it was found that observed micro-cavities and iridescence were not associated with dissolution, with these features instead associated with micro-vesicles and surface fracturing. Comparatively low density surface layers, however, may relate to dissolution, as these occurred preferentially on surfaces which were potentially accessible to groundwater. Similarly, theoretical considerations, optical observations and comparisons with previous sections of this work imply that iron-rich layers within vesicles may also represent alteration layers.

## 9.2. Suggestions for further work

Longer-term laboratory dissolution experiments would further enhance this study. Extended PCT-B investigations, for example, would allow more confident identification of potential rate resumption in HLW glasses. Similarly, additional longer-term MCC-1 tests could aid in elucidating whether vermiform features increase in abundance/complexity with dissolution duration and could be used to further follow alteration layer thickness trends. In light of this, select trial experiments (initiated at the beginning of this project) remain ongoing, as detailed in Table 9.1. These experiments, it is hoped, will eventually be terminated to provide additional data collection points. Experiments should be monitored and terminated, with the glass powder and leachate subsequently characterised, before or immediately after evaporative losses surpass the acceptable threshold (when vessel mass falls below 90% of the starting mass). In addition to these PCT-B and MCC-1 experiments, a fragment of both hillfort material and the replica hillfort glass have been placed into separate PTFE (MCC-1) vessels containing ultrahigh quality water. It is hoped that characterisation of these samples (currently stored at 90 °C) after their dissolution may assist in revealing dissolution features within the hillfort materials.

Vessel ID #	Experiment type	Contents	Start date (dd/mm/yyyy)	Starting mass (g)
255		ISG		43.14
212	PCT-B (90°C)	70Ca30Mg	17/03/2020	42.97
209		70Ca30Mg		42.98
208		100Ca0Mg		42.99
203		100Ca0Mg		43.00
251	MCC-1	100Ca0Mg	21/03/2019	121.28
248		0Ca100Mg		121.32

**Table 9.1.** Laboratory dissolution experiments which remain ongoing.

Re-analysing legacy datasets using the methods and insight developed in the present work may also be fruitful. For example, re-analysing datasets from studies where vermiform features were only cursorily observed and commented on may provide insight into the potential formation mechanisms and significance of these features. Alteration layer growth trends may also be strengthened or further elucidated by compiling pre-existing measurements (particularly from archaeological glasses) or collecting additional data (potentially using the Sphere Method) from pre-existing image datasets. Compiling published alteration layer thickness trends with dissolution duration for a range of glass and leachate compositions, including nuclear waste glasses dissolved in groundwaters, would also be beneficial in potentially elucidating alteration layer formation mechanisms and potential compositional dependencies.

Further characterisation of the dissolved glasses considered in the present study may also be conducted. Many of the ‘bright’ features observed within MW25 alteration layers (Chapter 4) and within the central region of vermiform features (Chapter 6) were below the SEM-EDS resolution limit and would benefit from micro-focus XRD or TEM analysis. This may provide further insight into the dissolution behaviour of these glasses. Micro-focus XRD or TEM analysis would also aid in more confidently identifying aluminous hectorites precipitated during the dissolution of high-magnesium basaltic glasses. Further characterisation of hillfort samples would also be beneficial, with particular focus on the relatively low atomic number (dark in BSE images) and low density (dark in XCT images) material within vesicles and

fractures. XCT datasets highlighting water-accessible surfaces, as generated during the methodology outlined in Appendix I, should allow improved ‘targeting’ of regions that would benefit from further characterisation.

Enhancing the methods of the present work may also be beneficial. For example, segmentation (of both XCT and SEM) images was a time-consuming and subjective process which may be improved by applying the artificial intelligence and algorithmic techniques already available within the *Dragonfly* software. Investigations via geochemical modelling (Chapters 4 and 5) may also benefit from application of more or alternative thermodynamic databases which may include data for more or more relevant mineral phases.

XCT appears unjustifiably underutilised in studies of glass dissolution, and could be further developed to gain insight. For example, this may allow comparisons of leachate-accessible surface area before and after dissolution via the PCT-B procedure, as would be beneficial in quantifying or proving any effects of particle adhesion. Similarly, if more than a single vermiform feature can be observed in XCT this may aid in elucidating the cause or potential impacts of this phenomenon. This may be achieved by undertaking high resolution XCT of regions where abundant vermiform features have already been observed in SEM cross sections (although regions ‘above’ the field of view will inevitably have been lost in order to reveal the monolith cross section). Finally, collection of XCT data whilst samples remain in their leachate would prevent any dehydration effects and, if samples are sufficiently low durability or leachates sufficiently aggressive, may allow alteration layer development to be visualised in four dimensions (via the collection of 3D time-series data). It is appreciated, however, that scanning samples containing liquid may be hampered by limited resolution and excessive diffraction through the liquid media. Similarly, collection of time-series data may be hampered by blurring associated with sample changes that occur as the sample (or detector) are rotated.

Additional numerical analyses may also be worthwhile. A statistical comparison of precipitate abundance in basaltic glasses with variable magnesium-content may aid in elucidating if aluminous hectorite precipitation occurs preferentially during the dissolution of high(er) magnesium basaltic glasses. Similarly, a more complete statistical analysis of vermiform feature (abundance, length, complexity etc.) with dissolution duration and glass composition may also aid in elucidating formation mechanisms and dependencies. Likewise, regression analysis of alteration layer growth trends may reveal a theoretical underpinning to observations.

Finally, general themes requiring further enquiry may be suggested. These include the properties and significance of the innermost alteration layer component developed on HLW glasses. In Chapter 6 these layers, with their unique morphologies and thickness increase trends, were speculated to account for many of the differences between HLW and basaltic glass dissolution. Studying these specific alteration layer components may thus be of high value to the nuclear waste disposal safety case. Similarly, continued investigations of vermiform features are strongly recommended with further research needed to justify and better calculate any surface area correction factors necessitated by these features. Experiments to elucidate the underlying cause or origin of these features would also be beneficial. These may include attempting to identify alkali channels via TEM, or MCC-1 dissolution of monoliths containing suspected precursor flaws including micro-scratches or indentations. Finally, a multidisciplinary research programme investigating these features would also be beneficial.

## 10. References

- [1] Department for Business Energy and Industrial Strategy (BEIS), “Energy white paper: Powering our Net Zero Future,” 2020. [Online]. Available: <https://www.gov.uk/government/publications/energy-white-paper-powering-our-net-zero-future>
- [2] Department for Business Energy and Industrial Strategy (BEIS), “Table 5.1: Fuel used in electricity generation and electricity supplied,” 2022. [Online]. Available: [www.gov.uk/government/uploads/system/uploads/attachment\\_data/file/338321/et5\\_1.xls](http://www.gov.uk/government/uploads/system/uploads/attachment_data/file/338321/et5_1.xls)
- [3] C. Corkhill and N. Hyatt, *Nuclear Waste Management*. Bristol: IOP Publishing, 2018.
- [4] Department for Business Energy and Industrial Strategy (BEIS) and The Nuclear Decommissioning Authority (NDA), “UK Radioactive Waste Inventory,” Cumbria, 2019.
- [5] United Nations Scientific Committee on the Effects of Atomic Radiation (UNSCEAR), “Sources, Effects and Risks of Ionizing Radiation.” United Nations, New York, pp. 1–301, 2019.
- [6] The Organisation for Economic Co-operation and Development (OECD) Nuclear Energy Agency (NEA), “Moving Forward With Geological Disposal of Radioactive Waste,” 2008. [Online]. Available: [https://www.oecd-nea.org/jcms/pl\\_14450/moving-forward-with-geological-disposal-of-radioactive-waste](https://www.oecd-nea.org/jcms/pl_14450/moving-forward-with-geological-disposal-of-radioactive-waste)
- [7] M. T. Harrison, “Vitrification of High Level Waste in the UK,” *Procedia Mater. Sci.*, vol. 7, pp. 10–15, 2014, doi: 10.1016/j.mspro.2014.10.003.
- [8] S. Gin, J. V Ryan, S. Kerisit, and J. Du, “Simplifying a solution to a complex puzzle,” *Mater. Degrad.*, vol. 2, no. 36, pp. 4–5, 2018, doi: 10.1038/s41529-018-0057-y.
- [9] Nuclear Energy Agency/Radioactive Waste Management, “The Safety Case for Deep Geological Disposal of Radioactive Waste: 2013 State of -the Art,” Organisation for Economic Co-operation & Development, Paris, 2014.
- [10] S. Gin *et al.*, “An international initiative on long-term behavior of high-level nuclear waste glass,” *Mater. Today*, vol. 16, no. 6, pp. 243–248, 2013, doi: 10.1016/j.mattod.2013.06.008.
- [11] G. S. Frankel *et al.*, “A comparative review of the aqueous corrosion of glasses, crystalline ceramics, and metals,” *npj Mater. Degrad.*, vol. 2, no. 15, pp. 1–15, 2018, doi: 10.1038/s41529-018-0037-2.
- [12] B. Parruzot, P. Jollivet, and D. Re, “Long-term alteration of basaltic glass : Mechanisms and rates,” vol. 154, pp. 28–48, 2015, doi: 10.1016/j.gca.2014.12.011.
- [13] S. Gin, P. Jollivet, M. Fournier, F. Angeli, P. Frugier, and T. Charpentier, “Origin and consequences of silicate glass passivation by surface layers,” *Nat. Commun.*, vol. 6, no. 6360, pp. 1–8, 2015, doi: 10.1038/ncomms7360.
- [14] R. K. Chinnam, P. C. M. Fossati, and W. E. Lee, “Degradation of partially immersed glass: A new perspective,” *J. Nucl. Mater.*, vol. 503, pp. 56–65, 2018, doi: 10.1016/j.jnucmat.2018.02.040.
- [15] D. E. Clark and B. K. Zaitos, “Corrosion of glass, ceramics and ceramic superconductors: Principles, testing, characterization and Applications,” New Jersey:

- Noyes Publications, 1992, pp. 1–672.
- [16] M. Fournier, S. Gin, and P. Frugier, “Resumption of nuclear glass alteration: State of the art,” *J. Nucl. Mater.*, vol. 448, no. 1–3, pp. 348–363, 2014, doi: 10.1016/j.jnucmat.2014.02.022.
- [17] H. Scholze, “Nature and Structure of Glass,” in *Glass: Nature, Structure, and Properties*, New York: Springer-Verlag, 1991, pp. 3–155.
- [18] Y. Inagaki, H. Furuya, K. Idemitsu, and T. Arima, “Review of Waste Glass Corrosion And Associated Radionuclide Release As A Part Of Safety Assessment Of Entire Disposal System,” *Prog. Nucl. Energy*, vol. 32, no. 3–4, pp. 501–508, 1998.
- [19] B. Grambow, “A General Rate Equation for Nuclear Waste Glass Corrosion,” *Mat. Res. Soc. Symp. Proc.*, vol. 44, pp. 15–27, 1985.
- [20] E. Vernaz, S. Gin, C. Jégou, and I. Ribet, “Present understanding of R7T7 glass alteration kinetics and their impact on long-term behavior modeling,” *J. Nucl. Mater.*, vol. 298, no. 1–2, pp. 27–36, 2001, doi: 10.1016/S0022-3115(01)00643-2.
- [21] S. Gin, “Protective Effect of the Alteration Gel: A Key Mechanism in the Long-Term Behavior of Nuclear Waste Glass,” *Mat. Res. Soc. Symp. Proc.*, vol. 663, pp. 207–215, 2001.
- [22] P. Frugier *et al.*, “SON68 nuclear glass dissolution kinetics: Current state of knowledge and basis of the new GRAAL model,” *J. Nucl. Mater.*, vol. 380, pp. 8–21, 2008.
- [23] C. Jégou, S. Gin, and F. Larché, “Alteration kinetics of a simplified nuclear glass in an aqueous medium: Effects of solution chemistry and of protective gel properties on diminishing the alteration rate,” *J. Nucl. Mater.*, vol. 280, pp. 216–229, 2000, doi: 10.1016/S0022-3115(00)00039-8.
- [24] P. Van Iseghem *et al.*, “GLAMOR – Or How We Achieved a Common Understanding on the Decrease of Glass Dissolution Kinetics,” in *Environmental Issues and Waste Management Technologies in the Materials and Nuclear Industries XII*, A. Cozzi and T. Ohji, Eds. New Jersey: John Wiley & Sons, Inc., 2009, pp. 115–126.
- [25] S. Gin, X. Beaudoux, F. Angéli, C. Jégou, and N. Godon, “Effect of composition on the short-term and long-term dissolution rates of ten borosilicate glasses of increasing complexity from 3 to 30 oxides,” *J. Non. Cryst. Solids*, vol. 358, no. 18–19, pp. 2559–2570, 2012, doi: 10.1016/j.jnoncrysol.2012.05.024.
- [26] B. Grambow and R. Muller, “First-order dissolution rate law and the role of surface layers in glass performance assessment,” *J. Nucl. Mater.*, vol. 298, pp. 112–124, 2001.
- [27] C. M. Jantzen, D. I. Kaplan, N. E. Bibler, D. K. Peeler, and M. J. Plodinec, “Performance of a buried radioactive high level waste ( HLW ) glass after 24 years,” *J. Nucl. Mater.*, vol. 378, pp. 244–256, 2008, doi: 10.1016/j.jnucmat.2008.06.040.
- [28] N. Rajmohan, P. Frugier, and S. Gin, “Composition effects on synthetic glass alteration mechanisms : Part 1 . Experiments,” *Chem. Geol.*, vol. 279, no. 3–4, pp. 106–119, 2010, doi: 10.1016/j.chemgeo.2010.10.010.
- [29] C. Poinssot and S. Gin, “Long-term Behavior Science : The cornerstone approach for reliably assessing the long-term performance of nuclear waste,” *J. Nucl. Mater.*, vol. 420, no. 1–3, pp. 182–192, 2012, doi: 10.1016/j.jnucmat.2011.09.012.
- [30] E. Curti, “Glass Dissolution parameters: Update for Entsorgungsnachweis (Technical Report 02-21).” National Cooperative for the Disposal of Radioactive Waste (NAGRA),

- Wettingen, Switzerland, pp. 1–46, 2003.
- [31] E. Curti, J. L. Crovisier, G. Morvan, and A. M. Karpoff, “Long-term corrosion of two nuclear waste reference glasses (MW and SON68): A kinetic and mineral alteration study,” *Appl. Geochemistry*, vol. 21, no. 7, pp. 1152–1168, 2006, doi: 10.1016/j.apgeochem.2006.03.010.
- [32] P. Frugier, S. Gin, J. E. Lartigue, and E. Deloule, “SON68 glass dissolution kinetics at high reaction progress: mechanisms accounting for the residual alteration rate,” in *Mat. Res. Soc. Symp. Proc.*, 2006, vol. 932.
- [33] D. Rebiscoul and P. Frugier, “Protective properties and dissolution ability of the gel formed during nuclear glass alteration,” *J. Nucl. Mater.*, vol. 342, pp. 26–34, 2005, doi: 10.1016/j.jnucmat.2005.03.018.
- [34] C. Cailleteau *et al.*, “Insight into silicate-glass corrosion mechanisms,” *Nat. Mater.*, vol. 7, no. 12, pp. 978–983, 2008, doi: 10.1038/nmat2301.
- [35] P. Jollivet, F. Angeli, C. Cailleteau, F. Devreux, P. Frugier, and S. Gin, “Investigation of gel porosity clogging during glass leaching,” *J. Non. Cryst. Solids*, vol. 354, pp. 4952–4958, 2008, doi: 10.1016/j.jnoncrystol.2008.07.023.
- [36] S. Gin, J. V. Ryan, D. K. Schreiber, J. Neeway, and M. Cabié, “Contribution of atom-probe tomography to a better understanding of glass alteration mechanisms: Application to a nuclear glass specimen altered 25 years in a granitic environment,” *Chem. Geol.*, vol. 349–350, pp. 99–109, 2013, doi: 10.1016/j.chemgeo.2013.04.001.
- [37] S. Gin *et al.*, “Nuclear glass durability: New insight into alteration layer properties,” *J. Phys. Chem. C*, vol. 115, no. 38, pp. 18696–18706, 2011, doi: 10.1021/jp205477q.
- [38] S. Ribet, I. S. Muller, I. L. Pegg, S. Gin, and P. Frugier, “Compositional Effects on the Long-Term Durability of Nuclear Waste Glasses: A Statistical Approach,” *Mat. Res. Soc. Symp. Proc.*, vol. 824, pp. 1–6, 2004.
- [39] S. Gin and J. P. Mestre, “SON 68 nuclear glass alteration kinetics between pH 7 and pH 11.5,” *J. Nucl. Mater.*, vol. 295, pp. 83–96, 2001.
- [40] D. M. Strachan, “Glass dissolution: testing and modeling for long-term behavior,” *J. Nucl. Mater.*, vol. 298, pp. 69–77, 2001.
- [41] W. L. Ebert and J. K. Bates, “The Importance of Secondary Phases in Glass Corrosion,” *Mater. Res. Soc. Symposium Proc.*, vol. 212, p. 8, 1990.
- [42] P. Frugier, C. Martin, I. Ribet, T. Advocat, and S. Gin, “The effect of composition on the leaching of three nuclear waste glasses: R7T7, AVM and VRZ,” *J. Nucl. Mater.*, vol. 346, no. 2–3, pp. 194–207, 2005, doi: 10.1016/j.jnucmat.2005.06.023.
- [43] S. Ribet and S. Gin, “Role of neoformed phases on the mechanisms controlling the resumption of SON68 glass alteration in alkaline media,” *J. Nucl. Mater.*, vol. 324, no. 2–3, pp. 152–164, 2004, doi: 10.1016/j.jnucmat.2003.09.010.
- [44] D. M. Strachan and T. L. Croak, “Compositional effects on long-term dissolution of borosilicate glass,” *J. Non. Cryst. Solids*, vol. 272, no. 1, pp. 22–33, 2000, doi: 10.1016/S0022-3093(00)00154-X.
- [45] P. Van Iseghem and B. Grambow, “The Long-Term Corrosion and Modelling of Two Simulated Belgian Reference High-Level Waste Glasses,” *Mater. Res. Soc. Symp. Proc.*, vol. 112, pp. 631–639, 1988.

- [46] C. M. Jantzen, K. G. Brown, and J. B. Pickett, "Durable Glass for Thousands of Years," *Int. J. Appl. Glas. Sci.*, vol. 1, no. 1, pp. 38–62, 2010, doi: 10.1111/j.2041-1294.2010.00007.x.
- [47] J. E. Mendel *et al.*, "Final Report of the Defense High-Level Waste Leaching Mechanisms Program," Washington: United States Department of Energy, 1984, p. 396.
- [48] C. Brigden and I. Farnan, "Experimental studies of the durability of UK HLW and ILW glasses. The effect of magnesium (Report #RWM005105)." Amec Foster Wheeler, Nuclear Decommissioning Authority (NDA), Didcot, pp. 1–73, 2016.
- [49] D. J. Backhouse, C. L. Corkhill, N. C. Hyatt, and R. J. Hand, "Investigation of the role of Mg and Ca in the structure and durability of aluminoborosilicate glass," *J. Non. Cryst. Solids*, vol. 512, pp. 41–52, 2019, doi: 10.1016/j.jnoncrysol.2019.03.003.
- [50] R. Guo, C. T. Brigden, S. Gin, S. W. Swanton, and I. Farnan, "The effect of magnesium on the local structure and initial dissolution rate of simplified UK Magnox waste glasses," *J. Non. Cryst. Solids*, vol. 497, pp. 82–92, 2018, doi: 10.1016/j.jnoncrysol.2018.03.002.
- [51] C. M. Jantzen, "Development of glass matrices for high level radioactive wastes," in *Handbook of Advanced Radioactive Waste Conditioning Technologies*, M. Ojovan, Ed. Woodhead Publishing Limited, 2011, pp. 230–292. doi: 10.1533/9780857090959.2.230.
- [52] M. T. Harrison, "The Effect of Composition on Short- and Long-term Durability of UK HLW Glass," *Procedia Mater. Sci.*, vol. 7, pp. 186–192, 2014, doi: 10.1016/j.mspro.2014.10.025.
- [53] J. M. Schofield *et al.*, "Experimental studies of the chemical durability of UK HLW and ILW glasses (Report #RWM005105)," Amec Foster Wheeler, Didcot, 2016.
- [54] B. M. J. Thien, N. Godon, A. Ballestero, S. Gin, and A. Ayrat, "The dual effect of Mg on the long-term alteration rate of AVM nuclear waste glasses," *J. Nucl. Mater.*, vol. 427, no. 1–3, pp. 297–310, 2012, doi: 10.1016/j.jnucmat.2012.05.025.
- [55] T. Maeda, H. Ohmori, S. Mitsui, and T. Banba, "Corrosion behavior of simulated HLW glass in the presence of magnesium ion," *Int. J. Corros.*, vol. 2011, 2011, doi: 10.1155/2011/796457.
- [56] P. M. Dove and D. A. Crerar, "Kinetics of quartz dissolution in electrolyte solutions using a hydrothermal mixed flow reactor," *Geochim. Cosmochim. Acta*, vol. 54, pp. 955–969, 1990.
- [57] L. Neill *et al.*, "Various effects of magnetite on international simple glass (ISG) dissolution: implications for the long-term durability of nuclear glasses," *npj Mater. Degrad.*, vol. 1, no. 1, pp. 1–11, 2017, doi: 10.1038/s41529-017-0001-6.
- [58] A. Michelin *et al.*, "Effect of iron metal and siderite on the durability of simulated archeological glassy material," *Corros. Sci.*, vol. 76, pp. 403–414, 2013, doi: 10.1016/j.corsci.2013.07.014.
- [59] A. Michelin *et al.*, "Silicate glass alteration enhanced by iron: Origin and long-term implications," *Environ. Sci. Technol.*, vol. 47, no. 2, pp. 750–756, 2013, doi: 10.1021/es304057y.
- [60] D. J. Backhouse, "A Study of the Dissolution of Nuclear Waste Glasses in Highly-Alkaline Conditions," PhD Thesis, The University of Sheffield, 2017.
- [61] K. Lemmens, "The effect of clay on the dissolution of nuclear waste glass," *J. Nucl.*

- Mater.*, vol. 298, pp. 11–18, 2001.
- [62] F. Angeli, T. Charpentier, S. Gin, and J. C. Petit, “<sup>17</sup>O 3Q-MAS NMR characterization of a sodium aluminoborosilicate glass and its alteration gel,” *Chem. Phys. Lett.*, vol. 341, no. 1–2, pp. 23–28, 2001, doi: 10.1016/S0009-2614(01)00423-7.
- [63] V. Piovesan *et al.*, “Chemical durability of peraluminous glasses for nuclear waste conditioning,” *npj Mater. Degrad.*, vol. 2, no. 1, 2018, doi: 10.1038/s41529-018-0028-3.
- [64] C. A. Utton, R. J. Hand, N. C. Hyatt, S. W. Swanton, and S. J. Williams, “Formation of alteration products during dissolution of vitrified ILW in a high-pH calcium-rich solution,” *J. Nucl. Mater.*, vol. 442, no. 1–3, pp. 33–45, 2013, doi: 10.1016/j.jnucmat.2013.08.026.
- [65] M. Fournier, “Contribution of zeolite-seeded experiments to the understanding of resumption of glass alteration,” *npj Mater. Degrad.*, vol. 1, no. 1, pp. 1–12, 2017, doi: 10.1038/s41529-017-0018-x.
- [66] R. Hellmann *et al.*, “Nanometre-scale evidence for interfacial dissolution – reprecipitation control of silicate glass corrosion,” vol. 14, no. 3, pp. 307–311, 2015, doi: 10.1038/NMAT4172.
- [67] J. C. Dran, J. C. Petit, and C. Brousse, “Mechanism of aqueous dissolution of silicate glasses yielded by fission tracks,” *Nature*, vol. 319, no. 6053, pp. 485–487, 1986, doi: 10.1038/319485a0.
- [68] S. Gin *et al.*, “The fate of silicon during glass corrosion under alkaline conditions: A mechanistic and kinetic study with the International Simple Glass,” *Geochim. Cosmochim. Acta*, vol. 151, pp. 68–85, 2015, doi: 10.1016/j.gca.2014.12.009.
- [69] R. H. Doremus, “Interdiffusion of Hydrogen and Alkali Ions in a Glass Surface,” *J. Non. Cryst. Solids*, vol. 19, pp. 137–144, 1975, doi: 10.1016/B978-0-7204-0419-7.50017-2.
- [70] T. Chave, P. Frugier, S. Gin, and A. Ayrat, “Glass – water interphase reactivity with calcium rich solutions,” *Geochim. Cosmochim. Acta*, vol. 75, no. 15, pp. 4125–4139, 2011, doi: 10.1016/j.gca.2011.05.005.
- [71] S. Mercado-Depierre, F. Angeli, F. Frizon, and S. Gin, “Antagonist effects of calcium on borosilicate glass alteration,” *J. Nucl. Mater.*, vol. 441, no. 1–3, pp. 402–410, 2013, doi: 10.1016/j.jnucmat.2013.06.023.
- [72] R. Hellmann *et al.*, “Unifying natural and laboratory chemical weathering with interfacial dissolution – reprecipitation: A study based on the nanometer-scale chemistry of fluid – silicate interfaces,” *Chem. Geol.*, vol. 294–295, pp. 203–216, 2012, doi: 10.1016/j.chemgeo.2011.12.002.
- [73] T. Geisler *et al.*, “The mechanism of borosilicate glass corrosion revisited,” *Geochim. Cosmochim. Acta*, vol. 158, pp. 112–129, 2015, doi: 10.1016/j.gca.2015.02.039.
- [74] L. Dohmen *et al.*, “Pattern Formation in Silicate Glass Corrosion Zones,” *Int. J. Appl. Glas. Sci.*, vol. 4, no. 4, pp. 357–370, 2013, doi: 10.1111/ijag.12046.
- [75] T. Lombardo *et al.*, “Characterisation of complex alteration layers in medieval glasses,” *Corros. Sci.*, vol. 72, pp. 10–19, 2013, doi: 10.1016/j.corsci.2013.02.004.
- [76] S. D. McLoughlin, “The Characterisation of Archaeological Glasses Using Advanced Analytical Techniques,” PhD Thesis, University of London: Imperial College of Science, Technology and Medicine, 2003.

- [77] S. Gin *et al.*, “The controversial role of inter-diffusion in glass alteration,” *Chem. Geol.*, vol. 440, pp. 115–123, 2016, doi: 10.1016/j.chemgeo.2016.07.014.
- [78] E. Ruiz-Agudo *et al.*, “Control of silicate weathering by interface-coupled dissolution precipitation processes at the mineral-solution interface,” *Geology*, vol. 44, no. 7, pp. 567–570, 2016, doi: 10.1130/G37856.1.
- [79] R. J. Hand, “The Ballidon Glass Burial Experiment – 35 years on,” *Glas. Technol.*, vol. 46, no. 3, pp. 221–226, 2005.
- [80] B. D. Pauly, “In Situ Micro-analytical Investigations of Palagonitization,” PhD Thesis, University of California, 2011.
- [81] J. L. Weaver *et al.*, “Pre-viking Swedish hillfort glass: A prospective long-term alteration analogue for vitrified nuclear waste,” *Int. J. Appl. Glas. Sci.*, vol. 9, no. 4, pp. 540–554, 2018, doi: 10.1111/ijag.12351.
- [82] C. Mann, “A study of the Dissolution of UK Nuclear Waste Glass in Cement Waters,” PhD Thesis, The University of Sheffield, 2018.
- [83] R. D. Aines, H. C. Weed, and J. Bates, “Hydrogen Speciation in Hydrated Layers on Nuclear Waste Glass,” *Mater. Res. Soc. Symp. Proc.*, vol. 84, p. 13, 1986.
- [84] S. Gin, P. Frugier, P. Jollivet, and F. Bruguier, “New Insight into the Residual Rate of Borosilicate Glasses: Effect of S/V and Glass Composition,” vol. 382, pp. 371–382, 2013, doi: 10.1111/ijag.12048.
- [85] S. Gin *et al.*, “Atom-Probe Tomography, TEM and ToF-SIMS study of borosilicate glass alteration rim: A multiscale approach to investigating rate-limiting mechanisms,” *Geochim. Cosmochim. Acta*, vol. 202, pp. 57–76, 2017, doi: 10.1016/j.gca.2016.12.029.
- [86] S. Gin *et al.*, “Dynamics of self-reorganization explains passivation of silicate glasses,” *Nat. Commun.*, vol. 9, no. 2169, pp. 1–9, 2018, doi: 10.1038/s41467-018-04511-2.
- [87] C. Cailleteau, F. Devreux, O. Spalla, F. Angeli, and S. Gin, “Why do certain glasses with a high dissolution rate undergo a low degree of corrosion?,” *J. Phys. Chem. C*, vol. 115, no. 13, pp. 5846–5855, 2011, doi: 10.1021/jp111458f.
- [88] X. Le Gal, J. Crovisiera, F. Gauthier-lafaye, J. Honnorez, and B. Grambow, “Altération météorique de verres volcaniques d’Islande: changement du mécanisme à long terme,” *Comptes Rendus l’Académie des Sci. - Ser. IIA - Earth Planet. Sci.*, vol. 329, no. 3, pp. 175–181, 1999.
- [89] R. Haaker, G. Malow, and P. Offermann, “The effect of phase formation on glass leaching,” *Mater. Res. Soc. Symp. Proc.*, vol. 44, pp. 121–128, 1984.
- [90] L. L. Hench and D. E. Clark, “Surface Properties and Performance Prediction of Alternative Waste Forms,” vol. 2, Washington: United States Nuclear Regulatory Commission, 1986, p. 240.
- [91] A. J. Fisher, “Dissolution of UK Vitrified High-Level Radioactive Waste Containing Zinc and Calcium,” PhD Thesis, The University of Sheffield, 2020.
- [92] A. J. Fisher, N. C. Hyatt<sup>1</sup>, R. J. Hand, and C. L. Corkhill, “The Formation of Pitted Features on the International Simple Glass during Dynamic Experiments at Alkaline pH,” *Mater. Res. Soc. Adv.*, vol. 4, no. 17–18, pp. 993–999, 2019, doi: 10.1557/adv.2019.9.
- [93] L. Gentaz *et al.*, “Ubiquitous presence of laminae in altered layers of glass artefacts,” in

- Proceedings of the SPIE (Integrated Approaches to the Study of Historical Glass)*, 2012, vol. 8422, no. 84220C, pp. 111–118. doi: 10.1117/12.981173.
- [94] A. Genga *et al.*, “Characterization of surface layers formed under natural environmental conditions on medieval glass from Siponto (Southern Italy),” *Mater. Chem. Phys.*, vol. 111, no. 2–3, pp. 480–485, 2008, doi: 10.1016/j.matchemphys.2008.04.057.
- [95] M. T. Doménech-Carbó, A. Doménech-Carbó, L. Osete-Cortina, and M. C. Saurí-Peris, “A study on corrosion processes of archaeological glass from the Valencian Region (Spain) and its consolidation treatment,” *Microchim. Acta*, vol. 154, no. 1–2, pp. 123–142, 2006, doi: 10.1007/s00604-005-0472-y.
- [96] M. Gulmini, M. Pace, G. Ivaldi, M. N. Ponzi, and P. Mirti, “Morphological and chemical characterization of weathering products on buried Sasanian glass from central Iraq,” *J. Non. Cryst. Solids*, vol. 355, no. 31–33, pp. 1613–1621, 2009, doi: 10.1016/j.jnoncrysol.2009.05.056.
- [97] M. Jercinovic and R. Ewing, “Basaltic glasses from Iceland and the deep sea: natural analogues to borosilicate nuclear waste-form glass.” Swedish Nuclear Fuel and Waste Management Co., Stockholm, Sweden, p. 221, 1987.
- [98] M. J. Jercinovic, K. Keil, M. R. Smith, and R. A. Schmitt, “Alteration of basaltic glasses from north-central British Columbia, Canada,” *Geochim. Cosmochim. Acta*, vol. 54, no. 10, pp. 2679–2696, 1990, doi: 10.1016/0016-7037(90)90004-5.
- [99] H. Staudigel and S. R. Hart, “Alteration of basaltic glass: Mechanisms and significance for the oceanic crust-seawater budget,” *Geochim. Cosmochim. Acta*, vol. 47, no. 3, pp. 337–350, 1983, doi: 10.1016/0016-7037(83)90257-0.
- [100] M. R. Fisk, J. L. Crovisier, and J. Honnorez, “Experimental abiotic alteration of igneous and manufactured glasses,” *Comptes Rendus - Geosci.*, vol. 345, no. 4, pp. 176–184, 2013, doi: 10.1016/j.crte.2013.02.001.
- [101] I. H. Thorseth, T. Torsvik, V. Torsvik, F. L. Daae, and R. B. Pedersen, “Diversity of life in ocean floor basalt,” *Earth Planet. Sci. Lett.*, vol. 194, no. 1–2, pp. 31–37, 2001, doi: 10.1016/S0012-821X(01)00537-4.
- [102] H. Staudigel, H. Furnes, N. McLoughlin, N. R. Banerjee, L. B. Connell, and A. Templeton, “3.5 billion years of glass bioalteration: Volcanic rocks as a basis for microbial life?,” *Earth-Science Rev.*, vol. 89, no. 3–4, pp. 156–176, 2008, doi: 10.1016/j.earscirev.2008.04.005.
- [103] C. Kruber, I. H. Thorseth, and R. B. Pedersen, “Seafloor alteration of basaltic glass: Textures, geochemistry, and endolithic microorganisms,” *Geochemistry, Geophys. Geosystems*, vol. 9, no. 12, pp. 1–18, 2008, doi: 10.1029/2008GC002119.
- [104] S. D. McLoughlin, N. C. Hyatt, R. J. Hand, and W. E. Lee, “Corrosion of archaeological model glasses after 32 years of burial at Ballidon,” *Mat. Res. Soc. Symp. Proc.*, vol. 932, 2006.
- [105] G. S. Frankel, “Pitting Corrosion of Metals: A Review of the Critical Factors,” *J. Electrochem. Soc.*, vol. 145, pp. 2186–2198, 1998.
- [106] C. Vargel, “Chapter 2: Pitting Corrosion,” in *Corrosion of Aluminium*, Second Edi., C. Vargel, Ed. Amsterdam: Elsevier Science, 2020, pp. 163–183. doi: 10.1016/B978-0-08-099925-8.00014-4.
- [107] B. Baroux, “The Pitting Corrosion of Stainless Steels (Further insights),” in *Corrosion*

- Mechanisms in Theory and Practice*, P. Marcus and J. Oudar, Eds. New York: Marcel Dekker Inc, 1995, pp. 265–309.
- [108] L. Gentaz, T. Lombardo, C. Loisel, A. Chabas, and M. Vallotto, “Early stage of weathering of medieval-like potash-lime model glass: Evaluation of key factors,” *Environ. Sci. Pollut. Res.*, vol. 18, no. 2, pp. 291–300, 2011, doi: 10.1007/s11356-010-0370-7.
- [109] J. P. Icenhower *et al.*, “Experimentally determined dissolution kinetics of Na-rich borosilicate glass at far from equilibrium conditions: Implications for Transition State Theory,” *Geochim. Cosmochim. Acta*, 2008, doi: 10.1016/j.gca.2008.02.026.
- [110] L. Sessegolo, A. Verney-Carron, P. Ausset, M. Saheb, and A. Chabas, “Effect of surface roughness on medieval-type glass alteration in aqueous medium,” *J. Non. Cryst. Solids*, vol. 505, pp. 260–271, 2019, doi: 10.1016/j.jnoncrysol.2018.10.051.
- [111] C. Lenting, O. Plümper, M. Kilburn, P. Guagliardo, M. Klinkenberg, and T. Geisler, “Towards a unifying mechanistic model for silicate glass corrosion,” *npj Mater. Degrad.*, vol. 2, no. 1, p. 28, 2018, doi: 10.1038/s41529-018-0048-z.
- [112] P. G. Heath, “Alternative Processing Methods for the Thermal Treatment of Radioactive Wastes,” PhD Thesis, The University of Sheffield, 2015.
- [113] T. Kautz, “Research on subsoil biopores and their functions in organically managed soils: A review,” *Renew. Agric. Food Syst.*, vol. 30, no. 4, pp. 318–327, 2015, doi: 10.1017/S1742170513000549.
- [114] C. Mann *et al.*, “Interactions between Simulant Vitrified Nuclear Wastes and high pH solutions: A Natural Analogue Approach,” *Mater. Res. Soc. Adv.*, vol. 2, no. 12, pp. 669–674, 2017, doi: 10.1557/adv.2017.59.
- [115] H. Furnes *et al.*, “Oceanic pillow lavas and hyaloclastites as habitats for microbial life through time – a review,” *Mod. Approaches Solid Earth Sci.*, vol. 4, pp. 1–68, 2008.
- [116] N. McLoughlin, M. D. Brasier, D. Wacey, O. R. Green, and R. S. Perry, “On biogenicity criteria for endolithic microborings on early Earth and beyond,” *Astrobiology*, vol. 7, no. 1, pp. 10–26, 2007, doi: 10.1089/ast.2006.0122.
- [117] S. Dultz *et al.*, “Alteration of a Submarine Basaltic Glass under Environmental Conditions Conducive for Microorganisms: Growth Patterns of the Microbial Community and Mechanism of Palagonite Formation,” *Geomicrobiol. J.*, vol. 31, no. 9, pp. 813–834, 2014, doi: 10.1080/01490451.2014.897774.
- [118] M. Garcia-Vallès, D. Gimeno-Torrente, S. Martínez-Manent, and J. L. Fernández-Turiel, “Medieval stained glass in a Mediterranean climate: Typology, weathering and glass decay, and associated biomineralization processes and products,” *Am. Mineral.*, vol. 88, no. 11-12 PART 2, pp. 1996–2006, 2003, doi: 10.2138/am-2003-11-1244.
- [119] R. L. Mitchell *et al.*, “Mineral weathering and soil development in the earliest land plant ecosystems,” *Geology*, vol. 44, no. 12, pp. 1007–1010, 2016, doi: 10.1130/G38449.1.
- [120] R. L. Mitchell, C. Strullu-Derrien, and P. Kenrick, “Biologically mediated weathering in modern cryptogamic ground covers and the early paleozoic fossil record,” *J. Geol. Soc. London.*, vol. 176, no. 3, pp. 430–439, 2019, doi: 10.1144/jgs2018-191.
- [121] N. R. Benerjee *et al.*, “Direct dating of Archean microbial ichnofossils,” *Geology*, vol. 35, no. 6, pp. 487–490, 2007, doi: 10.1130/G23534A.1.
- [122] C. Mann *et al.*, “Influence of young cement water on the corrosion of the International

- Simple Glass,” *npj Mater. Degrad.*, vol. 3, no. 1, pp. 1–9, 2019, doi: 10.1038/s41529-018-0059-9.
- [123] C. S. Cockell and A. Herrera, “Why are some microorganisms boring?,” *Trends Microbiol.*, vol. 16, no. 3, pp. 101–106, 2008, doi: 10.1016/j.tim.2007.12.007.
- [124] K. Lepot, K. Benzerara, and P. Philippot, “Biogenic versus metamorphic origins of diverse microtubes in 2.7Gyr old volcanic ashes: Multi-scale investigations,” *Earth Planet. Sci. Lett.*, vol. 312, no. 1–2, pp. 37–47, 2011, doi: 10.1016/j.epsl.2011.10.016.
- [125] I. H. Thorseth, H. Furnes, and O. Tumyr, “Textural and chemical effects of bacterial activity on basaltic glass: an experimental approach,” *Chem. Geol.*, vol. 119, no. 1–4, pp. 139–160, 1995, doi: 10.1016/0009-2541(94)00098-S.
- [126] K. Benzerara, N. Menguy, N. R. Banerjee, T. Tylizszczak, G. E. Brown, and F. Guyot, “Alteration of submarine basaltic glass from the Ontong Java Plateau: A STXM and TEM study,” *Earth Planet. Sci. Lett.*, vol. 260, no. 1–2, pp. 187–200, 2007, doi: 10.1016/j.epsl.2007.05.029.
- [127] H. Furnes, H. Staudigel, I. H. Thorseth, T. Torsvik, K. Muehlenbachs, and O. Tumyr, “Bioalteration of basaltic glass in the oceanic crust,” *Geochemistry, Geophys. Geosystems*, vol. 2, no. 8, pp. 1–30, 2001, doi: 10.1029/2000gc000150.
- [128] D. Caurant, P. Loiseau, O. Majerus, V. Aubin Chevaldonne, and I. Bardez, “Glasses, glass-ceramics and ceramics for immobilization of highly radioactive nuclear wastes,” New York: Nova Science Publishers, Inc., 2009, p. 359.
- [129] I. Bardez *et al.*, “Structural characterisation of rare earth rich glasses for nuclear waste immobilisation,” *Phys. Chem. Glas.*, vol. 46, no. 4, pp. 320–329, 2005.
- [130] J. Zhang *et al.*, “Nanoscale imaging of alteration layers of corroded international simple glass particles using ToF-SIMS,” *Nucl. Instruments Methods Phys. Res. Sect. B Beam Interact. with Mater. Atoms*, vol. 404, pp. 45–51, 2017, doi: 10.1016/j.nimb.2017.01.053.
- [131] W. Geilmann, “Contributions to the knowledge of old glasses VI): A peculiar weathering phenomenon on broken Roman glass,” *Glas. Berichte*, no. 33, pp. 291–296, 1960.
- [132] K. Bange *et al.*, “Multi-method characterization of soda-lime glass corrosion Part 1. Analysis techniques and corrosion in liquid water,” *Glas. Sci. Technol. Glas. Berichte*, vol. 74, no. 5, pp. 127–141, 2001.
- [133] K. Bange *et al.*, “Multi-method characterization of soda-lime glass corrosion. Part 2. Corrosion in humidity,” *Glas. Sci. Technol. Glas. Berichte*, vol. 75, no. 1, pp. 20–33, 2002.
- [134] W. H. Zachariasen, “The Atomic Arrangement in Glass,” *J. Am. Chem. Soc.*, vol. 54, no. 10, pp. 3841–3851, 1932.
- [135] B. E. Warren, “X-ray Determination of the Structure of Glass,” *J. Am. Ceram. Soc.*, vol. 17, pp. 249–254, 1934, doi: 10.1007/BF02533005.
- [136] G. N. Greaves, A. Fontaine, P. Lagarde, D. Raoux, and S. J. Gurman, “Local structure of silicate glasses,” *Nature*, vol. 293, pp. 611–616, 1981, doi: <https://doi.org/10.1038/293611a0>.
- [137] S. A. Tyler and E. S. Barghoorn, “Ambient pyrite grains in Precambrian cherts,” *American Journal of Science*, vol. 261, no. 5, pp. 424–432, 1963. doi:

10.2475/ajs.261.5.424.

- [138] N. McLoughlin *et al.*, “Assessing the biogenicity and syngenicity of candidate bioalteration textures in pillow lavas of the ~2.52 Ga Wutai greenstone terrane of China,” *Chinese Sci. Bull.*, vol. 55, no. 2, pp. 188–199, 2010, doi: 10.1007/s11434-009-0448-0.
- [139] J. L. Crovisier, J. Honnorez, and J. P. Eberhart, “Dissolution of basaltic glass in seawater: Mechanism and rate,” *Geochim. Cosmochim. Acta*, vol. 51, no. 11, pp. 2977–2990, 1987, doi: 10.1016/0016-7037(87)90371-1.
- [140] J. L. Weaver, P. T. Depriest, A. E. Plymale, C. I. Pearce, B. Arey, and R. J. Koestler, “Microbial interactions with silicate glasses,” *npj Mater. Degrad.*, pp. 1–18, 2021, doi: 10.1038/s41529-021-00153-w.
- [141] J. S. McCloy, “Frontiers in natural and un-natural glasses: An interdisciplinary dialogue and review,” *J. Non-Crystalline Solids X*, vol. 4, no. 100035, 2019, doi: 10.1016/j.nocx.2019.100035.
- [142] N. R. . M. Banerjee K.; Furnes, H.; Staudigel, H.; de Wit, M., “Potential for Early Life Hosted in Basaltic Glass on a Wet Mars,” in *Second Conference on Early Mars: Geologic, Hydrologic, and Climatic Evolution and the Implications for Life*, 2004, p. 8048.
- [143] H. Staudigel and H. Furnes, “Microbial mediation of oceanic crust alteration,” in *Hydrogeology of the oceanic lithosphere*, E. E. Davis and H. Elderfield, Eds. Cambridge: Cambridge University Press, 2004, pp. 606–624.
- [144] S. McMahon and J. Cosmidis, “False biosignatures on Mars: anticipating ambiguity,” *J. Geol. Soc. London.*, vol. 179, no. 2, pp. jgs2021-050, 2022, doi: 10.1144/jgs2021-050.
- [145] N. McLoughlin *et al.*, “Micro-bioerosion in volcanic glass: Extending the ichnofossil record to Archaean basaltic crust,” *Curr. Dev. Bioerosion*, pp. 371–396, 2008, doi: 10.1007/978-3-540-77598-0\_19.
- [146] G. Kamei, Y. Yusa, and T. Arai, “A natural analogue of nuclear waste glass in compacted bentonite,” *Appl. Geochemistry*, vol. 15, no. 2, pp. 141–155, 2000, doi: 10.1016/S0883-2927(99)00036-0.
- [147] R. C. Ewing and M. J. Jercinovic, “Natural Analogues: Their Application to the Prediction of the Long-term Behavior of Nuclear Waste Forms,” *Mater. Res. Soc. Symp. Proc.*, vol. 84, pp. 67–83, 1987.
- [148] M. J. Apted, “Natural analogues for predicting the reliability of the engineered barrier system for high-level waste,” *J. Geochemical Explor.*, vol. 46, no. 1, pp. 35–62, 1992, doi: 10.1016/0375-6742(92)90100-M.
- [149] G. Libourel, A. Verney-carron, A. Morlok, A. Michelin, D. Neff, and P. Dillmann, “The use of natural and archeological analogues for understanding the long-term behavior of nuclear glasses,” *Comptes Rendus Geosci.*, vol. 343, no. 2–3, pp. 237–245, 2011, doi: 10.1016/j.crte.2010.12.004.
- [150] A. P. Dickin, “Hydrothermal leaching of rhyolite glass in the environment has implications for nuclear waste disposal,” *Nature*, vol. 294, no. 5839, pp. 342–347, 1981.
- [151] G. Malow, W. Lutze, and R. C. Ewing, “Alteration effects and leach rates of basaltic glasses: Implications for the long-term stability of nuclear waste form borosilicate glasses,” *J. Non. Cryst. Solids*, vol. 67, no. 1–3, pp. 305–321, 1984, doi: 10.1016/0022-

3093(84)90156-X.

- [152] W. Lutze, G. Malow, R. C. Ewing, M. J. Jercinovic, and K. Keil, "Alteration of basalt glasses: Implications for modelling the long-term stability of nuclear waste glasses," *Nature*, vol. 314, no. 6008, pp. 252–255, 1985, doi: 10.1038/314252a0.
- [153] J. K. Bates, L. J. Jardine, and M. J. Steindler, "Hydration Aging of Nuclear Waste Glass," *Science (80-. )*, vol. 218, no. 4567, pp. 51–54, 1982.
- [154] W. R. Alexander, H. M. Reijonen, and I. G. McKinley, "Natural analogues: studies of geological processes relevant to radioactive waste disposal in deep geological repositories," *Swiss J. Geosci.*, vol. 108, no. 1, pp. 75–100, 2015, doi: 10.1007/s00015-015-0187-y.
- [155] J. L. Crovisier, T. Advocat, and J. L. Dussossoy, "Nature and role of natural alteration gels formed on the surface of ancient volcanic glasses (Natural analogs of waste containment glasses)," *J. Nucl. Mater.*, vol. 321, no. 1, pp. 91–109, 2003, doi: 10.1016/S0022-3115(03)00206-X.
- [156] I. Techer, T. Advocat, J. Lancelot, and J. M. Liotard, "Dissolution kinetics of basaltic glasses: Control by solution chemistry and protective effect of the alteration film," *Chem. Geol.*, vol. 176, no. 1–4, pp. 235–263, 2001, doi: 10.1016/S0009-2541(00)00400-9.
- [157] I. Techer, J. Lancelot, N. Clauer, J. M. Liotard, and T. Advocat, "Alteration of a basaltic glass in an argillaceous medium: The Salagou dike of the Iodéve Permian (France). Analogy with an underground nuclear waste repository," *Geochim. Cosmochim. Acta*, vol. 65, no. 7, pp. 1071–1086, 2001, doi: 10.1016/S0016-7037(00)00583-4.
- [158] N. A. Stroncik and H. U. Schmincke, "Palagonite - A review," *Int. J. Earth Sci.*, vol. 91, no. 4, pp. 680–697, 2002, doi: 10.1007/s00531-001-0238-7.
- [159] N. A. Chapman, I. G. McKinley, and J. A. T. Smellie, "The potential of natural analogues in assessing systems for deep disposal of high-level radioactive waste," *SKB Technical Report 84-16*. Swedish Nuclear Fuel and Waste Management Co, Stockholm, p. 112, 1984. doi: 10.1016/0265-931x(86)90029-9.
- [160] M. A. Peacock, "The Distinction between Chlorophaeite and Palagonite," *Geol. Mag.*, vol. 67, no. 4, pp. 170–178, 1930, doi: 10.1017/S0016756800099155.
- [161] R. Sjöblom, H. Ecke, and E. Brännvall, "On the possibility of using vitrified forts as anthropogenic analogues for assessment of long-term behaviour of vitrified waste," in *Waste Management and the Environment VI*, 2012, no. 163, pp. 225–236. doi: 10.2495/WM120211.
- [162] P. Kresten, C. Goedicke, and A. Manzano, "TL-dating of vitrified material," *Geochronometria*, vol. 22, pp. 9–14, 2003.
- [163] A. B. McHardy, "On vitrified forts, with results of experiments as to the probable manner in which their vitrification may have been produced," *Proc. Antiq. Scotl.*, vol. 40, pp. 136–150, 1906.
- [164] E. Youngblood, B. J. Fredriksson, F. Kraut, and K. Fredriksson, "Celtic vitrified forts: Implications of a chemical-petrological study of glasses and source rocks," *J. Archaeol. Sci.*, vol. 5, no. 2, pp. 99–121, 1978, doi: 10.1016/0305-4403(78)90027-4.
- [165] R. Sjöblom *et al.*, "Vitrified hillforts as anthropogenic analogues for nuclear waste glasses - Project planning and initiation," *Int. J. Sustain. Dev. Plan.*, vol. 11, no. 6, pp.

- 897–906, 2016, doi: 10.2495/SDP-V11-N6-897-906.
- [166] C. I. Pearce *et al.*, “Investigating alteration of pre-viking hillfort glasses from the broborg Hillfort Site, Sweden,” in *Materials Science and Technology Conference and Exhibition 2017*, 2017, vol. 2, pp. 957–959. doi: 10.7449/2017/MST-2017-957-959.
- [167] P. Kresten, L. Kero, and J. Chyssler, “Geology of the vitrified hill-fort Broborg in Uppland, Sweden,” *Geol. Föreningen i Stock. Förhandlingar*, vol. 115, no. 1, pp. 13–24, 1993.
- [168] P. Kresten and B. Ambrosiani, “Swedish vitrified forts — a reconnaissance study,” *Fornvännen*, vol. 87, 1992.
- [169] A. E. Plymale *et al.*, “Niche Partitioning of Microbial Communities at an Ancient Vitrified Hillfort: Implications for Vitrified Radioactive Waste Disposal,” *Geomicrobiol. J.*, vol. 38, no. 1, pp. 36–56, 2020, doi: 10.1080/01490451.2020.1807658.
- [170] B. Matthews, B. Arey, C. Pearce, and A. Kruger, “Tri-beam FIB Sample Preparation to Study Alterations in Ancient Glass from Broborg, a Vitrified Swedish Hillfort,” *Microsc. Microanal.*, vol. 25, no. S2, pp. 872–873, 2019, doi: 10.1017/s1431927619005099.
- [171] B. Matthews, B. Arey, C. Pearce, and A. Kruger, “Characterization of Glass Alterations in Ancient Glass from Various Environments from Broborg , a Vitrified Swedish Hillfort,” *Microsc. Microanal. 2020 Proc.*, pp. 1–2, 2020, doi: 10.1017/S1431927620022126.
- [172] J. L. Weaver *et al.*, “Microscopic Identification of Micro-Organisms on Pre-Viking Swedish Hillfort Glass,” *Microsc. Microanal.*, vol. 24, no. S1, pp. 2136–2137, 2018, doi: 10.1017/s1431927618011169.
- [173] S. Birch *et al.*, “Dun Deardail Hillfort, Lochaber: Year 1 Archaeological Excavation Data Structure Report.” AOC Archaeology, Loanhead, 2015.
- [174] J. Humble, “Dun Deardail, Glen Nevis,” in *Discovery and excavation in Scotland: The Journal of Archaeology Scotland*, vol. 16, P. Milburn, Ed. Wiltshire: Cathedral Communications Limited, 2015, p. 106. doi: 10.1017/CBO9781107415324.004.
- [175] C. Ellis, M. Cook, and M. Ritchie, “Dun Deardail: Archaeological Project Design.” Forestry Commission Scotland, Edinburgh, pp. 1–54, 2014.
- [176] M. Ritchie *et al.*, “The Archaeology of Dun Deardail.” Forestry Commission Scotland, Edinburgh, pp. 1–24, 2018.
- [177] J. Humble, “Dun Deardail, Glen Nevis,” in *Discovery and excavation in Scotland: The Journal of Archaeology Scotland*, vol. 17, P. Milburn, Ed. Wiltshire: Cathedral Communications Limited, 2016, p. 106. doi: 10.1017/CBO9781107415324.004.
- [178] M. Cook, A. Heald, and G. Shaw, “Dun Deardail Hillfort , Lochaber : Year 3 Archaeological Excavation Data Structure Report Dun Deardail Hillfort , Lochaber : Data Structure Report,” AOC Archeology, Inverness, 2017.
- [179] M. Collin *et al.*, “Structure of International Simple Glass and properties of passivating layer formed in circumneutral pH conditions,” *npj Mater. Degrad.*, vol. 2, no. 4, pp. 1–12, 2018, doi: 10.1038/s41529-017-0025-y.
- [180] X. Feng *et al.*, “Long-Term Comparison of Dissolution Behavior Between Fully Radioactive and Simulated Nuclear Waste Glasses,” *Nucl. Technol.*, vol. 104, no. 2, pp.

- 193–206, 1993, doi: 10.13182/NT93-A34883.
- [181] W. J. Weber *et al.*, “Waste and Plutonium Disposition,” *J. Mater. Res.*, vol. 12, no. 8, pp. 1946–1978, 1997, doi: 10.1089/ars.2013.5575.
- [182] S. Peugeot *et al.*, “Effect of alpha radiation on the leaching behaviour of nuclear glass,” *J. Nucl. Mater.*, vol. 362, no. 2–3, pp. 474–479, 2007, doi: 10.1016/j.jnucmat.2007.01.099.
- [183] H. Matzke and E. Vernaz, “Thermal and physicochemical properties important for the long term behavior of nuclear waste glasses,” *J. Nucl. Mater.*, vol. 201, pp. 295–309, 1993, doi: 10.1016/0022-3115(93)90186-3.
- [184] L. Werme *et al.*, “Chemical corrosion of highly radioactive borosilicate nuclear waste glass under simulated repository conditions,” *J. Mater. Res.*, vol. 5, no. 5, pp. 1130–1146, 1990, doi: 10.1557/jmr.1990.1130.
- [185] J. A. C. Marples, N. Godon, F. Lanza, and P. Van Iseghem, “Radionuclide Release from High-Level Waste Form Under Repository Conditions in Clay or Granite,” in *Proc. 3rd European Community Conf. Radioactive Waste Management Disposal*, 1991, pp. 287–301.
- [186] J. K. Bates, “Disposal of Vitrified Waste in an Unsaturated Environment,” in *Proc. 2nd Int. Conf. High Level Radioactive Waste Management*, 1991, p. 8.
- [187] X. Feng and J. K. Bates, “Initial Comparison of Leach Behavior Between Fully Radioactive and Simulated Waste Glass Through Long-Term Testing (ANL/CP--74200),” *Proc. 3rd Int. Conf. High Level Radioactive Waste Management*. Argonne National Laboratory, Argonne, 1992.
- [188] W. J. Weber *et al.*, “Radiation effects in glasses used for immobilization of high-level waste and plutonium disposition,” *J. Mater. Res.*, vol. 12, no. 8, pp. 1946–1978, 1997.
- [189] D. J. Wronkiewicz, “Radionuclide decay effects on waste glass corrosion,” *Mat. Res. Soc. Symp. Proc.*, vol. 333, pp. 83–97, 1994.
- [190] W. J. Weber, “Radiation effects in nuclear waste glasses,” *Nucl. Instruments Methods Phys. Res. Sect. B Beam Interact. with Mater. Atoms*, vol. 32, no. 1–4, pp. 471–479, 1988, doi: 10.1016/0168-583X(88)90257-1.
- [191] J. Marra, C. Crawford, and D. Peeler, “Letter Report on Compositional Measurements of ‘Common Simple’ Glass,” Savannah River National Laboratory, Aiken, South Carolina, 2012.
- [192] C. R. Scales, “Characterisation of simulated vitrified Magnox product manufactured on the VTR (Report 10929, Issue 6),” National Nuclear Laboratory (NNL), Didcot, 2011.
- [193] T. L. Goût, “Developing an understanding of the relationship between the durability of simplified and complex UK radioactive waste glasses,” no. September, 2019.
- [194] American Society for Testing and Materials (ASTM) International, “Standard Test Method for Static Leaching of Monolithic Waste Forms for Disposal of Radioactive Waste 1.” ASTM International, West Conshohocken, Pennsylvania, pp. 1–22, 2014. doi: 10.1520/C1220-10.Copyright.
- [195] American Society for Testing and Materials (ASTM) International, “Standard Test Methods for Determining Chemical Durability of Nuclear , Hazardous , and Mixed Waste Glasses and Multiphase Glass Ceramics : The Product Consistency Test ( PCT ) 1.” ASTM International, West Conshohocken, Pennsylvania, pp. 1–26, 2021. doi:

10.1520/C1285-14.2.

- [196] Radioactive Waste Management, “Waste Package Evolution Status Report,” Nuclear Decommissioning Authority (NDA), Didcot, 2016.
- [197] R. Wolfson, “Energy from Earth and Moon,” in *Energy, Environment, and Climate*, 2nd Editio., R. Wolfson, Ed. New York: W.W. Norton & Company, 2012, pp. 204–224.
- [198] J. H. Butler, D. C. Joy, G. F. Bradley, and S. J. Krause, “Low-voltage scanning electron microscopy of polymers,” *Polymer (Guildf)*., vol. 36, no. 9, pp. 1781–1790, 1995, doi: 10.1016/0032-3861(95)90924-Q.
- [199] R. C. Masters, “Novel techniques in the scanning electron microscope for characterising polymer-based photovoltaic materials,” PhD Thesis, The University of Sheffield, 2017.
- [200] Carl Zeiss X-ray Microscopy Inc., “ZEISS Xradia Versa User’ s Guide.” Carl Zeiss X-ray Microscopy Inc., Pleasanton, California, p. 388, 2014.
- [201] A. Clearfield, “Introduction to Diffraction,” in *Principles and Applications of Powder Diffraction Principles and Applications of Powder Diffraction*., A. C. Clearfield, J. H. Reibenspies, and N. Bhuvanesh, Eds. Chichester: Blackwell Publishing Ltd., 2008, pp. 73–121.
- [202] L. M. D. Cranswick, “An Overview of Powder Diffraction,” in *Principles and Applications of Powder Diffraction*, A. Clearfield, J. H. Reibenspies, and N. Bhuvanesh, Eds. Chichester: Blackwell Publishing Ltd., 2008, pp. 1–72. doi: 10.1002/9781444305487.ch1.
- [203] T. G. Fawcett, J. Faber, S. Kabbekodu, F. McClune, and D. Rafaja, “PDF-4+, the material identification database,” *Microstruct. Anal. Mater. Sci.*, pp. 1–3, 2005.
- [204] S. Amelinckx, D. Van Dyck, J. Van Landuyt, and G. Van Tendeloo, Eds., “Scanning Electron Microscopy,” in *Handbook of Microscopy: Applications in Materials Science, Solid-State Physics and Chemistry. Methods II*, Weinheim: Wiley-VCH, 1997, pp. 539–561. doi: 10.1002/9783527619283.
- [205] J. I. Goldstein *et al.*, “Introduction,” in *Scanning Electron microscopy and X-Ray microanalysis*, Third edit., New York: Springer Science + Business Media, 2007, pp. 1–20. doi: 10.1126/science.7054874.
- [206] John C. Russ, “X-ray emission,” in *Fundamentals of Energy Dispersive X-Ray Analysis*, First edit., Bodmin: Butterworths & Co. Ltd., 1984, pp. 1–10.
- [207] P. J. Goodhew, J. Humphreys, and R. Beanland, “The Scanning Electron Microscope,” in *Electron Microscopy and Analysis*, Third Edit., London: Taylor & Francis, 2001, pp. 122–169.
- [208] J. Kastner and C. Heinzl, “X-ray Tomography,” in *Handbook of Advanced Non-Destructive Evaluation*, N. Ida and N. Meyendorf, Eds. Cham: Springer International Publishing, 2019, pp. 321–349.
- [209] G. F. Knoll, “Radiation Interactions,” in *Radiation Detection and Measurement*, Third edit., New York: John Wiley & Sons, Inc., 2000, pp. 29–57. doi: 10.1109/PROC.1981.12016.
- [210] F. H. Attix, “Gamma- and X-Ray Interaction in Matter,” in *Introduction to Radiological Physics and Radiation Dosimetry*, Weinheim: Wiley-VCH Verlag GmbH & Co. KGaA, 2004, pp. 124–157.

- [211] V. Cnudde and M. N. Boone, “High-resolution X-ray computed tomography in geosciences: A review of the current technology and applications,” *Earth-Science Rev.*, vol. 123, pp. 1–17, 2013, doi: 10.1016/j.earscirev.2013.04.003.
- [212] S. M. Kak, A.C., “Algorithms for Reconstruction with Nondiffracting Source,” in *Principles of Computerized Tomographic Imaging*, New York: The Institute of Electrical and Electronics Engineers Inc., 1999, pp. 49–113.
- [213] D. J. M. Ngan-Tillard and D. J. Huisman, “Micro-CT Scanning,” in *Archaeological Soil and Sediment Micromorphology*, First edit., C. Nicosia and G. Stoops, Eds. Chichester: John Wiley & Sons Ltd., 2017, pp. 441–449. doi: 10.1002/9781118941065.ch42.
- [214] S. Sleutel *et al.*, “Comparison of different nano- and micro-focus X-ray computed tomography set-ups for the visualization of the soil microstructure and soil organic matter,” *Comput. Geosci.*, vol. 34, no. 8, pp. 931–938, 2008, doi: 10.1016/j.cageo.2007.10.006.
- [215] Y. Morishige and A. Kimura, “Ionization Interference in Inductively Coupled Plasma-Optical Emission Spectroscopy,” *SEI Tech. Rev.*, vol. 66, pp. 106–111, 2008.
- [216] Mettler-Toledo, “A Guide to pH Measurement: Theory & Practice of Laboratory pH Applications.” Mettler-Toledo, Ohio, pp. 1–52, 2016. [Online]. Available: [www.mt.com/pH](http://www.mt.com/pH)
- [217] D. L. Parkhurst and C. a. J. Appelo, “Description of Input and Examples for PHREEQC Version 3 — A Computer Program for Speciation, Batch-Reaction, One-Dimensional Transport, and Inverse Geochemical Calculations.,” in *U.S. Geological Survey Techniques and Methods, Book 6 (Modelling Techniques), Section A (Groundwater)*, Denver, Colorado: United States Geological Survey, 2013, p. 497.
- [218] S. R. Charlton and D. L. Parkhurst, “Modules based on the geochemical model PHREEQC for use in scripting and programming languages,” *Comput. Geosci.*, vol. 37, no. 10, pp. 1653–1663, 2011, doi: 10.1016/j.cageo.2011.02.005.
- [219] T. C. Kaspar *et al.*, “Physical and optical properties of the International Simple Glass,” *npj Mater. Degrad.*, vol. 3, no. 1, pp. 1–15, 2019, doi: 10.1038/s41529-019-0069-2.
- [220] B. E. Scheetz, W. P. Freeborn, D. K. Smith, C. Anderson, M. Zolensky, and W. B. White, “The Role of Boron in Monitoring the Leaching of Borosilicate Glass Waste Forms,” *MRS Proc.*, vol. 44, pp. 1–11, 1984.
- [221] C. R. Scales, “Characterisation of Simulated Vitrified Magnox product manufactured on the VTR (Report 10929, Issue 4),” *National Nuclear Laboratory*. Didcot, pp. 1–16, 2011.
- [222] C. M. Jantzen, W. E. Lee, and M. I. Ojovan, “Radioactive waste (RAW) conditioning, immobilization, and encapsulation processes and technologies: Overview and advances,” in *Radioactive Waste Management and Contaminated Site Clean-Up: Processes, Technologies and International Experience*, W. E. Lee, M. I. Ojovan, and C. M. Jantzen, Eds. Cambridge, UK: Woodhead Publishing Limited, 2013, pp. 171–272. doi: 10.1533/9780857097446.1.171.
- [223] H. Zhang, C. L. Corkhill, P. G. Heath, R. J. Hand, M. C. Stennett, and N. C. Hyatt, “Effect of Zn- and Ca-oxides on the structure and chemical durability of simulant alkali borosilicate glasses for immobilisation of UK high level wastes,” *J. Nucl. Mater.*, vol. 462, pp. 321–328, 2015, doi: 10.1016/j.jnucmat.2015.04.016.

- [224] T. L. Goût, M. T. Harrison, and I. Farnan, “Evaluating the temperature dependence of Magnox waste glass dissolution,” *J. Non. Cryst. Solids*, vol. 518, pp. 75–84, 2019, doi: 10.1016/j.jnoncrsol.2019.05.017.
- [225] Z. Wang, P. Lazor, S. K. Saxena, and G. Artioli, “High-pressure Raman spectroscopic study of spinel (ZnCr<sub>2</sub>O<sub>4</sub>),” *J. Solid State Chem.*, vol. 165, no. 1, pp. 165–170, 2002, doi: 10.1006/jssc.2002.9527.
- [226] Z. Wang, S. K. Saxena, P. Lazor, and H. S. C. O’Neill, “An in situ Raman spectroscopic study of pressure induced dissociation of spinel NiCr<sub>2</sub>O<sub>4</sub>,” *J. Phys. Chem. Solids*, vol. 64, no. 3, pp. 425–431, 2003, doi: 10.1016/S0022-3697(02)00328-1.
- [227] D. F. Bickford and C. M. Jantzen, “Devitrification Behaviour of SRL Defense Waste Glass,” in *Proceedings Materials Research Society Annual Meeting*, 1983, vol. 26, pp. 557–565.
- [228] C. M. Jantzen and D. F. Bickford, “Leaching of Devitrified Glass Containing Simulated SRP Nuclear Waste,” *Mat. Res. Soc. Symp. Proc.*, vol. 44, pp. 135–146, 1984.
- [229] M. I. Ojovan and W. E. Lee, “Topologically disordered systems at the glass transition,” *J. Phys. Condens. Matter*, vol. 18, no. 50, pp. 11507–11520, 2006.
- [230] T. M. Iwalewa, T. Qu, and I. Farnan, “Applied Geochemistry Investigation of the maximum dissolution rates and temperature dependence of a simulated UK nuclear waste glass in circum-neutral media at 40 and 90°C in a dynamic system,” *Appl. Geochemistry*, vol. 82, pp. 177–190, 2017, doi: 10.1016/j.apgeochem.2017.05.018.
- [231] J. D. Vienna, J. J. Neeway, J. V. Ryan, and S. N. Kerisit, “Impacts of glass composition, pH, and temperature on glass forward dissolution rate,” *npj Mater. Degrad.*, vol. 2, no. 1, pp. 1–12, 2018, doi: 10.1038/s41529-018-0042-5.
- [232] C. A. Utton, R. J. Hand, P. A. Bingham, N. C. Hyatt, S. W. Swanton, and S. J. Williams, “Dissolution of vitrified wastes in a high-pH calcium-rich solution,” *J. Nucl. Mater.*, vol. 435, no. 1–3, pp. 112–122, 2013, doi: 10.1016/j.jnucmat.2012.12.032.
- [233] C. L. Corkhill, N. J. Cassingham, P. G. Heath, and N. C. Hyatt, “Dissolution of UK high-level waste glass under simulated hyperalkaline conditions of a colocated geological disposal facility,” *Int. J. Appl. Glas. Sci.*, vol. 4, no. 4, pp. 341–356, 2013, doi: 10.1111/ijag.12042.
- [234] C. Brookes, M. T. Harrison, A. Riley, and C. J. Steele, “The Effect of Increased Waste Loading on the Durability of High Level Waste,” *Mater. Res. Soc. Symp. Proc.*, vol. 1265, 2011, doi: 10.1557/PROC-1265-AA03-05.
- [235] H. U. Zwicky *et al.*, “Corrosion Behaviour of British Magnox Waste Glass in Pure Water,” *Mat. Res. Soc. Symp. Proc.*, vol. 127, no. 1, pp. 129–136, 1988.
- [236] A. J. Fisher and C. L. Corkhill, “Experimental studies to investigate the durability of UK HLW glasses using a new base glass formulation and glasses from POCO operations (Final Report).” NucleUS Immobilisation Science Laboratory, The University of Sheffield, Sheffield, pp. 1–83, 2021.
- [237] J. Hopf *et al.*, “Toward an understanding of surface layer formation, growth, and transformation at the glass-fluid interface,” *Geochim. Cosmochim. Acta*, vol. 229, pp. 65–84, 2018, doi: 10.1016/j.gca.2018.01.035.
- [238] M. Lobanova, A. Ledieu, P. Barboux, F. Devreux, O. Spalla, and J. Lambard, “Effect of ZrO<sub>2</sub> on the glass durability,” *Mat. Res. Soc. Symp. Proc.*, vol. 713, p. JJ15.1.1-9, 2002,

doi: 10.1557/PROC-713-JJ15.1.

- [239] M. Arab, C. Cailleateau, and F. Angeli, “Aqueous alteration of five-oxide silicate glasses: Experimental approach and Monte Carlo modeling,” *J. Non. Cryst. Solids*, vol. 354, pp. 155–161, 2008, doi: 10.1016/j.jnoncrysol.2007.06.095.
- [240] B. Fleury, N. Godon, A. Ayrat, and S. Gin, “SON68 glass dissolution driven by magnesium silicate precipitation,” *J. Nucl. Mater.*, vol. 442, no. 1–3, pp. 17–28, 2013, doi: 10.1016/j.jnucmat.2013.08.029.
- [241] T. Ma *et al.*, “A mechanistic model for long-term nuclear waste glass dissolution integrating chemical affinity and interfacial diffusion barrier,” *J. Nucl. Mater.*, vol. 486, pp. 70–85, 2017, doi: 10.1016/j.jnucmat.2017.01.001.
- [242] T. Ohkubo, S. Gin, M. Collin, and Y. Iwadate, “Molecular Dynamics Simulation of Water Confinement in Disordered Aluminosilicate Subnanopores,” *Sci. Rep.*, vol. 8, no. 1, pp. 1–11, 2018, doi: 10.1038/s41598-018-22015-3.
- [243] B. Grambow, “Corrosion of glass,” in *Uhlig’s Corrosion Handbook*, Third Edit., H. H. Uhlig, Ed. Hoboken, New Jersey: John Wiley & Sons, 2011, pp. 399–419. doi: 10.1016/0039-6028(80)90444-6.
- [244] W. L. Gong, L. M. Wang, and R. C. Ewing, “Analytical electron microscopy study of surface layers formed on the French SON68 nuclear waste glass during vapor hydration at 200°C,” *J. Nucl. Mater.*, vol. 254, no. 2–3, pp. 249–265, 1998.
- [245] J. C. Petit, G. Della Mea, J. C. Dran, M. C. Magonthier, P. A. Mando, and A. Paccagnella, “Hydrated-layer formation during dissolution of complex silicate glasses and minerals,” *Geochim. Cosmochim. Acta*, vol. 54, no. 7, pp. 1941–1955, 1990, doi: 10.1016/0016-7037(90)90263-K.
- [246] T. A. Abrajano, “Secondary Phase Formation during Nuclear Waste-Glass Dissolution,” *Clays Clay Miner.*, vol. 38, no. 5, pp. 537–548, 2006, doi: 10.1346/ccmn.1990.0380511.
- [247] M. D. Wilson and E. D. Pittman, “Authigenic clays in sandstones; recognition and influence on reservoir properties and paleoenvironmental analysis,” *J. Sediment. Res.*, vol. 47, no. 1, pp. 3–31, 1977.
- [248] I. S. Muller, S. Ribet, I. L. Pegg, S. Gin, and P. Frugier, “Characterization of alteration phases on HLW glasses after 15 years of PCT leaching,” *Ceram. Trans.*, vol. 176, pp. 191–199, 2006, doi: 10.1002/9781118407950.ch19.
- [249] B. Thien, N. Godon, F. Hubert, F. Angéli, S. Gin, and A. Ayrat, “Structural identification of a trioctahedral smectite formed by the aqueous alteration of a nuclear glass,” *Appl. Clay Sci.*, vol. 49, no. 3, pp. 135–141, 2010, doi: 10.1016/j.clay.2010.04.016.
- [250] A. C. D. Newman, *Chemistry of Clays and Clay Minerals (Mineralogical Society Monograph No. 6)*. Harlow: Longman Scientific & Technical, 1987.
- [251] B. Grambow and R. Müller, “Chemistry of Glass Corrosion in High Saline Brines,” *Mat. Res. Soc. Symp. Proc.*, vol. 176, pp. 229–240, 1990.
- [252] J. M. Schofield *et al.*, “Experimental studies of the chemical durability of UK HLW and ILW glasses. First interim progress report (RWM005105),” no. 1. Amec Foster Wheeler, Didcot, pp. 1–321, 2017.
- [253] J. M. Schofield, A. Clacher, C. Utton, S. W. Swanton, and R. J. Hand, “Initial dissolution rate measurements for 25 wt % simulant waste-loaded Magnox VTR product in simulated groundwaters (Report #NPO004598).” Nuclear Decommissioning Authority

- (NDA), Didcot, 2012.
- [254] C. L. Thorpe *et al.*, “Forty years of durability assessment of nuclear waste glass: A review of standard methods,” *npj Mater. Degrad.*, vol. 5, no. 61, pp. 1–28, 2021, doi: 10.1038/s41529-021-00210-4.
- [255] H. Smith, “Transmutation of strontium to zirconium in high-level nuclear waste glass and the effect on dissolution behaviour.” Masters Dissertation, The University of Sheffield, 2017.
- [256] O. Majérus, P. Lehuédé, I. Biron, F. Alloteau, S. Narayanasamy, and D. Caurant, “Glass alteration in atmospheric conditions: crossing perspectives from cultural heritage, glass industry, and nuclear waste management,” *npj Mater. Degrad.*, vol. 4, no. 1, 2020, doi: 10.1038/s41529-020-00130-9.
- [257] R. H. Brill, “Crizzling – a problem in glass conservation,” *Stud. Conserv.*, vol. 20, pp. 121–134, 1975, doi: 10.1179/sic.1975.s1.021.
- [258] J. J. Kunicki-Goldfinger, “Unstable historic glass: symptoms, causes, mechanisms and conservation,” *Stud. Conserv.*, vol. 53, pp. 47–60, 2008, doi: 10.1179/sic.2008.53.supplement-2.47.
- [259] G. E. Lofgren, “Experimental Devitrification of Rhyolite Glass,” PhD Thesis, Stanford University, 1968.
- [260] M. Morgenstein and T. J. Riley, “Hydration-rind dating of basaltic glass: a new method for archaeological chronologies,” *Asian Perspect.*, vol. 17, no. 2, pp. 145–159, 1974.
- [261] J. A. Apps, “Alteration of Natural Glass in Radioactive Waste Repository Host Rocks: A Conceptual Review (LBNL Report #: LBL-22871).” Lawrence Berkeley National Laboratory, California, pp. 1–39, 1987.
- [262] P. Jollivet *et al.*, “Effect of clayey groundwater on the dissolution rate of the simulated nuclear waste glass SON68,” *J. Nucl. Mater.*, vol. 420, no. 1–3, pp. 508–518, 2012, doi: 10.1016/j.jnucmat.2011.10.026.
- [263] E. Huang, C. H. Chen, T. Huang, E. H. Lin, and J.-A. Xu, “Raman spectroscopic characteristics of Mg-Fe-Ca pyroxenes,” *Am. Mineral.*, vol. 85, no. 3–4, pp. 473–479, 2000.
- [264] A. Buzatu and N. Buzgar, “The Raman study of single-chain silicates,” *Analele Stiint. Univ. Al. Cuza din Iasi. Sect. 2, Geol.*, vol. 56, no. 1, pp. 107–125, 2010.
- [265] I. Techer, “Contributions of Vitreous Natural Analogs to the Investigation of Long-Term Nuclear Glass Behavior,” PhD Thesis, University of Montpellier II, 1999.
- [266] J. E. Shelby, “Compositions and Properties of Commercial Glasses,” in *Introduction to Glass Science and Technology*, Second Edi., Cambridge: The Royal Society of Chemistry, 2005, pp. 262–274.
- [267] R. N. Greenberger *et al.*, “Hydrothermal alteration and diagenesis of terrestrial lacustrine pillow basalts: Coordination of hyperspectral imaging with laboratory measurements,” *Geochim. Cosmochim. Acta*, vol. 171, pp. 174–200, 2015, doi: 10.1016/j.gca.2015.08.024.
- [268] W. F. Foshag and A. O. Woodford, “Bentonitic magnesian clay-mineral from California,” *Am. Mineral.*, vol. 21, no. 4, pp. 238–244, 1936.
- [269] J. W. Anthony, R. A. Bideaux, K. W. Bladh, and M. C. Nichols, Eds., *Hectorite:*

- Handbook of Mineralogy*. Chantilly, Virginia: Mineralogical Society of America, 2001. [Online]. Available: <http://www.handbookofmineralogy.org/>.
- [270] M. Debure, P. Frugier, L. De Windt, and S. Gin, “Borosilicate glass alteration driven by magnesium carbonates,” *J. Nucl. Mater.*, vol. 420, no. 1–3, pp. 347–361, 2012, doi: 10.1016/j.jnucmat.2011.09.032.
- [271] T. Ducasse *et al.*, “Alteration of synthetic basaltic glass in silica saturated conditions : Analogy with nuclear glass,” *Appl. Geochemistry*, vol. 97, no. July, pp. 19–31, 2018, doi: 10.1016/j.apgeochem.2018.08.001.
- [272] P. Dillmann, S. Gin, D. Neff, L. Gentaz, and D. Rebiscoul, “Effect of natural and synthetic iron corrosion products on silicate glass alteration processes,” *Geochim. Cosmochim. Acta*, vol. 172, pp. 287–305, 2016, doi: 10.1016/j.gca.2015.09.033.
- [273] L. Trotignon, J. C. Petit, G. Della Mea, and J. C. Dran, “The compared aqueous corrosion of four simple borosilicate glasses: Influence of Al, Ca and Fe on the formation and nature of secondary phases,” *J. Nucl. Mater.*, vol. 190, no. C, pp. 228–246, 1992, doi: 10.1016/0022-3115(92)90088-3.
- [274] S. Gin, I. Ribet, and M. Couillard, “Role and properties of the gel formed during nuclear glass alteration: Importance of gel formation conditions,” *J. Nucl. Mater.*, vol. 298, no. 1–2, pp. 1–10, 2001, doi: 10.1016/S0022-3115(01)00573-6.
- [275] A. Ledieu, F. Devreux, and P. Barboux, “The role of aluminium in the durability of alumino-borosilicate glasses,” *Phys. Chem. Glas.*, vol. 46, no. 1, pp. 12–20, 2005.
- [276] Z. Andriambololona, N. Godon, and E. Vernaz, “R717 Glass Alteration in the Presence of Mortar: Effect of the Cement Grade,” *Mater. Res. Soc. Proc.*, vol. 257, 1991, doi: 10.1557/proc-257-151.
- [277] Y. Oka, M. Tomozawa, and C. Refinement, “Calcium Deposition on Glass Surface as an Inhibitor to Alkaline Attack,” *J. Am. Ceram. Soc.*, vol. 62, pp. 631–632, 1979.
- [278] Y. Oka and M. Tomozawa, “Effect of alkaline earth ion as an inhibitor to alkaline attack on silica glass,” *J. Non. Cryst. Solids*, vol. 42, no. 1–3, pp. 535–543, 1980, doi: 10.1016/0022-3093(80)90052-6.
- [279] S. Depierre, F. Frizon, S. Gin, and F. Angeli, “Leaching of Nuclear Waste Glass in Cement Pore Water: Effect of Calcium in Solution,” in *Cement-Based Materials for Nuclear Waste Storage*, F. Bart, C. Cau-Di-Coumes, F. Frizon, and S. Lorente, Eds. New York: Springer Science+ Business Media, 2013, pp. 161–168. doi: 10.1007/978-1-4614-3445-0.
- [280] H. Aréna *et al.*, “Impact of Fe, Mg and Ca elements on glass alteration: Interconnected processes,” *Geochim. Cosmochim. Acta*, vol. 239, pp. 420–445, 2018, doi: 10.1016/j.gca.2018.08.007.
- [281] H. Maraghechi, F. Rajabipour, C. G. Pantano, and W. D. Burgos, “Effect of calcium on dissolution and precipitation reactions of amorphous silica at high alkalinity,” *Cem. Concr. Res.*, vol. 87, pp. 1–13, 2016, doi: 10.1016/j.cemconres.2016.05.004.
- [282] H. Frey, “Applications and Developments of Thin Film Technology,” in *Handbook of Thin-Film Technology*, First edit., H. Frey and H. R. Khan, Eds. Berlin: Springer-Verlag Berlin Heidelberg, 2015, pp. 279–296.
- [283] M. Inui, N. Umezu, K. Wakasaki, and S. Sato, “Thickness and clearance visualization based on distance field of 3D objects,” *J. Comput. Des. Eng.*, vol. 2, no. 3, pp. 183–194,

- 2015, doi: 10.1016/j.jcde.2015.04.001.
- [284] K. Subburaj, S. Patil, and B. Ravi, “Voxel-Based Thickness Analysis of Intricate Objects,” *Int. J. CAD/CAM*, vol. 6, no. 1, pp. 105–115, 2006.
- [285] Collins Dictionaries, *Collins Complete and Unabridged - English Dictionary*, 12th ed. Glasgow: Harper Collins Publishers, 2018.
- [286] D. Rebiscoul, A. Van der Lee, P. Frugier, A. Ayril, and S. Gin, “X-ray reflectometry characterization of SON 68 glass alteration films,” *J. Non. Cryst. Solids*, vol. 325, no. 1–3, pp. 113–123, 2003, doi: 10.1016/S0022-3093(03)00321-1.
- [287] B. E. Scheetz and C. M. Stevenson, “The Role of Resolution and Sample Preparation in Hydration Rim Measurement: Implications for Experimentally Determined Hydration Rates,” *Am. Antiq.*, vol. 53, no. 1, pp. 110–117, 1988.
- [288] J. E. Ericson, “Obsidian Hydration Rate Development,” *Mat. Res. Soc. Symp. Proc.*, vol. 123, pp. 215–224, 1988.
- [289] I. Friedman and R. L. Smith, “A new dating method using obsidian: Part I, the development of the method,” *Am. Antiq.*, vol. 25.4, no. 4, pp. 476–522, 1960.
- [290] J. W. Michels and I. S. T. Tsong, “Obsidian Hydration Dating: A Coming of Age,” *Adv. Archaeol. Method Theory*, vol. 3, pp. 405–444, 1980.
- [291] T. A. Smith, “Obsidian Hydration as an Independent Dating Technique,” PhD Thesis, University of Alaska, 1977.
- [292] J. W. Michels, “Archeology and dating by hydration of obsidian,” *Science (80-. )*, vol. 158, no. 3798, pp. 211–214, 1967, doi: 10.1126/science.158.3798.211.
- [293] D. W. Clark, “Some Practical Applications of Obsidian Hydration Dating in the Subarctic,” *Arctic*, vol. 37, no. 2, pp. 91–109, 1984.
- [294] C. M. Stevenson, I. M. Abdelrehim, and S. W. Novak, “Infra-red photoacoustic and secondary ion mass spectrometry measurements of Obsidian hydration rims,” *J. Archaeol. Sci.*, vol. 28, no. 1, pp. 109–115, 2001, doi: 10.1006/jasc.1999.0559.
- [295] M. D. Glascock, “An inter-laboratory comparison of hydration rim measurements,” *International Association of Obsidian Studies Newsletter*, vol. 1, pp. 7–13, 1989.
- [296] W. Haller, “Concentration-Dependent Diffusion Coefficient of Water in Glass,” *Phys. Chem. Glas.*, vol. 4, no. 6, pp. 217–220, 1963.
- [297] W. R. Ambrose, “Obsidian hydration dating of a Pleistocene age site from the Manus Islands, Papua New Guinea,” *Quat. Sci. Rev.*, vol. 13, no. 2, pp. 137–142, 1994, doi: 10.1016/0277-3791(94)90039-6.
- [298] B. Sinha and G. Limited, “Efficient Wall Thickness Analysis Methods for Optimal Design of Casting Parts,” in *Second National Conference on Recent Developments in Mechanical Engineering*, 2013, vol. 2, pp. 53–58.
- [299] D. Ngo *et al.*, “Spectroscopic ellipsometry study of thickness and porosity of the alteration layer formed on international simple glass surface in aqueous corrosion conditions,” *npj Mater. Degrad.*, vol. 2, no. 1, pp. 1–9, 2018, doi: 10.1038/s41529-018-0040-7.
- [300] S. Portal and R. Sempere, “Study of alkali silicate glass corrosion using spectroscopic ellipsometry and secondary ion mass spectrometry,” *Phys. Chem. Glas.*, vol. 44, no. 4, pp. 303–307, 2003.

- [301] L. Li, J. Lei, L. Wu, and F. Pan, "Spectroscopic ellipsometry," in *Handbook of Modern Coating Technologies: Advanced Characterization Methods*, M. Aliofkhazraei, A. Nasar, M. Chipara, N. B. Laidani, and J. T. M. De Hosson, Eds. Amsterdam, Netherlands: Elsevier, 2021, pp. 45–83. doi: 10.1016/b978-0-444-63239-5.00002-0.
- [302] S. Ogawa and I. T. Additional, "Glass transition of ultrathin films probed by X-ray reflectivity," in *Carbohydrate*, M. Caliskan, I. H. Kavakli, and G. C. Oz, Eds. London: IntechOpen, 2017. doi: 10.1051/jp4:2000749.
- [303] J. Als-Nielsen, D. Jacquemain, K. Kjaer, F. Leveiller, M. Lahav, and L. Leiserowitz, "Principles and applications of grazing incidence X-ray and neutron scattering from ordered molecular monolayers at the air-water interface," *Phys. Rep.*, vol. 246, no. 5, pp. 251–313, 1994, doi: 10.1016/0370-1573(94)90046-9.
- [304] G. A. R. Gualda and M. Rivers, "Quantitative 3D petrography using x-ray tomography: Application to Bishop Tuff pumice clasts," *J. Volcanol. Geotherm. Res.*, vol. 154, no. 1–2, pp. 48–62, 2006, doi: 10.1016/j.jvolgeores.2005.09.019.
- [305] E. Maire and P. J. Withers, "Quantitative X-ray tomography," *Int. Mater. Rev.*, vol. 59, no. 1, pp. 1–43, 2014, doi: 10.1179/1743280413Y.0000000023.
- [306] Object Research Systems (ORS) Inc., "Dragonfly (2021.1) Help Documentation: ROI Pop-Up Menu," 2022. <https://www.theobjects.com/dragonfly/dfhelp/2020-1/> (accessed Mar. 04, 2022).
- [307] A. C. Fischer-Cripps, "Linear Elastic Fracture Mechanics," in *Introduction to Contact Mechanics*, Second Edi., A. C. Fischer-Cripps, Ed. Boston: 2007 Springer Science & Business Media, LLC, 2007, pp. 31–48.
- [308] M. I. Ojovan, A. Pankov, and W. E. Lee, "The ion exchange phase in corrosion of nuclear waste glasses," *J. Nucl. Mater.*, vol. 358, no. 1, pp. 57–68, 2006, doi: 10.1016/j.jnucmat.2006.06.016.
- [309] J.-L. Chermant, "Why automatic image analysis? An introduction to this issue," *Cem. Concr. Compos.*, vol. 23, no. 2–3, pp. 127–133, 2007, doi: 10.1007/BF00381704.
- [310] P. Belhomme, D. Houivet, W. Lecluse, and J. M. Haussonne, "Image analysis of multiphased ceramics," *J. Eur. Ceram. Soc.*, vol. 21, no. 10–11, pp. 2149–2151, 2001, doi: 10.1016/S0955-2219(01)00191-1.
- [311] M. E. Hoque, R. M. Ford, and J. T. Roth, "Automated image analysis of microstructure changes in metal alloys," in *Machine Vision Applications in Industrial Inspection XIII*, 2005, vol. 5679, pp. 1–9. doi: 10.1117/12.592504.
- [312] C. W. McMillin, "Application of automatic image analysis to wood science.," *Wood Sci.*, vol. 14, no. 3, pp. 97–105, 1982.
- [313] J. L. Chermant, L. Chermant, M. Coster, A. S. Dequiedt, and C. Redon, "Some fields of applications of automatic image analysis in civil engineering," *Cem. Concr. Compos.*, vol. 23, no. 2–3, pp. 157–169, 2001, doi: 10.1016/S0958-9465(00)00059-7.
- [314] Z. Ma, J. M. R. S. Tavares, R. N. Jorge, and T. Mascarenhas, "A review of algorithms for medical image segmentation and their applications to the female pelvic cavity," *Comput. Methods Biomech. Biomed. Engin.*, vol. 13, no. 2, pp. 235–246, 2010, doi: 10.1080/10255840903131878.
- [315] P. Iassonov, T. Gebrenegus, and M. Tuller, "Segmentation of X-ray computed tomography images of porous materials: A crucial step for characterization and

- quantitative analysis of pore structures,” *Water Resour. Res.*, vol. 45, no. 9, pp. 1–12, 2009, doi: 10.1029/2009WR008087.
- [316] I. Techer, T. Advocat, J. Lancelot, and J. M. Liotard, “Basaltic glass: Alteration mechanisms and analogy with nuclear waste glasses,” *J. Nucl. Mater.*, 2000, doi: 10.1016/S0022-3115(00)00399-8.
- [317] R. L. Mitchell, P. Davies, P. Kenrick, T. Volkenandt, C. Pleydell-Pearce, and R. Johnston, “Correlative Microscopy: a tool for understanding soil weathering in modern analogues of early terrestrial biospheres,” *Sci. Rep.*, vol. 11, no. 1, pp. 1–14, 2021, doi: 10.1038/s41598-021-92184-1.
- [318] W. L. Ebert and J. K. Bates, “A Comparison of Glass Reaction at High and Low Glass Surface / Solution Volume,” *Nucl. Technol.*, vol. 104, no. 3, 1993, doi: 10.13182/NT93-A34898.
- [319] W. L. Ebert, “The Effects of the Glass Surface Area/Solution Volume Ratio on Glass Corrosion: A Critical Review (Report #ANL- 94/34).” Argonne National Laboratory, Argonne, Illinois, 1995. doi: 10.2172/67461.
- [320] D. E. Clark and L. L. Hench, “An overview of the physical characterization of leached surfaces,” *Nucl. Chem. Waste Manag.*, vol. 2, no. 2, pp. 93–101, 1981, doi: 10.1016/0191-815X(81)90023-1.
- [321] L. L. Hench, D. E. Clark, and E. Lue Yen-Bower, “Corrosion of glasses and glass-ceramics,” *Nucl. Chem. Waste Manag.*, vol. 1, no. 1, pp. 59–75, 1980, doi: 10.1016/0191-815X(80)90029-7.
- [322] H. Furnes, N. R. Banerjee, K. Muehlenbachs, H. Staudigel, and M. De Wit, “Early Life Recorded in Archean Pillow Lavas,” *Science (80-. )*, vol. 304, no. 5670, pp. 578–581, 2004, doi: 10.1126/science.1095858.
- [323] M. R. M. Izawa, N. R. Banerjee, R. L. Flemming, N. J. Bridge, and C. Schultz, “Basaltic glass as a habitat for microbial life: Implications for astrobiology and planetary exploration,” *Planet. Space Sci.*, vol. 58, no. 4, pp. 583–591, 2010, doi: 10.1016/j.pss.2009.09.014.
- [324] A. G. Jongmans *et al.*, “Rock-eating fungi,” *Nature*, vol. 389, no. 6652, pp. 682–683, 1997.
- [325] E. Hoffland, R. Giesler, T. Jongmans, and N. Van Breemen, “Increasing feldspar tunneling by fungi across a North Sweden podzol chronosequence,” *Ecosystems*, vol. 5, no. 1, pp. 11–22, 2002, doi: 10.1007/s10021-001-0052-x.
- [326] E. Hoffland *et al.*, “The role of fungi in weathering,” *Front. Ecol. Environ.*, vol. 2, no. 5, pp. 258–264, 2004, doi: 10.1890/1540-9295(2004)002[0258:TROFIW]2.0.CO;2.
- [327] Ł. Pawlik, J. D. Phillips, and P. Šamonil, “Roots, rock, and regolith: Biomechanical and biochemical weathering by trees and its impact on hillslopes - A critical literature review,” *Earth-Science Rev.*, vol. 159, pp. 142–159, 2016, doi: 10.1016/j.earscirev.2016.06.002.
- [328] L. Vingataramin and E. H. Frost, “A single protocol for extraction of gDNA from bacteria and yeast,” *Biotechniques*, vol. 58, no. 3, pp. 120–125, 2015, doi: 10.2144/000114263.
- [329] R. J. Hand and A. B. Seddon, “An hypothesis on the nature of Griffith’s cracks in alkali silicate and silica glasses,” *Phys. Chem. Glas.*, vol. 38, no. 1, pp. 11–14, 1997.

- [330] R. Landeweert, E. Hoffland, R. D. Finlay, H. W. Kuyper, and N. van Breemen, “Linking plants to rocks: ectomycorrhizal fungi mobilize nutrients from minerals,” *Trends Ecol. Evol.*, vol. 16, no. 5, pp. 248–254, 2001, doi: 10.5506/APhysPolBSupp.6.131.
- [331] G. R. J. Holdren and R. A. Bener, “Mechanism of feldspar weathering - II Observations of feldspars from soils,” *Geochim. Cosmochim. Acta*, vol. 43, no. 8, pp. 1173–1186, 1979.
- [332] M. Ivarsson *et al.*, “Intricate tunnels in garnets from soils and river sediments in Thailand – Possible endolithic microborings,” *Public Libr. Sci. ONE*, vol. 13, no. 8, pp. 1–20, 2018, doi: 10.1371/journal.pone.0200351.
- [333] S. Dultz *et al.*, “Alteration of a Submarine Basaltic Glass under Environmental Conditions Conducive for Microorganisms: Growth Patterns of the Microbial Community and Mechanism of Palagonite Formation,” *Geomicrobiol. J.*, vol. 31, no. 9, pp. 813–834, 2014, doi: 10.1080/01490451.2014.897774.
- [334] N. McLoughlin, H. Furnes, N. R. Banerjee, K. Muehlenbachs, and H. Staudigel, “Ichnotaxonomy of microbial trace fossils in volcanic glass,” *J. Geol. Soc. London.*, vol. 166, no. 1, pp. 159–169, 2009, doi: 10.1144/0016-76492008-049.
- [335] M. R. Fisk, S. J. Giovannoni, and I. H. Thorseth, “Alteration of oceanic volcanic glass: Textural evidence of microbial activity,” *Science (80-. )*, vol. 281, no. 5379, pp. 978–980, 1998, doi: 10.1126/science.281.5379.978.
- [336] R. Ellis and R. Hermanis, “Trichophyton mentagrophytes var. mentagrophytes,” *Kaminski’s Digital Image Library of Medical Mycology, University of Adelaide*, 2006. <https://www.adelaide.edu.au/mycology/fungal-descriptions-and-antifungal-susceptibility/dermatophytes/> (accessed Apr. 05, 2022).
- [337] C. S. Chan, S. M. McAllister, A. H. Leavitt, B. T. Glazer, S. T. Krepski, and D. Emerson, “The architecture of iron microbial mats reflects the adaptation of chemolithotrophic iron oxidation in freshwater and marine environments,” *Front. Microbiol.*, vol. 7, pp. 1–18, 2016, doi: 10.3389/fmicb.2016.00796.
- [338] H. Furnes, K. Muehlenbachs, O. Tumyr, T. Torsvik, and C. Xenophontos, “Biogenic alteration of volcanic glass from the Troodos ophiolite, Cyprus,” *J. Geol. Soc. London.*, vol. 158, no. 1, pp. 75–84, 2001, doi: 10.1144/jgs.158.1.75.
- [339] H. Furnes, I. H. Thorseth, T. Torsvik, K. Muehlenbachs, H. Staudigel, and O. Tumyr, “Identifying bio-interaction with basaltic glass in oceanic crust and implications for estimating the depth of the oceanic biosphere: A review,” *Geol. Soc. Spec. Publ.*, vol. 202, pp. 407–421, 2002, doi: 10.1144/GSL.SP.2002.202.01.21.
- [340] N. McLoughlin, H. Staudigel, H. Furnes, B. Eickmann, and M. Ivarsson, “Mechanisms of microtunneling in rock substrates: Distinguishing endolithic biosignatures from abiotic microtunnels,” *Geobiology*, vol. 8, no. 4, pp. 245–255, 2010, doi: 10.1111/j.1472-4669.2010.00243.x.
- [341] Y. Oaki and H. Imai, “Experimental Demonstration for the Morphological Evolution of Crystals Grown in Gel Media,” *Cryst. Growth Des.*, vol. 3, no. 5, pp. 711–716, 2003.
- [342] J. M. García-Ruiz, “Geochemical Scenarios for the Precipitation of Biomimetic Inorganic Carbonates,” in *Carbonate Sedimentation and Diagenesis in the Evolving Precambrian World*, J. P. Grotzinger and N. P. James, Eds. Tulsa, Oklahoma: Society for Sedimentary Geology, 2000, pp. 75–89. doi: 10.2110/pec.00.67.0075.

- [343] S. Ji and J. Ding, “A macroscopic helix formation induced by the shrinking of a cylindrical polymeric hydrogel,” *Polym. J.*, vol. 33, no. 9, pp. 701–703, 2001, doi: 10.1295/polymj.33.701.
- [344] L. M. Barge *et al.*, “From chemical gardens to chemobrionics,” *Chem. Rev.*, vol. 115, no. 16, pp. 8652–8703, 2015, doi: 10.1021/acs.chemrev.5b00014.
- [345] J. H. E. Cartwright, J. M. García-Ruiz, M. L. Novella, and F. Otálora, “Formation of chemical gardens,” *J. Colloid Interface Sci.*, vol. 256, no. 2, pp. 351–359, 2002, doi: 10.1006/jcis.2002.8620.
- [346] T. H. Hazlehurst, “Structural precipitates: The silicate garden type,” *J. Chem. Educ.*, pp. 286–289, 1941, doi: 10.1021/ed018p286.
- [347] M. Copisarow, “The Liesegang phenomenon and stratification,” *J. Chem. Soc.*, no. 222, pp. 222–234, 1927, doi: 10.1039/jr9270000222.
- [348] J. M. Garcia-Ruiz and J. L. Amoros, “Crystal aggregates with induced morphologies grown by silica gel technique.,” *Bull. Mineral.*, vol. 104, pp. 107–113, 1981, doi: 10.3406/bulmi.1981.7442.
- [349] J. M. García-Ruiz and J. L. Amorós, “Morphological aspects of some symmetrical crystal aggregates grown by silica gel technique,” *J. Cryst. Growth*, vol. 55, no. 2, pp. 379–383, 1981, doi: 10.1016/0022-0248(81)90038-5.
- [350] P. Kresten and F. Kresten, “Hill-forts with vitrified or calcined ramparts: index and reference list (Report #R02-1996).” Geoarchaeological Laboratory (GAL), The Central Board of National Antiquities, Department of Archaeological Excavations, Uppsala, Sweden, pp. 1–100, 1996.
- [351] R. J. Hijmans, S. E. Cameron, J. L. Parra, P. G. Jones, and A. Jarvis, “Very high resolution interpolated climate surfaces for global land areas,” *Int. J. Climatol.*, vol. 25, no. 15, pp. 1965–1978, 2005, doi: 10.1002/joc.1276.
- [352] C. Koeberl, C. Denison, R. A. Ketcham, and W. U. Reimold, “High-resolution X-ray computed tomography of impactites,” *J. Geophys. Res. E Planets*, vol. 107, no. 10, pp. 19–1, 2002, doi: 10.1029/2001je001833.
- [353] D. R. Brothwell, A. C. Bishop, and A. R. Woolley, “Vitrified forts in Scotland: A problem in interpretation and primitive technology,” *J. Archaeol. Sci.*, vol. 1, pp. 101–107, 1974, doi: 10.1016/0305-4403(74)90020-X.
- [354] C. R. L. Friend, N. R. Charnley, H. Clyne, and J. Dye, “Experimentally produced glass compared with that occurring at The Torr, NW Scotland, UK: vitrification through biotite melting,” *J. Archaeol. Sci.*, vol. 35, no. 12, pp. 3130–3143, 2008, doi: 10.1016/j.jas.2008.06.022.
- [355] E. Díaz Martínez, A. M. M. Soares, P. Kresten, and L. Glazovskaya, “Evidence for wall vitrification at the Late Bronze Age settlement of Passo Alto (Vila Verde de Ficalho, Serpa, Portugal),” *Rev. Port. Arqueol.*, vol. 8, no. 1, pp. 151–161, 2005.
- [356] R. Grapes, “Anthropogenic Pyrometamorphism,” in *Pyrometamorphism*, Edition 2., R. Grapes, Ed. Berlin: Springer-Verlag Berlin Heidelberg, 2011, pp. 191–218.
- [357] C. R. L. Friend, J. Dye, and M. B. Fowler, “New field and geochemical evidence from vitrified forts in South Morar and Moidart, NW Scotland: further insight into melting and the process of vitrification,” *J. Archaeol. Sci.*, vol. 34, no. 10, pp. 1685–1701, 2007, doi: 10.1016/j.jas.2006.12.007.

- [358] E. Díaz-Martínez, “Origin of the Vesicular Glass of the El Gasco (Caceres , Spain): Vitrification of a Protohistoric Human Construction,” *Geo-Temas*, vol. 6, no. 1, pp. 33–36, 2004.
- [359] G. Salviulo, A. Silvestri, G. Molin, and R. Bertoncello, “An archaeometric study of the bulk and surface weathering characteristics of Early Medieval (5th-7th century) glass from the Po valley, northern Italy,” *J. Archaeol. Sci.*, vol. 31, no. 3, pp. 295–306, 2004, doi: 10.1016/j.jas.2003.08.010.
- [360] V. Lampropoulos, A. Kalagri, and L. Valsamis, “An Attempt to Face the Problem of Iridescence on Archaeological Glass,” in *Hyalos Vitrum Glass: History, Technology and Conservation of Glass and Vitreous Materials in the Hellenic World*, G. Kordas, Ed. Athens: Glasnet Publications, 2002, pp. 311–316.
- [361] D. J. M. Ngan-tillard, D. J. Huisman, F. Corbella, and A. Van Nass, “Over the rainbow? Micro-CT scanning to non-destructively study Roman and early medieval glass bead manufacture,” *J. Archaeol. Sci.*, vol. 98, pp. 7–21, 2018, doi: 10.1016/j.jas.2018.07.007.
- [362] R. A. Ketcham and W. D. Carlson, “Acquisition, optimization and interpretation of x-ray computed tomographic imagery: Applications to the geosciences,” *Comput. Geosci.*, vol. 27, no. 4, pp. 381–400, 2001, doi: 10.1016/S0098-3004(00)00116-3.
- [363] D. R. Baker *et al.*, “An introduction to the application of X-ray microtomography to the three-dimensional study of igneous rocks,” *Lithos*, vol. 148, pp. 262–276, 2012, doi: 10.1016/j.lithos.2012.06.008.
- [364] R. K. Rai, V. P. Singh, and A. Upadhyay, “Soil Analysis,” in *Planning and Evaluation of Irrigation Projects: Methods and Implementation*, London: Elsevier, 2017, pp. 505–523. doi: 10.1016/B978-0-12-811748-4.00017-0.
- [365] The James Hutton Institute, “National Soil Map of Scotland,” *Used with the permission of The James Hutton Institute. All rights reserved. Any public sector information contained in these data is licensed under the Open Government License v.2.0.*, 2017. <https://soils.environment.gov.scot/> (accessed Sep. 22, 2020).
- [366] G. Nuyts, S. Cagno, J. Jaroszewicz, H. Wouters, and K. De Vis, “High-resolution Desktop Microcomputed Tomography for the Evaluation of Reducing Treatments on Historical Glass Suffering From Manganese Browning,” in *Recent Advances in Glass, Stained-Glass, and Ceramics Conservation 2013*, H. Roemich and K. Van Lookeren Campagne, Eds. Zwolle, Netherlands: SPA Uitgevers, 2013, pp. 201–209. doi: 10.13140/RG.2.1.1362.6009.
- [367] D. K. Smith, “Mineralogical, Textural And Compositional Data On The Alteration Of Basaltic Glass From Kilauea, Hawaii To 300°C: Insights To The Corrosion Of A Borosilicate Glass Waste-Form,” *Mat. Res. Soc. Symp. Proc.*, vol. 212, pp. 115–121, 1991.
- [368] I. H. Thorseth, H. Furnes, and O. Tumyr, “A textural and chemical study of Icelandic palagonite of varied composition and its bearing on the mechanism of the glass-palagonite transformation,” *Geochim. Cosmochim. Acta*, vol. 55, no. 3, pp. 731–749, 1991, doi: 10.1016/0016-7037(91)90337-5.
- [369] B. Grambow, M. J. Jercinovic, R. C. Ewing, and C. D. Byers, “Weathered Basalt Glass: A Natural Analogue for the Effects of Reaction Progress on Nuclear Waste Glass Alteration,” *Mat. Res. Soc. Symp. Proc.*, vol. 50, pp. 263–272, 1985.
- [370] S. R. Gislason and H. P. Eugster, “Meteoric water-basalt interactions. I: A laboratory

- study,” *Geochemica Cosmochim. Acta*, vol. 51, pp. 2827–2840, 1987.
- [371] S. R. Gislason, D. R. Veblen, and K. J. T. Livi, “Experimental meteoric water-basalt interactions: Characterization and interpretation of alteration products,” *Geochim. Cosmochim. Acta*, vol. 57, no. 7, pp. 1459–1471, 1993, doi: 10.1016/0016-7037(93)90006-I.
- [372] F. Mees, E. Cornelis, P. Jacobs, M. T. D. Cárbo, and H. Römich, “Microfocus X-ray computed tomography analysis of corroded glass objects,” *Eng. Geol.*, vol. 103, no. 3–4, pp. 93–99, 2009, doi: 10.1016/j.enggeo.2008.06.012.
- [373] R. C. Ewing, R. A. Whittleston, and B. W. D. Yardley, “Geological disposal of nuclear waste: A primer,” *Elements*, vol. 12, no. 4, pp. 233–237, 2016, doi: 10.2113/gselements.12.4.233.
- [374] T. Keith and L. Staples, “Zeolites in Eocene basaltic pillow lavas of the Siletz River volcanics, central Coast Range, Oregon,” *Clays Clay Miner.*, vol. 33, no. 2, pp. 135–144, 1985, doi: 10.1346/CCMN.1985.0330208.
- [375] S. Morad and A. A. Aldahan, “Alteration of detrital Fe-Ti oxides in sedimentary rocks,” *Geol. Soc. Am. Bull.*, vol. 97, pp. 567–578, 1986, doi: 10.1130/0016-7606(1986)97<567.
- [376] S. Morad, “Diagenesis of titaniferous minerals in Jurassic sandstones from the Norwegian Sea,” *Sediment. Geol.*, vol. 57, no. 1–2, pp. 17–40, 1988, doi: 10.1016/0037-0738(88)90016-4.

# 11. Appendix I: XCT Analysis Method

A semi-automated quantitative analysis method was developed (in the ‘Dragonfly’ software from Object Research Systems) to investigate if low density surface layers evident in XCT of vitrified hillfort materials may have been formed via glass dissolution (Chapter 8). Evident as darker regions in XCT data, the distribution of these layers/regions relative to sample surfaces which were both accessible and inaccessible to the external environment was probed by segmenting XCT datasets into various volumes. The overlap of these volumes was calculated and compared to the equivalent overlap generated by a random surface distribution of material. This method was then tested and verified, with errors estimated during a sensitivity analysis.

## 11.1. Data segmentation

Hillfort XCT datasets were first segmented into Regions Of Interest (ROIs). Segmentation of the chamber environment (Less Attenuating Material; LAM), bulk sample and dark regions of interest (DROI) was completed via thresholding. Multiple attempts were made to determine threshold values via semi-quantitative methods, however none were deemed as reliable as performing this operation by eye. Compromises were necessarily made whilst performing this (Figure 11.1), however efforts were made to reduce human bias by repeating visual threshold determinations five times per sample. The final utilised threshold values were the calculated mean of these five values, with the standard deviation on this used for the sensitivity analysis.

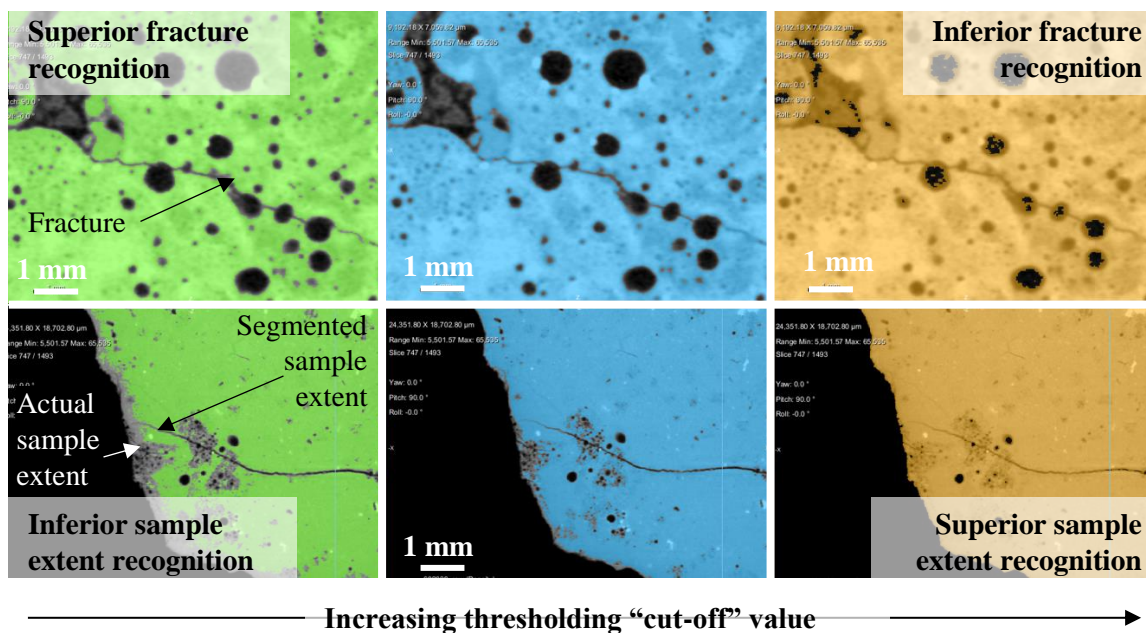


**Figure 11.1:** Screenshots collected during samples segmentation illustrate the compromise made between fracture recognition (top row of images) and sample extent recognition (bottom row) when determining thresholds. A compromise (central images) was made between these.

After implementing threshold values, limited smoothing and filtering of all segmented volumes was undertaken to remove a small number of mis-identified voxels. Segmented volumes were visually inspected to ensure acceptability. In one sample (#601-602) manual adjustments were also made using the “three-dimensional paintbrush function,” after it was observed that some solid sample was incorrectly segmented as DROI based on greyscale intensity alone. ROIs were then further divided. The LAM ROI was subdivided into accessible and inaccessible

regions, with inaccessible LAM defined as LAM that is *not* accessible to the ‘outside’ environment in any dimension (at the resolution of the image) and accessible LAM *vice versa*.

Regions within a given vicinity of the solid/LAM interface were also segmented, as identified in Table 11.2. “Vicinity” is defined by default as being within ~200 μm of the boundary, though other definitions of this were initially trialled and later utilised during the sensitivity analysis. This “vicinity” region was subdivided across the solid/LAM interface: *Solid* in the vicinity of the boundary was made distinct from *LAM* in the vicinity of the boundary. Regions were also subdivided by the accessibility of the solid/LAM interface: Solid in the vicinity of an *accessible* surface was distinguished from solid in the vicinity of an *inaccessible* surface. A region comprising the Solid and LAM outside the vicinity of *any* surface was also created. The intersections between these generated regions and those of interest from a dissolution perspective (Dark Regions Of Interest; DROI) were then determined, as in Table 11.3.

Greyscale-based ROI	Initial contextual location-based ROI	Final contextual location-based ROIs
Solid/LAM	Region in the vicinity of any <i>inaccessible</i> surface	Solid in vicinity of any inaccessible surface LAM in vicinity of any inaccessible surface
	Region in the vicinity of any <i>accessible</i> surface	Solid in vicinity of any accessible surface LAM in vicinity of any accessible surface
	Region in vicinity of acc- & inaccessible surface	Solid in vicinity of acc- & inaccessible surface LAM in vicinity of acc- & inaccessible surface
	Region outside the vicinity of any surface	Solid outside the vicinity of any surface LAM outside the vicinity of any surface

**Table 11.2:** XCT dataset was segmented into Regions of Interest (ROIs) on the basis of greyscale intensity (Column 1) and whether regions were in the vicinity of an inaccessible and/or accessible surface (Column 2). These ROIs were then combined to give ROIs reflecting the material type, potential vicinity to sample surfaces, and in/accessibility of that surface.

ROI ID	Contextual location-based ROIs	Intersection ROIs
DROI	LAM in vicinity of <i>inaccessible</i> surface	DROI intersects LAM in the vicinity of any inaccessible surface
	LAM in vicinity of <i>accessible</i> surface	DROI intersect LAM in the vicinity of any accessible surface
	LAM in the vicinity of <i>both accessible &amp; inaccessible</i> surface	DROI intersects LAM in the vicinity of both accessible & inaccessible surface
	LAM outside the vicinity of any surface	DROI intersects LAM outside the vicinity of any surface

**Table 11.3:** The intersection between ROIs comprising potential dissolution features (DROI) and ROIs based on contextual location within the sample. Cell shading referred to in-text.

## 11.2. Statistical treatment

To quantify the distribution of DROI, the volume of the DROI intersection ROIs (grey cells in Table 11.3) were calculated and re-expressed as percentages of all analysed DROI. Notably, the latter total excludes any DROI occurring outside the vicinity of sample surfaces. This fortuitously eliminates both the majority of misidentified DROI within the sample interior and material physically unconnected to the sample (e.g. loose debris/soil) from subsequent analysis.

Statistical summaries were calculated to show the difference between the observed distribution of DROI and a calculated “null hypothesis” distribution ( $N_0$ ) resulting from random distribution of DROI across the sample surface. This methodology was necessary to ensure results were not affected by the raw quantity of accessible/inaccessible regions.

$N_0$  was determined using the surface area of each region (green cells in Table 11.3), because DROI occurs on (and is analysed relative to) sample surfaces. Surface areas were thus calculated and re-expressed as a percentage of total surface area.  $N_0$  was then calculated by assuming that the amount of DROI in the vicinity of a given surface (as a percentage of DROI within the vicinity of *any* surface) should be equal to the surface area of this same region (as a percentage of the entire sample surface area).

Deviations from  $N_0$  were determined by subtracting  $N_0$  from the observed quantified distributions. A positive deviation thus indicates more DROI within a region than expected if  $N_0$  were satisfied.

## 11.3. Method verification

To verify methodological validity, the above method was applied *verbatim* to a synthesised “Test Dataset”. This dataset was generated, in the *Dragonfly* software, by re-shaping a cube of gaussian noise (to replicate the “solid sample”), before manually removing random areas of a “darker” region that was initially added to all sample faces (generating DROI). A second larger cube of gaussian noise with lower greyscale intensities was added surrounding this first dataset to replicate “LAM” surrounding the sample.

Within the applied method, thresholding values were reliably and consistently determinable by eye, hence no mean or standard deviation was calculable for the Test Dataset. “Vicinity” was also defined by eye, as was necessary given the arbitrary (and potentially unrepresentative) resolution of the Test Dataset.

Results from the test case are presented alongside the results from hillfort sample analysis in Figure 11.2. These indicate negligible deviation from  $N_0$  (<3%) for the test dataset, showing that the statistical analysis employed is reliable. Minimal deviations from random (<3%) may be statistical noise, potentially amplified by limited test dataset dimensions and the only *pseudo*-randomly generated dataset. This testing offers no information on segmentation reliability.

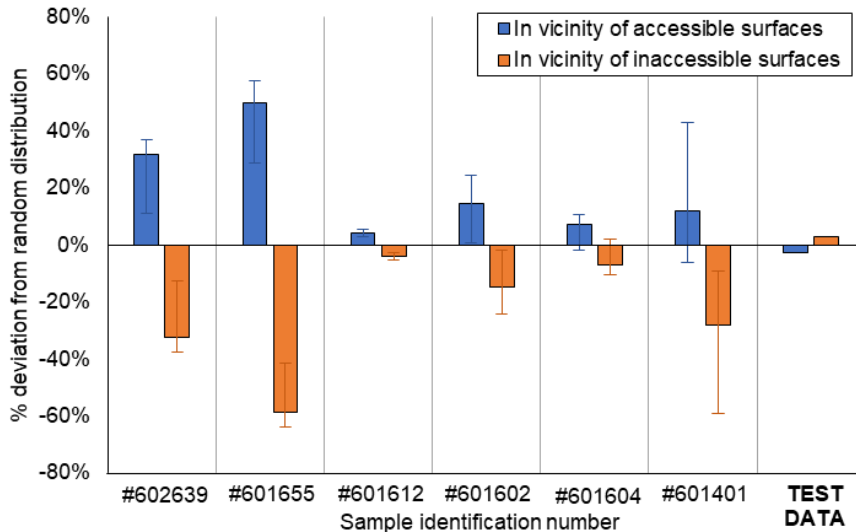


**Figure 11.2:** Results from analysis of all data, including the artificially generated Test Dataset. Values show deviation from random surface distribution, with error bars produced by varying thresholding values (by  $\pm 1SD$ ) as in Section 11.4.

### 11.4. Sensitivity/error analysis

A sensitivity analysis was completed to allow approximate error estimation. A series of trials were conducted (utilising the method above) with variability in the most subjective parameters: the numerically arbitrary vicinity definition and the visually assessed thresholding boundaries.

Sensitivity to thresholding was determined by repeating the analysis using variable DROI upper and lower threshold values (Table 11.4). Though more thresholding boundaries (and combinations of these) could have been varied, extensive trials on two datasets revealed that the results obtained by varying the DROI thresholds alone bound the limits of all other possible trials. Hence, additional trials (Trials 3-8) were not completed for other datasets.

Trial #	Threshold value for...	
	DROI lower/ LAM upper	DROI upper/ Solid lower
Trial 0 (default case)	$\mu$	$\mu$
Trial 1	$\mu - SD$	$\mu + SD$
Trial 2	$\mu + SD$	$\mu - SD$

**Table 11.4:** DROI threshold values used in ‘trial runs’ performed during the error analysis. Values used in trials were calculated using the mean threshold value ( $\mu$ ) and the Standard Deviation (SD) on this mean value, as determined in Section 11.1.

To quantify sensitivity to vicinity definitions/quantifications, the method was then also repeated (in Trials 9-10) using vicinity definitions that varied by approximately  $\pm 30\%$  from the original value (Trial 0), as shown in Table 11.5. Achieving exactly  $\pm 30\%$  for all datasets was impossible due to image resolutions. To avoid the time intensive process of repeating the entire methodology, these trials were completed by recalling the output of the default case (Trial 0) and eroding or dilating the location-based ROIs (see Table 11.3) by the amounts specified in Table 11.5. After manually verifying the new “vicinity” definition was  $\pm 30\%$  of the original, intersections were then recalculated.

Dataset ID #	No. of voxels added or subtracted in Trials 9/10	Resulting “vicinity” change in microns (as % of original “vicinity”)
602639	2	65.4 (31%)
601401	3	61.9 (26%)
601604	1	61 (29%)
601602	2	85.5 (36%)
601612	1	60.1 (29%)
601655	2	53.1 (27%)

**Table 11.5:** Parameters used in the vicinity definition sensitivity analysis. The number of voxels required to vary the “vicinity” by circa  $\pm 30\%$  is shown in column two, with the resulting actual change shown in microns and as a percentage of the original definition in column three.

Sensitivity analysis results are summarised in Table 11.6. This showed that DROI analysis is highly sensitive to thresholding: Varying thresholding parameters by one standard deviation on the threshold value on average causes  $\sim 25\%$  variation in the outputted values for DROI.

Sensitivity analyses imply a high dependence on quantities (thresholding values) that can only be qualitatively estimated “by eye”. These values have significant uncertainty which arises principally due to difficulties associated with identifying DROI using greyscale values exclusively. Future work may investigate additional segmentation methods, however at present this limits confidence. Promisingly, however, sensitivity analysis revealed low dependence on arbitrary definitions of vicinity.

			Hillfort sample number				
			602639	601655	601612	601604	601401
Thresholding	Accessible	Max	36.8%	57.6%	5.5%	10.5%	42.7%
		Min	10.8%	28.8%	2.9%	-1.8%	-6.2%
		Range	25.9%	28.8%	2.6%	12.3%	48.9%
	Inaccessible	Max	-12.6%	-41.4%	-2.9%	1.8%	-9.1%
		Min	-37.9%	-63.9%	-5.5%	-10.5%	-59.2%
		Range	25.3%	22.5%	2.6%	12.3%	50.1%
Vicinity definition	Accessible	Max	31.6%	57.6%			
		Min	30.0%	37.6%			
		Range	1.7%	20%			
	Inaccessible	Max	-31.7%	-57.9%			
		Min	-33.0%	-59.4%			
		Range	1.2%	1.5%			

**Table 11.6:** Results from the sensitivity analysis completed by varying thresholding values by  $\pm 1SD$  and vicinity definitions by  $\pm 30\%$ , as outlined in text and in Table 11.4 and Table 11.5. (Positive numbers indicate more dark layer occurrence in a given region than could expected from a random distribution, with negative numbers indicating less than expected).